universität wien

DISSERTATION / DOCTORAL THESIS

Titel der Dissertation /Title of the Doctoral Thesis

Towards reconstitution of autophagy initiation and phagophore expansion

verfasst von / submitted by

Verena Baumann, MSc

angestrebter akademischer Grad / in partial fulfilment of the requirements for the degree of

Doctor of Philosophy (PhD)

Wien, 2022 / Vienna 2022

Studienkennzahl lt. Studienblatt / degree programme code as it appears on the student record sheet:	A 794 685 490
Dissertationsgebiet lt. Studienblatt / field of study as it appears on the student record sheet:	Molekulare Biologie
Betreut von / Supervisor:	Univ. Prof. Dipl.-Biol. Dr. Sascha Martens

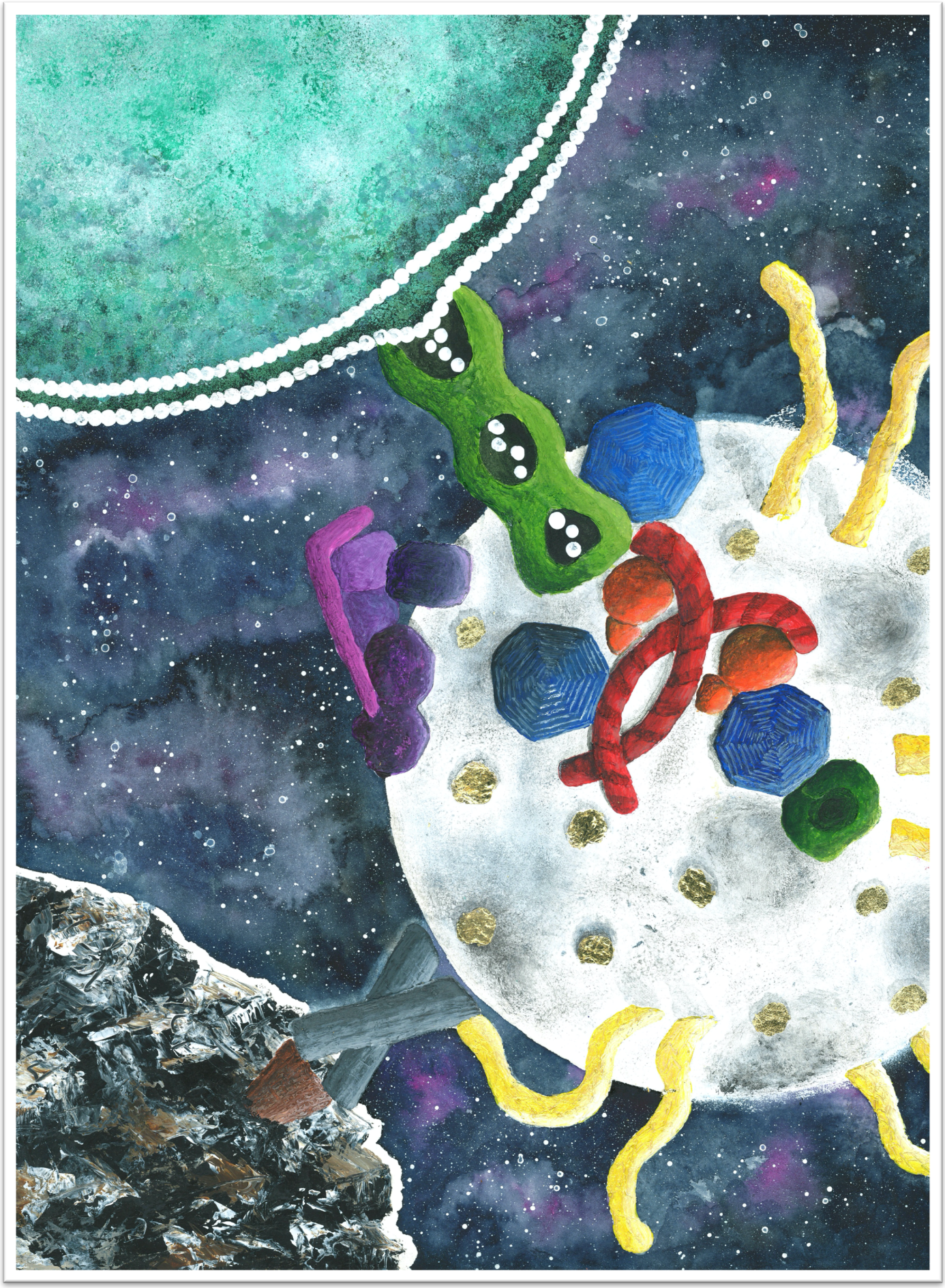

Acknowledgements

The years towards a PhD cause changes in all of us and I am no exception. I learned a lot, not only in scientific terms but also on a personal level and not for one moment have I ever regretted my choice of coming to Vienna for this adventure.

First of all, my gratitude goes to Sascha for entrusting me with this very special project and letting me be part of the best yeast team ever. His enthusiasm and guidance made and still make it a real joy to come to the lab.
Another big “thanks” goes to Justyna. Being allowed to learn from you and walk this path in your company shaped me a lot as a scientist but also as a person.
Next, I want to thank the old and new members of the yeast group, in particular Martina and Nico. You showed me what teamwork really means and without you this work would not have been possible.
I further want to thank all the former and current colleagues and lab mates for making the last years so enjoyable and fruitful. Although the constellation continuously changed over the years, the spirit was always clear: We are all pulling in the same direction.
Thanks to the members of my TAC committee, Thomas Leonard and David Teis for your input and feedback. Furthermore, I want to thank Fulvio Reggiori, Tassula Proikas-Cezanne and Yasin Dagdas for agreeing to review my thesis.

Special thanks go to Justyna, Martina and Manuel for taking the exhausting task of proof-reading this thesis.

I want to thank all of my friends that stood by me over the last years and made life so much more awesome. And last but not least my gratitude goes to my beloved ones around me, namely my family and Manuel. Without your continuous support and encouragement and love, I would not be where or who I am today and I am eternally grateful to have you in my life.

Zusammenfassung

Damit Zellen gesund und funktionsfähig bleiben, müssen schadhafte und überschüssige Bestandteile rasch und effizient beseitigt werden. Der dafür verantwortliche Prozess, der den Abbau und die Wiederverwertung von cytoplasmatischem Material wie defekten Organellen, gefährlichen Pathogenen oder aggregierten Proteinen (Cargo) ermöglicht, wird als Makroautophagie (im Folgenden Autophagie) bezeichnet. Die Autophagie ist hoch konserviert, vom einzelligen Pilz bis hinauf zum Menschen. Am Anfang des Abbauweges wird eine Membranstruktur, die Phagophore, von Grund auf neu gebildet. Diese wächst in weiterer Folge um das abzubauende Material herum, bis sie es gänzlich umschließt. Die dabei entstehende Doppelmembran-Organelle, das Autophagosom, fusioniert im letzten Schritt mit dem Lysosom, wo ihr Inhalt enzymatisch verdaut wird.

Die einzelnen Faktoren, die eine erfolgreiche Autophagie gewährleisten, konnten in den letzten Jahren identifiziert und ihre Funktionen Schritt für Schritt entschlüsselt werden. Wie all diese Bausteine jedoch zusammenarbeiten um ein Autophagosom zur richtigen Zeit am richtigen Ort zu generieren, ist in vielen Bereichen noch ungeklärt. Diese Doktorarbeit legt einen speziellen Fokus auf Atg9 Vesikel, die als Plattform für die Rekrutierung weiterer Autophagie-Faktoren identifiziert werden konnten. Dabei werden sie zum Keim für die Entstehung des Autophagosoms. Unter den assemblierten Proteinen finden sich Atg21 und Atg2-Atg18. Mit Hilfe biochemischer und zellbiologischer Methoden konnte gezeigt werden, dass Atg2-Atg18 die Rekrutierung des Atg12 – Atg5-Atg16 Komplexes an die Phagophore-Assembly-Site (PAS), die hauptsächlich von Atg21 forciert wird, unterstützt. Die Hauptfunktion von Atg2 scheint darin zu bestehen, Kontakt zwischen dem ER und der Isolationsmembran herzustellen und Lipide in das sich bildende Autophagosom zu transferieren. In der vorliegenden Arbeit wurde auch gezeigt, dass der Lipidtransfer durch Atg2, Atg9 Proteoliposomen zu einem potenten Substrat für Atg8 Lipidierung macht. Zusätzlich wurde die Interaktion zwischen Atg9 und Atg11 untersucht, mittels derer das Cargo-Material mit der Isolationsmembran verbunden wird.

Abstract

To stay healthy and functional, cells have to dispose any harmful and superfluous material in a fast and efficient manner. The responsible process that manages the degradation and recycling of cargo material like damaged organelles, invading pathogens or aggregated proteins is called macroautophagy (hereafter referred to as autophagy). Autophagy employs molecular mechanisms that are highly conserved from single cell fungi up to humans. It starts with a *de novo* formation of a membranous structure termed isolation membrane that continues to grow all around the material destined for degradation. The thereby generated double-membrane organelle is called an autophagosome. In the last step an autophagosome fuses with the lytic compartment of the cell where its content is degraded.

Factors required for successful autophagic degradation have been identified and currently their individual contributions to the process are extensively studied. Yet, many aspects regarding the spatiotemporal organization of autophagosome formation are still enigmatic. Of particular interest for this thesis are Atg9 vesicles, which are shown to function as a platform for the assembly of the downstream autophagic machinery. Thus, they become seeds for the newly generated autophagosome. Among the recruited proteins are Atg21 and Atg2-Atg18. By employing biochemical and cell biological assays, it is shown that Atg2-Atg18 supports the Atg21-driven recruitment of the Atg12–Atg5-Atg16 complex to the PAS. However, the main function of Atg2 seems to be the establishment of ER – isolation membrane contact sites and lipid transfer into the growing isolation membrane. The study demonstrates that Atg2 lipid transfer renders Atg9 proteoliposomes a potent target for Atg8 conjugation. An additional focus was put on the analysis of the interaction between Atg9 and a scaffold protein Atg11, which directly links the formation of the isolation membrane to the cargo.

Table of contents

Acknowledgements iii
Zusammenfassung vii
Abstract ix
Table of contents xi
Abbreviations xiii
Introduction 1
Autophagy – a cellular recycling process 1
The three major types of autophagy 1
Chaperone-mediated autophagy (CMA) 2
Microautophagy 2
Macroautophagy 3
The molecular mechanisms behind autophagy 6
Bulk autophagy induction in budding yeast 7
Initiation of selective autophagy in budding yeast 7
Atg9 vesicles, the seeds for autophagosome formation 10
The PI3KC3-complex 1 12
PI3P binding factors (PROPPINs) 13
Atg2-Atg18 – the membrane binding and lipid transfer complex 14
Atg8 and its two conjugation systems 16
Reconstitution of autophagosome nucleation defines Atg9 vesicles as seeds for membrane formation 19
Mechanism of Atg9 recruitment by Atg11 in the cytoplasm-to-vacuole targeting pathway 77
Discussion 92
References 98

Abbreviations

ACS	acyl-coenzyme A synthetase
Ams1	alpha-mannosidase1
Ape1	aminopeptidase 1
Ape4	aspartyl aminopeptidase 4
Atg	AuTophaGy-related
CMA	chaperone-mediated autophagy
COPII	coat protein complex II
Cvt	cytoplasm to vacuole targeting
ER	endoplasmic reticulum
ERES	ER exit sites
FIP200	family interacting protein of 200 kDa
GABARAP	ɣ-amino butyric acid receptor associated protein
GUV	giant unilamellar vesicle
HORMA	HOP1, REV7 and MAD2
HSC70	heat shock cognate protein of 70 kDa
LC3	microtubule-associated protein 1 light chain 3
LP	lateral pore
LAMP2A	lysosome-associated membrane protein type 2A
LIR	LC3-interacting region
LTP	lipid transfer protein
mApe	mature Ape1
mTORC1	mechanistic target of rapamycin complex 1
NMR	nuclear magnetic resonance
PAS	phagophore assembly site
PE	phosphatidylethanolamine
PI	phosphatidylinositol
PI3KC3-C1	class III phosphatidylinositol 3-kinase complex 1
PI3P	phosphatidylinositol 3-phosphate
PMN	piecemeal microautophagy of the nucleus
prApe1	pre-aminopeptidase 1
TGN	trans-Golgi network
TORC1	target of rapamycin complex 1
ULK1	unc-51-like kinase 1
UPS	ubiquitin-proteasome-system
VP	vertical pore
Vps	vacuolar protein sorting
WIPI	WD-repeat protein interacting with phosphoinositides

Introduction

Autophagy – a cellular recycling process

In 1962, K.R. Porter and T. Ashford were the first to describe a process that mediates the degradation of cytoplasmic material in the lysosome (Ashford & Porter, 1962). One year later, Christian de Duve named the new biological pathway 'autophagy' (greek for self-eating). From then on it took 30 more years before more light was shed on the actual molecular players of the pathway. In the 1990s, several groups studying the process in yeast identified a number of conserved autophagy related genes (Baba et al., 1994; Harding et al., 1995; Thumm, Egner, Koch, Schlumpberger, Straub, Veenhuis, et al., 1994; Tsukada & Ohsumi, 1993). Since then, autophagy research has been driven towards a complete understanding of the molecular mechanism, its regulation and function.

Autophagy is highly conserved from yeast to humans being important for various processes in the cell. Initially observed as a response pathway to nutrient starvation, later studies have revealed that autophagy acts as a dynamic recycling system which is crucial for the maintenance of cellular homeostasis. In order to ensure protein and organelle turnover it is constantly active at a basal level. Stress conditions such as nutrient starvation, but also metabolic stress, cytotoxic stress caused by aggregated proteins and invading pathogens upregulate autophagy (Levine & Kroemer, 2008, 2019; Mizushima & Komatsu, 2011). Therefore, it is not surprising that defects in autophagy have been linked to various pathologies like cancer, neurodegeneration and lysosomal disorders (Saha et al., 2018). Autophagy has been shown to play a key role during differentiation, cell growth and development (Mizushima & Levine, 2010) and was further identified as an important player for the innate and adaptive immune response (Crotzer & Janice, 2010; Randow et al., 2013).

The three major types of autophagy

Autophagy can be divided into three types: chaperone-mediated autophagy (CMA), microautophagy and macroautophagy. They are distinguished by the mechanisms that transport the material designated for degradation (referred to as cargo) to the lysosomal compartment.

Chaperone-mediated autophagy (CMA)

During chaperone-mediated autophagy cytosolic target proteins carrying a certain pentapeptide motif (KFERQ or KFERQ-like) are recognized and bound by the heat shock-cognate protein of 70 kDa (hsc70) (Chiang et al., 1989). After recognition, the substrate-chaperone complex translocates to the lysosomal membrane where it interacts with the cytosolic tail of the monomeric lysosome-associated membrane protein type 2A (LAMP-2A) (Cuervo & Dice, 1996). Upon binding, LAMP-2A assembles into a multimeric protein complex, which is further stabilized by the luminal Hsp90 protein (Bandyopadhyay et al., 2008). To enable translocation of the substrate into the lysosome it has to be unfolded by Hsc70 and further co-chaperones that can be found on the lysosomal membrane (Salvador et al., 2000). Another form of Hsc70 being present in the lysosome (lys-hsc70) is required for the translocation through the membrane (Agarraberes et al., 1997). Once inside the lysosome the substrate can be degraded (Cuervo & Wong, 2014).

Chaperone-mediated autophagy has been observed in almost all mammalian cell types as a response mechanism to nutrient deprivation. However, in contrast to the other forms of autophagy it takes much longer (8-10 hours into starvation) to be initiated. A screen for substrates analysing the presence of the recognition motif in protein sequences revealed that ~30% of the cytosolic proteins are putative targets of CMA (Wing et al., 1991). Later studies validated glycolytic enzymes, transcription factors, Ca^{2+}-binding, lipid binding proteins and components of other proteolytic systems as targets. While one task of CMA is clearly to provide the cell with building blocks for essential proteins during starvation it can also act in a selective manner. Due to the necessity of the recognition sequence in the target substrate, damaged superfluous soluble proteins can be selectively degraded while the levels of others stay unaffected (Kaushik et al., 2011).

Microautophagy

Similar to macroautophagy also microautophagy was initially observed in mammals and subsequent studies mainly in yeast revealed more about its functions and the underlying mechanisms. During microautophagy the cytoplasmic cargo material is directly taken up by the lytic compartment. This is facilitated by the deformation of the lysosomal or endosomal membrane that thereby engulfs the material destined for

degradation. By budding off towards the lumen of the organelle a microautophagic body is formed which is further on degraded and recycled. Microautophagy can target any kind of cellular structure and a variety of different types of microautophagy has been observed and described so far. General microautophagy can act in a selective or non-selective manner. Endosomal microautophagy for example plays a crucial role during amino acid starvation by rapid degradation of particular proteins. Thereby selective autophagy is shut down and the cell is prepared for bulk autophagy initiation (Olsvik et al., 2019). Other types of microautophagy are the more specialized micropexophagy, piecemeal microautophagy of the nucleus (PMN) and micromitophagy that sequester organelles in a selective way (Li et al., 2012; Schuck, 2020).

Macroautophagy

The most extensively studied among the three types of autophagy is macroautophagy. It is highly conserved in all eukaryotes and it is also the main focus of the work described here.

In contrast to the above-mentioned forms, macroautophagy sequesters its cargo within *de novo* formed organelles separated from the lysosome. These new double membrane vesicles are called autophagosomes and are generated at endoplasmic-reticulum (ER)-associated sites. Autophagosome biogenesis starts with the nucleation of a small crescent-shaped membrane structure termed isolation membrane or phagophore. The isolation membrane further expands all around the cargo material. Through scission of the growing membrane the autophagosome is sealed and completed. In a last step the outer membrane of the autophagosome fuses with the lysosome in metazoans (or vacuole in fungi and plants). The inner membrane containing the cargo is released into the lumen of the lytic compartment as an autophagic body. This autophagic body is then degraded by lysosomal hydrolases thereby generating building blocks that can be recycled back into the cytosol (Figure 1) (Ohsumi, 2014; Wen & Klionsky, 2016).

Analogous to microautophagy also macroautophagy can occur in a selective or non-selective manner. Non-selective macroautophagy, also referred to as bulk autophagy, targets all kinds of cytoplasmic material in a random manner. It is induced upon nutrient and energy deprivation and its aim is to facilitate cell survival by recycling building blocks for the most essential components of the cell (Wen & Klionsky, 2016).

Unlike bulk autophagy, cargo selection during selective macroautophagy is tightly regulated. Only material destined for degradation is recognized by specific cargo receptors and tethered to the autophagosome. Further it is important that surplus material is efficiently excluded from the process (Zaffagnini & Martens, 2016). Selective macroautophagy plays an important role for the maintenance of cellular homeostasis by keeping the balance between production and degradation of cellular components. Another important cellular quality control mechanism is the ubiquitin-proteasome-system (UPS). However, while the UPS deals with short-lived, small proteins, macroautophagy is able to target long-lived proteins and large structures like protein complexes, organelles and even pathogens (Gubas & Dikic, 2021; Wen & Klionsky, 2016).

Since the process was first described, several genetic screens carried out in budding yeast (*Saccharomyces cerevisiae*) have identified over 40 so-called autophagy-related (Atg) genes (Baba et al., 1994; Harding et al., 1995; Klionsky et al., 2003; Thumm, Egner, Koch, Schlumpberger, Straub, Veenhuisb, et al., 1994; Tsukada, Miki; Ohsumi, 1993).

In order to gain a better understanding of the importance of autophagy for human health it has further on been closely studied in a wide range of model organisms. These studies revealed that a systemic homozygous deletion of many essential autophagic factors leads to embryonic or post-natal lethality. Tissue-specific knock-outs could then show that the functions of autophagy are critical throughout the body (Kawabata & Yoshimori, 2020; Kuma et al., 2017).

Especially in neuronal cells autophagy is of uttermost importance for function and survival. Neurons are post-mitotic cells and stay alive and functional for decades. This makes a well-functioning clearance of cellular waste crucial in order to prevent build-up of toxic debris. An impairment of autophagic function can lead to severe pathologies like Parkinson's disease, Alzheimer's disease or Huntington's disease. All these disorders are characterized by the accumulation of abnormal aggregates of misfolded proteins (Kawabata & Yoshimori, 2020; Khandia et al., 2019).

As far as cancer is concerned autophagy at the beginning was considered to act in a tumour-suppressive way. Due to its role of removing damaged factors specifically at early stages of tumorigenesis, tumour-growth is restricted and genome stability is preserved. However, by now it is clear that autophagy also has a major protective role of cancer cells by providing the cells with the necessary building blocks during nutrient

deprivation. It could further be shown that tumour cells facilitate their own growth by inducing non-autonomous autophagy in their microenvironment and are even capable of invoking organ wasting (Chavez-Dominguez et al., 2020; Katheder et al., 2017; Khezri et al., 2021; Saha et al., 2018; Sousa et al., 2016; Yang et al., 2018).

The core set of the genes necessary is shared by all types of autophagy while others are only involved in specific autophagic pathways. Although most of the participating proteins are known, it is still unclear how the factors combine their molecular functions to orchestrate the formation of a new organelle.

A commonly used model pathway to study selective macroautophagy in budding yeast is the cytoplasm-to-vacuole targeting (Cvt) pathway. This constitutively active pathway highjacks the autophagic machinery in order to transport the precursors of lysosomal hydrolases from the cytoplasm to the vacuole where they are proteolytically activated (Yamasaki & Noda, 2017). The Cvt-pathway is a very suitable model to study the mechanisms of autophagosome formation due to the high level of conservation of the involved factors from yeast to the mammalian system. It was therefore the model of choice for the here presented work.

In the following section the different phases and factors of macroautophagy (hereafter autophagy) will be presented in closer detail with a specific focus on the budding yeast system. Differences to the mammalian system will be described separately.

The molecular mechanisms behind autophagy

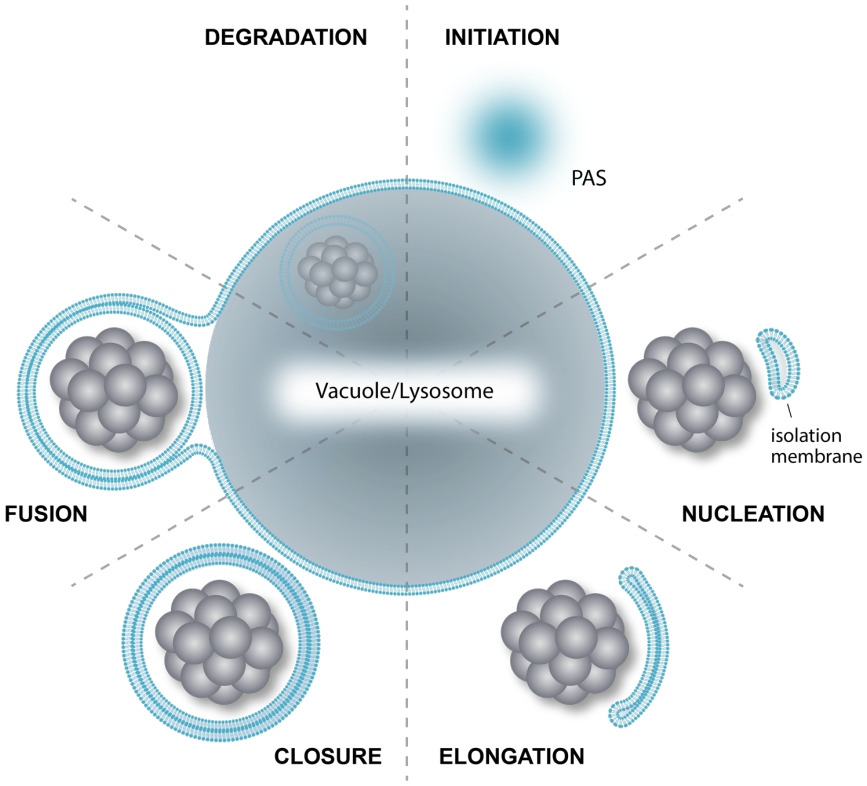

Figure 1: Schematic illustration of autophagosome formation
Upon initiation of autophagy, a membrane structure is formed de-novo. This so-called isolation membrane enwraps the cargo material. After closure the formed autophagosome fuses with the lysosome/vacuole, where the cargo is degraded by lysosomal/vacuolar hydrolases.

The autophagic process can be separated into several distinct stages covering the initiation, membrane nucleation, elongation, closure, fusion of the autophagosome with the lytic compartment and finally degradation and recycling of the cargo material (Figure 1). These steps require a well orchestrated interplay of various components. Although some types of autophagy require more specialized factors, a core machinery of proteins being responsible for the biogenesis of the autophagosome can be found in all types of autophagy (Feng et al., 2014). This machinery is recruited to the site of autophagosome formation, also referred to as isolation membrane-assembly site (PAS) in a strictly hierarchical manner after autophagy induction (Suzuki et al., 2007). In budding yeast the PAS has been described as a single perivacuolar region. Autophagy initiation, and therefore also PAS formation, differ between bulk and selective autophagy.

Bulk autophagy induction in budding yeast

During nutrient rich conditions, autophagy happens at a basal level. However, upon nutrient deprivation a strong induction can be observed. This is based on the inhibition of the target of rapamycin complex 1 (TORC1) (Kamada et al., 2000). Downstream of TORC1 we find the Atg1 complex, the first and most upstream component of the core autophagy machinery. The Atg1 complex consists of the Atg1-Atg13 and Atg17-Atg31-Atg29 sub-complexes (Feng et al., 2014). Both complexes are constitutively present in the cell. After autopagy induction they assemble into a supra-complex that further on recruits the downstream machinery, serving as PAS (Kabeya et al., 2009; Kraft et al., 2012; Yamamoto et al., 2016). The decreased activity of TORC1 leads to a dephosphorylation of its direct target Atg13, which is hyperphosphorylated under nutrient-rich conditions (Kamada et al., 2000, 2010). Due to the dephosphorylation of Atg13 the affinity towards Atg1 is increased. Atg1 is a serine-threonine kinase and so far the only identified protein kinase among the autophagic core machinery (Matsuura et al., 1997). Impairment of Atg1 kinase activity or the deletion of Atg1 lead to an accumulation of autophagic factors at the PAS and halt autophagy. (Suzuki et al., 2007). Starvation also increases the interaction between Atg1 and Atg17 via Atg13. Atg17 acts as a scaffold protein and is needed for the recruitment of Atg1-Atg13 to the PAS Suzuki et al., 2007a). Stronger binding of Atg1 to Atg13 and Atg17 goes hand in hand with an increased activity of Atg1 (Kabeya et al., 2005; Kamada et al., 2000). Especially the interaction with Atg13 induces the assembly of Atg1 into dimers or higher order structures. Subsequent auto-phosphorylation of Atg1 at T226 within its kinase activation loop *in trans* is then needed for Atg1 activity and induction of autophagy (Yeh et al., 2010, 2011).

Initiation of selective autophagy in budding yeast

In the following paragraph, the biosynthetic Cvt-pathway will be discussed in detail as a model for selective autophagy in yeast (Figure 2).

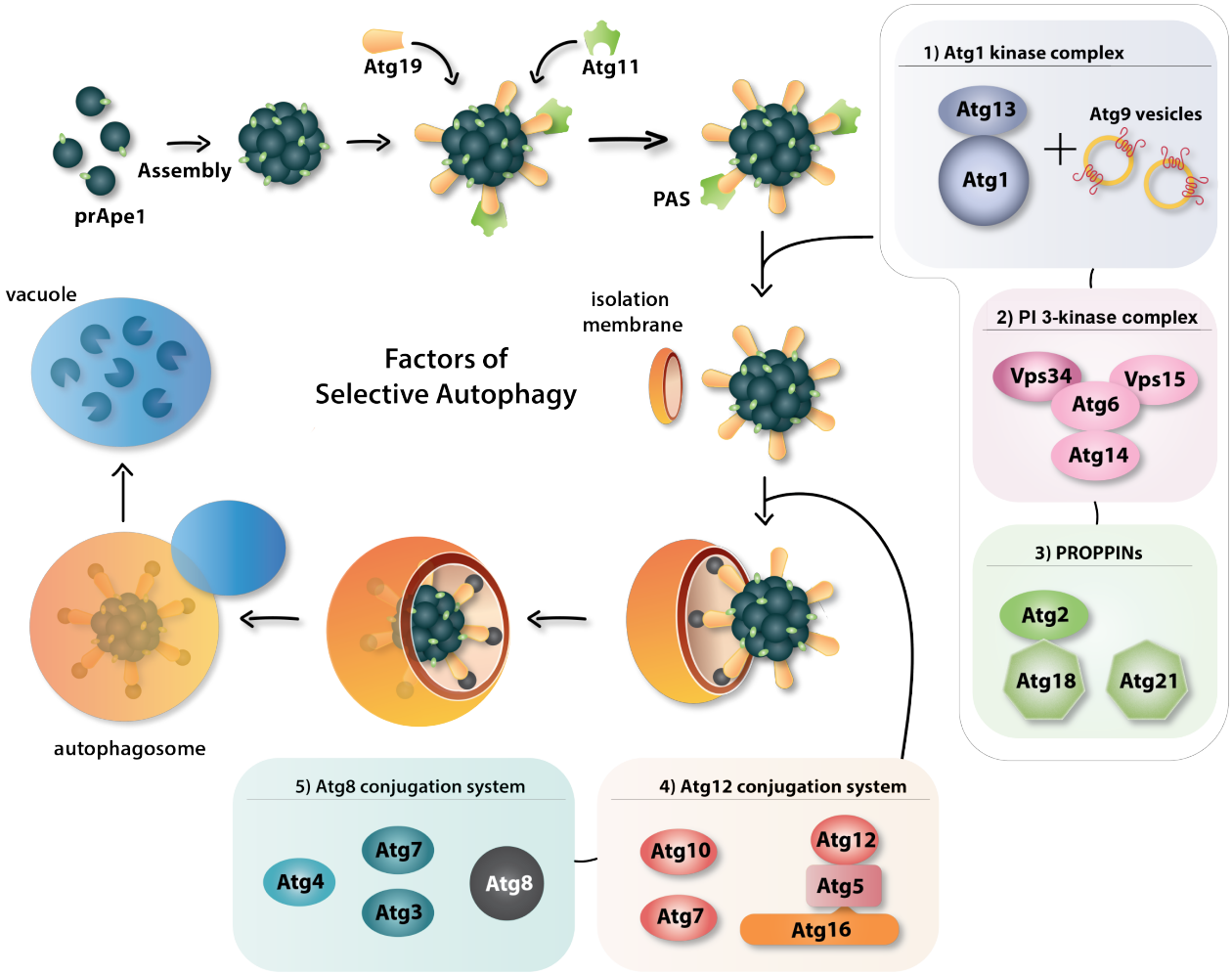

Figure 2: **Overview of the autophagic core machinery during the CVT pathway**

In contrast to bulk autophagy, selective autophagy starts with a designated cargo. In case of the Cvt-pathway the main cargo material are the zymogens of the hydrolase vacuolar aminopeptidase 1 (prApe1) but also the enzymes alpha-mannosidase1 (Ams1) and aspartyl aminopeptidase 4 (Ape4) use the autophagic machinery in order to be transported to the vacuole (Lynch-Day & Klionsky, 2010; Shintani & Klionsky, 2004; Yamasaki & Noda, 2017). Before they can undergo autophagic transport the Ape1 cargo monomers have to assemble into higher order structures that phase separate and generate semi-liquid droplets (Kim et al., 1997; Yamasaki et al., 2020). These structures are then specifically recognized by binding of the cargo receptor Atg19 to the N-terminal propeptide of Ape1 (Scott et al., 2001). Additionally to Atg19 further cargo receptors have been identified in budding yeast. Atg34 is a specific receptor for Ams1 and important for its transport to the vacuole during starvation

conditions (Suzuki et al., 2010). Atg39 and Atg40 mediate the targeting of the ER and the nucleus, while Atg32 and Atg36 recognize mitochondria or peroxisomes respectively (Mochida et al., 2015; Motley et al., 2012; Okamoto et al., 2009).

In the next step the formed cargo receptor complex is transported to the PAS in an Atg11 dependent manner. While Atg11 is not required for bulk autophagy, it is crucial for selective autophagy where it takes over the scaffolding function of Atg17 and thereby facilitates PAS formation at the vacuole (Kim et al., 2001; Lynch-Day & Klionsky, 2010; Yorimitsu & Klionsky, 2005). With its size of 135 kDa Atg11 is the second largest component of the Atg core machinery. It contains four coiled-coil domains (CC1, CC2 within the N-terminus and CC3, CC4 within the c-terminus). In contrast to Atg17 that forms anti-parallel homodimers, biophysical analysis revealed that Atg11 assembles into parallel homodimers. Important for the dimerization is the binding of CC4 to the cargo receptors. The Atg11-cargo receptor interaction requires phospho-activation of Atg19 by the Hrr25 kinase and is mediated by the C-terminal region of Atg11 (Chew et al., 2013; Pfaffenwimmer et al., 2014; Suzuki & Noda, 2018; Tanaka et al., 2014; Turco et al., 2019; Yorimitsu & Klionsky, 2005; Zientara-Rytter & Subramani, 2020). Apart from its role in dimerization and cargo receptor recognition Atg11 is also involved in the interaction with several other autophagy core components. Among the interaction partners we find the Atg1-Atg13 complex (Kim et al., 2001). Atg1 localizes to the PAS in an Atg13 dependent manner (Suzuki et al., 2007). The Atg11 homodimer bridges the cargo receptor complex with Atg1-Atg13 and facilitates clustering of Atg1 on the cargo. Similar to bulk autophagy also during selective autophagy this oligomerization and trans-autophosphorylation is sufficient to induce kinase activity (Kamber et al., 2015; Torggler et al., 2016). By employing bioinformatics searching for the known consensus sequence of Atg1 substrates, as well as in vitro kinase assays several core factors of the autophagic machinery were identified as Atg1 kinase substrates. Among them are Atg2 and Atg9 but also Atg18 and members of the lipidation machinery like Atg12, Atg5 or Atg8 (Papinski et al., 2014; Schreiber et al., 2021). In mammals the homologues of the Atg1 kinase are ULK1 and ULK2 (uncoordinated-51-like kinases 1 and 2) (Yan et al., 1998, 1999). A deletion of ULK1 in the mouse model only led to minor deficiencies, suggesting that ULK2 compensates for the loss of ULK1 (Kundu et al., 2008). ULK1 is part of a protein complex together with the mammalian ATG13, FIP200 (focal adhesion kinase family

interacting protein of 200 kDa) and ATG101 (Mizushima, 2010). Like in the budding yeast system mammalian ULK1 and ATG13 are targets of the mTORC1 complex. However, the mechanisms of ULK1 activation seem to be quite different compared to Atg1 since nutrient deprivation does not alter the affinities within the complex. It is rather likely that mTORC1 directly regulates ULK1 activity (Ganley et al., 2009; Hosokawa et al., 1981; Hwa Jung et al., 1992). Cargo recognition in mammalian selective autophagy requires more complex mechanisms but still employs a variety of different cargo receptors depending on the targeted substrate (Kirkin & Rogov, 2019). Although there is no direct homologue of the *S. cerevisiae* Atg11/Atg17 in mammals, FIP200, a component of the ULK1 complex is supposed to take over a comparable scaffolding function. FIP200 shows a highly conserved C-terminus and crystal structure analysis has identified a dimeric globular shape. This so-called claw-domain binds the mammalian cargo receptor p62 and plays an important role for the degradation of unfolded, ubiquitinated proteins (aggrephagy) (Hara et al., 2008; Mizushima & Levine, 2010; Turco et al., 2019).

Atg9 vesicles, the seeds for autophagosome formation

Atg9 is 115 kDa large, highly conserved in yeast and mammals and the only integral membrane protein among the family of autophagy core factors (Lang et al., 2000; T. Noda et al., 2000; Young et al., 2006). Suzuki et al. (2007) could show that Atg9 deletion mutants fail in recruiting further factors like Atg14, Atg2, Atg18 and Atg8 to the PAS rendering Atg9 an important factor for the nucleation of autophagosome formation.

In the cell, Atg9 is embedded into single membrane vesicles termed Atg9 vesicles. These vesicles are about 30-60 nm in diameter and harbor between 24 and 32 Atg9 molecules each (Yamamoto et al., 2012). Atg9 vesicles are formed at the *trans*-Golgi with the help of Atg23 and Atg27. Atg23 and Atg27 form a complex with Atg9 and are required for proper packaging of Atg9 into the vesicles and their budding from the Golgi. Upon autophagy induction they are recruited to the PAS. This trafficking of Atg9 is referred to as anterograde Atg9 transport (Backues et al., 2015; Legakis et al., 2007; Ohashi & Munro, 2010; Tucker et al., 2003).

How Atg9 vesicles are targeted to the PAS is different for bulk and selective autophagy. Its recruitment during nutrient deprivation relies on the binding of its N-

terminal disorderd region to Atg17 (Sekito et al., 2009). Further interaction of the Atg9 N-terminus with the HORMA domain of Atg13 is needed for bulk autophagy (Suzuki et al., 2015). For selective autophagy Atg9 vesicles are recruited to the PAS via interaction with Atg11. He et al. (2006) could show that the N-terminus of Atg9 binds to the CC2 of Atg11. This interaction was also the main focus of one of the two publications presented in this thesis and will therefore be described in more detail below. Once recruited to the PAS, Atg9 is phosphorylated by Atg1 at six distinct sites (S19, S657, S802, S831, S948, and S969). These phosphorylations are important for the elongation of the autophagosomal membrane (Papinski et al., 2014).

Recent structural studies employing cryo-electron microscopy have revealed that Atg9 features 4 transmembrane helices and 2 helices that are buried in the outer leaflet of the membrane. Additionally, Atg9 has disordered N- and C-termini as well as three loops connecting the transmembrane helices, all of them facing the cytosol. Atg9 forms two different types of pores. While the Atg9 protomer forms a lateral pore (LP) which opens towards the membrane, another vertical pore (VP) is created upon trimerization of Atg9 in the trimer center. Both pores seem to be required for autophagy activity and autophagosome formation which is most likely connected to another function of Atg9 that was discovered only recently. Atg9 is able to act as a lipid scramblase, meaning it translocates phospholipids between the outer to the inner monolayers. This function might be coupled with the lipid transfer activity of Atg2 in order to facilitate growth of the autophagosomal membrane, which is discussed in more detail in another paragraph of this thesis (Guardia et al., 2020; Lai et al., 2020; Matoba et al., 2020; Orii et al., 2020).

For a long time it was hypothesized that Atg9 vesicles might be the membrane source necessary for autophagosome formation. Studies in yeast however have shown that only about 3 Atg9 vesicles are recruited to the PAS, which is by far not enough to provide the bulk of the autophagosomal membrane (Yamamoto et al., 2012). The second study presented in this thesis is dealing with the role of Atg9 vesicles in more detail. In this study we could show, that Atg9 vesicles serve as a recruiting platform for the further downstream components of the autophagic machinery and thereby provide the seed for autophagosome formation.

Mammals have two homologues of ATG9. However, only one of them is uiquititous expressed (mAtg9 or ATG9A) while the other is restricted to very specific tissues (ATG9B) (Yamada et al., 2005; Young et al., 2006). The sequence homology of

ATG9A with yeast Atg9 is very high as far as their membrane domains are concerned. Just like yeast Atg9 also mammalian ATG9A features four transmembrane helices and two helices that are only partially inserted into the membrane but do not span it completely (Guardia et al., 2020). ATG9A is embedded into small vesicles that are generated at the trans-golgi-network (TGN) and that are recruited to LC3-positive structures (mammalian homologue of Atg8) upon induction of autophagy. In contrast to *S. cerevisiae,* mammalian ATG9A vesicles are not detectably incorporated into the growing isolation membrane but their lipid scramblase activity seems to be conserved (Maeda et al., 2020; Orsi et al., 2012; Young et al., 2006).

The PI3KC3-complex 1

The presence of Atg9 vesicles at the PAS is required for the recruitment of Atg14 (Suzuki et al., 2007; Suzuki et al., 2015). Atg14, together with Vps34, Vps15, Atg38 and Vps30/Atg6 is part of the class III phosphatidylinositol 3-kinase complex 1 (PI3KC3-C1). In yeast two different types of the PI3KC3 have been identified. While Vps34, Vps15 and Vps30/Atg6 are core components, Atg14 in PI3KC3-C1 is exchanged for Vps38 in PI3KC3-C2. With the different compositions of the complexes also their functions vary. The PI3KC3-C1 is important for autophagy whereas PI3KC3-C2 is involved in vacuole protein sorting (VPS) (Kihara et al., 2001). Atg14 is involved in correct localization of the PI3KC3-C1 to the PAS. Vps34 (Vacuolar protein sorting 34) is the kinase that actually catalyzes phosphorylation of phosphatidylinositol (PI) to phosphatidylinositol 3-phosphate (PI3P) (Nascimbeni et al., 2017; Obara et al., 2006; Schu et al., 1993). Vps15 is a pseudokinase that is important for the stability of the complex and regulates the correct localization and activity of Vps34 (Ohashi et al., 2019a; Rostislavleva et al., 2015; Stack et al., 1995; Stack & Emr, 1994). Vps30/Atg6 contains a C-terminal BARA domain (three β-sheet-α-helix repeats) which plays a role in succesful PI3KC3-C1 targeting to the membrane at the PAS (Noda et al., 2012; Rostislavleva et al., 2015). Atg38 takes over a stabilizing function during complex formation (Araki et al., 2013).

PI3P is an important signalling molecule in autophagy by setting the stage for the assembly of downstream PI3P-binding autophagy factors like Atg18 and Atg21 at the PAS (Nascimbeni et al., 2017).

Mammalian PI3-kinases can be categorized into three different classes. While classes I and II contain several enzymes each that produce PI(3,4,5)P3 or PI(3,4)P2, class III is only represented by VPS34, which phosphorylates PI to PI3P. However, comparable to yeast Vps34, also mammalian VPS34 can be part of two different complexes. PI3KC3-C1 and PI3KC3-C2 both contain VPS34, VPS15 and Beclin1 (Atg30/Atg6 in yeast). PI3KC3-C1 further contains ATG14 and NRBF2 (Atg38 in yeast). PI3KC3-C2 instead has UVRAG (UV-resistance-associated gene product) as an equivalent of Vps38. During autophagy PI3KC3-C1 plays a critical role for PI3P production at early stages. Analogous to yeast it is necessary for the recruitment of the PI3P effector proteins to the site of autophagosome formation (Ohashi et al., 2019).

PI3P binding factors (PROPPINs)

The term PROPPINs stands for β-propellers that bind polyphosphoinositides. In yeast three members of this family, namely Atg18, Atg21 and Hsv2 (homologous with swollen vacuole phenotype 2), have been identified so far. They are highly conserved and characterized by their ability to bind PI3P and PI(3,5)P_2 which is facilitated by a FRRG motif (Dove et al., 2004; Krick et al., 2006; Strømhaug et al., 2004). While Atg18 is essential for bulk and selective autophagy, Atg21 is essential for the Cvt pathway and piecemeal autophagy of the nucleus (PMN). Bulk autophagy can still proceed but with decreased efficiency after Atg21 deletion. Hsv2 so far only was observed to contribute to PMN (Barth et al., 2001; Guan et al., 2001; Krick et al., 2008).

Binding of the PROPPINs to PI3P is required for their autophagic functions. PI(3,5)P_2 binding by Atg18 however targets it to the vacuole where it regulates vacuolar morphology and function (Efe et al., 2007; Gopaldass et al., 2017).

Structural studies revealed that PROPPINs are WD40 repeat proteins, forming 7-bladed β-propellers with two individual PIP binding sites located at blade 5 and 6. Both of these domains are able to bind PI3P but only one can bind PI(3,5)P_2. Additionally to these two sites a hydrophobic loop in blade 6 that inserts into the membrane contributes to membrane binding. While the initial attraction between the membrane and the PROPPINs is mediated by non-specific electrostatic interactions, the PIP binding sites together with a loop at blade 6 that penetrates the membrane retain the proteins bound in position (Baskaran et al., 2012; Busse et al., 2015; Krick et al.,

2012). Mutations of a single PI binding sites result in decreased autophagic activity whereas mutation of both sites enhanced the defect, strongly suggesting, that the two sites are partly redundant. When the membrane binding of loop 6CD is impaired on top, membrane association is lost completely which results in a complete block of autophagy (Baskaran et al., 2012).
Atg18 and Atg21 are recruited to the PAS in a PI3P dependent manner (Juris et al., 2015; Krick & Thumm, 2016; Obara et al., 2008). Atg21 subsequently recruits further downstream factors to the isolation membrane, namely the E3-like Atg12 – Atg5-Atg16 complex via direct interaction with Atg16. This is supported by experiments showing that a deletion of Atg21 leads to a decreased co-localization of Atg16 with the PAS. Also expression of a membrane binding deficient Atg21-FTTG version showed decreased Atg16 punctae formation, stressing the importance of Atg21 membrane recruitment via PI3P. Atg21 is further needed for efficient lipidation of Atg8, a ubiquitin-like protein that represents a hallmark of autopaghy and will be discussed in closer detail below (Juris et al., 2015).

Homologues of the PROPPINs in humans are the so-called WIPIs (WD-repeat protein interacting with phosphoinositides). The WIPI family consists of four members, WIPI1 to WIPI4. WIPI1, WIPI2 and WIPI4 play critical and non-redundant roles during autophagy. They have been described as PI3P effector proteins that subsequently recruit downstream Atg factors during autophagosome formation (Proikas-Cezanne et al., 2015). In particular, studies revealed that WIPI2, a homologue of yeast Atg18, binds Atg16L1 and tethers it to the isolation membrane together with Atg5 and Atg12. Thereby it facilitates LC3 conjugation to the isolation membrane (Dooley et al., 2014; Strong et al., 2021). WIPI1 and WIPI4 have been observed to interact with ATG2 and stabilize its binding to PI3P positive membranes, thereby also promoting a more efficient lipid transfer (Maeda et al., 2019).

Atg2-Atg18 – the membrane binding and lipid transfer complex

For its role during autophagy, Atg18 forms a complex with Atg2. Deletion of Atg2 and Atg18 leads to an accumulation of Atg8 at the PAS. Further, these mutants show a defect in isolation membrane elongation (Suzuki et al., 2007, 2013).
The Atg2-Atg18 complex is found at the PAS only in the presence of PI3P. However, complex formation was also observed in cells without PI3P or upon expression of

Atg18 FTTG, a membrane binding deficient mutant. Obara et. al (2008) could show, that in cells expressing the membrane binding deficient Atg18 also localization of Atg2 to the isolation membrane was lost, suggesting that Atg18 recruits the complex to the PAS. However, (Kotani et al., 2018) and (Rieter et al., 2013) observed, that Atg2 targets to the isolation membrane independently of Atg18. This is supported by the fact, that a direct interaction between Atg2 and Atg9 has been described and that this promotes Atg2-Atg18 interaction on membranes. The binding of Atg2 to Atg9 further determines the correct localization of Atg2-Atg18 to the edges of the growing isolation membrane (Gómez-Sánchez et al., 2018).

Atg2 is the largest of the autophagic core components with a size of 180 kDa. Although it was identified as protein required for autophagy already in 1993, its actual function was unclear for a long time (Tsukada, Miki; Ohsumi, 1993). An affinity of Atg2 for lipids had already been described earlier in mammals (Pfisterer et al., 2014; Velikkakath et al., 2012). Several studies then supported the idea, that Atg2 might directly be involved in the elongation of the autophagosomal membrane. (Graef et al., 2013; K. Suzuki et al., 2013) and (Gómez-Sánchez et al., 2018) could localize Atg2 to the IM-ERES (isolation membrane – ER-exit site) contact site. Structural and biochemical studies together with an AlphaFold structure prediction of Atg2 (https://alphafold.ebi.ac.uk/entry/A6ZRK1) further allowed deeper insights into its potential function. Atg2 has a rod-like structure that features two membrane binding domains at its N- and c-terminus. Each of these sites was sufficient for membrane binding but only the presence of both allowed membrane tethering. The C-terminus is required for isolation membrane interaction, while the N-terminus was suggested to establish contact to the ER (Jumper et al., 2021; Kotani et al., 2018; Zheng et al., 2017). Further, the N-terminus contains a so-called chorein_N region which is characterized by an opened hydrophobic cavity in the center of the fold (Maeda et al., 2019; Osawa et al., 2019). This fold is a common feature in lipid transfer proteins (LPTs) (Wong et al., 2017). Another similarity to other LPTs like Vps13 (vacuolar protein sorting 13) is a hydrophobic groove that is predicted to run along the length of Atg2, forming a channel-like structure (Jumper et al., 2021; Kumar et al., 2018; Li et al., 2020; Valverde et al., 2019). Follow-up experiments identified the lipid transfer activity of Atg2. The chorein_N domain is able to extract phospholipids with little headgroup specifitiy out of a membrane (Maeda et al., 2019; Osawa et al., 2019, 2020; Valverde et al., 2019). The lipids most likely travel through the hydrophobic cavity and

can then be released into acceptor membranes. A mechanism like that could supply the lipids necessary for autophagosome elongation.

Atg8 and its two conjugation systems

Atg8 is a ubiquitin-like protein that plays an important role for autophagosome biogenesis in bulk autophagy and selective autophagy (Lang et al., 1998; Scott et al., 1996; Tsukada & Ohsumi, 1993). Structural analysis revealed that Atg8 is characterized by a ubiquitin-like fold (Kumeta et al., 2010; Paz et al., 2000). During the autophagic process it is crucial for a variety of events ranging from isolation membrane elongation, maturation and closure to fusion of the autophagosome with the vacuole (Nair et al., 2012; Nakatogawa et al., 2007; Xie et al., 2008; Yu et al., 2012). A special task during selective autophagy is the interaction with cargo receptors which enables a tight wrapping of the growing isolation membrane around the cargo and thereby mediates specificity of the degradation process (Nakatogawa et al., 2007; Xie et al., 2008) (Noda et al., 2008; Sawa-Makarska et al., 2014).

In contrast to a conjugation reaction to a lysine residue in a target polypeptide typical for ubiquitin, Atg8 is covalently conjugated to the phospholipid phosphatidylethanolamine (PE) via an attachment to its amino headgroup. This reaction requires two ubiquitin-like conjugation systems.

First, another ubiquitin-like protein, Atg12, has to be conjugated to a lysine of Atg5. For Atg12 conjugation to Atg5, Atg12 is coupled to Atg7 under the consumption of one ATP (Kim et al., 1999; Tanida et al., 1999). Next, Atg12 is transferred to the E2-like enzyme Atg10 (Shintani et al., 1999). Finally, Atg12 is conjugated to Atg5 (Mizushima et al., 1998). The Atg12 – Atg5 conjugate subsequently forms a complex with the homodimeric coiled-coil protein Atg16 via Atg5, resulting in a multimeric complex with an approximate size of 350 kDa (Fujioka et al., 2010; Kuma et al., 2002; Matsushita et al., 2007). This Atg12 – Atg5-Atg16 complex functions as an E3-like enzyme in the second conjugation system that couples Atg8 to PE (Hanada et al., 2007; Mizushima et al., 1999).

Before Atg8 can be lipidated, a C-terminal arginine has to be cleaved off by the Atg4 protease, exposing a glycine at position 116 (Kirisako et al., 2000). Next, a conjugation system very similar to the one already described for Atg12 – Atg5 occurs. Atg7 acts not only as an E1 enzyme for Atg12, but also activates Atg8 by binding the Atg8 Gly116. Then, activated Atg8 is transferred to the E2-like enzyme Atg3, which

subsequently conjugates it to PE (Taherbhoy et al., 2011). Atg12 – Atg5-Atg16 acts as an E3-like enzyme by mediating Atg8 lipidation at the right place and stimulating the activity of Atg3 as an E2-like enzyme (Ichimura et al., 2000; Sakoh-Nakatogawa et al., 2013).

The two conjugation systems are highly conserved from yeast to humans. Yeast Atg8 however has six ATG8 homologues in mammals which can be divided into two sub-families, based on sequence similarities: microtubule-associated protein 1 light chain 3 (LC3) and γ-aminobutyric acid receptor-associated protein (GABARAP). Like Atg8 in budding yeast, in mammals LC3B is commonly used as a marker for autophagosomes and the most studied among the family members (Kabeya et al. 2000). While a deletion of Atg8 in yeast leads to an almost complete block of autophagosome formation, in mammals they can still form upon deletion of all LC3 and GABARAP family members (Kirisako et al., 1999; Martens, 2016; Nguyen et al., 2016; Tsuboyama et al., 2016). However, the generated autophagosomes were smaller and their formation rate was slower, supporting the observations of several labs that Atg8 proteins are acting as fusion/tethering factors and that they are involved in the recruitment and activation of other Atg factors (Martens, 2016; Martens & Fracchiolla, 2020; Nguyen et al., 2016) The ATG8 conjugation machinery is further needed for the proper degradation of the inner autophagosomal membrane (Tsuboyama et al., 2016). The function of the ATG8 proteins is mediated by a LC3-interacting region (LIR-motif) present in unstructured regions of the interaction partners. LIR-motifs are usually characterized by two hydrophobic residues that are flanked by two variable residues followed by negatively charged amino acids (Birgisdottir et al., 2013). The K_D between the ATG8 proteins and the LIR-motif can be found in the low μM range (Rozenknop et al., 2011). Due to clustering of the lipidated ATG8 proteins on the isolation membrane, a high avidity effect leads to efficient recruitment of further autophagy factors containing LIR-motifs which results in a positive feedback loop.

The field of autophagy has been moving with great speed towards a complete understanding of successful autophagosome biogenesis. Many components necessary have been identified and studies in various model organisms have shed more light on how the different phases of autophagic degradation are orchestrated.

Among the most enigmatic factors was Atg9, the only transmembrane protein of the autophagy core machinery. This thesis focuses to a large extent on Atg9 vesicles and their role as a recruiting platform for the downstream autophagic machinery during autophagy nucleation.
Another player whose role has been unclear until recently is the lipid transfer protein Atg2. By employing in vitro reconstitution approaches I was able to couple the Atg2 mediated lipid transfer with Atg8 conjugation on Atg9 PLs.
In the cell Atg2 forms a complex with Atg18. I observed that Atg2-Atg18 further binds specific subunits of the E3-like Atg12 – Atg5-Atg16 complex and thereby supports its robust recruitment to the membrane which is mainly driven by Atg21. Last but not least my thesis deals with the Atg11/Atg19 cargo receptor interaction which was deciphered by a variety of biochemical and *in vivo* studies.

Yet, multiple questions regarding the spatiotemporal formation of autophagosomes remain. So far, lipid transfer from the ER to the autophagosome has not been shown directly. Furthermore, the growing autophagosome requires directionality of the lipid transfer and the mechanisms that retain the lipids on the side of the growing autophagosome are so far unknown. Another subject that will need closer investigation is the role of Atg9 as a scramblase and its interaction with Atg2-Atg18 in order to re-establish membrane balance after lipid transfer.

In this part, two published research articles will be presented.

Reconstitution of autophagosome nucleation defines Atg9 vesicles as seeds for membrane formation

In Sawa-Makarska et al. (2020) the aim was to reconstitute the nucleation of isolation membranes during selective autophagy *in vitro* to better understand the molecular mechanisms of the initial steps of autophagosome formation. Particular focus was the role of Atg9 vesicles, which were demonstrated to act as platforms for the recruitment of further downstream components of the autophagic machinery.

To this end we purified and assembled 21 proteins in the test tube. To conduct high quality *in vitro* experiments it is first necessary to obtain high quality components (Figure 1A). Purification protocols for several of the proteins employed were already available in our lab from previous studies. The purification of Atg11, Atg21, Atg2-Atg18, the PI3KC3-C1 and Atg9 vesicles first had to be established in our lab. My specific contribution to this was the optimization of the Atg21 purification as well as the establishing of the Atg2-Atg18 complex purification.

In Juris et al. (2015) Atg21 was shown to be necessary for the recruitment of Atg12–Atg5-Atg16 to the isolation membrane. By making use of giant unilamellar vesicles (GUVs), which are artificial membranes suitable for *in vitro* analysis of protein-membrane interactions, I showed that Atg21 is able to recruit the Atg12 – Atg5-Atg16 complex to PI3P positive membranes *in vitro* (Figure 1B). Further, the lipid binding/lipid transfer complex Atg2-Atg18 was targeted to the same membranes via a direct interaction with Atg12–Atg5-Atg16, leading to an increased binding of the E3-like enzyme to the GUVs (Figure 1C, 1G, S1A). By employing microscopy-based pull-down experiments I was able to map this interaction in more detail. Using GFP/RFP-trap agarose beads and fluorescently tagged proteins I observed that Atg2 directly binds Atg5 while Atg18 needs Atg12 for its interaction with the Atg12–Atg5-At16 complex (Figure 1D-F, S1D). The fact that Atg21 and Atg2-Atg18 targeted different subunits within the complex suggested the formation of a holo-complex at the membrane with Atg21 being the main driver of the recruitment (Figure 1F, S1E). To test whether these results would be relevant in *in vivo*, I generated knock-out strains of the PROPPINs and Atg2 and evaluated Atg5-mCherry recruitment to Ape1-BFP, as marker for the PAS (Fig. S2). The live cell microscopy supported the *in vitro* data showing that both PROPPINs and Atg2 contribute to the recruitment of the E3-like

enzyme to the PAS. More *in vivo* experiments carried out by my colleagues revealed that also Atg8 lipidation was negatively affected in *atg2*Δ*, atg18*Δ *and atg21*Δ cells (Figure S3).

In the cell the recruitment of Atg2, Atg18, Atg21 and subsequently also the targeting of the Atg12–Atg5-Atg16 complex to the isolation membrane depends on the phosphorylation of PI to PI3P by the PI3KC3-C1. As a consequence, also Atg8 conjugation to the isolation membrane requires an active PI3KC3-C1 (Suzuki et al., 2007). By purifying and adding the PI3K3-C1 to our system my colleagues could see that this is also true for our *in vitro* system. Both, recruitment of Atg12–Atg5-Atg16 and Atg8 conjugation to the GUVs were dependent on PI 3-kinase activity. A lack of Atg2-Atg18 lead to a decreased lipidation efficiency while missing Atg21 resulted in complete loss of Atg8 conjugation to the membrane (Figure 2A-B, S4).

Upstream of the PI3KC3-C1, Atg9 was shown to be crucial for the assembly of the autophagic machinery at the PAS making them a putative recruiting platform for downstream factors. In order to introduce Atg9 vesicles into our reconstitution my colleagues generated artificial Atg9 proteoliposomes (Atg9 PLs). This enabled us to keep full control over the added factors and generate sufficient amounts of material that mimicked endogenous Atg9 vesicles (Figure S5). The composition of the membrane for the Atg9 PLs was based on results of a lipidomics analysis of endogenous Atg9 vesicles (Figure S6). Native Atg9 vesicles were isolated from yeast cells by expressing Atg9-EGFP-TAP and isolating the vesicles via IgG agarose beads. The analysis revealed strikingly high PI content, making them a good substrate for the PI3KC3-C1. The reconstituted Atg9 PLs were immobilized on GFP-trap beads and the recruitment of the fluorescently labelled downstream factors was visualized under the microscope. Comparable to the GUV system also Atg9 PLs displayed Atg8 conjugation in an Atg21 dependent manner (Figure 2E-F). Atg2-Atg18 under these conditions did not play a major role for lipidation, suggesting that the main task of Atg2-Atg18 might be lipid transfer.

In the next set of experiments a “cargo” was introduced into the reconstitution system by coupling agarose beads to the Ape1 propeptide (Figure 3). This cargo-mimicking construct is then recognized by Atg19 – the cargo receptor. Microscopy experiments that used fluorescently labelled Atg11 and Atg9 showed that Atg11 was sufficient to recruit Atg9 to the cargo-receptor complex through a direct interaction between Atg11 and Atg9 that had already been described in the literature before (He et al., 2006;

Matscheko et al., 2019). The cargo-receptor-scaffold-Atg9 axis could then recruit the PI3KC3-C1, Atg21, Atg2-Atg18, Atg12 – Atg5-Atg16 and facilitate Atg8 conjugation onto Atg9 proteoliposomes. At this stage we exchanged the Atg9 PLs for endogenous Atg9 vesicles and observed that also those are a substrate for machinery recruitment and Atg8 conjugation (Figure 3D).

Atg2 has been described to bind Atg9 and bridge the isolation membrane with the ER (Gómez-Sánchez et al., 2018). Consistent with this, we found that Atg2-Atg18 is recruited to native Atg9 vesicles (Figure 4B). Additionally, Atg2 has been shown to act as a lipid transfer protein (Maeda et al., 2019; Osawa et al., 2019, 2020; Valverde et al., 2019). This lipid transfer activity I could also validate for the Atg2-Atg18 purified in our lab by employing a FRET-assay (Förster energy transfer) (Figure S11). Next, I used the same assay to demonstrate that Atg9 PLs can act as acceptors for Atg2-Atg18 mediated lipid transfer (Figure 4D-E). By using Atg9 PLs lacking PE and PS as donors and further employing almost the complete autophagic machinery (PI3KC3-C1, Atg21, Atg12 – Atg5-Atg16, Atg7, Atg3, Atg8) I could show that the addition of Atg2-Atg18 can increase the efficiency of Atg8 conjugation onto Atg9 PLs.

Taken together these results identify Atg9 vesicles as a platform for the recruitment of the downstream autophagy factors. We could show that Atg11 is sufficient to establish a link between the cargo-receptor complex and Atg9 vesicles, harboring the complete downstream autophagic machinery. We hypothesize that Atg2, that bridges Atg9 vesicles with the ER, transfers lipids from the ER into the vesicles and thereby facilitates growth of the autophagosomal membrane.

I contributed to the presented work by designing and conducting experiments, generating tools (protein purifications, liposomes and GUVs preparation, vesicle isolation) as well as analyzing and interpreting acquired data. Further I was involved in drafting and revising the article.

I performed the experiments/designed graphics shown in Figure 1A, B, D, E, F, G, Figure 4C, D, E, Figure 5, S1D, S2, S11A, B, C, D, and E.

RESEARCH ARTICLE SUMMARY

CELL BIOLOGY

Reconstitution of autophagosome nucleation defines Atg9 vesicles as seeds for membrane formation

Justyna Sawa-Makarska*†, Verena Baumann*, Nicolas Coudevylle*, Sören von Bülow, Veronika Nogellova, Christine Abert, Martina Schuschnig, Martin Graef, Gerhard Hummer, Sascha Martens†

INTRODUCTION: Macroautophagy (hereafter autophagy) is an evolutionarily conserved lysosomal degradation pathway. It ensures cellular homeostasis and health by removing harmful material from the cytoplasm. Among the many substances that are degraded by autophagy are protein aggregates, damaged organelles, and pathogens. Defects in this pathway can result in diseases such as cancer and neurodegeneration. During autophagy, the harmful material, referred to as cargo, is sequestered by double-membrane vesicles called autophagosomes, which form de novo around the cargo. Autophagosome formation occurs at sites close to the endoplasmic reticulum (ER). The process is catalyzed by a complex machinery that includes protein and lipid kinases, membrane binding and transfer proteins, and ubiquitin-like conjugation systems. How these components and biochemical activities act in concert to mediate autophagosome formation is incompletely understood. Particularly enigmatic are autophagy related protein 9 (Atg9)–containing vesicles that are required for the assembly of the autophagy machinery but do not supply the bulk of the autophagosomal membrane.

RATIONALE: To understand the mechanism of how the various biochemical activities of the autophagy machinery are orchestrated during the nucleation and expansion of the precursors to autophagosomes at the cargo, we fully reconstituted these events using the yeast machinery. Specifically, we used recombinantly expressed and purified proteins in combination with reconstituted Atg9 proteoliposomes and endogenous Atg9 vesicles isolated from cells. Our reconstituted system included 21 polypeptides, as well as membrane platforms, making up almost the entire yeast core machinery required for selective autophagy. This approach allowed us to exert full control over the biochemical reactions and to define the organization principles of the early autophagy machinery.

RESULTS: We found that Atg9 vesicles and proteoliposomes were recruited to the autophagy cargo via the Atg19 receptor and Atg11 scaffold axis. The vesicles in turn recruited the Atg2-Atg18 lipid transfer complex and the class III phosphatidylinositol 3-phosphate kinase complex 1(PI3KC3-C1), which produced the signaling lipid phosphatidylinositol 3-phosphate (PI3P). PI3P production triggered the subsequent recruitment of the PI3P-binding protein Atg21, which together with the Atg2-Atg18 complex efficiently attracted the E3-like Atg12–Atg5-Atg16 complex. Together with the E1-like Atg7 and the E2-like Atg3 proteins, the recruitment of the E3-like complex ultimately resulted in the conjugation of the ubiquitin-like Atg8 protein to the headgroup of phosphatidylethanolamine (PE) on the Atg9 vesicles and proteoliposomes. Atg8 conjugation is a hallmark of autophagy and necessary for membrane expansion. Furthermore, we discovered that sustained Atg8 conjugation required the Atg2-mediated transfer of PE from a donor membrane into Atg9 proteoliposomes.

CONCLUSION: We conclude that Atg9 vesicles form seeds that establish membrane contact sites to initiate the transfer of lipids from donor compartments such as the ER. It has become increasingly clear that lipid transport between different compartments occurs at membrane contact sites and that it is mediated by lipid transfer proteins. Notably, lipid transfer at membrane contact sites requires two preexisting compartments. We propose that during the de novo formation of autophagosomes, the Atg9 vesicles recruit the autophagy machinery and serve as nucleators to establish membrane contact sites with a donor compartment such as the ER. Atg2-mediated lipid transfer in conjunction with energy-consuming reactions such as PI3K-dependent PI3P production and Atg8 lipidation on the Atg9 vesicles drive net flow of lipids into the vesicles, resulting in their expansion for autophagosome formation. ■

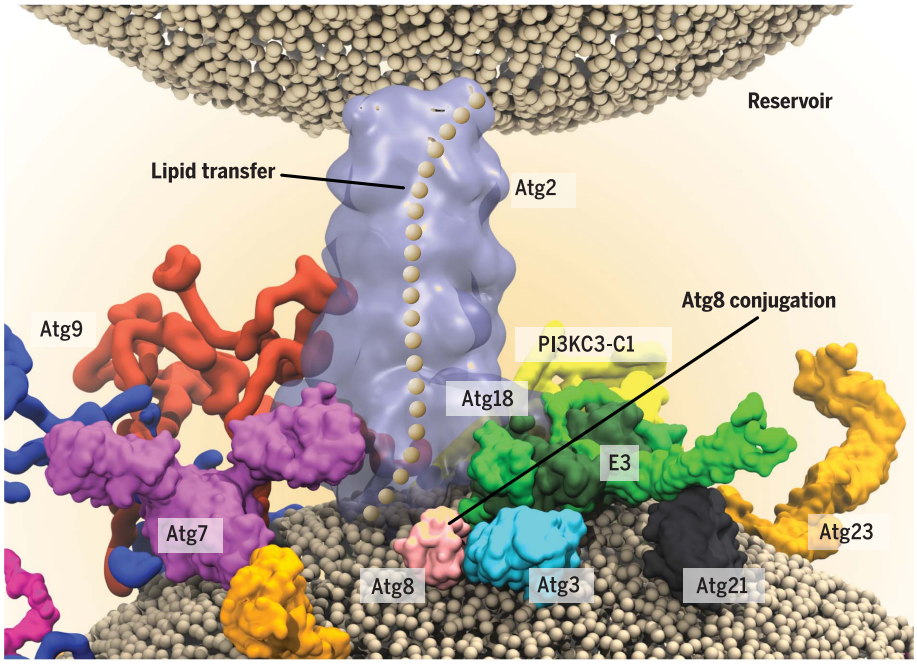

Assembly of the yeast autophagy machinery. Model for the assembly of the yeast autophagy machinery and Atg2-mediated lipid transfer into Atg9 vesicles from a donor compartment, such as the endoplasmic reticulum, during the nucleation of autophagosomes.

The list of author affiliations is available in the full article online.
*These authors contributed equally to this work.
†Corresponding author. Email: justyna.sawa-makarska@univie.ac.at (J.S.-M.); sascha.martens@univie.ac.at (S.M.)
Cite this article as J. Sawa-Makarska *et al.*, *Science* **369**, eaaz7714 (2020). DOI: 10.1126/science.aaz7714

RESEARCH ARTICLE

CELL BIOLOGY

Reconstitution of autophagosome nucleation defines Atg9 vesicles as seeds for membrane formation

Justyna Sawa-Makarska[1]*†, Verena Baumann[1]*, Nicolas Coudevylle[1]*, Sören von Bülow[2], Veronika Nogellova[1], Christine Abert[1], Martina Schuschnig[1], Martin Graef[3,4], Gerhard Hummer[2,5], Sascha Martens[1]†

Autophagosomes form de novo in a manner that is incompletely understood. Particularly enigmatic are autophagy-related protein 9 (Atg9)–containing vesicles that are required for autophagy machinery assembly but do not supply the bulk of the autophagosomal membrane. In this study, we reconstituted autophagosome nucleation using recombinant components from yeast. We found that Atg9 proteoliposomes first recruited the phosphatidylinositol 3-phosphate kinase complex, followed by Atg21, the Atg2-Atg18 lipid transfer complex, and the E3-like Atg12–Atg5-Atg16 complex, which promoted Atg8 lipidation. Furthermore, we found that Atg2 could transfer lipids for Atg8 lipidation. In selective autophagy, these reactions could potentially be coupled to the cargo via the Atg19-Atg11-Atg9 interactions. We thus propose that Atg9 vesicles form seeds that establish membrane contact sites to initiate lipid transfer from compartments such as the endoplasmic reticulum.

Autophagy mediates the degradation of cytoplasmic material (the cargo) within lysosomes and ensures cellular homeostasis (*1*). Defects in autophagy have been associated with severe pathologies such as neurodegeneration, cancer, and infections (*2*). Cargo degradation is achieved by its sequestration within double-membrane vesicles called autophagosomes. These form de novo in an inducible manner and first appear as small membrane structures called isolation membranes (or phagophores), which gradually enclose the cargo as they grow. The assembly and growth of the isolation membranes is dependent on a number of conserved autophagy-related (Atg) proteins that act together in a hierarchical manner to nucleate and expand the isolation membranes (*3*–*5*). In yeast, these include the Atg1 protein kinase complex, vesicles containing the Atg9 protein, the class III phosphatidylinositol 3-phosphate kinase complex 1 (PI3KC3-C1) producing the signaling lipid phosphatidylinositol 3-phosphate (PI3P), the PI3P-binding PROPPIN proteins, the lipid transfer protein Atg2, and the ubiquitin-like Atg12 and Atg8 conjugation systems (Fig. 1A). During selective autophagy, the interaction of cargo receptors with scaffold proteins directs this machinery toward specific cargos (*6*, *7*). The attachment of Atg8 to the membrane lipid phosphatidylethanolamine (PE), referred to as lipidation, is the most downstream event of this cascade. How the biochemical activities of the autophagy machinery are orchestrated to mediate the formation of autophagosomes is not well understood. Especially enigmatic is the role of Golgi-derived Atg9 vesicles that are required for nucleation of the isolation membrane but that do not provide the bulk of the autophagosomal membrane (*8*–*11*). The bulk of the lipids appears to be derived from other donor compartments, in particular the endoplasmic reticulum (ER) (*12*–*19*).

Previous work has demonstrated that membrane contact sites are major mediators of nonvesicular lipid flow between compartments within the cell (*20*, *21*). The flow of lipids is mediated by lipid transfer proteins that extract lipids from a donor membrane and transport them to an acceptor membrane. To elucidate how the various activities of the autophagy machinery act together during the nucleation of isolation membranes, we reconstituted a large part of the yeast autophagy machinery in vitro.

Membrane recruitment of Atg12–Atg5-Atg16 by Atg21 and Atg2-Atg18

A hallmark of isolation membranes and completed autophagosomes is the conjugation of the ubiquitin-like Atg8 proteins to the headgroup of the lipid PE (*22*, *23*). The Atg8 proteins are required for isolation membrane expansion, closure, and cargo selectivity (*24*). The conjugation of Atg8 to PE is mediated by the E1-like Atg7 and the E2-like Atg3 proteins (*22*) as well as the Atg12–Atg5-Atg16 complex that acts in an E3-like manner (*25*) by activating and localizing Atg8-loaded Atg3 to the membrane (*26*, *27*). Thus, the localization of the Atg12–Atg5-Atg16 complex is a crucial determinant of the site of Atg8 lipidation (*28*). Atg16 binds to the PI3P-binding PROPPIN protein Atg21 (*29*). We sought to determine whether this interaction could mediate the recruitment of the Atg12–Atg5-Atg16 complex to PI3P-containing membranes, such as the isolation membrane, and found that Atg21 bound to PI3P-containing giant unilamellar vesicles (GUVs) (Fig. 1B). As expected (*27*), the Atg12–Atg5-Atg16 complex did not directly bind to this lipid composition and was recruited only in the presence of Atg21 (Fig. 1B). In cells, the PI3P at the pre-autophagosomal structure (PAS) recruits another PROPPIN, the Atg18 protein in complex with the membrane tethering and lipid transfer protein Atg2 (*16*, *30*–*33*). We examined whether the Atg2-Atg18 complex could also interact with Atg12–Atg5-Atg16 and thereby contribute to its recruitment to PI3P-positive membranes. Indeed, we detected a direct interaction between the two protein complexes in a pull-down assay (Fig. 1C). We also observed that the presence of Atg2-Atg18 tended to accelerate the recruitment of the Atg12–Atg5-Atg16 complex to PI3P-containing GUVs (fig. S1A). Microscopy-based pull-down and membrane recruitment experiments indicated that, as expected, Atg21 bound to the Atg12–Atg5-Atg16 complex via Atg16 (fig. S1, B and C) (*29*), while the interaction of Atg2 was mediated by Atg5 and the interaction of Atg18 required the presence of Atg12 (Fig. 1, D to F, and fig. S1D).

These results suggested the formation of a holocomplex on the membrane, containing Atg21, Atg12–Atg5-Atg16, and Atg2-Atg18, and so we dissected the recruitment of the individual components in more detail. Atg21 was the main driving force for the recruitment of Atg12–Atg5-Atg16 under the conditions tested (Fig. 1G). In cells, both PROPPINS (Atg18 and Atg21) and Atg2 contributed to the localization of Atg12–Atg5-Atg16 to the PAS (fig. S2) (*29*). The residual recruitment of Atg12–Atg5-Atg16 in the triple-deficient cells could be mediated by the Atg1 complex (*34*). In addition, deletion of Atg2, Atg18, and Atg21 strongly reduced Atg8 lipidation (fig. S3A), and deletion of any of the three proteins stalled the progression of the autophagic pathway (fig. S3, B and C) (*29*, *30*).

At the PAS, the PI3KC3-C1 [consisting of the vacuolar protein sorting 34 (Vps34), Vps15, Atg6, and Atg14 subunits] phosphorylates phosphatidylinositol (PI) to PI3P (*35*). To address whether the recruitment of the Atg12–Atg5-Atg16 complex and Atg8 lipidation could be driven by the activity of the PI3KC3-C1 through the PI3P-dependent recruitment of Atg2-Atg18 and Atg21, we added the purified PI3KC3-C1 to PI-containing GUVs in the presence of Atg21 and Atg2-Atg18 (Fig. 2A). The Atg12–Atg5-Atg16

[1]Department of Biochemistry and Cell Biology, Max Perutz Labs, University of Vienna, 1030 Vienna, Austria. [2]Department of Theoretical Biophysics, Max Planck Institute of Biophysics, 60438 Frankfurt am Main, Germany. [3]Max Planck Institute for Biology of Ageing, 50931 Cologne, Germany. [4]Cologne Excellence Cluster on Cellular Stress Responses in Aging-Associated Diseases (CECAD), University of Cologne, 50931 Cologne, Germany. [5]Institute for Biophysics, Goethe University Frankfurt, 60438 Frankfurt am Main, Germany.
*These authors contributed equally to this work.
†Corresponding author. Email: justyna.sawa-makarska@univie.ac.at (J.S.-M.); sascha.martens@univie.ac.at (S.M.)

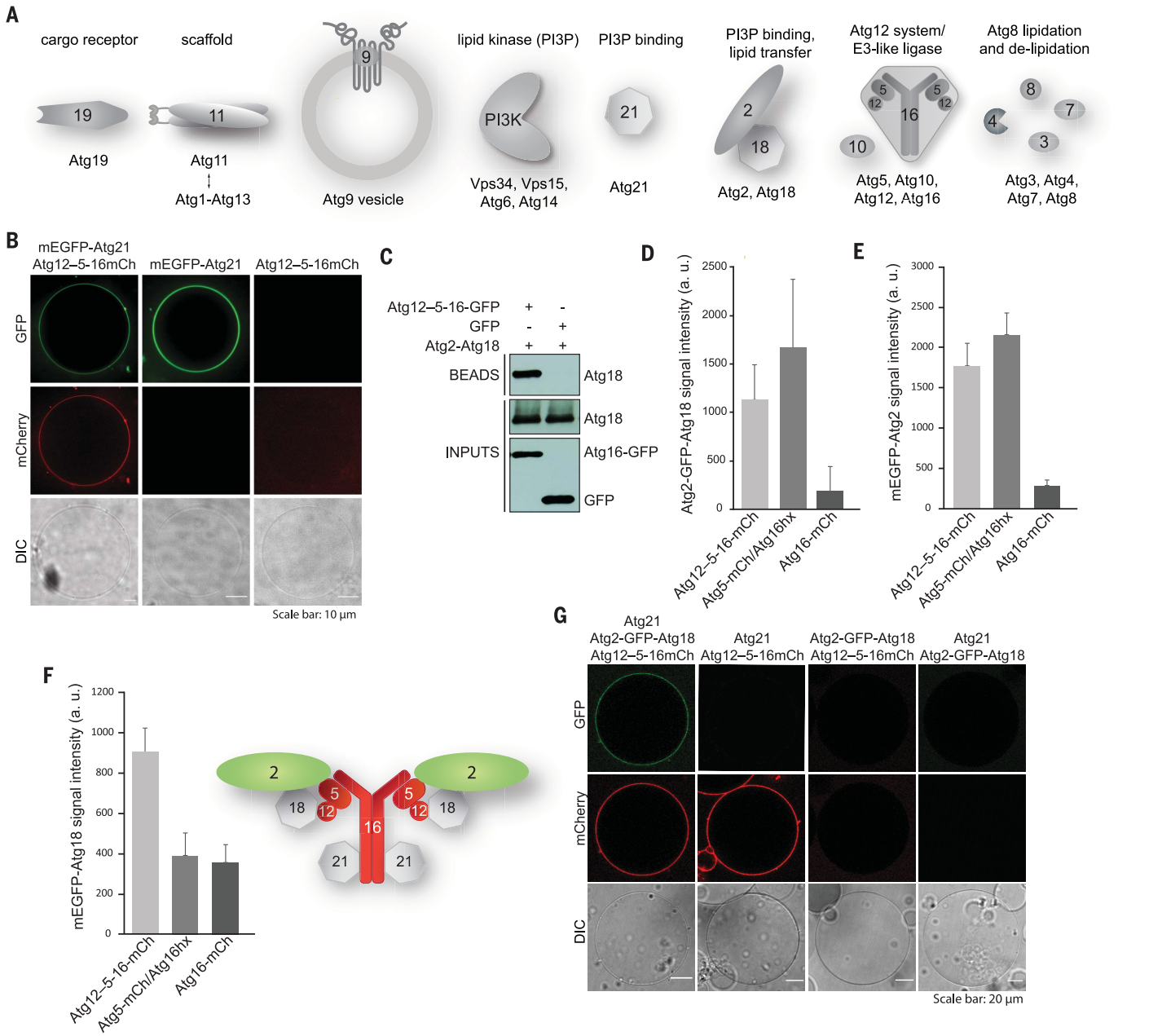

Fig. 1. Membrane recruitment of the Atg12–Atg5-Atg16 complex by PROPPINs. (**A**) Cartoon showing proteins used in this study. PI3KC3-C1 is labeled as PI3K in all figures. (**B**) GUVs containing PI3P (57% POPC, 25.5% POPS, 15% POPE, 2.5% PI3P; see table S2 for lipid definitions) were incubated with either 1 µM Atg12–Atg5-Atg16-mCherry supplemented with 1 µM eGFP-Atg21, 1 µM eGFP-Atg21, or 1 µM Atg12–Atg5-Atg16-mCherry and imaged by microscopy. DIC, differential interference contrast microscopy. (**C**) GFP-Trap pulldown using Atg12–Atg5-Atg16-GFP or GFP as bait and Atg2-Atg18 as prey. The bait and the prey proteins were detected by immunoblotting with anti-GFP and anti-CBP antibodies, respectively. (**D** to **F**) Quantification of the pull-down experiment mapping the interaction between Atg12–Atg5-Atg16 and Atg2-Atg18 shown in fig. S1D. The quantification is based on three independent experiments. Standard deviations are shown. A schematic representation of the putative holocomplex composed of Atg12–Atg5-Atg16, Atg2-Atg18, and Atg21 is shown as a cartoon insert in (F). a.u., arbitrary units. (**G**) GUVs of the same lipid composition as in (B) were incubated with Atg12–Atg5-Atg16-mCherry, Atg21, or Atg2-GFP-Atg18 at 1 µM final concentration each, and the recruitment of the proteins to the membrane was imaged by microscopy.

complex was recruited to the GUV membrane, and this recruitment was dependent on the activity of the PI3KC3-C1 (Fig. 2A and fig. S4A). Atg21 alone was sufficient to recruit the Atg12–Atg5-Atg16 complex and to induce Atg8 lipidation on the GUVs (Fig. 2B). These effects were enhanced when Atg2-Atg18 was also present (Fig. 2B). We interpreted the localization of green fluorescent protein (GFP)–Atg8 on the membrane as lipidation because it was abolished when using a nonconjugatable form of Atg8 (GFP-Atg8-6xHis) and it strictly depended on the presence of the conjugation machinery Atg7 and Atg3 (fig. S4B).

Reconstitution of Atg8 lipidation on Atg9 proteoliposomes

Autophagosome nucleation depends on the presence of Atg9 vesicles (*8*–*11*). In *Saccharomyces cerevisiae*, a few of these vesicles translocate to the autophagosome formation site (*8*). Because Atg9 is required for the recruitment of

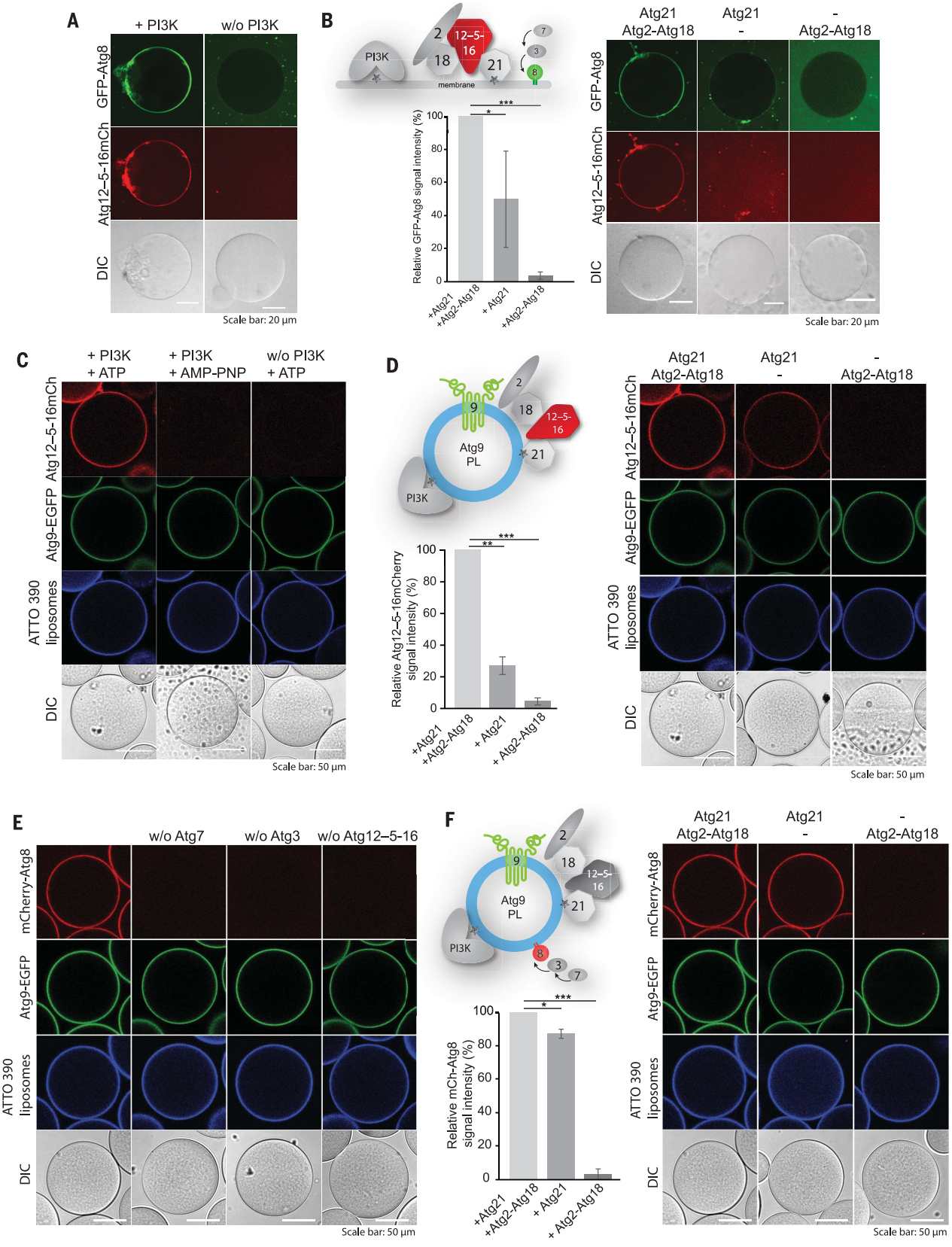

Fig. 2. In vitro reconstitution of PI3KC3-C1–dependent Atg8 lipidation. (**A**) The Atg8–PE conjugation machinery (Atg7, Atg3, Atg12–Atg5-Atg16-mCherry, and GFP-Atg8ΔR117) and PROPPINs (Atg21 and Atg2-Atg18) were added to GUVs (55% DOPC, 10% DOPS, 17% DOPE, 18% liver PI) and incubated in the presence or absence of PI3KC3-C1 and cofactors (ATP, $MnCl_2$, $MgCl_2$, and EGTA). Microscopy images of representative GUVs are shown. The proteins included in the experiment are depicted in the cartoon inserts. (**B**) Atg8 lipidation to GUVs depends on the presence of Atg21. GUVs were incubated with Atg8–PE conjugation machinery proteins as in (A) and PI3KC3-C1 in the presence of either one or both PROPPINs. The quantification of the GFP signal on GUVs from three independent experiments is shown to the left. (**C**) Atg12–Atg5-Atg16 recruitment to Atg9 PLs depends on the activity of PI3KC3-C1. GFP-Trap beads were coated with Atg9-EGFP PLs and incubated with Atg21, Atg2-Atg18, and Atg12–Atg5-Atg16-mCherry in the presence or absence of PI3KC3-C1 and ATP or in the presence of PI3KC3-C1 and AMP-PNP. Microscopy images of representative beads are shown. (**D**) Beads as in (C) were incubated with Atg12–Atg5-Atg16-mCherry and PI3KC3-C1 in the presence of either one or both PROPPINs. The quantification of mCherry signal on beads from three independent experiments is shown to the left. (**E**) Reconstitution of Atg8 lipidation to Atg9 PLs. Beads as in (C) were incubated with PI3KC3-C1, ATP, Atg21, Atg2-Atg18, mCherry-Atg8ΔR117, Atg7, Atg3, and Atg12–Atg5-Atg16, each time omitting one of the Atg8–PE conjugation machinery proteins, as indicated above the microscopy images of representative beads. (**F**) Atg8 lipidation to Atg9 PLs depends on the presence of Atg21. Beads as in (C) were incubated with PI3KC3-C1, ATP, mCherry-Atg8ΔR117, Atg7, Atg3, and Atg12–Atg5-Atg16 in the presence of either one or both PROPPINs. The quantification of mCherry signal on the beads from three independent experiments is shown to the left. Significance is indicated using *P* values from Student's *t* test: $*P \le 0.05$, $**P \le 0.01$, $***P \le 0.001$.

the PI3KC3-C1 to the site of autophagosome formation (*36*), we wondered whether the Atg9 vesicles could serve as platforms for the assembly of the autophagy machinery and thereby nucleate autophagosome formation. To this end, we reconstituted the purified Atg9 protein into small unilamellar vesicles (SUVs) to form proteoliposomes (PLs) (fig. S5, A to D). To mimic the natural lipid composition of these vesicles, we isolated Atg9 vesicles from *S. cerevisiae* and determined their lipid composition by lipidomics (fig. S6A). The vesicles had a high PI content (44%) (fig. S6B) (*37*), suggesting that they should be particularly good substrates for the PI3KC3-C1. To test this, we tethered PLs containing Atg9–enhanced green fluorescent protein (EGFP) to GFP-Trap beads to image the recruitment of other factors by microscopy. The membrane of the PLs was labeled by incorporation of a blue membrane dye (ATTO390-DOPE). Upon incubation of the vesicles with the PI3KC3-C1, Atg21, Atg2-Atg18, and the Atg12–Atg5-Atg16 complex, we observed recruitment of Atg12–Atg5-Atg16 to the Atg9 PLs (Fig. 2C). Consistent with the results above (Figs. 1G and 2B), recruitment was strongest in the presence of both Atg2-Atg18 and Atg21 (Fig. 2D). We then added Atg7 and Atg3 to the reaction (now containing 14 polypeptides) to test whether Atg8 could be conjugated to the Atg9 PLs in a manner that depends on PI3KC3-C1, Atg21, Atg2-Atg18, and Atg12–Atg5-Atg16. We observed efficient Atg8 lipidation to the Atg9 PLs (Fig. 2E). Reduction of the Atg8 signal upon addition of the wild-type delipidating enzyme Atg4 but not its catalytic mutant (fig. S7A) showed that the detected mCherry-Atg8 signal at the beads was indeed attributable to lipidation.

Analogous to the results we observed for Atg12–Atg5-Atg16 recruitment, Atg8 conjugation was relatively independent of the Atg2-Atg18 complex and was also weakly detectable in the absence of the PI3KC3-C1 (Fig. 2F and fig. S7, B and C), likely because Atg21 shows residual binding to PI-containing membranes. These results suggested a division of labor between Atg21 and Atg2-Atg18, where Atg21 plays a major role in the initial recruitment of Atg12–Atg5-Atg16, and the main function of Atg2-Atg18 could be membrane tethering and lipid transfer (*16*, *30*–*33*).

Reconstitution of autophagosome nucleation in selective autophagy

In selective autophagy, autophagosome nucleation must be coupled to the presence of cargo material (*7*). The cargo is recognized by cargo receptors such as p62 in human cells and Atg19 in *S. cerevisiae*. These cargo receptors link the autophagy machinery to the cargo via the FIP200/Atg11 proteins (*6*). Atg11 was shown to interact with Atg9 (*38*, *39*). We purified full-length Atg11 and, in agreement with (*40*) but in contrast to (*39*), found Atg11 to be a constitutive dimer (fig. S8B). Atg11 bound directly to the N terminus of Atg9 (fig. S8C). Next, we examined whether the Atg19 cargo receptor could recruit the autophagy machinery, including Atg9 vesicles, to the cargo and subsequently initiate Atg8 conjugation. The cargo was mimicked by attachment of the GST-prApe1 propeptide (residues 1 to 41) to glutathione beads. These were incubated with the Atg19 cargo receptor and subsequently with Atg11. Atg11 was recruited to the beads in an Atg19-dependent manner. The recruitment was enhanced when a phospho-mimicking mutant of Atg19 [$Ser^{390,391,396}$→Asp (S390D, S391D, and S396D)] (*41*) was used (fig. S8A). Atg9 PLs and Atg9 vesicles isolated from cells (fig. S9) bound to the cargo beads in an Atg11-dependent manner (Fig. 3, A and B, and fig. S8D). When we added the PI3KC3-C1, Atg2-Atg18, Atg21, Atg12–Atg5-Atg16, Atg3, Atg7, and Atg8 to the Atg9 PLs bound to the cargo beads—a reaction now containing almost the entire autophagy machinery—Atg8 was efficiently lipidated and anchored to the Atg9 PLs (Fig. 3C). Isolated Atg9 vesicles could also serve as substrates for the lipidation reaction (Fig. 3D), although the lipidation was markedly less prominent on the vesicles than on the reconstituted PLs (fig. S10A). The Atg8 signal on the Atg9 vesicles was attributable to lipidation because it depended on the Atg12–Atg5-Atg16 complex (Fig. 3D) and decreased upon addition of Atg4 (Fig. 3E). Thus, the autophagy machinery can be redirected toward the cargo via the cargo receptor (Atg19)–scaffold (Atg11)–Atg9 axis (Fig. 3 and fig. S10B). The Atg1-Atg13 complex was also recruited to these beads (fig. S10C). Thus, Atg11 and Atg9 vesicles are sufficient to recruit (almost) the entire autophagy machinery to the cargo.

Atg9 vesicles as acceptors for lipid transfer by Atg2

Owing to their small size, Atg9 vesicles provide only limited surface for Atg8 lipidation and isolation membrane expansion. Furthermore, in addition to Atg9, these vesicles contain other proteins, which further reduce the effective surface for lipidation. This is consistent with our finding that Atg9 vesicles were less efficient substrates for Atg8 lipidation than Atg9 PLs (Fig. 3 and fig. S10A). To estimate the available membrane surface of these vesicles, we built a three-dimensional model of an Atg9 vesicle (Fig. 4A and movie S1). We based this model on an average diameter of 60 nm (fig. S9) (*8*), our proteomics data (fig. S6C and data S1), and an average of 28 Atg9 molecules per vesicle (*8*). In addition, we placed one molecule each of PI3KC3-C1, Atg2-Atg18, Atg21, Atg12–Atg5-Atg16, and Atg3 loaded with Atg8 on the vesicular membrane (see Materials and methods section for details). With 70 proteins present in the modeled Atg9 vesicle, the accessibility of the membrane would be very limited. We calculated an effective dynamic surface coverage of 82% of the membrane area. Given that peripheral membrane proteins may have been lost during the isolation, the very stringent selection of proteins from mass spectrometric data used for modeling, and the fact that we assumed the Atg9 N and C termini not to interact with the vesicular membrane, the actual free surface may be even lower and more difficult to reach for incoming proteins. Thus, Atg9 vesicles may require lipid influx to transform into an efficient substrate for Atg8 lipidation.

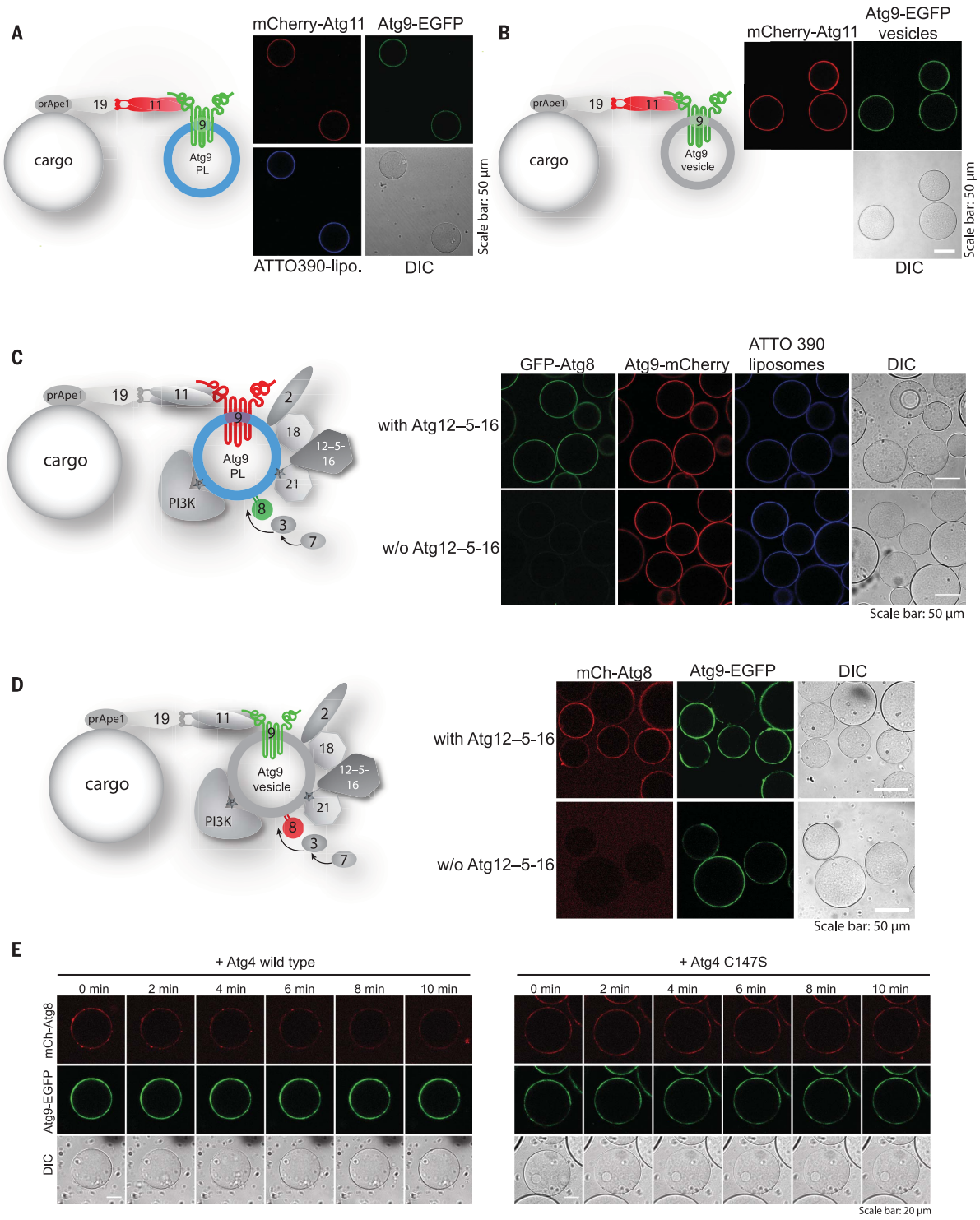

Fig. 3. Reconstitution of cargo-directed Atg8 lipidation to Atg9 PLs and Atg9 endogenous vesicles. (**A** and **B**) Recruitment of Atg PLs and endogenous Atg9 vesicles to the cargo. Cargo-mimetic beads (glutathione sepharose) were prepared by coating with GST-prApe1 (1-41), Atg19-3D, and mCherry-Atg11. For details of the pull-down, see fig. S8A. The preassembled cargo-mimetic beads were subsequently incubated with either Atg9-EGFP PLs (A) or endogenous Atg9-EGFP vesicles (B), washed, and imaged. Microscopy images of representative beads are shown. The Atg9-eGFP PLs were additionally labeled with ATTO390-PE. The experimental setup is shown by the accompanying cartoons. (**C** and **D**) Atg8-lipidation on the Atg9 PLs (C) and endogenous Atg9 vesicles (D) bound to the cargo-mimetic beads. Glutathione sepharose beads were coated with GST-prApe1 (1-41), Atg19-3D, and Atg11, incubated with Atg9-mCherry PLs (C) or Atg9-EGFP vesicles (D), washed with buffer, and incubated with PI3KC3-C1, ATP, Atg21, Atg2-Atg18, Atg3, Atg12–Atg5-Atg16, eGFP-Atg8ΔR117 (C) or mCherry-Atg8ΔR117 (D) and with or without Atg12–Atg5-Atg16 (see cartoons for the experimental setup). Microscopy images of representative beads are shown. (**E**) Time course experiment of the Atg8-deconjugation reaction on Atg9 vesicles. Atg4 wild type or the Atg4 C147S inactive mutant were added to the beads, as in (D). Microscopy images were taken at the indicated time points after the addition of Atg4.

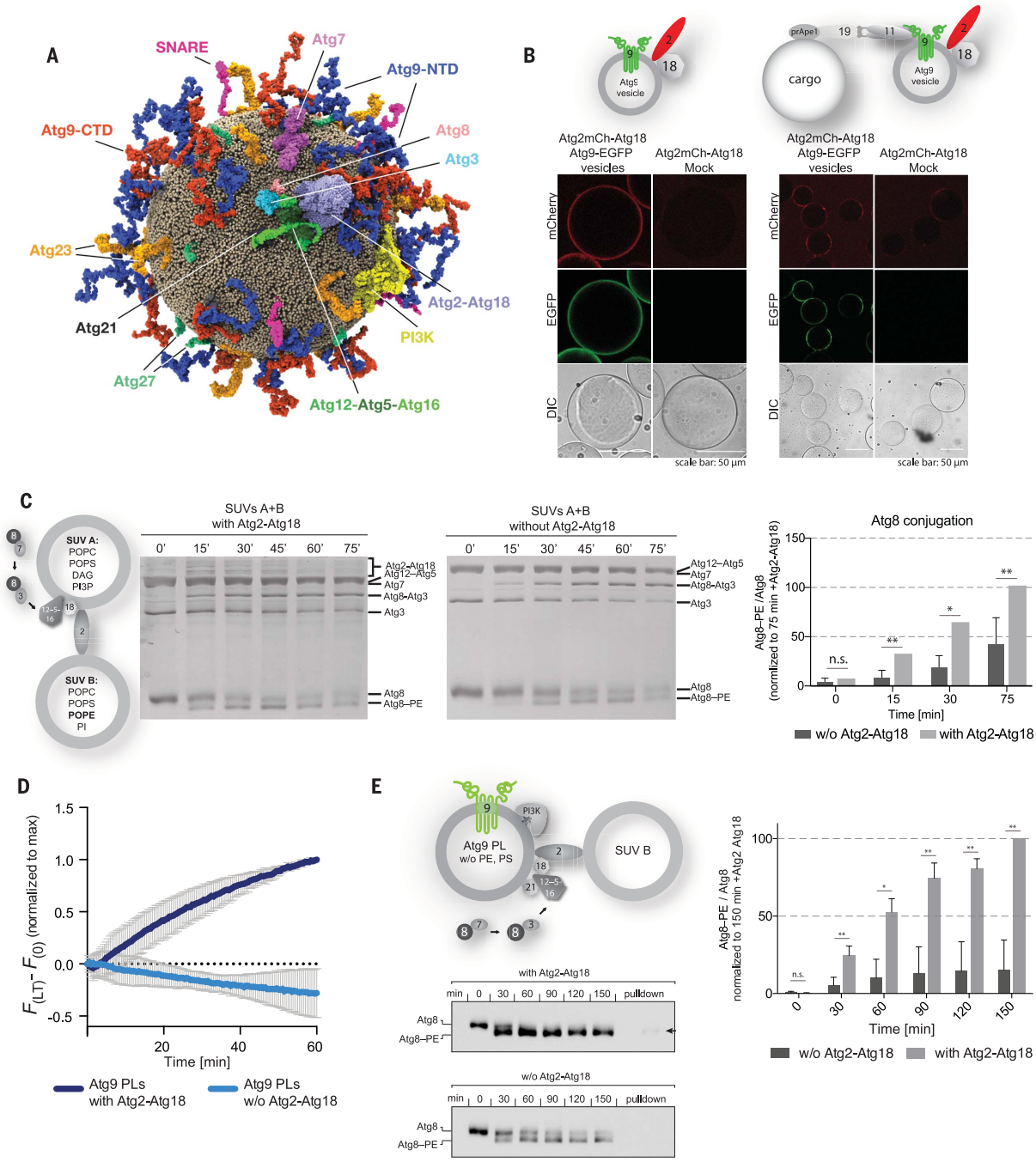

Fig. 4. Atg2-mediated lipid transfer into Atg9 PLs. (**A**) Molecular model of an endogenous Atg9 vesicle. The model contains the following proteins (copy numbers in parentheses): Atg9 (28), Atg27 (10), Atg23 (10), and the SNAP receptors (SNAREs) SFT1 (1), TLG1 (1), VTI1 (1), SSO1 (1), and GOS1 (1). Copy numbers are based on literature and mass spectrometry analysis of isolated Atg9 vesicles (see main text, fig. S6C, and methods section). Single copies of membrane-interacting autophagy proteins (PI3KC3-C1, Atg21, Atg2-Atg18, Atg3, Atg12–Atg5-Atg16, and Atg8) were additionally positioned on the surface of the Atg9 vesicle. Atg9-NTD and Atg9-CTD indicate N-terminal and C-terminal domains, respectively. Lipid headgroups are shown as small tan spheres. (**B**) Atg2-Atg18 is recruited to Atg9 vesicles and cargo-mimetic beads. GFP-Trap beads were coated with endogenous Atg9-EGFP vesicles. Glutathione sepharose beads were coated with GST-prApe1 (1-41), Atg19-3D, Atg11, and Atg9-EGFP vesicles and incubated with Atg2-mCherry-Atg18. Mock membranes were derived from a wild-type yeast strain. (**C**) Coomassie-stained gels showing Atg8–PE conjugation assays using the depicted experimental setup. Atg8–PE conjugation was detected as a band shift. Numbers above the gels indicate the time in minutes. (**D**) Phospholipid transfer assay based on the dequenching of NBD fluorescence. $F_{(LT)}$ and $F_{(0)}$ represent the nitrobenzoxadiazole (NBD) fluorescence intensity at each time point after and before addition of Atg2-Atg18, respectively, measured at 535 nm. Atg9 PLs were used as acceptor liposomes. Data are the mean values from five independent experiments. SD is shown. (**E**) Anti-Atg8 immunoblots showing Atg8–PE conjugation assays mediated by lipid transfer of Atg2-Atg18. The arrow indicates the Atg8 signal after pulling down Atg9-EGFP with GFP-Trap beads. [(C) and (E)] Quantification shows the averaged Atg8-PE/Atg8 ratio for each time point. Error bars represent SD. The quantification is based on four independent experiments. *P* values were calculated using Student's *t* test. Significance is indicated with $*P \leq 0.05$ and $**P \leq 0.01$ n.s., not significant.

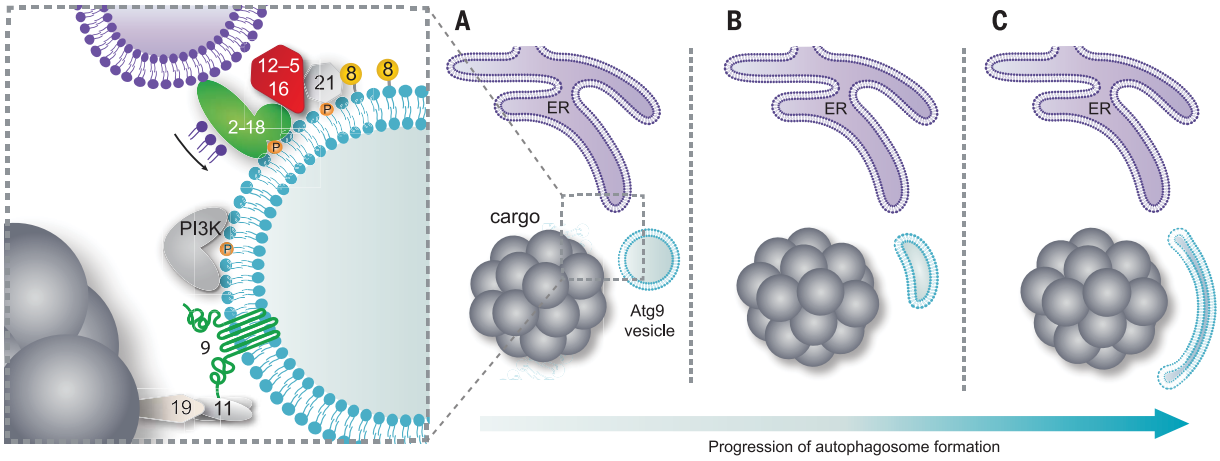

Fig. 5. Model for the initial steps of the isolation membrane generation. (**A**) Recruitment of Atg9 vesicles to the prApe1 cargo via the Atg19 receptor and Atg11 scaffold axis. The Atg9 vesicles recruit Atg2-Atg18 and PI3KC3-C1 (labeled PI3K). Production of PI3P by PI3KC3-C1 recruits Atg21 and the E3-like Atg12–Atg5-Atg16 complex. The membrane-positioned E3-like complex directs Atg8–PE conjugation to the vesicle. Atg8 lipidation is sustained by Atg2-mediated lipid transfer from a donor compartment such as the ER. (**B** and **C**) Lipid influx expands the vesicle surface resulting in isolation membrane expansion.

The lipid transfer protein Atg2 is recruited to the Atg9 vesicles (Fig. 4B) and tethers Atg9 to the ER in cells (*16*). The interaction between ATG2A and ATG9A is important for isolation membrane expansion in mammalian cells (*42*). Atg2-mediated lipid transfer from the ER into the membrane of the Atg9 vesicle may therefore enable Atg8 lipidation and subsequent expansion of the spherical Atg9 vesicles, converting them into the disk-shaped isolation membranes.

To test whether Atg2 can transport lipids for Atg8 conjugation, we mixed two populations of liposomes. One population (SUV A) contained a lipid composition that efficiently recruited the lipidation machinery (*27*) but did not contain PE as substrate for Atg8 conjugation. The other population (SUV B) contained PE but was not efficiently targeted by the lipidation machinery (Fig. 4C and fig. S11C). Upon addition of Atg2-Atg18, which is active in lipid transport (fig. S11, A and B), we detected a significantly increased lipidation of Atg8, demonstrating that Atg2-Atg18 could directly enhance Atg8 lipidation (Fig. 4C). Because phosphatidylserine (PS) can also serve as substrate for Atg8 lipidation in vitro (*43*), the actual stimulatory effect of Atg2-Atg18 on Atg8 lipidation may be even higher. To exclude the possibility that Atg2-Atg18 allosterically activated the E3 by direct binding, we conjugated Atg8 to PE-containing SUVs in the presence or absence of Atg2-Atg18 and found that we could not observe significant differences in Atg8 lipidation (fig. S11D). Atg9 PLs also served as acceptors for Atg2-mediated lipid transport (Fig. 4D). We therefore sought to determine whether the lipids transported into Atg9 PLs could serve as substrates for Atg8 lipidation. Atg9 PLs lacking PE and PS were mixed with a second population of liposomes containing these lipids. We then added Atg2-Atg18 in the presence of the PI3KC3-C1, Atg21, Atg12–Atg5-Atg16, Atg7, Atg3, and Atg8 (Fig. 4E). We found that Atg8 lipidation, as monitored by immunoblotting, was accelerated in the presence of Atg2-Atg18 (Fig. 4E). To confirm that Atg8 lipidation occurred on the Atg9 PLs, we pulled down the Atg9 PLs using GFP-Trap beads and found lipidated Atg8 only in the presence of Atg2-Atg18 (Fig. 4E, arrow in top immunoblot).

Outlook

Here, we present a near-full in vitro reconstitution of the events occurring during autophagosome nucleation in selective autophagy. Specifically, we demonstrate that Atg9 vesicles are substrates of PI3KC3-C1 and that the PI3P generated in situ mediates the successive recruitment of Atg21, Atg2-Atg18, and the Atg12–Atg5-Atg16 complex as prerequisites for the subsequent Atg8 lipidation.

The role of Atg9 vesicles has remained mysterious. They are required for early steps of autophagosome formation but make up only a minor fraction of the lipids required to form the autophagosomal membrane (*8*–*11*). Autophagosomes are generated in proximity to the ER, but their membranes are clearly distinct from the ER membrane (*13*–*19*). Our results show that Atg9 vesicles form a platform for the recruitment of the autophagy machinery. Among them is the membrane tethering and lipid transfer protein Atg2 (*16*, *30*–*33*), which can transfer lipids at a rate that enables it to be a major contributor to isolation membrane expansion (*44*). It has become clear that lipid transfer at membrane contact sites provides the communication and membrane flow between intracellular compartments. However, lipid transfer can only occur between existing donor and acceptor compartments. Atg9 vesicles may thus form seeds for the initial establishment of membrane contact sites. Therefore, quantitative Atg8 lipidation may only occur after lipid influx from the ER into the Atg9 vesicle, gradually converting it into the disk-shaped isolation membrane (Fig. 5). In this manner, Atg9 vesicles could seed a biochemically distinctive membrane, the isolation membrane, largely devoid of transmembrane proteins (*45*, *46*). To ensure the expansion of the isolation membrane, the incoming lipids must be distributed to its inner leaflet, an action that would require flippase or scramblase activity. Notably, we found two flippases (Drs2 and Neo1) present in our Atg9 vesicle proteomics analysis. Multiple individual nucleation events followed by ESCRT (endosomal sorting complexes required for transport)–mediated membrane sealing may be required for the formation of larger autophagosomes (*47*–*49*).

In addition, the Golgi-derived Atg9 vesicles isolated from cells might be tightly packed with proteins. The influx of loosely packed lipids from the ER might thus render them good substrates for subsequent Atg8 lipidation apart from the expansion of the free membrane area. In fact, autophagosomal membranes contain a high proportion of lipids with unsaturated fatty acids (*12*). Apart from serving as acceptors

for lipid influx, Atg9 vesicles may also kickstart local lipid synthesis (*12*). Accordingly, we found Faa1 and Faa4 in our Atg9 vesicle proteomics.

During selective autophagy, cargo material is specifically sequestered by autophagosomes. It has become clear that cargo receptors act upstream of the autophagy machinery by recruiting scaffold proteins to the cargo (*50*–*56*). Here, we fully reconstitute the cargo receptor and scaffold dependent recruitment of the autophagy machinery to the cargo material and demonstrate that this system is sufficient to promote local Atg8 lipidation. Future work will reveal how the recruitment of the autophagy machinery, including the Atg9 vesicles, is sterically and temporally coupled to the formation of membrane contact sites with the ER.

Materials and methods summary

The full version of the materials and methods is available in the supplementary materials.

Protein expression and purification

Atg19 (residues 1 to 374) and the Atg19-3D and Atg19-3DΔLIR mutants were expressed and purified as described elsewhere (*57*, *58*). mEGFP/mCherry-Atg8-ΔR117 was expressed and purified as described in (*27*).

6xHis-TEV-Atg21, 6xHis-TEV-mEGFP-Atg21, 6xHis-TEV-mCherry-Atg21, 6xHis-Atg18-mEGFP, and Atg9-NTD(1-285)-mEGFP were all expressed in *E. coli* Rosetta pLysS.

Atg2-Atg18-CBP (CBP, calmodulin binding protein), Atg2-GFP-Atg18-CBP, and Atg2-mCherry-Atg18-CBP were purified from the SMY373, SMY374, and SMY439 yeast strains, respectively.

6xHis-TEV-Atg2-mEGFP, PI3KC3-C1, protA-TEV-Atg1-Atg13, 6xHis-TEV-mEGFP/mCherry-Atg11, and 6xHis-TEV-Atg9- mEGFP/mCherry were all expressed in the baculovirus expression system.

All soluble proteins were purified via affinity chromatography followed by size-exclusion chromatography.

For full length Atg9-mEGFP/mCherry, cell membranes were collected by centrifuging the cleared cell lysate at 40,000 revolutions per minute (rpm) for 1 hour. The membranes were resuspended for 2 hours at 4°C in lysis buffer containing 2% n-dodecyl β-D-maltoside (DDM). After 2 hours of incubation, the insoluble material was removed by centrifugation at 40,000 rpm for 1 hour. Atg9 was then purified by affinity chromatography followed by size-exclusion chromatography in the presence of 0.2% DDM. To concentrate the protein without increasing the detergent concentration, the fractions containing protein were incubated with 150 μl of nickel nitrilotriacetic acid (NiNTA) beads for 3 hours at 4°C. The beads were washed several times with 25 mM Tris pH 7.4, 300 mM NaCl, 0.04% DDM. The protein was eluted in the desired volume of buffer supplemented with 300 mM imidazole. A final dialysis was performed overnight at 4°C against 25 mM Tris pH 7.4, 300 mM NaCl, 0.04% DDM.

Atg9 PLs formation and analysis

Small unilamellar vesicles (SUVs; i.e., liposomes) destined for the reconstitution of Atg9 PLs were prepared with a lipid composition mimicking the lipid composition of the endogenous Atg9 vesicles determined in this study (for details, see table S2). For the incorporation of Atg9, the SUVs were treated with 3-[(3-cholamidopropyl)dimethylammonio]-1-propanesulfonate (CHAPS) (Avanti Polar Lipids, Inc.). The SUV suspension was brought up to 2.5% CHAPS and incubated at room temperature (RT) for 1 hour. The SUV suspension was then mixed at a 1:1 ratio with a 1-μM Atg9 solution in 0.04% DDM. The mixture was incubated at RT for another 90 min and then diluted by a factor of 10 in Tris 25 mM Tris pH 7.4, 300 mM NaCl to reach a detergent concentration below the critical micelle concentration (CMC) of both detergents. The resulting PL solution was dialyzed overnight at 4°C against 25 mM Tris pH 7.4, 300 mM NaCl supplemented with 0.1 g of BioBeads SM2 (BioRad) per liter of buffer. Finally, BioBeads were added directly to the sample and incubated for 1 hour at RT. The insoluble material that did not get incorporated into liposomes was removed by centrifuging 30 min at 18,000 rpm. The supernatant containing Atg9 PLs was collected and used for subsequent experiments.

Membrane recruitment—GUV assays

To image Atg21, Atg2-Atg18, and Atg12–Atg5-Atg16 membrane recruitment, 15 μl of the electroformed GUVs were transferred to a 96-well glass-bottom microplate (Greiner Bio-One), and the respective proteins were added to the final concentration of 1 μM in a final reaction volume of 30 μl in a reaction buffer 25 mM 4-(2-hydroxyethyl)-1-piperazineethanesulfonic acid (HEPES) at pH 7.5, 150 mM NaCl. In every experiment involving GUVs, before the GUVs and proteins were pipetted onto the plate, the wells were blocked with a blocking solution [2.5 mg/ml bovine serum albumin (BSA) in 50 mM TrisHCl pH 7.4, 150 mM NaCl] for 1 hour and washed twice with the reaction buffer.

For Atg21, Atg2-Atg18, and Atg12–Atg5-Atg16 membrane recruitment in the presence of PI3KC3-C1 experiments, mixes containing respective proteins, 0.1 mM adenosine triphosphate (ATP) or 0.1 mM adenylyl-imidodiphosphate (AMP-PNP), 0.5 mM $MgCl_2$, 2 mM $MnCl_2$, and 1 mM egtazic acid (EGTA) in a final volume of 15 μl were prepared. The final concentration of proteins in the reaction mixes were 50 nM for PI3KC3-C1, 400 nM for Atg21, 400 nM for Atg2-GFP-Atg18, and 40 nM for Atg12–Atg5-Atg16-mCherry. The reaction mixes were added to the well already containing 15 μl of the electroformed GUVs. For the time course experiment, the imaging started 5 min after the addition of the reaction mix to GUVs. The images were acquired for 45 min at the indicated time points of reaction.

In vitro reconstitution of Atg8 lipidation on GUVs

To image the PI3KC3-C1–dependent Atg8–PE conjugation to GUVs, mixes containing respective proteins (according to the experimental setup), 0.5 mM ATP, 0.5 mM $MgCl_2$, 2 mM $MnCl_2$, and 1 mM EGTA in a final volume of 15 μl were prepared. The reaction buffer contained 25 mM HEPES at pH 7.5, 150 mM NaCl. The final concentrations of proteins in the reaction mixes were 50 nM for PI3KC3-C1, 400 nM for Atg21, 400 nM for Atg2-Atg18, 40 nM for Atg12–Atg5-Atg16-mCherry, 80 nM for Atg7, 80 nM for Atg3, 400 nM GFP-Atg8ΔR117, and 400 nM GFP-Atg8-6xHis. The reaction mixes were added to wells of a 96-well glass-bottom microplate (Greiner Bio-One) already containing 15 μl of the electroformed GUVs. Concentrations of proteins and cofactors used were calculated for the final 30 μl volume of the experiment.

Microscopy-based protein-protein interaction assay

For the experiments shown in Fig. 2, B and G, giant unilamellar vesicles (GUVs) were prepared. Preparation was carried out as described above. Assays were performed under equilibrium conditions, and mEGFP-Atg21, 6xHis-Atg21, Atg12–Atg5-Atg16-mCherry, and Atg2-GFP-Atg18-CBP were added at a final concentration of 500 nM.

For Fig. 1, D to F, Atg12–Atg5-Atg16-mCherry, Atg5-mCherry-Atg16(1-46), and Atg16-mCherry were recruited to red fluorescent protein (RFP)–TRAP beads (Chromotek). Assays were performed under equilibrium conditions with 2 μM of the prey proteins Atg2-GFP-Atg18-CBP, Atg2-mEGFP, and Atg18-mEGFP.

Isolation of endogenous Atg9 vesicles

To isolate endogenous Atg9 vesicles, we cloned versions of Atg9 tagged with a fluorophore (mEGFP or mCherry) and a tobacco etch virus (TEV) cleavable affinity tag (9xmyc or TAP). These constructs were used to replace the endogenous *ATG9* gene in haploid BY474x *S. cerevisiae* cells, putting the expression under the control of the endogenous *ATG9* promoter. Constructs were then integrated into wild type or *pep4*Δ strains.

Strains were grown, harvested, and lysed. Cleared cell lysate was incubated with the appropriate affinity beads (coated with either immunoglobulin G or anti-myc antibody) at 4°C for 1 hour. The beads were then washed, the vesicles were released by TEV cleavage at 4°C for an hour, and the supernatant was collected.

In vitro reconstitution of Atg8 lipidation on Atg9 PLs or Atg9 vesicles bound to cargo-mimetic beads

Assembly of the cargo-mimetic beads

Glutathione sepharose 4B beads (GE Healthcare) were first equilibrated in 25 mM Tris pH 7.4, 300 mM NaCl. Beads were mixed with the same volume of a 30-μM solution of GST-prApe1 (1-41), 30-μM solution of Atg19-3DΔLIR mutant, and 30 μM of Atg11. The mixture was incubated for 1 hour at 4°C, and the beads were subsequently washed three times.

Recruitment of Atg9 PLs or Atg9 vesicles to the cargo-mimetic beads

Ten microliters of cargo-mimetic beads were mixed with either 200 μl of Atg9-mCherry PLs solution or an equal volume of TEV-eluted Atg9-EGFP vesicles. The mixture was incubated for 2 hours at 4°C, and the beads were subsequently washed once

In vitro Atg8 lipidation

Five tenths of a microliter of cargo-mimetic beads coated with Atg9-mCherry PL or Atg9-EGFP vesicles were pipetted into the wells of a 384-well glass-bottom microplate (Greiner Bio-One) containing 0.5 mM ATP, 0.5 mM $MgCl_2$, 2 mM $MnCl_2$, and 1 mM EGTA in a final volume of 15 μl. The final concentrations of proteins in the reaction mixes were 50 nM for PI3KC3-C1, 400 nM for Atg21, 400 nM for Atg2-Atg18, 40 nM for Atg12–Atg5-Atg16, 100 nM for Atg7, 100 nM for Atg3, and 400 nM for EGFP-Atg8ΔR117 (200 nM of mCherry-Atg8ΔR117 for Atg9 vesicles). The reactions were incubated for 2 hours at RT in the dark, and the beads were imaged using confocal microscope LSM700 (Zeiss) with 20× objective and processed with ImageJ software.

To deconjugate Atg8 from Atg9 vesicles, Atg4 or Atg4C147S was added at a final concentration of 0.5 μM together with EDTA at a final concentration of 2 mM, and microscopy images were taken at the indicated time points.

REFERENCES AND NOTES

1. N. Mizushima, M. Komatsu, Autophagy: Renovation of cells and tissues. *Cell* **147**, 728–741 (2011). doi: 10.1016/j.cell.2011.10.026; pmid: 22078875
2. B. Levine, G. Kroemer, Biological functions of autophagy genes: A disease perspective. *Cell* **176**, 11–42 (2019). doi: 10.1016/j.cell.2018.09.048; pmid: 30633901
3. Z. Xie, D. J. Klionsky, Autophagosome formation: Core machinery and adaptations. *Nat. Cell Biol.* **9**, 1102–1109 (2007). doi: 10.1038/ncb1007-1102; pmid: 17909521
4. N. Mizushima, T. Yoshimori, Y. Ohsumi, The role of Atg proteins in autophagosome formation. *Annu. Rev. Cell Dev. Biol.* **27**, 107–132 (2011). doi: 10.1146/annurev-cellbio-092910-154005; pmid: 21801009
5. C. A. Lamb, T. Yoshimori, S. A. Tooze, The autophagosome: Origins unknown, biogenesis complex. *Nat. Rev. Mol. Cell Biol.* **14**, 759–774 (2013). doi: 10.1038/nrm3696; pmid: 24201109
6. E. Turco, D. Fracchiolla, S. Martens, Recruitment and activation of the ULK1/Atg1 kinase complex in selective autophagy. *J. Mol. Biol.* **432**, 123–134 (2020). doi: 10.1016/j.jmb.2019.07.027; pmid: 31351898
7. G. Zaffagnini, S. Martens, Mechanisms of selective autophagy. *J. Mol. Biol.* **428**, 1714–1724 (2016). doi: 10.1016/j.jmb.2016.02.004; pmid: 26876603
8. H. Yamamoto *et al.*, Atg9 vesicles are an important membrane source during early steps of autophagosome formation. *J. Cell Biol.* **198**, 219–233 (2012). doi: 10.1083/jcb.201202061; pmid: 22826123
9. A. Orsi *et al.*, Dynamic and transient interactions of Atg9 with autophagosomes, but not membrane integration, are required for autophagy. *Mol. Biol. Cell* **23**, 1860–1873 (2012). doi: 10.1091/mbc.e11-09-0746; pmid: 22456507
10. A. R. J. Young *et al.*, Starvation and ULK1-dependent cycling of mammalian Atg9 between the TGN and endosomes. *J. Cell Sci.* **119**, 3888–3900 (2006). doi: 10.1242/jcs.03172; pmid: 16940348
11. Y. Ohashi, S. Munro, Membrane delivery to the yeast autophagosome from the Golgi-endosomal system. *Mol. Biol. Cell* **21**, 3998–4008 (2010). doi: 10.1091/mbc.e10-05-0457; pmid: 20861302
12. M. Schütter, P. Giavalisco, S. Brodesser, M. Graef, Local fatty acid channeling into phospholipid synthesis drives phagophore expansion during autophagy. *Cell* **180**, 135–149.e14 (2020). doi: 10.1016/j.cell.2019.12.005; pmid: 31883797
13. E. L. Axe *et al.*, Autophagosome formation from membrane compartments enriched in phosphatidylinositol 3-phosphate and dynamically connected to the endoplasmic reticulum. *J. Cell Biol.* **182**, 685–701 (2008). doi: 10.1083/jcb.200803137; pmid: 18725538
14. M. Graef, J. R. Friedman, C. Graham, M. Babu, J. Nunnari, ER exit sites are physical and functional core autophagosome biogenesis components. *Mol. Biol. Cell* **24**, 2918–2931 (2013). doi: 10.1091/mbc.e13-07-0381; pmid: 23904270
15. M. Hamasaki *et al.*, Autophagosomes form at ER-mitochondria contact sites. *Nature* **495**, 389–393 (2013). doi: 10.1038/nature11910; pmid: 23455425
16. R. Gómez-Sánchez *et al.*, Atg9 establishes Atg2-dependent contact sites between the endoplasmic reticulum and phagophores. *J. Cell Biol.* **217**, 2743–2763 (2018). doi: 10.1083/jcb.201710116; pmid: 29848619
17. M. Hayashi-Nishino *et al.*, A subdomain of the endoplasmic reticulum forms a cradle for autophagosome formation. *Nat. Cell Biol.* **11**, 1433–1437 (2009). doi: 10.1038/ncb1991; pmid: 19898463
18. P. Ylä-Anttila, H. Vihinen, E. Jokitalo, E.-L. Eskelinen, 3D tomography reveals connections between the phagophore and endoplasmic reticulum. *Autophagy* **5**, 1180–1185 (2009). doi: 10.4161/auto.5.8.10274; pmid: 19855179
19. T. Nishimura *et al.*, Autophagosome formation is initiated at phosphatidylinositol synthase-enriched ER subdomains. *EMBO J.* **36**, 1719–1735 (2017). doi: 10.15252/embj.201695189; pmid: 28495679
20. H. Wu, P. Carvalho, G. K. Voeltz, Here, there, and everywhere: The importance of ER membrane contact sites. *Science* **361**, eaan5835 (2018). doi: 10.1126/science.aan5835; pmid: 30072511
21. S. Cohen, A. M. Valm, J. Lippincott-Schwartz, Interacting organelles. *Curr. Opin. Cell Biol.* **53**, 84–91 (2018). doi: 10.1016/j.ceb.2018.06.003; pmid: 30006038
22. Y. Ichimura *et al.*, A ubiquitin-like system mediates protein lipidation. *Nature* **408**, 488–492 (2000). doi: 10.1038/35044114; pmid: 11100732
23. Y. Kabeya *et al.*, LC3, a mammalian homologue of yeast Apg8p, is localized in autophagosome membranes after processing. *EMBO J.* **19**, 5720–5728 (2000). doi: 10.1093/emboj/19.21.5720; pmid: 11060023
24. M. R. Slobodkin, Z. Elazar, The Atg8 family: Multifunctional ubiquitin-like key regulators of autophagy. *Essays Biochem.* **55**, 51–64 (2013). doi: 10.1042/bse0550051; pmid: 24070471
25. T. Hanada *et al.*, The Atg12-Atg5 conjugate has a novel E3-like activity for protein lipidation in autophagy. *J. Biol. Chem.* **282**, 37298–37302 (2007). doi: 10.1074/jbc.C700195200; pmid: 17986448
26. Y. Zheng *et al.*, A switch element in the autophagy E2 Atg3 mediates allosteric regulation across the lipidation cascade. *Nat. Commun.* **10**, 3600 (2019). doi: 10.1038/s41467-019-11435-y; pmid: 31399562
27. J. Romanov *et al.*, Mechanism and functions of membrane binding by the Atg5-Atg12/Atg16 complex during autophagosome formation. *EMBO J.* **31**, 4304–4317 (2012). doi: 10.1038/emboj.2012.278; pmid: 23064152
28. N. Fujita *et al.*, The Atg16L complex specifies the site of LC3 lipidation for membrane biogenesis in autophagy. *Mol. Biol. Cell* **19**, 2092–2100 (2008). doi: 10.1091/mbc.e07-12-1257; pmid: 18321988
29. L. Juris *et al.*, PI3P binding by Atg21 organises Atg8 lipidation. *EMBO J.* **34**, 955–973 (2015). doi: 10.15252/embj.201488957; pmid: 25691244
30. K. Obara, T. Sekito, K. Niimi, Y. Ohsumi, The Atg18-Atg2 complex is recruited to autophagic membranes via phosphatidylinositol 3-phosphate and exerts an essential function. *J. Biol. Chem.* **283**, 23972–23980 (2008). doi: 10.1074/jbc.M803180200; pmid: 18586673
31. D. P. Valverde *et al.*, ATG2 transports lipids to promote autophagosome biogenesis. *J. Cell Biol.* **218**, 1787–1798 (2019). doi: 10.1083/jcb.201811139; pmid: 30952800
32. T. Osawa *et al.*, Atg2 mediates direct lipid transfer between membranes for autophagosome formation. *Nat. Struct. Mol. Biol.* **26**, 281–288 (2019). doi: 10.1038/s41594-019-0203-4; pmid: 30911189
33. T. Kotani, H. Kirisako, M. Koizumi, Y. Ohsumi, H. Nakatogawa, The Atg2-Atg18 complex tethers pre-autophagosomal membranes to the endoplasmic reticulum for autophagosome formation. *Proc. Natl. Acad. Sci. U.S.A.* **115**, 10363–10368 (2018). doi: 10.1073/pnas.1806727115; pmid: 30254161
34. K. Harada *et al.*, Two distinct mechanisms target the autophagy-related E3 complex to the pre-autophagosomal structure. *eLife* **8**, e43088 (2019). doi: 10.7554/eLife.43088; pmid: 30810528
35. A. Kihara, T. Noda, N. Ishihara, Y. Ohsumi, Two distinct Vps34 phosphatidylinositol 3-kinase complexes function in autophagy and carboxypeptidase Y sorting in *Saccharomyces cerevisiae*. *J. Cell Biol.* **152**, 519–530 (2001). doi: 10.1083/jcb.152.3.519; pmid: 11157979
36. S. W. Suzuki *et al.*, Atg13 HORMA domain recruits Atg9 vesicles during autophagosome formation. *Proc. Natl. Acad. Sci. U.S.A.* **112**, 3350–3355 (2015). doi: 10.1073/pnas.1421092112; pmid: 25737544
37. G. van Meer, D. R. Voelker, G. W. Feigenson, Membrane lipids: Where they are and how they behave. *Nat. Rev. Mol. Cell Biol.* **9**, 112–124 (2008). doi: 10.1038/nrm2330; pmid: 18216768
38. C. He *et al.*, Recruitment of Atg9 to the preautophagosomal structure by Atg11 is essential for selective autophagy in budding yeast. *J. Cell Biol.* **175**, 925–935 (2006). doi: 10.1083/jcb.200606084; pmid: 17178909
39. N. Matscheko, P. Mayrhofer, Y. Rao, V. Beier, T. Wollert, Atg11 tethers Atg9 vesicles to initiate selective autophagy. *PLOS Biol.* **17**, e3000377 (2019). doi: 10.1371/journal.pbio.3000377; pmid: 31356628
40. H. Suzuki, N. N. Noda, Biophysical characterization of Atg11, a scaffold protein essential for selective autophagy in yeast. *FEBS Open Bio* **8**, 110–116 (2017). doi: 10.1002/2211-5463.12355; pmid: 29321961
41. T. Pfaffenwimmer *et al.*, Hrr25 kinase promotes selective autophagy by phosphorylating the cargo receptor Atg19. *EMBO Rep.* **15**, 862–870 (2014). doi: 10.15252/embr.201438932; pmid: 24968893
42. Z. Tang *et al.*, TOM40 targets Atg2 to mitochondria-associated ER membranes for phagophore expansion. *Cell Rep.* **28**, 1744–1757.e5 (2019). doi: 10.1016/j.celrep.2019.07.036; pmid: 31412244
43. K. Oh-oka, H. Nakatogawa, Y. Ohsumi, Physiological pH and acidic phospholipids contribute to substrate specificity in lipidation of Atg8. *J. Biol. Chem.* **283**, 21847–21852 (2008). doi: 10.1074/jbc.M801836200; pmid: 18544538
44. S. von Bülow, G. Hummer, Kinetics ofAtg2-mediated lipid transfer from the ER can account for phagophore expansion. bioRxiv 2020.05.12.090977 [Preprint]. 14 May 2020. https://doi.org/10.1101/2020.05.12.090977.
45. M. Baba, K. Takeshige, N. Baba, Y. Ohsumi, Ultrastructural analysis of the autophagic process in yeast: Detection of autophagosomes and their characterization. *J. Cell Biol.* **124**, 903–913 (1994). doi: 10.1083/jcb.124.6.903; pmid: 8132712
46. M. Fengsrud, E. S. Erichsen, T. O. Berg, C. Raiborg, P. O. Seglen, Ultrastructural characterization of the delimiting membranes of isolated autophagosomes and amphisomes by freeze-fracture electron microscopy. *Eur. J. Cell Biol.* **79**, 871–882 (2000). doi: 10.1078/0171-9335-00125; pmid: 11152279
47. Y. Takahashi *et al.*, An autophagy assay reveals the ESCRT-III component CHMP2A as a regulator of phagophore closure. *Nat. Commun.* **9**, 2855 (2018). doi: 10.1038/s41467-018-05254-w; pmid: 30030437
48. Y. Zhen *et al.*, ESCRT-mediated phagophore sealing during mitophagy. *Autophagy* **16**, 826–841 (2020). doi: 10.1080/15548627.2019.1639301; pmid: 31366282
49. F. Zhou *et al.*, Rab5-dependent autophagosome closure by ESCRT. *J. Cell Biol.* **218**, 1908–1927 (2019). doi: 10.1083/jcb.201811173; pmid: 31010855
50. B. J. Ravenhill *et al.*, The cargo receptor NDP52 initiates selective autophagy by recruiting the ULK complex to cytosol-invading bacteria. *Mol. Cell* **74**, 320–329.e6 (2019). doi: 10.1016/j.molcel.2019.01.041; pmid: 30853402

51. M. D. Smith, S. Wilkinson, CCPG1, an unconventional cargo receptor for ER-phagy, maintains pancreatic acinar cell health. *Mol. Cell. Oncol.* **5**, e1441631 (2018). doi: 10.1080/23723556.2018.1441631; pmid: 30263939
52. J. N. S. Vargas *et al*., Spatiotemporal control of ULK1 activation by NDP52 and TBK1 during selective autophagy. *Mol. Cell* **74**, 347–362.e6 (2019). doi: 10.1016/j.molcel.2019.02.010; pmid: 30853401
53. E. Turco *et al*., FIP200 claw domain binding to p62 promotes autophagosome formation at ubiquitin condensates. *Mol. Cell* **74**, 330–346.e11 (2019). doi: 10.1016/j.molcel.2019.01.035; pmid: 30853400
54. T. Shintani, D. J. Klionsky, Cargo proteins facilitate the formation of transport vesicles in the cytoplasm to vacuole targeting pathway. *J. Biol. Chem.* **279**, 29889–29894 (2004). doi: 10.1074/jbc.M404399200; pmid: 15138258
55. R. A. Kamber, C. J. Shoemaker, V. Denic, Receptor-bound targets of selective autophagy use a scaffold protein to activate the Atg1 kinase. *Mol. Cell* **59**, 372–381 (2015). doi: 10.1016/j.molcel.2015.06.009; pmid: 26166702
56. R. Torggler *et al*., Two independent pathways within selective autophagy converge to activate Atg1 kinase at the vacuole. *Mol. Cell* **64**, 221–235 (2016). doi: 10.1016/j.molcel.2016.09.008; pmid: 27768871
57. D. Fracchiolla *et al*., Mechanism of cargo-directed Atg8 conjugation during selective autophagy. *eLife* **5**, e18544 (2016). doi: 10.7554/eLife.18544; pmid: 27879200
58. J. Sawa-Makarska *et al*., Cargo binding to Atg19 unmasks additional Atg8 binding sites to mediate membrane-cargo apposition during selective autophagy. *Nat. Cell Biol.* **16**, 425–433 (2014). doi: 10.1038/ncb2935; pmid: 24705553

ACKNOWLEDGMENTS

We thank G. Warren for comments on the manuscript. We thank S. Brodesser and the CECAD Lipidomics/Metabolomics Facility for performing lipidomics analyses. We thank M. Hartl from the Max Perutz Labs Mass Spectrometry Facility, the Max Perutz Labs BioOptics Facility, and the VBCF Electron Microscopy Facility for technical support and the VBCF for providing the MS instrument pool. Anti-CBP antibody and yeast strains carrying Atg2-Atg18 expression cassettes were provided by C. Ungermann. We thank L. Pietrek for help with the simulation setup and D. Fracchiolla for expressing and purifying unlabeled Atg21. **Funding:** This work was supported by ERC grant 646653 (S.M.), Austrian Science Fund FWF P32814-B (S.M.) and T724-B20 (J.S.-M.), Human Frontier Science Program RGP0026/2017 (S.M., G.H., and S.v.B.), an OEAW Doc fellowship (C.A.), and the Max Planck Society (G.H., S.v.B., and M.G.). **Author contributions:** S.M., J.S.-M., and G.H. designed and supervised research. V.B., N.C., S.v.B., and V.N. designed research. J.S.-M., V.B., N.C., S.v.B., V.N., C.A., and M.S. performed research. All authors analyzed data and commented on the manuscript. S.M. and J.S.-M. wrote the manuscript. **Competing interests:** S.M. is a member of the scientific advisory board of Casma Therapeutics. **Data and materials availability:** All data are available in the manuscript or the supplementary materials.

SUPPLEMENTARY MATERIALS

science.sciencemag.org/content/369/6508/eaaz7714/suppl/DC1
Materials and Methods
Figs. S1 to S11
Tables S1 to S5
References (*59*–*95*)
MDAR Reproducibility Checklist
Movie S1
Data S1

View/request a protocol for this paper from *Bio-protocol*.

9 October 2019; resubmitted 16 May 2020
Accepted 6 July 2020
10.1126/science.aaz7714

Science

Reconstitution of autophagosome nucleation defines Atg9 vesicles as seeds for membrane formation

Justyna Sawa-Makarska, Verena Baumann, Nicolas Coudevylle, Sören von Bülow, Veronika Nogellova, Christine Abert, Martina Schuschnig, Martin Graef, Gerhard Hummer and Sascha Martens

Science **369** (6508), eaaz7714.
DOI: 10.1126/science.aaz7714

Reconstituting autophagosome nucleation

To stay healthy, our cells must constantly dispose of harmful material. Autophagy, or self-eating, is an important mechanism to ensure the clearance of bulky material. Such material is enwrapped by cellular membranes to form autophagosomes, the contents of which are then degraded. The formation of autophagosomes is a complicated process involving a large number of factors. How they act together in this process is still enigmatic. Sawa-Makarska *et al.* recapitulated the initial steps of autophagosome formation using purified autophagy factors from yeast. This approach elucidated some of the organizational principles of the autophagy machinery during the assembly of autophagosomes.

Science, this issue p. eaaz7714

Science (print ISSN 0036-8075; online ISSN 1095-9203) is published by the American Association for the Advancement of Science, 1200 New York Avenue NW, Washington, DC 20005. The title *Science* is a registered trademark of AAAS.

Supplementary Materials for

Reconstitution of autophagosome nucleation defines Atg9 vesicles as seeds for membrane formation

Justyna Sawa-Makarska*, Verena Baumann*, Nicolas Coudevylle*, Sören von Bülow, Veronika Nogellova, Christine Abert, Martina Schuschnig, Martin Graef, Gerhard Hummer and Sascha Martens

* These authors contributed equally to this work
correspondence to: justyna.sawa-makarska@univie.ac.at or sascha.martens@univie.ac.at

This PDF file includes:

Materials and Methods
Figs. S1 to S11
Tables S1 to S5
Captions for Movies S1
Captions for Data S1
References

Other Supplementary Materials for this manuscript includes the following:

Movies S1
Data S1

Materials and Methods

Protein expression and purification

A list of constructs for protein expression can be found in Table S1. The purification procedures of proteins from constructs generated in this study are described below. The information of the published purification procedures can be found in the references listed in the Table S1.

6xHis-TEV-Atg21, 6xHis-TEV-mEGFP-Atg21, 6xHis-TEV-mCherry-Atg21 and 6xHis-Atg18-mEGFP were expressed from pETDuet-1 in *E. coli*. Rosetta pLysS. Cells were grown Terrific Broth (TB) medium at 37°C until an OD600 of 0.4. Then the temperature was decreased to 18°C. At an OD600 of 0.8 they were induced with 100 µM IPTG and grown for 16h at 18°C. Cells were pelleted and resuspended in a buffer containing 50 mM HEPES pH 7.5, 300 mM NaCl, 10mM imidazole, 2 mM $MgCl_2$, 2 mM β−mercaptoethanol, Roche complete protease inhibitors and DNAse. Cells were lysed by freeze thawing and 2x 30 s sonication. Lysates were cleared by ultracentrifugation (40 000 rpm for 30 min at 4°C in a Beckman SW45Ti rotor). Supernatant was filtered (0.45 µm) applied to a 5 ml Ni-NTA column (GE Healthcare, Sweden) and eluted via a stepwise imidazole gradient (50, 75, 100, 150, 200, and 300 mM). Protein-containing fractions were pooled and cleaved overnight at 4°C with TEV protease (6xHis-Atg21 and 6xHis-Atg18-mEGFP were not cleaved). The sample was concentrated and applied onto a Superdex 200 column (16/60 prep grade or 10/300 prep grade for 6xHis-Atg18-mEGFP, GE Healthcare) and eluted with a buffer containing 50 mM HEPES pH 7.5, 150 mM NaCl and 1 mM dithiothreitol (DTT). Fractions containing pure fusion proteins were pooled, concentrated, snap frozen in liquid nitrogen and stored at -80°C.

Atg2-Atg18-CBP, Atg2-GFP-Atg18-CBP and Atg2-mCherry-Atg18-CBP were purified from the SMY373, SMY374 and SMY439 strains, respectively. Cells were grown at 30°C in YPG up to an OD600 of 5-10. Cells were pelleted, washed once with cold H_2O, once with lysis buffer (200 mM NaCl, 50 mM Hepes pH 7.5, 1.5 mM $MgCl_2$, 1 mM DTT) and resuspended in lysis buffer containing complete protease inhibitors (Roche), an FY-inhibitor mix (Serva), DNAse I (Sigma) and benzonase (Sigma). Resuspended cells were frozen in liquid nitrogen as pearls and lysed via freezer milling. The milled powder was thawed and resuspended in lysis buffer containing protease inhibitors by rolling gently at 4°C. Lysates were cleared by centrifugation (30,000 g for 40 min at 4°C in a Beckman SW45Ti rotor). The supernatant was incubated with IgG Sepharose beads (GE Healthcare) on a rotary wheel for 30 min at 4°C. Beads with bound protein were washed 2 times with lysis buffer, once with high salt buffer (700 mM NaCl, 25mM HEPES + DTT) and further 2 times with lysis buffer. Bound proteins were eluted by cleavage using TEV protease at 16°C for 1 h. The cleaved sample was concentrated, applied onto a Superdex 6 column (10/300 prep grade, GE Healthcare) and eluted with a buffer containing 50 mM HEPES pH 7.5, 150 mM NaCl and 1 mM DTT. Fractions containing the purified proteins were pooled, concentrated, frozen in liquid nitrogen, and stored at -80°C.

6xHis-TEV-Atg2-mEGFP was expressed in the baculovirus expression system. Codon optimized versions of yAtg2 were purchased from GenScript. For expression a pFastBac vector was used. The Atg2-mEGFP construct was designed with a N-terminal

6xHis-tag followed by a TEV cleavage site. yAtg2 was c-terminally fused with a mEGFP fluorophore. Sf9 cells were grown to 1.10^6 cells/ml in 1 l of medium supplemented with penicillin and streptomycin and infected by the addition of 1 ml of P1 virus. Cells were harvested after 90 h at 95% viability, pelleted at 4000 rpm for 15 min and flash frozen in liquid nitrogen. The cell pellet was resuspended in 50 ml of ice-cold lysis buffer (50 mM HEPES pH 7.5, 500 mM NaCl, 2 mM b-mercaptoethanol, 1 mM $MgCl_2$, 10 mM imidazole) containing benzonase (Sigma) and protease inhibitors (Roche, Serva). The cells were lysed using a tissue homogenizer and the lysate was cleared by ultracentrifugation at 40000 rpm for 30 min. The cleared lysate was filtered through a 0.45 µm filter and applied to a 5 ml Ni-NTA column (GE Healthcare, Sweden). The protein was eluted via a stepwise imidazole gradient (50, 75, 100, 150, 200, and 300 mM). The protein containing fractions were pooled, concentrated, applied to a Superdex 6 column (10/300 prep grade, GE Healthcare) and eluted with a buffer containing 50 mM HEPES pH 7.5, 150 mM NaCl and 1 mM DTT. Fractions containing the purified proteins were pooled, concentrated, frozen in liquid nitrogen, and stored at -80°C.

Full-length *S. cerevisiae* PI3KC3-C1 subunits (Vps15, Vps34, Atg6 and Atg14) were sub-cloned into the pBig2ab vector using the biGBac method (*1*) for co-expression in baculovirus-infected Sf9 insect cells. All four genes were codon optimized for insect cell expression and their ORFs were purchased from GenScript. Atg14 protein was cloned with an N-terminal protein A tag followed by a TEV cleavage site. The recombinant bacmid carrying all four genes was generated with a DH10Bac *E. coli* strain (Invitrogen). For PI3KC3-C1 expression Sf9 cells were grown to $1x10^6$ cells/ml in 4 l of ESF 921 medium (Insect Cell Culture Medium, Protein Free, Expression Systems) supplement with penicillin and streptomycin and infected by the addition of 1 ml of P1 virus per 1l medium. Cells were harvest after 5 days, pelleted at 715 x g for 15 min, washed with 30 ml of PBS and flash frozen. For protein purification cells were lysed in lysis buffer (50 mM Tris pH 8.8, 300 mM NaCl, 1 mM DTT, 0.5 % CHAPS, 1 µl benzonase (Sigma), protease inhibitor cocktails (Sigma) and cOmplete protease inthibitor cocktail (Roche)). The lysate was cleared by centrifugation at 16 000 × g for 40 min, mixed with 1 ml of IgG sepharose fast flow beads (GE Healthcare) and incubated for 1 hour at 4°C rotating. The beads were then washed twice with wash 1 buffer (50 mM Tris pH 8.0, 300 mM NaCl, 1mM DTT, 0.5 % CHAPS) and twice with wash 2 buffer (50 mM Tris pH 8.0, 300 mM NaCl, 1 mM DTT). The protein A tag was cleaved by TEV protease in wash 2 buffer overnight at 4°C and the eluted PI3KC3-C1 was concentrated and subjected to size exclusion chromatography on a Superdex 200 10/300 column (GE Healthcare) equilibrated in 20 mM Tris pH 8.0, 150 mM NaCl, 1 mM DTT. Peak fractions were collected, concentrated, flash frozen and stored in -80°C.

Atg19 (1-374 residues), the Atg19 phosphomimetic S390D, S391D, S396D (3D) and Atg19 S390D, S391D, S396D, W412A (3DΔLIR) mutants were expressed and purified as described elsewhere (*2, 3*). mCherry-Atg8ΔR117 was subcloned to pET-Duet1 vector with 6xHis followed by a TEV cleavage site. The construct was expressed and the protein purified as EGFP-Atg8-ΔR117 described in (*4*).

Full-length *S. cerevisiae* Atg1 and Atg13 were sub-cloned into the pBig1b vector using the biGBac method (*1*) for co-expression in baculovirus-infected Sf9 insect cells. All genes were codon optimized for insect cell expression and their ORFs were purchased from GenScript. Atg1 protein was cloned with an N-terminal protein A tag

followed by a TEV cleavage site. The recombinant bacmid carrying the two genes was generated with a DH10Bac *E. coli* strain (Invitrogen). For expression Sf9 cells were grown to $1x10^6$ cells/ml in 4 l of ESF 921 medium (Insect Cell Culture Medium, Protein Free, Expression Systems) supplement with penicillin and streptomycin and infected by the addition of 1 ml of P1 virus per 1l medium. Cells were harvest after 4 days, pelleted at 800 x g for 15 min, washed with 30 ml of PBS and flash frozen. For protein purification cells were lysed in lysis buffer (50 mM TRIS pH 7.4, 300 mM NaCl, 2 mM MgCl2, 1 mM beta-mercaptoethanol, benzonase (Sigma), DNase, protease inhibitor cocktails (Sigma) and cOmplete protease inhibitor cocktail (Roche)) and further resuspended with a homogenizer. The lysate was cleared by centrifugation at 16 000 × g for 45 min, mixed with 0.8 ml of IgG sepharose fast flow beads (GE Healthcare) and incubated for 1 hour at 4°C rotating. The beads were then washed three times with wash buffer (50 mM Tris pH 7.4, 300 mM NaCl, 1mM DTT). The protein A tag was cleaved by TEV protease in the wash buffer overnight at 4°C and the eluted Atg1-Atg13 was concentrated and subjected to size exclusion chromatography on a Superdex 200 10/300 column (GE Healthcare) equilibrated in 25 mM Tris pH 7.4, 150 mM NaCl, 1 mM DTT. Peak fractions were collected, concentrated, flash frozen and stored in -80°C.

Atg11 and the full length Atg9 were expressed in the baculovirus expression system. Codon optimized versions of yeast Atg11 and Atg9 ORFs were purchased from GenScript. Atg11 constructs were all designed with a N-terminal 6xHis tag followed by a TEV cleavage site, a fluorophore (mEGFP, mCherry or no fluorophore) and the coding sequence for Atg11. Atg9 full length constructs were all designed with a N-terminal 6xHis tag followed by a TEV cleavage site, the coding sequence for Atg9, a fluorophore (mEGFP or mCherry) and a Twin-Strep tag. For both full length Atg9 and Atg11, Sf9 cells were grown to $1x10^6$ cells/ml in 1 L of medium supplement with penicillin and streptomycin and infected by the addition of 10 ml of P3 virus. Cells were harvested after 60 hours, pelleted at 2000 rpm for 15 min, washed with 30 ml of PBS and flash frozen. For both Atg9 and Atg11, the cell pellet was resuspended in 30 ml of ice cold lysis buffer per billion cells (50 mM HEPES pH 7.5, 500 mM NaCl, 10 % glycerol, 2 mM b-mercaptoethanol, 1 mM $MgCl_2$, benzonase and Roche Complete protease inhibitors). The cells were lysed using a tissue homogenizer and the lysate was cleared by centrifugation at 20000 rpm for 30 min. For Atg11, the cleared lysate was filtered through a 45 μm filter, brought up to 30 mM imidazole and loaded on a 5 ml HisTrap. The protein was eluted through a linear gradient from 0 to 300 mM imidazole in 25 mM Tris pH 7.4, 300 mM NaCl. The protein containing fractions were pooled, dialyzed overnight at 4°C against a low salt buffer (25 mM Tris, 100 mM NaCl) and loaded on a Q-sepharose column. The protein was eluted through a salt gradient (from 100 mM to 1 M NaCl in 25 mM Tris pH 7.4). The protein containing fractions were pooled, concentrated and loaded on a size exclusion column S6 equilibrated with 25 mM Tris pH 7.4, 300 mM NaCl. The identity and purity of the final sample was assessed by SDS-PAGE, immunoblot and mass spectrometry.

For full length Atg9, the cleared lysate was subjected to another round of centrifugation at 40 000 rpm for 1h. The membrane containing pellet was resuspended for 2h at 4°C in lysis buffer containing 2% DDM. After 2h of incubation the insoluble material was removed by centrifugation at 40 000 rpm for 1h. The supernatant was brought to 20 mM imidazole and loaded onto a 1 ml HisTrap. The protein was eluted by a

stepwise gradient of imidazole, from 0 to 300 mM imidazole in 50 mM HEPES pH 7.5, 500 mM NaCl, 10% glycerol, 0.3% DDM. The protein containing fractions were pooled, concentrated and loaded onto a size exclusion column S6 equilibrated with 50 mM HEPES pH 7.5, 500 mM NaCl, 10% glycerol, 0.2% DDM. In order to concentrate the protein without increasing the detergent concentration, the fractions containing protein were incubated with 150 µl of NiNTA beads for 3h at 4°C. The beads were washed several times with 25 mM Tris pH 7.4, 300 mM NaCl, 0.04% DDM. The protein was eluted in the desired volume of buffer supplemented with 300 mM imidazole. A final dialysis was performed overnight at 4°C against 25 mM Tris pH 7.4, 300 mM NaCl, 0.04 % DDM. The identity and purity of the final sample was assessed by SDS-PAGE and immunoblot.

Atg9 N-terminal domain (residues 1 to 285) was designed with a N-terminal 6xHis tag and a C-terminal mCherry tag. The protein was expressed in *E. coli* Rosetta (DE3) pLysS cells. Cells were grown at 37°C until an OD of 0.6. The expression was then induced by the addition of 0.1 mM IPTG and carried out at 18°C. Cells were harvested after 16 hours, pelleted at 5000 rpm for 15 min and resuspended in lysis buffer (50 mM HEPES pH 7.4, 300 mM NaCl, 2 mM $MgCl_2$, 2 mM b-mercaptoethanol, benzonase and Roche cOmplete protease inhibitors). The cells were lysed by sonication and the lysate was cleared by centrifugation at 20 000 rpm for 30 min. The cleared lysate was filtered through a 45 µm filter, brought up to 30 mM imidazole and loaded on a 5 ml HisTrap. The protein was eluted through a linear gradient from 0 to 300 mM imidazole in 25 mM Tris pH 7.4, 300 mM NaCl. The protein containing fractions were pooled, concentrated and loaded on a size exclusion column S6 equilibrated with 25 mM Tris pH 7.4, 300 mM NaCl. The identity and purity of the final sample was assessed by SDS-PAGE.

Atg9 PLs formation and analysis

Small unilamellar vesicles (SUVs, liposomes) destined for the reconstitution of Atg9 PLs were prepared with a lipid composition mimicking the lipid composition of the endogenous Atg9 vesicles determined in this study. The SUVs were composed of 44% liver PI, 40% POPC, 6% POPS, 6% POPE, 3% ATTO-390 DOPE, 1% POPA (for details see Table 2). Lipids were mixed in a glass vial and dried under an argon stream. The dry lipids were then dried further one hour under vacuum. The lipid film was rehydrated in 25 mM Tris pH 7.4, 300 mM NaCl. The lipids were resuspended by gentle mixing and sonicated for 2 min. The resuspended SUVs were then extruded first through 0.4 µm, then 0.1 µm membrane (Whatman, Nucleopore, UK) using the Mini Extruder from Avanti Polar Lipids Inc.. The final SUV suspension has a concentration of 0.8 mg lipids/ml.

For the incorporation of Atg9, the SUVs were treated with CHAPS (Avanti Polar Lipids, Inc.). The SUV suspension was brought up to 2.5 % CHAPS and incubated at RT for 1 h. The SUV suspension was then mixed 1 to 1 with a 1 µM Atg9 solution in 0.04 % DDM. The mixture was then incubated at RT for another 90 min. The mixture was then diluted by a factor of 10 in Tris 25 mM Tris pH 7.4, 300 mM NaCl in order to reach a detergent concentration below the CMC of both detergents. The resulting PLs solution was then dialyzed overnight at 4°C against 25 mM Tris pH 7.4, 300 mM NaCl supplemented with 0.1 g of BioBeads SM2 (BioRad) per liter of buffer. Finally, BioBeads were added directly to the sample and incubated 1 hour at RT. The insoluble

material that did not get incorporated into liposomes was removed by centrifuging 30 min at 18000 rpm. The supernatant containing Atg9 PLs was collected and used for subsequent experiments.

A sample of the PLs solution was subjected to ultracentrifugation at 100 000 rpm for 1 h in order to pellet the PLs. The yield of incorporation is defined as the ratio of the amount of protein contained in the pellet divided by the initial amount of protein before detergent removal (as determined by SDS-PAGE and immunoblot).

Atg9 PLs were submitted to limited proteolysis at room temperature in the presence of 0.25 µg/ml of trypsin and with or without 1% TWEEN.

Static light Scattering (SLS)

A sample of 300 µl at 10 µM of purified mCherry-Atg11 was applied to a Superose 6 Increase 10/300 GL column in 25 mM Tris pH 7,4, 300 mM NaCl. The column was coupled to a Wyatt TREOS II instrument (Wyatt Technology Corporation, Santa Barbara, CA, USA). Data were analyzed using the ASTRA V software (Wyatt).

Dynamic light Scattering (DLS)

DLS measurements were performed with a DynaPro NanoStar dynamic light scattering instrument (Wyatt Technology) using a quartz cuvette. All measurements were done at 25°C and each measurement consisted of 15 consecutive acquisitions of 10 sec. each. The scattering data were measured and analyzed with Dynamics 7.6.1.9 software using the globular protein model**.**

Negative stain EM

The Atg9 vesicles or Atg9 PLs were applied on the carbon-coated copper-palladium grids (glow-discharged for 60 s immediately before use), stained twice for 30 s with 5 µl of 2 % uranyl acetate, air dried, and stored under vacuum until imaging. The stained grids were imaged using a FEI Morgagni 268D transmission electron microscope equipped with a tungsten filament emitter operated at 80 kV and an 11 megapixel Morada CCD camera (Olympus). The images were taken at 44 000x or 71 000x magnification and analysed with Fiji.

Preparation of giant unilamellar vesicles (GUVs)

GUVs were prepared by electroformation as described previously (*4*). For Atg21, Atg2-Atg18 and Atg12–Atg5-Atg16 recruitment to the membrane the following mix was used: 57% POPC, 25.5% POPS, 15% POPE, 2.5% PI3P. To carry out the PI3KC3-C1-dependent Atg12–Atg5-Atg16 membrane recruitment and Atg8–PE conjugation and de-conjugation the following lipid mix was used: 55% DOPC, 10% DOPS, 17% DOPE, 18% liver PI. The percentage of lipids used was calculated as a mole fraction. The electroformation was conducted at 30°C and the GUVs were used for experiments directly afterwards.

Membrane recruitment - GUV assays

To image Atg21, Atg2-Atg18 and Atg12–Atg5-Atg16 membrane recruitment 15 µl of the electroformed GUVs were transferred to a 96-well glass-bottom microplate (Greiner Bio-One) and the respective proteins were added to the final concentration of 1

μM in a final reaction volume of 30 μl in a reaction buffer 25 mM HEPES at pH 7.5, 150 mM NaCl. In every experiment including GUVs, before the GUVs and the proteins were pipetted onto the plate, the wells were blocked with a blocking solution (2.5 mg/ml BSA in 50 mM TrisHCl pH 7.4, 150mM NaCl) for 1 h and washed twice with the reaction buffer. Images were acquired after 1h incubation in room temperature on LSM700 (Zeiss) microscope with 20x objective and processed with ImageJ software.

For Atg21, Atg2-Atg18 and Atg12–Atg5-Atg16 membrane recruitment in the presence of PI3KC3-C1 experiments mixes containing respective proteins, 0.1 mM ATP or 0.1 mM AMP-PNP, 0.5 mM $MgCl_2$, 2 mM $MnCl_2$ and 1 mM EGTA in a final volume of 15 μl were prepared. The reaction buffer contained 25 mM HEPES at pH 7.5, 150 mM NaCl. The final concentration of proteins in the reaction mixes were: 50 nM for PI3KC3-C1, 400 nM for Atg21, 400 nM for Atg2-GFP-Atg18 and 40 nM for Atg12–Atg5-Atg16-mCherry. The reaction mixes were added to the well already containing 15 μl of the electroformed GUVs. Concentrations of proteins and cofactors used were calculated for the final 30 μl volume of the experiment. The images were acquired after 1h incubation in room temperature in the dark using a confocal spinning disc microscope (Visitron) with 20x objective processed with ImageJ software. For the time course experiment, the imaging started 5 min after the addition of the reaction mix to GUVs. The images were acquired for 45 min at the indicated time points of reaction.

In vitro reconstitution of Atg8 lipidation on GUVs

To image the PI3KC3-C1-dependent Atg8–PE conjugation to GUVs, mixes containing respective proteins (according to the experimental setup), 0.5 mM ATP, 0.5 mM $MgCl_2$, 2 mM $MnCl_2$ and 1 mM EGTA in a final volume of 15 μl were prepared. The reaction buffer contained 25 mM HEPES at pH 7.5, 150 mM NaCl. The final concentrations of proteins in the reaction mixes were: 50 nM for PI3KC3-C1, 400 nM for Atg21, 400 nM for Atg2-Atg18, 40 nM for Atg12–Atg5-Atg16-mCherry, 80 nM for Atg7, 80 nM for Atg3, 400 nM GFP-Atg8ΔR117 and 400 nM GFP-Atg8-6xHis. The reaction mixes were added to wells of a 96-well glass-bottom microplate (Greiner Bio-One) already containing 15 μl of the electroformed GUVs. Concentrations of proteins and cofactors used were calculated for the final 30 μl volume of the experiment. The images were acquired after 1 h incubation in room temperature in the dark using a confocal spinning disc microscope (Visitron) with 20x objective processed with ImageJ software.

Microscopy-based protein-protein interaction assay

For the experiments shown in Figures 2B and 2G giant unilamellar vesicles (GUVs) were prepared. Preparation was carried out as described above. The lipid mixture was composed of 57% POPC, 25.5% POPS, 15% POPE, 2.5% PI3P. Buffer was composed of 50 mM HEPES pH 7.5, 150 NaCl and 1 mM DTT. Assays were performed under equilibrium conditions and mEGFP-Atg21, 6xHis-Atg21, Atg12–Atg5-Atg16-mCherry and Atg2-GFP-Atg18-CBP were added at a final concentration of 500 nM. The mixtures were incubated for at least 30 min at room temperature before imaging. Confocal images were acquired using a Visitron spinning disk microscope with a LD Achroplan 20x/0.4 Corr or a Zeiss LSM 700 with a Plan-Apochromat 20x/0.8 objective.

For Figure 1 D-F Atg12–Atg5-Atg16-mCherry, Atg5-mCherry-Atg16(1-46) and Atg16-mCherry were recruited to RFP-TRAP beads (Chromotek). Assays were performed under equilibrium conditions with 2 µM of the prey proteins Atg2-GFP-Atg18-CBP, Atg2-mEGFP and Atg18-mEGFP in SEC buffer (50 mM HEPES pH 7.5, 150 mM NaCl and 1 mM DTT). Beads were imaged either under a Zeiss LSM700 confocal microscope with a Plan-Apochromat 20x/0.8 objective. For quantification, a line was drawn across each bead in Fiji and the maximal value across the line was taken. Values were averaged for each sample within each replicate, and then among replicates. Beads from three independent experiments were quantified for the Atg2-GFP-Atg18-CBP, Atg2-mEGFP and Atg18-mEGFP signal.

GFP pulldown assay

To probe the direct interaction between Atg12–Atg5-Atg16 and Atg2-Atg18 (for Figure 1C) the purified Atg12–Atg5-Atg16-mEGFP or mEGFP (10 µM) was incubated with 10 µM of Atg2-Atg18-CBP and GFP_Trap_A beads (ChromoTek) for 1 h at 4°C. After washing the beads three times with 25 mM HEPES at pH 7.5, 150 mM NaCl and 1 mM DTT, the GFP_Trap_A beads together with bound proteins were subjected to immunoblot analysis. To detect the bait proteins anti GFP antibody (Max Perutz Labs, Monoclonal antibody facility) was used, to detect bound Atg2-Atg18-CBP anti CBP (a kind gift from Prof. Dr. Christian Ungermann, Osnabrück University, Germany) antibody was used.

Atg9 vesicle isolation – yeast growth conditions

Strains used for Atg9 vesicle isolation were either grown in 5 l baffled flasks in an overnight log-phase culture (strain SMY193 and SMY227) or using fermenter to obtain large quantities (strain SMY276) (see below for details of the fermentation). When reached OD600 of 2 the cultures were centrifuged at 3,000 x g for 10 min at room temperature, washed with 50 ml PBS with 2 % glucose, centrifuged again, and the resulting pellet resuspended in the HSE lysis buffer (15 mM HEPES pH 7.5, 50 mM NaCl, 750 mM sorbitol, 5 mM EDTA, Roche cOmplete protease inhibitor cocktail). The cell suspension was flash-frozen in liquid nitrogen in a form of small droplets. The cells were opened using a Freezer/Mill High Capacity Cryogenic Grinder (Spex SamplePrep) with the following settings: 1 min pre-cooling, 3 min graining, 2 min cooling, 15 CPS, 5 cycles. The milled powders were stored at -80°C.

Yeast fermentation

The large amounts of SMY276 strain expressing integrated Atg9-EGFP-TAP were produced by fermentation using a New Brunswick 13 l vessel containing 6 l starting media (Table S3). The fermenter set-up allowed the cells to stay in a rich growth phase at extremely high densities by maintaining a favourable environment in terms of nutrient supply, oxygenation, and pH balance. The final harvest target OD600 was between 110 and 130, with a cell paste target mass of 450–600 g, and a run time between 38–45 h. The vessel was inoculated with a 125 ml of YPD pre-culture (OD600 of 1.28) to an initial OD600 of 0.025 and run according to the settings outlined in Table S4. The target cell density was reached after 38 hours. The cell culture was harvested by centrifugation at 2 500 x g for 20 minutes at 4 °C. 500 g of the cell paste was washed with 5 l of cold PBS

buffer pH 6.8 containing 2 % of glucose (w/v). The material was then centrifuged again and resuspended in 2 l of cold HSE lysis buffer (25 mM HEPES pH 7.5, 50 mM NaCl, 750 mM sorbitol, 5 mM EDTA, Roche cOmplete protease inhibitor cocktail). This resulted in a total volume of 2.5 l suspension of yeast cells in lysis buffer. The cell suspension was flash-frozen in liquid nitrogen in a form of small droplets. The cells were opened using a Freezer/Mill High Capacity Cryogenic Grinder (Spex SamplePrep). The milled powders were stored at -80°C.

Isolation of Atg9 vesicles

The freezer-milled powder was weighed out using 10 g of powder per 300 µl of dynabeads coupled to appropriate antibody. The M-270 epoxy dynabeads (Invitrogen) were previously coupled with rabbit IgG (Sigma-Aldrich, No. 15006) and the Protein A dynabeads (Invitrogen) with rabbit anti-myc antibody (Max Perutz Labs, Monoclonal antibody facility) following the manufacturer's instructions. In the final step the beads were washed three times with HSE 135 buffer (15 mM HEPES pH 7.5, 135 mM NaCl, 750 mM sorbitol, 5 mM EDTA, and cOmplete protease inhibitor cocktail (Roche)). The yeast powder was thawed on ice with addition of 10 ml of HSE 135 buffer, transferred into 10 ml ultracentrifuge tubes and cleared by centrifugation at 40 000 rpm, 4°C, in a Beckman 70.1 Ti rotor (146 680x g). The supernatant was mixed with 300 µl of appropriate IgG dynabeads and incubated on a rotating wheel at 4°C for 1 h. The beads were then separated and washed one time with HSE 135 buffer, one time with HSE 250 buffer (15 mM HEPES pH 7.5, 250 mM NaCl, 750 mM sorbitol, 5 mM EDTA, cOmplete protease inhibitor, Roche), one time with HSE 135 buffer, and one time with HSE no sorbitol buffer (15 mM HEPES pH 7.5, 135 mM NaCl, 5 mM EDTA). The beads were then resuspended in the original volume, and separated from the buffer again. For mass spectrometry analysis of the Atg9 vesicles, this was the final fraction used. A cleavage mixture of 6xHis-TEV protease diluted in HSE no sorb buffer to a final concentration of 0.25 mg/ml or 1.0 mg/ml was then added to the beads, using 25 µl of the mixture per 100 µl of the IgG dynabeads. The reaction was incubated on a roller at 4°C for an hour and the supernatant was collected. This was the final fraction used for EM, DLS, MS and lipidomics analysis. For Atg9 vesicles recruitment to cargo beads experiments the supernatant containing Atg9 vesicles was incubated with the cargo mimetic beads. For experiments with Atg12–Atg5-Atg16 recruitment and Atg8–PE conjugation to Atg9 vesicles the supernatant containing TEV-eluted Atg9-EGFP vesicles was mixed with 10 µl of pre-equillibrated with HSE no sorbitol buffer GFP-Trap_A beads (ChromoTek), incubated on a roller at 4°C for an hour, washed twice with HSE 135 buffer and used for subsequent experiments.

Recruitment of Atg12–Atg5-Atg16 complex to Atg9 PLs.

The supernatant obtained from Atg9 PLs formation containing Atg9-EGFP PLs was incubated with 20 µl GFP-Trap_A beads (ChromoTek) overnight at 4°C slowly rotating. The beads were washed three times with 25 mM Tris pH 7.4, 300 mM NaCl buffer. The generation of GFP-Trap_A beads coated with Atg9-EGFP vesicles was described above (Atg9 vesicles isolation). To test for PI3KC3-C1-dependent Atg12–Atg5-Atg16 recruitment to the Atg9 PLs reaction mixes containing respective proteins (according to the experimental setup), 0.1 mM ATP or 0.1 mM AMP-PNP, 0.5 mM $MgCl_2$, 2 mM

$MnCl_2$ and 1 mM EGTA in a final volume of 15 µl were prepared. The final concentrations of proteins in the reaction mixes were: 50 nM for PI3KC3-C1, 400 nM for Atg21, 400 nM for Atg2-Atg18 and 40 nM for Atg12–Atg5-Atg16-mCherry. The reaction mixes were transferred to the wells of a 384-well glass-bottom microplate (Greiner Bio-One) and 0.5 µl of the washed GFP-Trap_A beads coated with Atg9-EGFP PLs were added to the respective wells. The images were acquired after 1 h incubation at room temperature in the dark using a confocal microscope LSM700 (Zeiss) with 20x objective and processed with ImageJ software.

Recruitment of the Atg2-Atg18 complex to Atg9 vesicles

The generation of GFP-Trap_A beads coated with Atg9-EGFP vesicles was described above (Atg9 vesicles isolation). Mock isolation from a strain carrying an untagged *ATG9* gene was used as a negative control. To test for Atg2-Atg18 recruitment to the Atg9 vesicles reaction mixes containing 1 µM of Atg2-Atg18 in a final volume of 15 µl were prepared in a 384-well glass-bottom microplate (Greiner Bio-One). 0.5 µl of the washed GFP-Trap_A beads coated with Atg9-EGFP vesicles were added to the respective wells. The images were acquired after 10 min incubation at room temperature in the dark using a confocal microscope LSM700 (Zeiss) with 20x objective and processed with ImageJ software.

In vitro reconstitution of Atg8 lipidation on Atg9 PLs

The GFP-Trap_A beads coated with Atg9 PLs were prepared as for the recruitment of Atg12–Atg5-Atg16 complex to Atg9 PLs experiments. To reconstitute Atg8–PE conjugation to the Atg9 PLs, reaction mixes containing respective proteins (according to the experimental setup), 0.5 mM ATP, 0.5 mM $MgCl_2$, 2 mM $MnCl_2$ and 1 mM EGTA in a final volume of 15 µl were prepared. The final concentration of proteins in the reaction mixes were: 50 nM for PI3KC3-C1, 400 nM for Atg21, 400 nM for Atg2-Atg18, 40 nM for Atg12–Atg5-Atg16, 100 nM for Atg7, 100 nM for Atg3 and 400 nM for mCherry-Atg8ΔR117. For all Atg8 lipidation experiments we use the Atg8 mutant lacking the last C-terminal arginine to expose the penultimate glycine which is coupled to PE in the Atg8–PE conjugation reaction. The reaction mixes were transferred to the wells of a 384-well glass-bottom microplate (Greiner Bio-One) and 0.5 µl of the washed GFP-Trap_A beads coated with Atg9-EGFP PLs were added to the respective wells. The images were acquired after 1 h incubation in room temperature in the dark using confocal microscope LSM700 (Zeiss) with 20x objective and processed with ImageJ software.

For the de-conjugation experiment, first the Atg8–PE conjugation to Atg9 PLs bound to GFP-Trap_A beads was carried out as described above. After 30 min, once the Atg8–PE conjugation signal was detected, Atg4 or Atg4C147S was added at a final concentration of 1 µM together with EDTA at a final concentration of 2 mM. Beads were imaged immediately after with a Spinning Disk microscope at the indicated time points of reaction.

Assembly of the cargo-mimetic beads (pulldown)

Glutathione sepharose 4B beads (GE Healthcare) were first equilibrated in 25 mM Tris pH 7.4, 300 mM NaCl. Beads were mixed with the same volume of a 30 µM solution of GST-prApe1 (1-41) or GST-prApe1 (1-45), 30 µM solution of Atg19 (wt or 3D) and

30 µM of Atg11 (wt, EGFP or mCherry tagged). The mixture was incubated for 1 h at 4°C and the beads were subsequently washed 3 times with 25 mM Tris pH 7.4, 300 mM NaCl. The beads were either imaged with a confocal microscope or analyzed by SDS-PAGE and immunoblot.

Recruitment of Atg9 PLs to the cargo-mimetic beads

10 µl of cargo beads were mixed with 200 µl of Atg9 PLs solution. Here the beads were coated with GST-prApe1 (1-41), Atg19-3D and mCherry-Atg11 or without mCherry-Atg11. The mixture was incubated overnight at 4°C and the beads were subsequently washed once with 25 mM Tris pH 7.4, 300 mM NaCl. The beads were imaged with a confocal microscope LSM700 (Zeiss) and analyzed by SDS-PAGE and immunoblot.

Recruitment of Atg9 vesicles to the cargo-mimetic beads

To test for Atg9-vesicles binding to Atg11 on the cargo-mimetic beads 10 µl of the cargo beads coated with GST-prApe1 (1-41), Atg19-3D and mCherry-Atg11 or without mCherry-Atg11 were mixed with equal volume of TEV-depleted supernatant containing TEV-eluted Atg9-EGFP-vesicles. The mixtures were incubated for 2 h at 4°C gently rotating, and the beads were subsequently washed once with 25 mM Tris pH 7.4, 150 mM NaCl. The beads were imaged with a confocal microscope LSM700 (Zeiss) and analyzed by SDS-PAGE and immunoblot.

In vitro reconstitution of Atg8 lipidation on Atg9 PLs bound to cargo-mimetic beads

The generation of cargo-mimetic beads and coating with Atg9 PLs thereof was described above ('Assembly of the cargo-mimetic beads (pulldown)' and 'Recruitment of Atg9 PLs on the cargo-mimetic beads'). In this reconstitution experiment the beads were coated with GST-prApe1 (1-41), Atg19-3D and Atg11. After the overnight coating with Atg9 PLs, the beads were washed once with 25 mM Tris pH 7.4, 150 mM NaCl and 0.5 µl pipetted into the wells of a 384-well glass-bottom microplate (Greiner Bio-One) containing 15 µl of respective conjugation reactions. The final concentrations of proteins in the reaction mixes were: 50 nM for PI3KC3-C1, 400 nM for Atg21, 400 nM for Atg2-Atg18, 40 nM for Atg12–Atg5-Atg16, 100 nM for Atg7, 100 nM for Atg3 and 400 nM for EGFP-Atg8ΔR117. The reactions were incubated for 2h at room temperature in the dark and the beads were imaged using confocal microscope LSM700 (Zeiss) with 20x objective and processed with ImageJ software.

In vitro reconstitution of Atg8 lipidation on Atg9 vesicles bound to cargo-mimetic beads.

The experiment was performed as for Atg9 PLs with slight following modifications. For assembling the cargo beads Atg19-3DΔLIR mutant was used to reduce background binding of Atg8 to the beads. In the conjugation reaction 200 nM of_mCherry-Atg8ΔR117 was used. To de-conjugate Atg8 from Atg9 vesicles Atg4 or Atg4C147S was added at a final concentration of 0.5 µM together with EDTA at a final concentration of 2 mM and microscopy images were taken at the indicated time points.

Atg1-Atg13 and Atg9 vesicles interaction with cargo beads (pulldown).

Cargo-mimetic beads were prepared as described above in 'Assembly of the cargo-mimetic beads (pulldown)' using GST-prApe1 (1-41), Atg19-3D and Atg11. 10 µl of the cargo beads were mixed with Atg9-EGFP vesicles ('Atg9 vesicles isolation') and Atg1-Atg13 at the final concentration of 250 nM. The mixtures were incubated overnight at 4°C gently rotating, and the beads were subsequently washed three times with 25 mM Tris pH 7.4, 150 mM NaCl. The beads were imaged with a confocal microscope LSM700 (Zeiss) and analyzed by SDS-PAGE and immunoblot using anti Atg1 and Atg13 antisera kindly provided by C. Kraft.

Quantification and statistical analysis

For quantification of protein recruitment to GUVs or beads and Atg8–PE conjugation to GUVs or bead-bound Atg9 PLs, four lines were drawn across each GUV/bead and the maximum brightness value along each the line was taken. Next, the average brightness of an empty area of each picture was measured (background fluorescence) and subtracted from the maximal fluorescence for each bead. The average values for each sample were averaged between 3 independent replicates and plotted with the relative standard errors.

For Atg8 de-conjugation and Atg12–Atg5-Atg16, Atg2-Atg18, Atg21 recruitment to the GUVs time course experiments the pictures of shown time points were assembled in time-lapse stacks and the same positions in every slice were quantified as described.

For all the quantifications described above, statistical analysis was performed. Statistical significance of the difference between 2 samples was established by 2 samples unpaired Student's t-test. Significant differences are indicated with * ($p \leq 0.05$), ** ($p \leq 0.01$) and *** ($p \leq 0.001$)

FRET-based basic lipid transfer assay with SUVs and Atg9 PLs

Lipid-transfer experiments with SUVs were set up at RT in 384-well plates, with 100-µl reaction volumes. Concentration of donor liposomes (63% DOPC, 12.75% DOPE, 19.25% NBD-PE, 5% Rhodamine) was 32 µM. Acceptor liposomes (75% DOPC, 25% DOPE) had a concentration of 80 µM each. Protein:total lipid ratio was 1:400 for each sample. Fluorescence intensity of NBD was measured via excitation at 485 nm and detection at 535 nm every 30 sec for 30 min using an Infinite F500 Microplate Reader (Tecan).

For the lipid transfer assays with Atg9 PLs the Atg9 PLs were generated as described above (Atg9 PLs formation). The lipid transfer experiment itself was set up as described before but instead of standard acceptor liposomes Atg9 PLs were used as acceptors in an equimolar ratio. Fluorescence intensity of NBD was measured via excitation at 485 nm and detection at 535 nm every 30 sec for 60 min.

For the dithionite assay lipid transfer was performed as described. After the last timepoint freshly prepared dithionite (5 mM final concentration) was added and NBD fluorescence was measured for further 60 min.

Lipid transfer assay with bulk conjugation on SUVs and Atg9 PLs

Preparation of small unilamellar vesicles (SUVs) for the Atg2-Atg18 transfer assay was carried out essentially as described elsewhere (*2*). The used lipid mixtures were composed of: Donors (SUV A): 39.5% POPC, 35% POPS, 20.5% POPE, 5% liver PI and acceptors (SUV B: 40% POPC, 35% POPS, 20% DAG, 5% PI3P. Buffer was composed of 50 mM HEPES pH 7.5, 150 NaCl and 1 mM DTT.

For lipid transfer with Atg9 PLs the lipid composition for the Atg9 PLs was: 55% POPC, 44% liver PI, 1% POPA. The generation of the PLs was carried out as described above (Atg9 PLs formation).

For the conjugation experiment, donors (SUV A) and acceptors (SUV B/Atg9 PLs) were mixed in an equimolar ratio and incubated overnight at RT with/without 1 µM Atg2-GFP-Atg18-CBP/Atg2-Atg18-CBP. On the next day, for Atg8 conjugation onto Atg9 PL, 50 nM PI3KC3-C1, 400 nM Atg21, 0.5 mM $MgCl_2$, 2 mM $MnCl_2$ and 1 mM EGTA were added to the mix and incubated for 1 h. This step was not required for the basic SUVs. The conjugation reactions were performed at 30°C and all buffers and solutions with the exception of the proteins were pre-warmed to this temperature. Atg3 and Atg7 were used at final concentrations of 0.1 µM. Atg8ΔR117 was used at a final concentration of 50 nM. Atg12 – Atg5-16mCherry was used at 0.1 µM. Additionally, 100 µM of ATP and 0.5 µM of $MgCl_2$ was used in the assay. The reactions were stopped at the respective time points by the addition of loading dye (12% SDS, 6% beta-mercaptoethanol, 30% glycerol, 0.05% Coomassie Brilliant blue G-250, 150 mM Tris-HCl pH 7) and boiling at 98°C for 10 minutes. The reactions were run on 15% SDS/polyacrylamide gels containing 6 M urea in the separating parts.

For the conjugation assay on SUVs, the gels were stained with Coomassie staining solution (40% ethanol, 10% acetic acid, 0.2% Coomassie Brilliant Blue). Gels of four independent experiments were quantified using the Analyze Gel tool of Fiji software. For statistical analysis, t-tests (unpaired, two-tailed, Welch's type) were carried out and a p-value < 0.05 was considered to be significant.

For the conjugation assay with Atg9 PLs, 6M urea gels were analyzed by immunoblotting using rabbit anti-Atg8 antibody.

Mass spectrometry analysis of proteins

Atg9-EGFP-9xmyc vesicles bound to magnetic beads or bands excised from silver- or Coomassie-stained SDS-PAGE were submitted to the mass spectrometry analysis at Max Perutz Labs (Vienna). The magnetic beads were resuspended in 2 M urea, 50 mM ammonium bicarbonate (ABC), 10 mM DTT. 300 ng trypsin (Promega, Trypsin Gold) were added and incubated for 90 min at room temperature. Free thiols were alkylated with 50 mM iodoacetamide in the dark for 10 minutes. The supernatant was transferred to a clean tube and digestion was completed over night at 37° C. Digestion was stopped with trifluoroacetic acid. After digestion the peptide solutions were desalted on custom-made C18 StageTips. Tryptic digests were separated on an Ultimate 3000 RSLC nano-flow chromatography system (Thermo Fisher Scientific), using a pre-column for sample loading (PepMapAcclaim C18, 2 cm x 0.1 mm, 5 µm, Dionex-Thermo-Fisher) and a C18 analytical column (PepMapAcclaim C18, 50 cm x 0.75 mm, 2 µm, Dionex-Thermo-Fisher), applying a linear gradient from 2 to 35 % solvent B (80 % acetonitrile, 0.1 % formic acid; solvent A 0.1 % formic acid) at a flow rate of 230 nl/min over 30 min for gel

bands and 120 min for bead samples. Eluting peptides were either analysed on a Q Exactive Plus Orbitrap mass spectrometer (or a Velos LTQ Orbitrap), equipped with a Proxeon nanospray source (all Thermo Fisher Scientific), operated in a data-dependent mode. Survey scans were obtained in a mass range of 380–1 650 m/z with lock mass on, at a resolution of 70,000 at 200 m/z and an AGC target value of 3E6. The 12 most intense ions were selected with an isolation width of 2 Da, fragmented in the HCD cell at 27 % collision energy and the spectra recorded at a target value of 1E5 and a resolution of 17500. The Velos orbitrap was set to 60 000 resolution for the MS1 scan. Selected precursors were fragmented in the linear ion trap at 35 % normalised collision energy. Peptides with a charge of +1 were excluded from fragmentation, the peptide match and exclude isotope features were enabled and selected precursors were dynamically excluded from repeated sampling for 10 s (or 60 s for 120 min gradient). Raw data were processed using the MaxQuant software package and searched against the uniprot *Saccharomyces cerevisiae* database (www.uniprot.org). The search was performed with full trypsin specificity and a maximum of two missed cleavages. Carbamidomethylation of cysteine residues was set as fixed, oxidation of methionine and N-terminal protein acetylation as variable modifications – all other parameters were set to default. Results were filtered at a protein and peptide false discovery rate of 1%. LFQ (label free quantification) was used to quantify proteins in the pull downs. Raw summed peptide intensities were log2 transformed, reverse hits and completely missing values removed, missing values imputed for hits with valid intensity level in one of the two samples. The results were then filtered for higher confidence hits: ≥ 2 unique peptides/protein, ≥ 2 MS/MS count in Atg9-EGFP sample, log2(ATG9-EGFP/wt) ≥ 3, potential contaminants (such as keratin) removed. Statistical analysis was performed in Perseus.

MS analysis of lipids

Atg9 vesicles for mass spectrometry analysis of the lipid composition were prepared as described above, using 60 g of Atg9-EGFP-TAP fermented powder (SMY276) and 6 ml epoxy dynabeads cross-linked to rabbit IgG. The vesicles bound on beads were flash-frozen with liquid nitrogen and shipped on dry ice for analysis. Lipid analyses were performed at the CECAD Lipidomics Facility, University of Cologne, as previously described (*5*).

Atg9 vesicle modeling.

Coarse-grained simulation of a 58-nm diameter lipid vesicle. We set up a lipid bilayer with composition DOPC (41.8%) : DOPE (6.1%) : POPS (7.2%) : POPI (44.9%) using the insane.py python script (*6*) and the MARTINI 2.2 coarse-graining scheme (*7, 8*). In the simulation setup, the lipid bilayer was oriented in the *xy*-plane, with water above and below. Molecular dynamics (MD) simulations of the system were performed with Gromacs 2018.6 (*9*) and standard MARTINI parameters (*8*). After steepest-descent energy minimization, the system was equilibrated for 300 ns. The pressure was controlled with semiisotropic pressure coupling (20 ns equilibration with Berendsen barostat (*10*), followed by 300 ns equilibration with Parrinello-Rahman barostat (*11*) at 1 bar, and the temperature of 300 K was maintained using the velocity-rescaling thermostat (*12*). Timesteps of 20 fs and 30 fs were used in the first and second equilibration step, respectively.

To form a vesicle, the equilibrated lipid bilayer was transferred to a larger water box, in which the bilayer was separated from the box walls in *x* and *y* dimensions by 16 nm of water. By breaking the connections via periodic boundaries, we created a square-shaped bilayer patch with open edges. An MD simulation of this patch in aqueous solution was performed with parameters as given above for a total simulation time of 1.4 μs. Within 570 ns, the lipid bilayer patch closed to form a spherical vesicle. Proteins were added to the vesicle in the subsequent modeling steps.

Addition of Atg9 to the vesicle. The HIV gp41 six-helix bundle (PDB ID: 3F4Y (*13*)) was used as model for the transmembrane domain (TMD) of Atg9. 28 molecules of this rough Atg9 TMD model were inserted into the vesicle membrane at random positions. The TMDs were oriented with the α-helices approximately perpendicular to the vesicle surface.

The N- and C-terminal disordered regions of Atg9 were represented as intrinsically disordered regions (IDRs). Models of these regions were built using the in-house biomeccano python library (*14*), briefly described here. First, the amino-acid sequence of the Atg9 N-terminus (res. 1-318) and C-terminus (res. 746-997) were cut into overlapping pentamer fragments. Then, all-atom explicit-solvent replica-exchange MD simulations (REMD) of the individual pentamer fragments were run using the Amber99SB*-ILDN-Q protein force field (*15-17*) with TIP3P water (*18*) to sample the conformational space of the individual fragments. Following steepest-descent energy minimization, the systems were equilibrated for 50 ps in NVT ensemble (velocity-rescaling thermostat (*12*) with a 1 fs timestep and for 1 ns in NPT ensemble (Berendsen barostat (*10*)) with a 2 fs timestep. REMD production simulations were carried out with 24 temperatures ranging from 280 K to 440 K in NPT ensemble (Parrinello-Rahman barostat (*11*)) with a 2 fs timestep.

Following REMD simulations, 70 models of the Atg9 N- and C-terminal disordered regions were built from the pentamer fragments. Overlapping fragments were linked together, growing the IDR chain piecewise from N-terminus to C-terminus. The orientation of the newly added fragment was determined by RMSD fitting to the overlapping residue. For each linking event, fragment conformations were drawn from random snapshots of the lowest-temperature MD simulation (280 K). Random models of the Atg9 termini were attached to the TMDs and rotated until none of the α-carbon atoms clashed with the lipid beads or other Atg9 α-carbon atoms (clash distance cutoff: 0.8 nm).

Addition of remaining proteins to the vesicle model. The TMD and cytosol-facing C-terminus of Atg27 were built from homology models using the RaptorX webserver (*19*). The TMD of Atg27 (res. 198-220) was built from a homology model based on PDB ID: 5XTC, chain I (*20*). The cytosol-facing C-terminus of Atg27 (res. 221-271) was built from a homology model based on PDB ID: 1BY1, chain A (*21*). Ten Atg27 TMDs were inserted into the membrane and the C-terminal Atg27 models were connected to the TMD as described above for Atg9.

The remaining major constituents of Atg9 vesicles were assembled using different levels of coarse graining, depending on the available structural data. Atg21 was modeled according to hsv2, a member of the PROPPIN family (PDB ID: 3VU4 (*22*)). A low-resolution particle model of the Atg2-Atg18 complex was constructed from its electron density map (EMDB: 8899 (*23*)) using in-house code. The Atg12-Atg5-Atg16 complex was assembled from the Atg12-Atg5(-Atg16) core (PDB ID: 3W1S (*24*)) and the Atg16

coiled-coiled domain (PDB 3A7P (*25*)). Missing linker residues were added with MODELLER (*26*). The resulting Atg12-Atg5-Atg16 model is comprised of Atg12 residues 98-183, Atg5 residues 1-294, and Atg16 residues 1-150.

The structure of Atg3 was taken from PDB 2DYT (*27*). Missing structural parts of Atg3 were added with *MODELLER*, enforcing α-helices at residues 2-13 and 150-155. The structure was relaxed by 100 ns all-atom MD simulation following energy minimization and equilibration with parameters as above for the IDR fragments (with the exception that a 2 fs timestep was used for all equilibration steps). The structure of Atg8 was taken from the solution structure (PDB ID: 2KWC (*28*)). The Atg7 dimer was taken from the crystal structure (PDB ID: 4GSL (*29*)), removing both Atg3 molecules. The crystal structure of the Vps34 complex was taken from PDB ID: 5DFZ (*30*). No structural information of Atg23 is known. Therefore, we performed homology modeling of Atg23 with the *I-TASSER* webserver (*31, 32*) using the PDB template ID: 4UXV, chain A (*33*), followed by 5 ns equilibration and 60 ns production of atomistic MD with run parameters as above. We note that the homology model of Atg23 was built from a template of only 21% sequence identity and should only be considered as a rough sketch of the real structure of Atg23. The SNAREs SFT1, TLG1, VTI1, and GOSR1 were modeled from a generic TMD (using the Atg27 TMD), a generic IDP (using the Atg9 N-terminal model cut to appropriate length) and – where applicable – the structures of the respective N-terminal head groups of TLG1 (PDB ID: 2C5J (*34*)) and VTI1 (PDB ID: 3ONJ (*35*)). In lack of a structure of the GOSR1 N-terminal domain or any suitable homology model, the structure of the TLG1 head group (PDB ID: 2C5J (*34*)) was also used for the head group model of GOSR1. The SNARE SSO1 was built from a generic TMD (Atg27 TMD) and a merge of two crystal structures (PDB IDs: 1FIO (*36*) and 3B5N (*37*)). All SNARE models were built manually using Pymol (Schrödinger).

Assembly of the proteins on the vesicle. All proteins except Atg9 and Atg27 were placed manually on the Atg9 vesicle model using Pymol. The following protein-protein and protein-membrane interaction interfaces were considered in the modeling procedure: Atg2 – Atg9, Atg2 – Atg5, Atg19 – Atg12, Atg21 (FRRG) – membrane, Atg21 – Atg16 (residues 101-102), Atg3 – Atg12 (residues 149, 154), Atg3 (residue 4) – Atg8 (C-terminal Gly), Atg3 (residues 1-7) – membrane, Atg23 (residues 46-61) – membrane, PI3KC3 BARA domain – membrane, PI3KC3 kα12 helix – membrane.

Estimating the effective surface coverage of Atg9 vesicles. We describe two metrics to estimate the effective surface coverage of the vesicle, using (A) a geometric criterion and (B) a diffusive binding model. To calculate a geometric coverage, we generated 2 x 5000 straight rays pointing outward in random directions from the vesicle center-of-mass. The coverage was defined as the fraction of lines passing within 0.4 nm of any protein α-carbon atom (where the Atg2-Atg18 bead representation of the electron density map consisted entirely of α-carbon beads). This effective geometric surface coverage accounts for protein segments that do not directly touch the vesicle surface. However, proteins farther away from the vesicle contribute less to the effective geometric surface coverage. In this way, we obtained an effective geometric surface coverage of 19%.

We also defined a coverage in terms of the fraction of diffusive binders hitting a protein first, before reaching the lipid-covered vesicle surface. We initiated random walks at random positions on a sphere around the vesicle center-of-mass, with a radius 15 nm

beyond the most distant protein α-carbon atom. From the starting point, the particle underwent three-dimensional random walks with a step size of 1.5 nm. If the test particle came within 0.8 nm of a protein α-carbon atom, the particle was "caught" by the protein; if it came within 0.8 nm of a lipid PO4 bead, it "reached" the vesicle; if it migrated 15 nm beyond the starting sphere, it had "escaped". The ratio "caught" / ("caught" + "reached") then defined a dynamic surface coverage that takes into account the Brownian motion of the incoming particle. We obtain a dynamic surface coverage of 82%.

Yeast strains and manipulation

Yeast strains are listed in Table S5. All experiments were performed with BY4741 yeast strains unless stated otherwise. Genetic modifications were done by PCR and/or homologous recombination using standard techniques. Multiple deletions were generated by mating and dissection. The strains for expression and purification of Atg2-GFP-Atg18-CBP and Atg2-Atg18-CBP (SMY373, SMY374) were generated by crossing strains that were kind gifts of Prof. Dr. Christian Ungermann (#9058, #9059, Osnabrück University, Germany) with a *pep4Δ* strain.

Quantitative live cell imaging

Plasmid DNA was transformed to yeast in stationary phase grown on YPD-agar according to a LiOAc/ssDNA/PEG transformation protocol. Transformed yeast strains were grown in synthetic defined minimal medium (SD; 1.7 g/l yeast nitrogen base without amino acids and ammonium sulphate (Formedium, UK), 5 g/l ammonium sulfate, 2 g/l glucose) supplemented with the appropriate amino acid drop-out mix (CSM; Formedium) to log phase and treated with 220 nM rapamycin for 2 hours before imaging. Cells were immobilized with concavalinA (Sigma). Widefield images were obtained on a Deltavision ULTRA Epifluorescence Microscope using a UPlanSApo 100x/1.4 Oil objective. Deconvolution of the live cell images was carried out with the softWoRx – Border Rolloff. Images were analyzed using the Fiji software. For the quantification of Atg5 puncta approximately 150 cells were counted per experiment per construct (3 experiments each). Box-Plot was generated with Python.

prApe1 processing assay

Yeast cells were grown in rich medium (YPD: 1% yeast extract, 2% peptone, 2% glucose) to mid-log phase and, where indicated, treated with 220 nM rapamycin or starved in nitrogen starvation medium (SD-N: 0.17% yeast nitrogen base without amino acids, 2% glucose) for 4 h at 30°C. Cultures were precipitated with 7% trichloroacetic acid (TCA) and incubated for 10 min on ice. Precipitated proteins were pelleted at 13 000 rpm for 2 min at 4°C, washed with 1 ml acetone, air-dried and resuspended in urea loading buffer (120 mM Tris-HCl pH 6.8, 5% glycerol, 8 M urea, 143 mM b-mercaptoethanol, 8% SDS) and analyzed by immunoblotting using rabbit anti-Ape1 antiserum kindly provided by C. Kraft.

GFP-Atg8 cleavage assay

Yeast strains were transformed with a GFP-Atg8 expressing plasmid, grown to mid-log phase in synthetic selection medium (SD: 0.17% yeast nitrogen base, 0.5% ammonium sulfate, 2% glucose, amino acids as required) and, where indicated, treated

with 220 nM rapamycin or starved in nitrogen starvation medium for 4 h at 30°C. Whole cell lysates were prepared by TCA extraction (described above) and analyzed by immunoblotting using a mouse anti-GFP antibody (Max Perutz Labs, Monoclonal antibody facility).

In vivo Atg8 lipidation assay

Yeast cells were grown in YPD to mid-log phase and starved for 4h in nitrogen starvation medium. Whole cell lysates were prepared by TCA extraction (described above), separated on a 15% SDS-polyacrylamide gel containing 6M urea and analyzed by immunoblotting. The Atg8 and Atg8-PE bands were detected using a rabbit anti-Atg8 antibody.

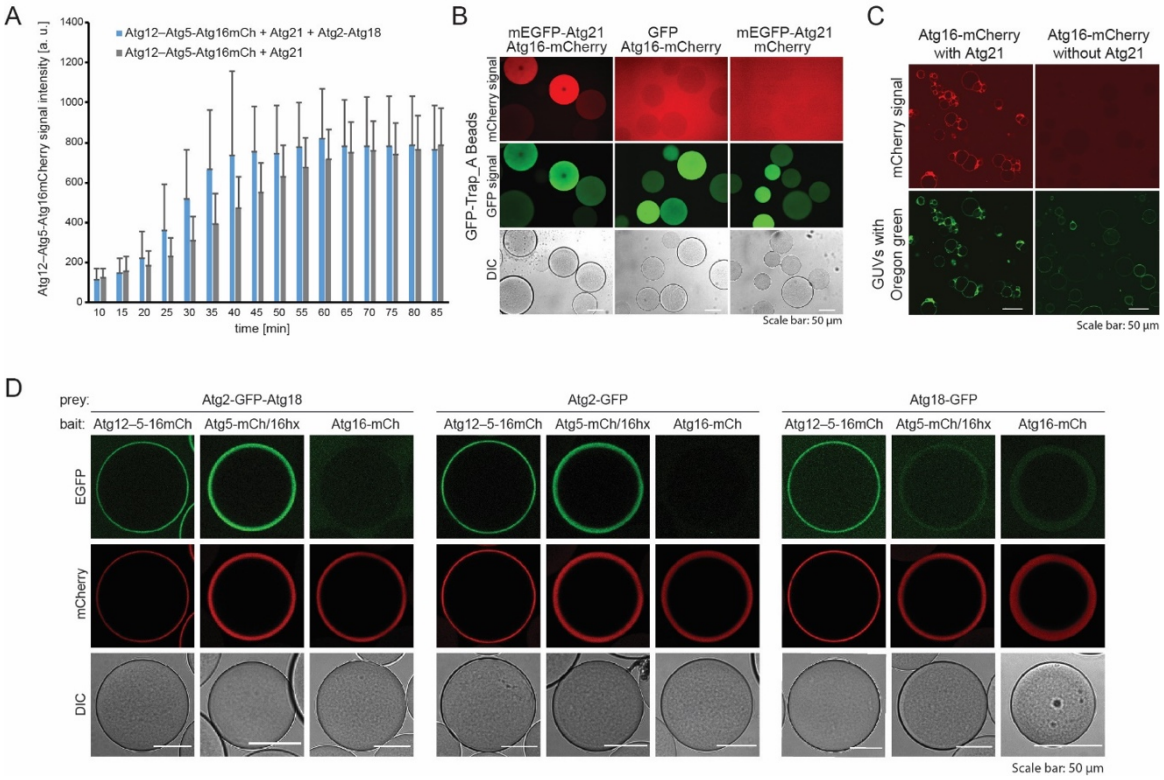

Fig. S1.

(A) Quantification of Atg12–Atg5-Atg16-mCherry intensity on GUVs in the presence of either both PROPPINs (Atg21, Atg2-Atg18) or only Atg21 over time. The quantification included at least 50 GUVs per condition. The error bars represent the standard deviations among the GUVs within one experiment. (B) Microscopy based protein interaction assay between Atg21 and Atg16. GFP-Trap beads were coated with either mEGFP-Atg21 or EGFP and imaged in the presence of either Atg16-mCherry or mCherry. (C) Microscopy images of GUVs (39.5% DOPC, 35% DOPS, 20% DOPE, 5% PI3P, 0.5% Oregon Green) incubated with Atg16-mCherry in the presence or absence of Atg21. The GUV membrane was labeled with Oregon Green. (D) Microscopy images of the interaction mapping experiment between Atg12–Atg5-Atg16 and Atg2-Atg18 of the experiment shown in Figure 1 (D-F). RFP-Trap beads were coated with indicated mCherry labelled bait proteins and incubated with indicated GFP-labelled prey proteins at 2 µM final concentration. The Atg16hx stands for N-terminal Atg16 helix (residues 1-46) used for stabilizing Atg5 during purification.

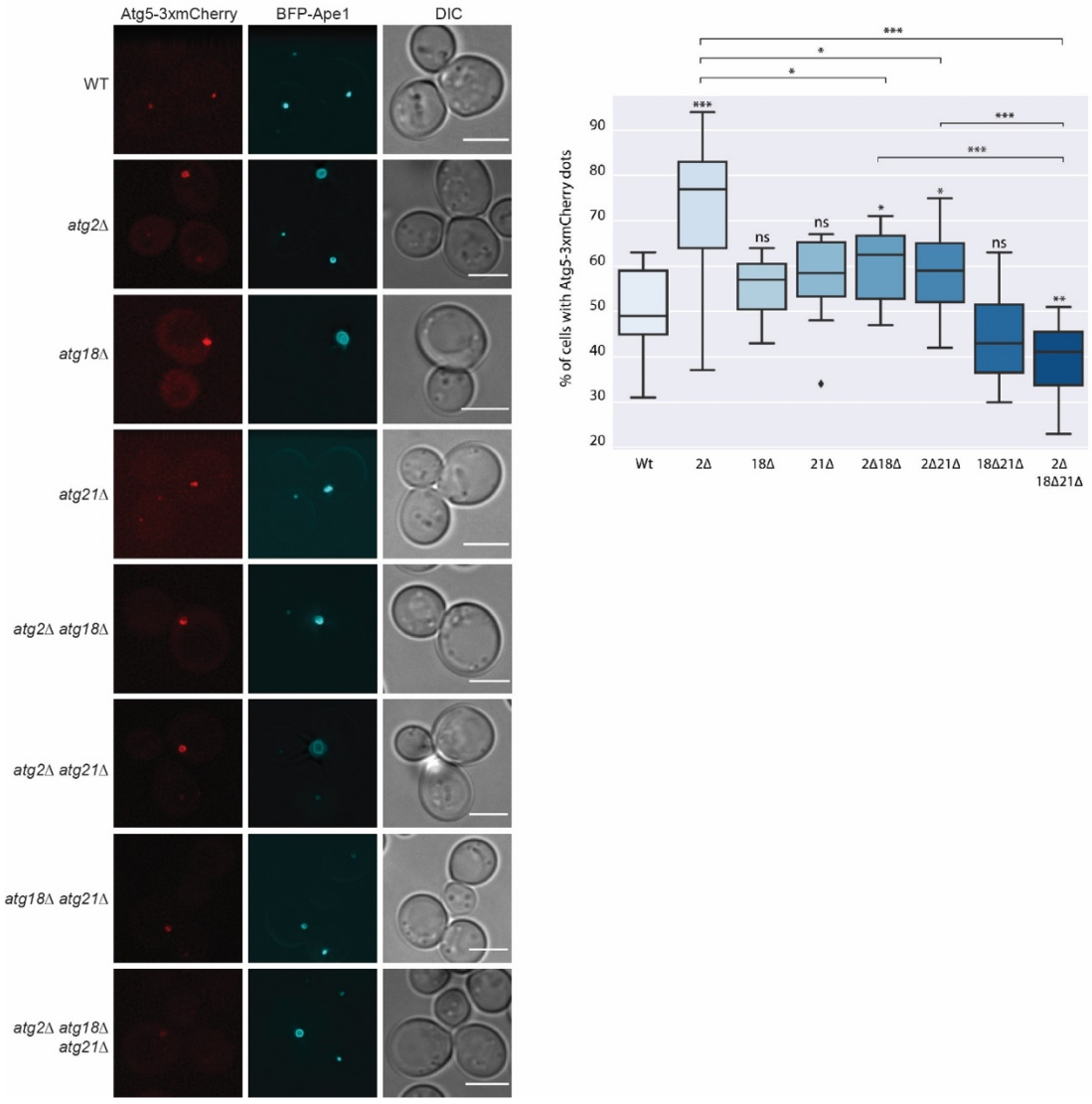

Fig. S2.

Recruitment of Atg5 to the autophagosome formation site. Yeast cells of the indicated genotype expressing Atg5-3xmCherry were treated with 220 nM rapamycin for 2 h and imaged using a Deltavision ULTRA Epifluorescence microscope. Graph shows the percentage of cells displaying Atg5–3xmCherry dots. In total, 3 independent experiments were conducted. The graphs show the averages and the error bars represent the standard deviations. P-values were calculated using Student's t-test. Scale bars: 4 µm. Significances are indicated with * when p value ≤ 0.05, ** when p value ≤ 0.01, and *** when p value ≤ 0.001.

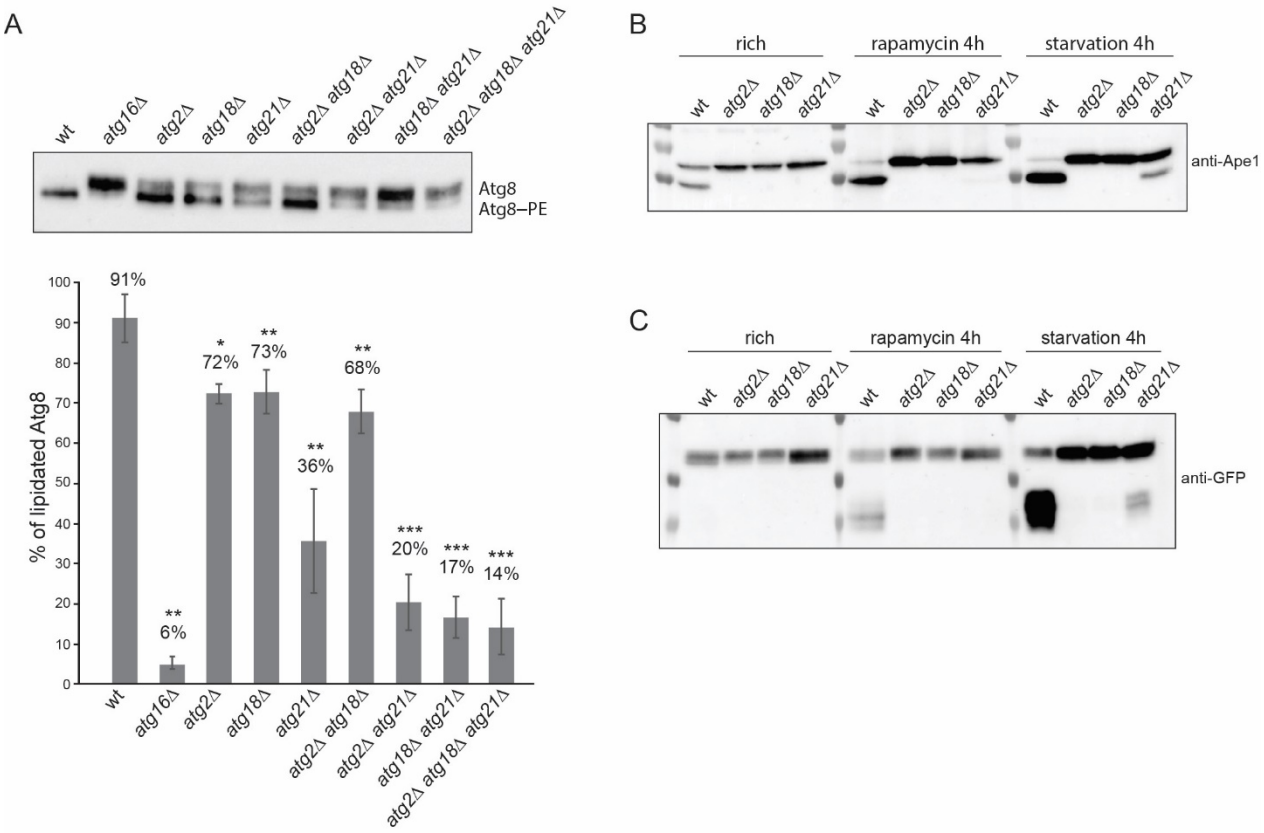

Fig. S3.

(A) Anti-Atg8 immunoblot using cell lysates of the indicated yeast strains. The bar diagram shows the average values of three independent experiments and the error bars represent the standard deviations. *P*-values were calculated using Student's *t*-test. Significance is indicated with * ($p \leq 0.05$), ** ($p \leq 0.01$) and *** ($p \leq 0.001$). (B) Anti-Ape1 immunoblot showing a prApe1 processing assay using the indicated deletion strains under nutrient-rich condition, after treatment with 220 nM rapamycin or starvation for 4 hours. The lower Ape1 band indicates prApe1 processing and thus its delivery into the vacuole. (C) Anti-GFP immunoblot of a GFP-Atg8 cleavage assay used to monitor bulk autophagy in the indicated deletion strains under the indicated conditions.

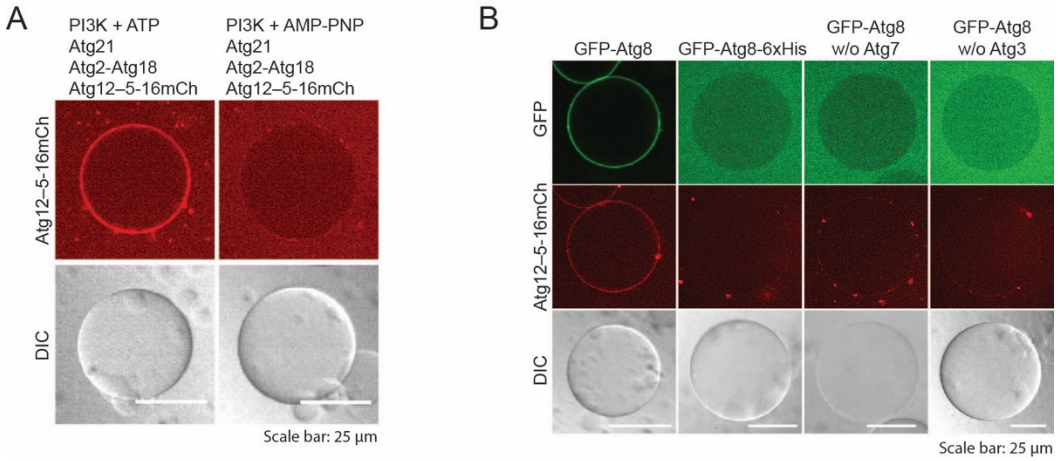

Fig. S4.

(A) Microscopy images of GUVs (55% DOPC, 10% DOPS, 17% DOPE, 18% liver PI) incubated with Atg21, Atg12–Atg5-Atg16-mCherry, PI3KC3-C1, and with either ATP or AMP-PNP. (B) Microscopy images of GUVs as in (A) incubated with PI3KC3-C1, ATP, Atg21, Atg2-Atg18, Atg7, Atg3, Atg12–Atg5-Atg16-mCherry, GFP-Atg8ΔR117 or GFP-Atg8-6xHis. The two right panels show Atg8 lipidation without either Atg7 or Atg3 added to the reaction.

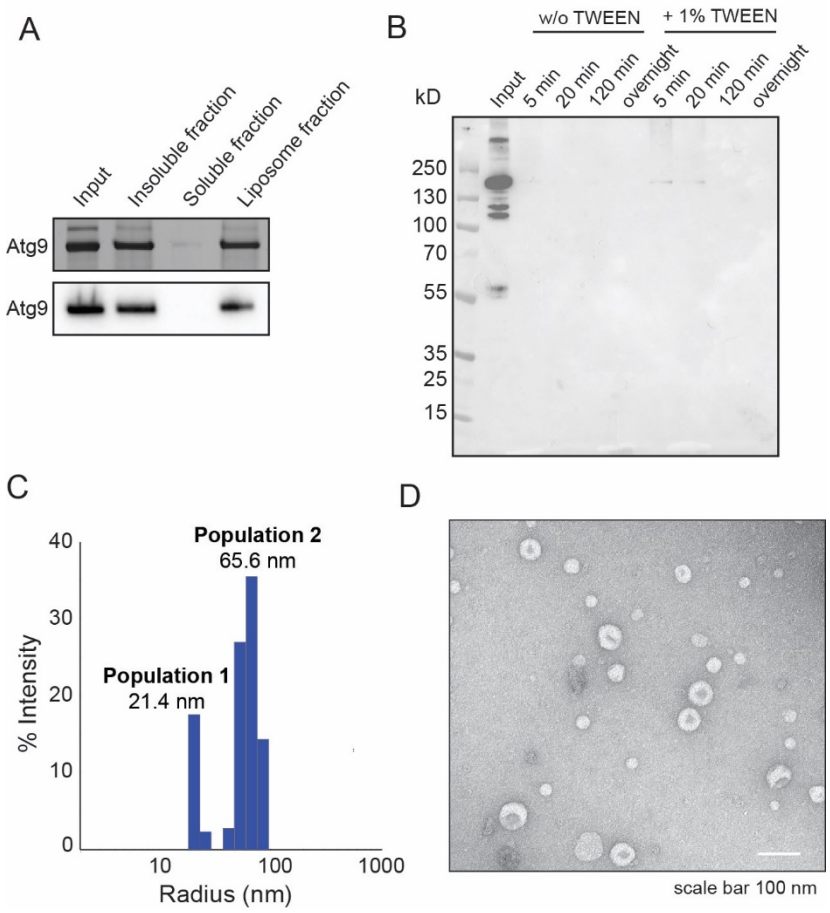

Fig. S5.

(A) Silver stained SDS-PAGE gel (top) and anti-GFP immunoblot (bottom) showing the different steps of Atg9 reconstitution into liposomes. (B) anti-GFP immunoblot showing different time points of Atg9 PLs treated with trypsin in the absence or presence of 1% TWEEN. (C) Size distribution of the Atg9 PLs measured by DLS, the average size of the two detectable populations are indicated. (D) Electron micrograph of negatively stained Atg9 PLs.

A

	GPL class	Rep 1	Rep 2	Rep 3
Atg9-EGFP sample	PC	46.13	51.78	50.02
	PE	11.20	11.64	10.64
	PS	11.93	11.74	10.77
	PI	39.66	56.49	45.33
	PA	2.01	2.47	2.16
	pmol total GPL	110.93	134.13	118.92
wt background	PC	18.85	16.02	15.79
	PE	6.93	6.10	6.34
	PS	7.07	5.20	5.66
	PI	14.96	12.92	6.90
	PA	1.01	0.80	0.89
	pmol total GPL	48.82	41.03	35.57
background subtracted	PC	27.27	35.77	34.23
	PE	4.27	5.54	4.30
	PS	4.87	6.54	5.11
	PI	24.70	43.58	38.44
	PA	1.00	1.67	1.27
	pmol GPL total	62.11	93.10	83.35
percentage	PC	43.91	38.42	41.07
	PE	6.88	5.95	5.16
	PS	7.84	7.02	6.14
	PI	39.77	46.81	46.12
	PA	1.61	1.80	1.52

	mean %	SD
PC	41.13	2.74
PE	6.00	0.86
PS	7.00	0.85
PI	44.23	3.88
PA	1.64	0.14

B

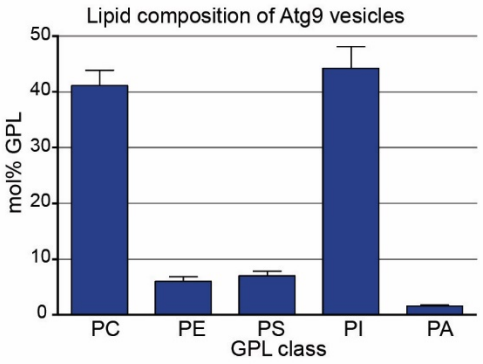

C

Protein names	Gene names	log2 ratio (Atg9 - wt)	iBAQ (Atg9)	No. molecules per one Atg9 vesicle (MS)	No. molecules in the model	TMDs
Autophagy-related protein 9	ATG9	14.44	1.31E+08	**28**	**28**	**6**
Autophagy-related protein 23	ATG23	12.71	4.77E+07	**10**	**10**	**0**
Autophagy-related protein 27	ATG27	8.64	4.17E+06	**1**	**10**	**1**
Protein transport protein SFT1	SFT1	8.31	2.90E+06	**1**	**1**	**1**
T-SNARE affecting a late Golgi compartment protein 1	TLG1	7.68	2.86E+06	**1**	**1**	**1**
t-SNARE VTI1	VTI1	4.70	4.06E+06	**1**	**1**	**1**
Protein SSO1	SSO1	2.86	6.06E+06	**1**	**1**	**1**
Golgi SNAP receptor complex member 1	GOS1	2.71	2.92E+06	**1**	**1**	**1**
PI3Kc1 (Vps15, Vps34, Atg6, Atg14)					**1**	**0**
Atg2-Atg18					**1**	**0**
Atg21					**1**	**0**
Atg12–Atg5-Atg16					**1**	**0**
Atg3-Atg8					**1**	**0**
Atg7					**1**	**0**

Fig. S6.

(A) Phospholipid composition of Atg9 vesicles. Atg9-EGFP-TAP vesicles were isolated and their phospholipid content was determined using mass spectrometry. Mock isolation from a strain carrying an untagged *ATG9* gene was used to subtract any lipids that bound

to the beads non-specifically. Rep 1 – 3: technical replicates; GPL: glycerophospholipid; PC: phosphatidylcholine; PE: phosphatidylethanolamine; PS: phosphatidylserine; PI: phosphatidylinositol; PA: phosphatidic acid; SD: standard deviation. (B) Graphs showing the phospholipid content of Atg9 vesicles determined using mass spectrometry. Bars indicate the standard deviation. (C) List of proteins used for generating the Atg9 vesicle model. The proteins found by mass spectrometry analysis of endogenous Atg9 vesicles are shown with corresponding log2 ratio and iBAQ values. To estimate the number of molecules per vesicle the iBAQ value of each protein was divided by the iBAQ value of Atg9 and related to estimated 28 molecules of Atg9. TMDs: transmembrane domains. An extended list of proteins identified in the Atg9 vesicle fraction is included in the appended Excel file. The proteins of the autophagy machinery included in the model are listed in blue.

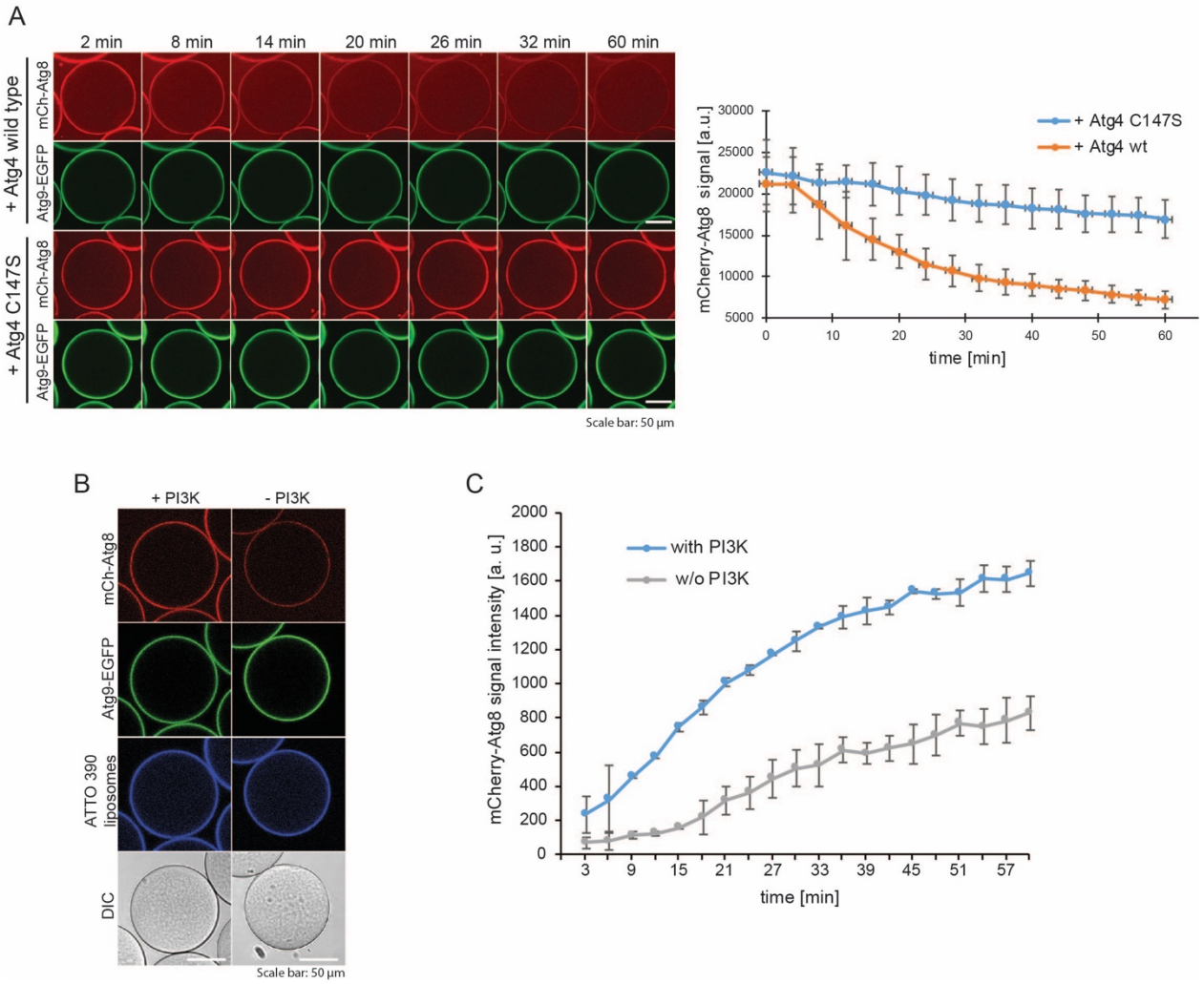

Fig. S7.

Atg8 lipidation to Atg9 PLs as in Figure 2E. (A) Microscopy images of an Atg4-mediated Atg8 de-conjugation time course experiment. In the first step the Atg8 lipidation reaction was performed on Atg9-EGFP PLs bound to GFP-Trap beads as shown in Figure 2B. After 30 min, 1 µM Atg4 or 1 µM Atg4C147S together with 2 mM EDTA were added to the reaction. Beads were imaged immediately at the indicated time points post Atg4 addition. The graph shows a quantification of the mCherry-Atg8 signal measured on four beads per condition. (B) GFP-Trap beads were coated with Atg9-EGFP PLs and incubated with Atg21, Atg2-Atg18, mCherry-Atg8ΔR117, Atg7, Atg3, Atg12–Atg5-Atg16, and ATP in the presence or absence of PI3KC3-C1. Microscopy images of representative beads are shown. (C) The graph shows a quantification of the mCherry-Atg8 signal intensity measured on at least eight beads per condition at the indicated time points. The error bars represent standard deviation among the beads within one experiment.

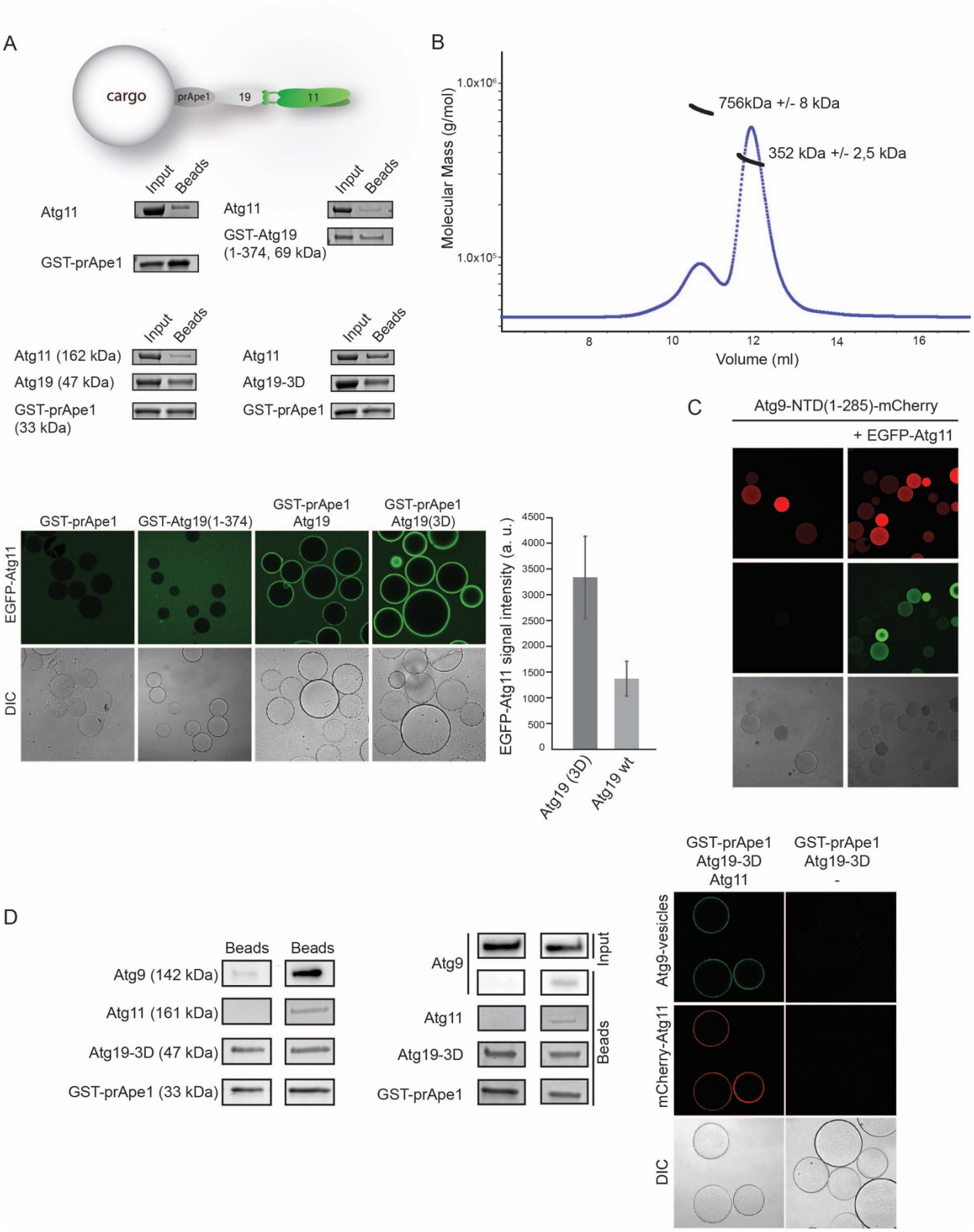
A
cargo
prApe1
19
11
Input
Beads
Atg11
GST-prApe1
Atg11
GST-Atg19
(1-374, 69 kDa)
Atg11 (162 kDa)
Atg19 (47 kDa)
GST-prApe1
(33 kDa)
Atg11
Atg19-3D
GST-prApe1
B
Molecular Mass (g/mol)
1.0x10⁶
1.0x10⁵
756kDa +/- 8 kDa
352 kDa +/- 2,5 kDa
8
10
12
14
16
Volume (ml)
C
Atg9-NTD(1-285)-mCherry
+ EGFP-Atg11
GST-prApe1
GST-Atg19(1-374)
GST-prApe1
Atg19
GST-prApe1
Atg19(3D)
EGFP-Atg11
DIC
EGFP-Atg11 signal intensity (a. u.)
4500
4000
3500
3000
2500
2000
1500
1000
500
0
Atg19 (3D)
Atg19 wt
D
Beads
Beads
Atg9 (142 kDa)
Atg11 (161 kDa)
Atg19-3D (47 kDa)
GST-prApe1 (33 kDa)
Atg9
Atg11
Atg19-3D
GST-prApe1
Input
Beads
GST-prApe1
Atg19-3D
Atg11
GST-prApe1
Atg19-3D
-
Atg9-vesicles
mCherry-Atg11
DIC

Fig. S8.

(A) In vitro pulldown assays of Atg11 using glutathione sepharose beads coated with different versions of the prApe1/Atg19 complex. The experimental setup is shown above the Coomassie stained SDS-PAGE images. Microscopy based protein interaction assays between EGFP-Atg11 and glutathione sepharose beads coated with different versions of the prApe1/Atg19 complex (bottom). The quantification of EGFP-Atg11 average signal intensities is shown to the right. The error bars correspond to the standard deviation between at least 30 the beads per Atg19 version. (B) Elution profile of a size exclusion chromatography (Sepharose 6 10/300) run with EGFP-Atg11. The size distribution of EGFP-Atg11 measured by SLS is shown as black traces, the average mass for each peak is also reported. (C) Microscopy based protein interaction assays between EGFP-Atg11 and RFP-Trap beads coated with Atg9-NTD(1-285)-mCherry. (D) Cargo mimetic beads (glutathione-sepharose) were prepared by coating with GST-prApe1 (1-41), Atg19-3D and with or without mCherry-Atg11 (as shown in (A)). Corresponding bands of a Coomassie-stained SDS gel are shown. The pre-assembled cargo mimetic beads were subsequently incubated with either Atg9-EGFP PLs (left panel) or endogenous Atg9-EGFP vesicles (right panel), washed with buffer and analyzed by immunoblotting using anti GFP antibody. Microscopy images of representative beads coated with indicated proteins and incubated with Atg9-EGFP vesicles are shown. This panel corresponds to the Figure 3A in the main text.

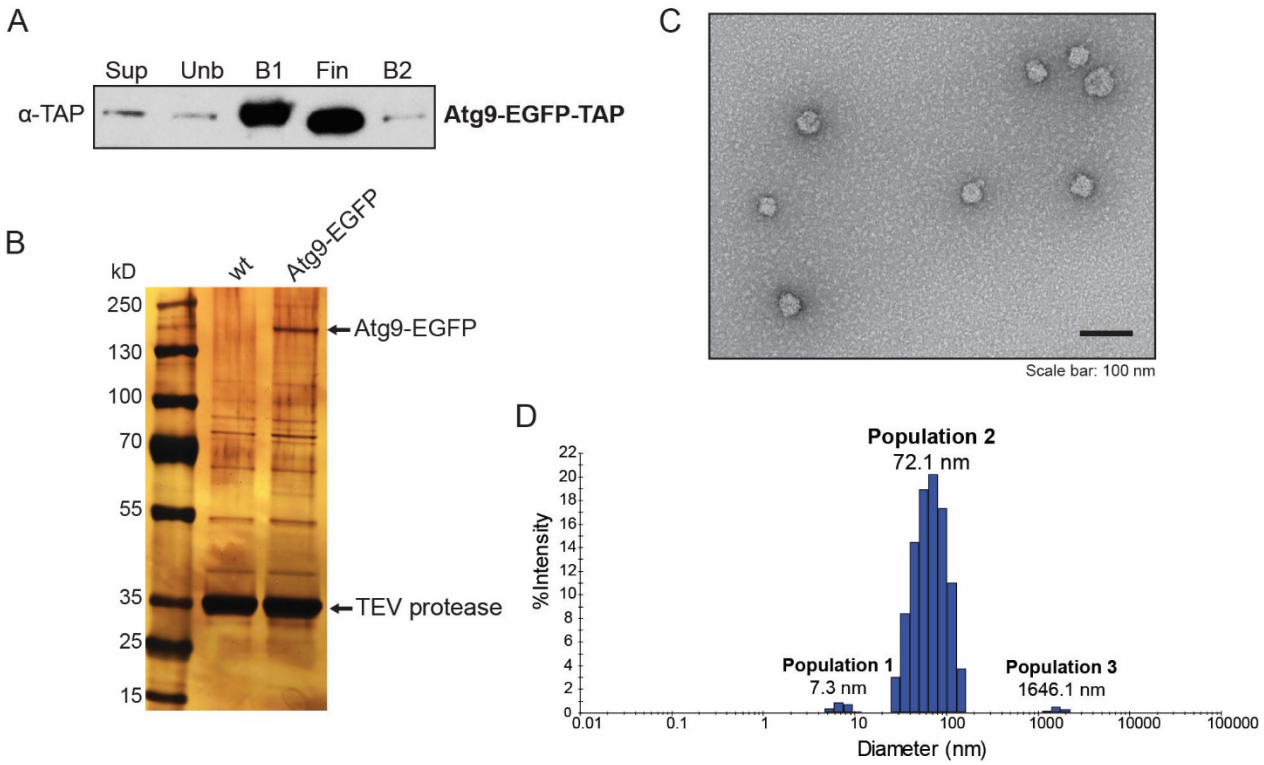

Fig. S9.

(A) Immunoblot showing the steps of Atg9-EGFP-TAP vesicle isolation. Yeast cells grown in log phase were harvested, opened, and cleared by centrifugation. The yeast extracts were incubated with magnetic beads cross-linked to rabbit IgGs, washed, and the vesicles were released into the final fraction by TEV protease cleavage located between EGFP and the TAP tag. Sup: cleared yeast extract; Unb: unbound fraction; B1: vesicles isolated on beads; Fin: final fraction showing a size shift after TEV cleavage; B2: protein remaining on beads after cleavage. (B) Silver-stained SDS-PAGE of final fractions from a mock isolation using wild type strain carrying an untagged *ATG9* gene and an isolation from SMY193 carrying a tagged *ATG9-EGFP-9xmyc* gene (9-GFP). (C) Negative stain electron micrograph of Atg9 vesicles. Scale bar, 100 nm (D) Dynamic light scattering measurement of a final Atg9 vesicle fraction (Atg9-mCherry-9xmyc), indicating mean particle sizes of the three populations.

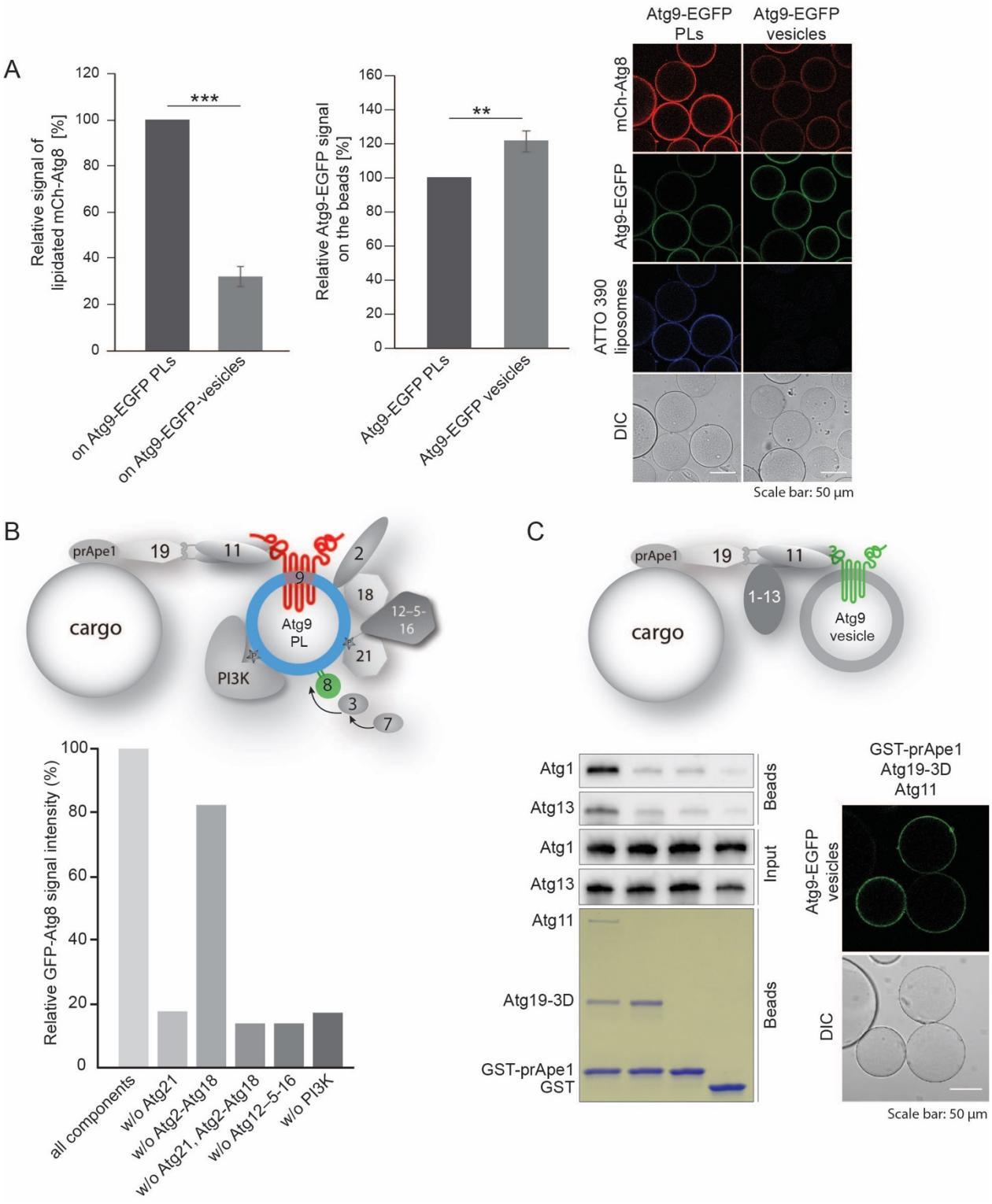

Fig. S10.

(A) Comparison of Atg8 lipidation on Atg9 PLs and Atg9 vesicles. GFP-Trap beads were coated with either Atg9-EGFP PLs or Atg9-EGFP vesicles, washed and incubated with PI3KC3-C1, Atg21, mCherry-Atg8ΔR117, Atg7, Atg3, Atg12–Atg5-Atg16, and ATP.

Microscopy images of representative beads are shown. The graphs show the relative intensities of mChAtg8 and EGFP signals normalized to the Atg9 PLs probe. Significance is indicated with * ($p \leq 0.05$), ** ($p \leq 0.01$) and *** ($p \leq 0.001$). (B) Quantification of Atg8 lipidation on the Atg9 PLs-coated cargo mimetic beads. Glutathione-sepharose beads were coated with GST-prApe1 (1-41), Atg19-3D and Atg11, incubated with Atg9-mCherry-PLs, washed with buffer and incubated with PI3KC3-C1, ATP, Atg21, Atg2-Atg18, Atg3, Atg12–Atg5-Atg16, EGFP-Atg8ΔR117, as in Figure 4C (see cartoon with the experimental scheme). The graph shows a quantification of the EGFP-Atg8 signal intensities measured on at least 30 beads per condition in one experiment where either all proteins were present or individual components were omitted. The GFP signal was normalized to the Atg8 lipidation in the presence of all proteins. (C) A pulldown assay of Atg1-Atg13 and Atg9 vesicles binding to cargo beads. Cargo mimetic beads (glutathione-sepharose) were prepared by coating with GST-prApe1 (1-41), Atg19-3D and Atg11 in combinations as indicated in the Coomassie-stained SDS gel. The pre-assembled cargo mimetic beads were subsequently incubated simultaneously with endogenous Atg9-EGFP vesicles and Atg1-Atg13 complex, washed with buffer and analyzed by immunoblotting using anti Atg1 and anti Atg13 antibody. Binding of Atg9-EGFP vesicles to the beads was monitored by microscopy as shown to the right.

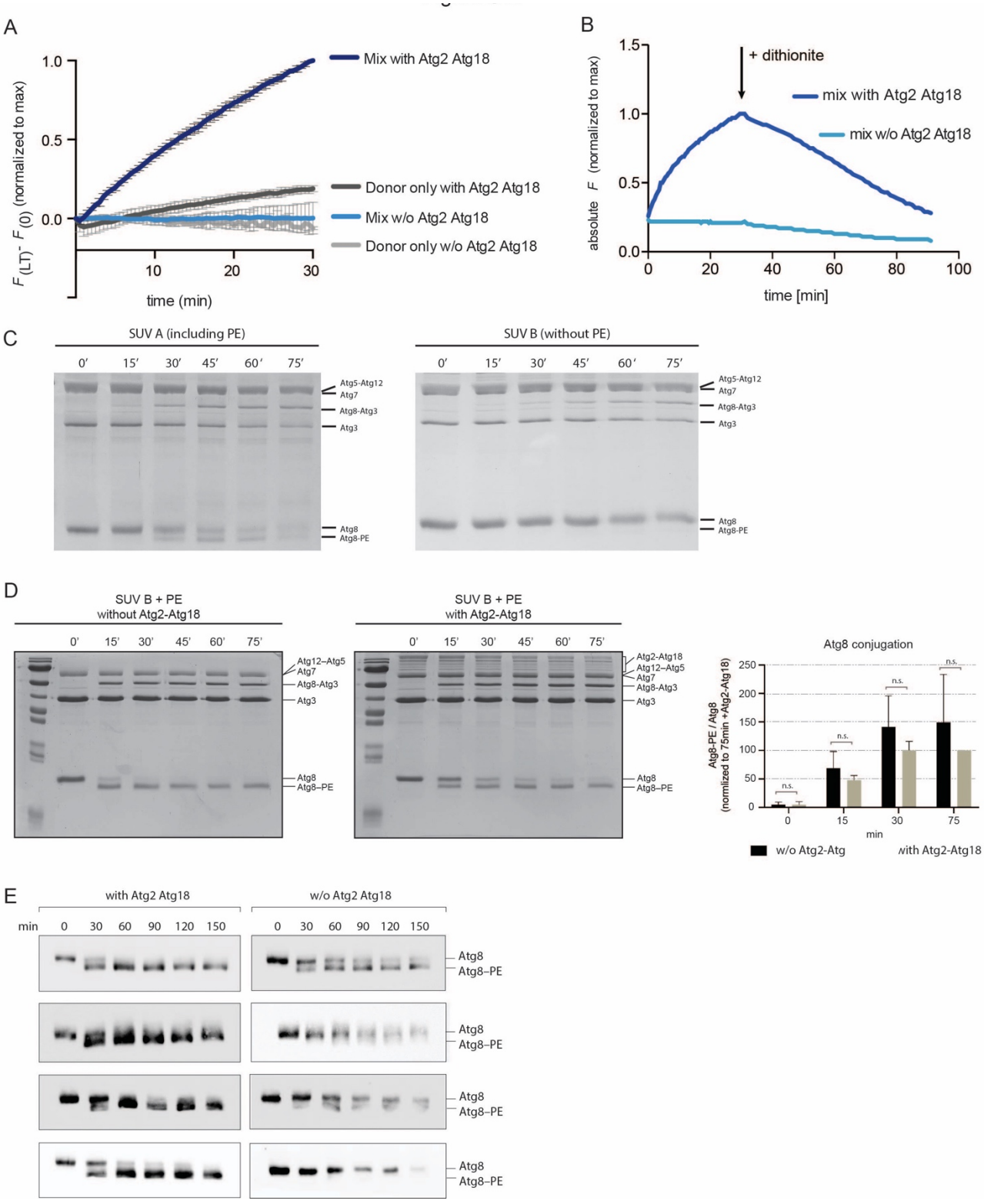

Fig. S11.

Atg2-Atg18 acts as lipid transfer protein (A) Phospholipid transfer assay based on the dequenching of NBD fluorescence. $F_{(LT)}$ and $F_{(0)}$ represent the NBD fluorescence

intensity at each time point before and after addition of Atg2-Atg18, respectively, measured at 535 nm. (B) shows the decrease of NBD fluorescence after addition of 5 mM dithionite after 30 min lipid transfer. After dithionite treatment NBD fluorescence was monitored for another 60 min. (C-D) Coomassie-stained gels showing the results of Atg8–PE conjugation assays using the experimental set-up depicted in Figure 4C. Atg8–PE conjugation was detected as a band shift. The numbers above the gels indicate the time in minutes. For (C) instead of mixing SUV A and SUV B only one type of liposomes was added per set up. For (D) POPE was added to the lipid composition of SUV B. Quantification for (D) shows the averages of Atg8-PE/Atg8 ratio for each time point. Error bars represent the standard deviation. The quantification is based on three independent experiments. P-values were calculated using Student's t-test. Significance is indicated with * when p value ≤ 0.05, ** when p value ≤ 0.01, and *** when p value ≤ 0.001. (E) Immunoblots showing the results of four independent Atg8–PE conjugation assays using the experimental set-up depicted in Figure 4E. Atg8–PE conjugation was detected as a band shift. The numbers above the blots indicate the time in minutes.

Table S1.

Table of constructs

Identification Number	Expressing	Vector	Expression system	Published
SMC3	GST-Atg3	pGEX-4T-3	*E. coli* Rosetta pLysS	(*4*)
SMC17	6xHis-Atg7	pOPTH	*E. coli* Rosetta pLysS	(*4*)
SMC34	GST-Atg16	pOPTG	*E. coli* Rosetta pLysS	(*4*)
SMC58	6xHis-Atg8ΔR117	pET-Duet-1	*E. coli* Rosetta pLysS	(*4*)
SMC126	6xHis-Atg5, Atg12	pET Duet-1	*E. coli* Rosetta pLysS	(*4*)
SMC131	Atg7, Atg10	pCOLA Duet-1	*E. coli* Rosetta pLysS	(*4*)
SMC159	GST-Atg19	pGEX-4T-1	*E. coli* Rosetta pLysS	(*3*)
SMC178	6xHis-Atg16-EGFP	pET Duet-1	*E. coli* Rosetta pLysS	(*4*)
SMC179	6xHis-mEGFP-Atg8ΔR117	pET Duet-1	*E. coli* Rosetta pLysS	(*4*)
SMC180	Atg16(1-46)	pCOLA-Duet1	*E. coli* Rosetta pLysS	(*4*)
SMC564	GST-Atg4	pGEX-4T-3	*E. coli* Rosetta pLysS	(*38*)
SMC609	GST-Atg4 C147S	pGEX-4T-3	*E. coli* Rosetta pLysS	(*39*)
SMC300	GST-prApe1(1–45)	pGEX-4T-1	*E. coli* Rosetta pLysS	(*3*)
SMC595	GST-prApe1(1–41)	pGEX-4T-1	*E. coli* Rosetta pLysS	(*2*)
SMC782	6xHis-Atg5-mCherry	pET Duet-1	*E. coli* Rosetta pLysS	(*2*)
SMC819	6xHis-Atg16-mCherry	pET Duet-1	*E. coli* Rosetta pLysS	(*4*)
SMC162	mEGFP-Atg8-6xHis	pET Duet-1	*E. coli* Rosetta pLysS	(*3*)
SMC159	GST-Atg19	pGEX-4T-1	*E. coli* Rosetta pLysS	(*3*)
SMC1180	6xHis-mCherry-Atg8ΔR117	pET Duet-1	*E. coli* Rosetta pLysS	This study
SMC499	GST-Atg19-3D (S390D, S391D, S396D)	pGEX-4T-1	*E. coli* Rosetta pLysS	This study
SMC1297	GST-Atg19-3DΔLIR (S390D, S391D, S396D, W412A)	pGEX-4T-1	*E. coli* Rosetta pLysS	This study
SMC346	GST-Atg19(1-374)	pGEX-4T-1	*E. coli* Rosetta pLysS	This study
SMC916	6xHis-TEV-Atg11	pFastBac HT	Sf9 cells	This study
SMC1070	6xHis-TEV-mCherry-Atg11	pFastBac HT	Sf9 cells	This study
SMC1064	6xHis-TEV-mEGFP-Atg11	pFastBac HT	Sf9 cells	This study

SMC1246	6xHis-Atg9-NTD(285)-mCherry	pET Duet-1	*E. coli* Rosetta pLysS	This study
SMC1229	6xHis-TEV-Atg9-mCherry-2xStrep	pFastBac HT	Sf9 cells	This study
SMC1230	6xHis-TEV-Atg9-mEGFP-2xStrep	pFastBac HT	Sf9 cells	This study
SMC1130	6xHis-TEV-Atg2-mEGFP	pFastBac	Sf9 cells	This study
SMC1164	6xHis-TEV Atg18-mEGFP	pET Duet-1	*E. coli* Rosetta pLysS	This study
SMC872	6xHis-TEV-Atg21	pET Duet-1	*E. coli* Rosetta pLysS	This study
SMC930	6xHis-TEV-mEGFP-Atg21	pET Duet-1	*E. coli* Rosetta pLysS	This study
SMC929	6xHis-TEV-mCherry-Atg21	pET Duet-1	*E. coli* Rosetta pLysS	This study
SMC1181	Vps34/Vps15/Atg6/ProteinA-TEV-Atg14	pBig2ab	Sf9 cells	This study
SMC1336	ProtA-TEV-Atg1/Atg13	pBig1b	Sf9 cells	This study
SMC506	prom-Atg5-3xmCherry-cyc1term	pRS316	*S. cerevisiae*	(*4*)
pDP103	prom-Ape1-BFP-Ape1-cyc1term	pRS415	*S. cerevisiae*	(*40*)
SMC199	GFP-Atg8	pRS315	*S. cerevisiae*	(*41*)

Table S2.

Table of lipids.

	Name	Supplier	Catalog number	Concentration
POPC	1-palmitoyl-2-oleoyl-sn-glycero-3-phosphocholine	Avanti Polar Lipids, Inc.	850457C	10 mg/ml
POPE	1-hexadecanoyl-2-(9Z-octadecenoyl)-sn-glycero-3-phosphoethanolamine	Avanti Polar Lipids, Inc.	850757C	10 mg/ml
POPS	1-palmitoyl-2-oleoyl-sn-glycero-3-phospho-L-serine (sodium salt)	Avanti Polar Lipids, Inc.	840034C	10 mg/ml
POPA	**1-palmitoyl-2-oleoyl-sn-glycero-3-phosphate (sodium salt)**	Avanti Polar Lipids, Inc.	840857C	10 mg/ml
PI3P	1,2-dioleoyl-sn-glycero-3-phospho-(1'-myo-inositol-3'-phosphate) (ammonium salt)	Avanti Polar Lipids, Inc.	850150P	1 mg/ml
Liver PI	**L-α-phosphatidylinositol (Liver, Bovine) (sodium salt)**	Avanti Polar Lipids, Inc.	840042C	10 mg/ml
DOPC	1,2-dioleoyl-sn-glycero-3-phosphocholine	Avanti Polar Lipids, Inc.	850375C	10 mg/ml
DOPE	1,2-dioleoyl-sn-glycero-3-phosphoethanolamine	Avanti Polar Lipids, Inc.	850725C	10 mg/ml
DOPS	1,2-dioleoyl-sn-glycero-3-phospho-L-serine (sodium salt)	Avanti Polar Lipids, Inc.	840035C	10 mg/ml
DAG	1-2-dioleoyl-sn-glycerol	Avanti Polar Lipids, Inc	800811C	10 mg/ml
ATTO390-DOPE	ATTO390-labelled 1,2-Dioleoyl-sn-glycero-3-phosphoethanolamine	ATTO-Tec	AD380-16	10 mg/ml
NBD-PE	1,2-dipalmitoyl-*sn*-glycero-3-phosphoethanolamine-N-(7-nitro-2-1,3-benzoxadiazol-4-yl) (ammonium salt)	Avanti Polar Lipids, Inc	810144C	1 mg/ml
Rhodamine PE	Lissamine™ rhodamine B 1,2-dihexadecanoyl-sn-glycero-3-phosphoethanolamine, triethylammonium salt	Invitrogen	L-1392	1 mg/ml

Table S3.

Composition of media used in the 10 l fermentation run of the SMY276 strain.

Main culture media	**g/l**	**Trace elements stock**	**g/l**
Yeast extract	3.00	$(NH_4)_2Fe(II)(SO_4)_2 \cdot 6H_2O$	10.00
Peptone	5.00	$CuSO_4 \cdot 5H_2O$	0.80
Malt extract	3.00	$ZnSO_4 \cdot 7H_2O$	3.00
Glycerol	15.00	$MnSO_4 \cdot H_2O$	4.00
$NH_4H_2PO_4$	13.30	EDTA	10.00
KCl	3.30	$NiSO_4 \cdot 6H_2O$	0.20
NaCl	0.30	$CoCl_2 \cdot 6H_2O$	0.20
$MgSO_4 \cdot 7H_2O$	3.00	Boric Acid	0.20
$CaCl_2 \cdot 2H_2O$	1.00	KJ	0.20
Antifoam 204	1.00	$Na_2MoO_4 \cdot 2H_2O$	0.20
		Vitamin stocks	**g/l**
Additions to the main medium	**ml/l**	D-Biotin	0.06
Trace elements	4.00	Thiamin-HCl	20.00
Vitamins	12.00		
Histidine	8.00	**Other stocks**	**mg/ml**
Leucine	8.00	Histidine	25.00
		Leucine	25.00

Table S4.

Initial parameters used in the 10 l fermentation run of the SMY276 strain.

Initial fermenter setup	
Growth temperature	30°C
DO setting	30%
Stirrer setting	400–1,200 rpm
Flow cascade order	1. stirrer, 2. flow, 3. pure oxygen
Mass Flow setting	40–60 l/h
Starting volume	6 l
Fermenter volume	13 l
μ	0.05/h
initial OD	0.025

Table S5.

Table of yeast strains.

Name	Genotype	Background	Reference
SMY002	*atg5*::*kanMX* MAT a	BY4741	(*4*)
SMY276	*pep4::NAT ATG9-EGFP-TAP:URA;* MAT a	s288c	This study
SMY227	*pep4::NAT ATG9-mCherry-TEV-9xmyc;* MAT a	s288c	This study
SMY193	*pep4::NAT ATG9-EGFP-TEV-9xmyc:URA;* MAT a	s288c	This study
SMY373	*atg2pr::hphNT1-GAL1pr atg18pr::URA3-GAL1pr ATG18-TAP-*kanMX *pep4::natMX* MAT a	BY4741	This study
SMY374	*atg2pr::hphNT1-GAL1pr ATG2-GFP-kanMX atg18pr::URA3-GAL1pr ATG18-TAP-kanMX pep4::natMX* MATa	BY4741	This study
SMY395	*atg21::natMX atg5::kanMX* MAT a	BY4741	This study
SMY396	*atg18::natMX atg2::kanMX atg5::kanMX* MAT a	BY4741	This study
SMY406	*atg2::natMX atg5::kanMX* MAT a	BY4741	This study
SMY408	*atg21::natMX atg5::kanMX* MAT a	BY4741	This study
SMY423	*atg21::natMX atg2::natMX atg5::kanMX* MAT alpha	BY4742	This study
SMY432	*atg18::natMX atg21::natMX atg5::kanMX* MAT a	BY4741	This study
SMY433	*atg18::natMX atg21::natMX atg2::natMX atg5::kanMX* MAT alpha	BY4742	This study
BY4741	his3Δ1 leu2Δ0 met15Δ0 ura3Δ0 MAT a	S288c	Euroscarf
BY4742	his3Δ1 leu2Δ0 met15Δ0 ura3Δ0 MAT alpha	S288c	Euroscarf
SMY013	*atg16::kan* MAT a	BY4741	Euroscarf
SMY111	*atg18::kan* MAT a	BY4741	Euroscarf
SMY378	*atg2::kan* MAT a	BY4741	Euroscart
SMY236	*atg21::nat* MAT alpha	BY4742	Euroscarf
SMY383	*atg2::kan atg18::nat* MAT a	BY4741	This study
SMY385	*atg2::kan atg21::nat* MAT a	BY4741	This study
SMY436	*atg18::nat atg21::kan* MAT alpha	BY4742	This study
SMY438	atg2::hph atg18::nat atg21::kan MAT alpha	BY4742	This study
SMY439	*atg2pr::hphNT1-GAL1pr ATG2-mCherry-kanMX atg18pr::URA3-GAL1pr ATG18-TAP-kanMX pep4::natMX* MATa	BY4741	This study

Movie S1

Animation of the Atg9 vesicle three-dimensional model assembly.

Data S1

Excel file with proteomics data: An extended list of proteins identified by mass spectrometry in the Atg9 vesicle fraction. The list includes proteins with log2 (ATG9-EGFP/WT) ≥ 2 and iBAQ values ≥ 2.36E+06. The proteins included in the model of the Atg9 vesicle are highlighted in grey.

References and Notes

1. F. Weissmann *et al.*, biGBac enables rapid gene assembly for the expression of large multisubunit protein complexes. *Proc Natl Acad Sci U S A* **113**, E2564-2569 (2016).

2. D. Fracchiolla *et al.*, Mechanism of cargo-directed Atg8 conjugation during selective autophagy. *Elife* **5**, e18544 (2016).

3. J. Sawa-Makarska *et al.*, Cargo binding to Atg19 unmasks additional Atg8 binding sites to mediate membrane–cargo apposition during selective autophagy. *Nat Cell Biol* **16**, 425-433 (2014).

4. J. Romanov *et al.*, Mechanism and functions of membrane binding by the Atg5-Atg12/Atg16 complex during autophagosome formation. *EMBO J* **31**, 4304-4317 (2012).

5. V. Kumar *et al.*, A keratin scaffold regulates epidermal barrier formation, mitochondrial lipid composition, and activity. *J Cell Biol* **211**, 1057-1075 (2015).

6. T. A. Wassenaar, H. I. Ingólfsson, R. A. Böckmann, D. P. Tieleman, S. J. Marrink, Computational lipidomics with insane: A versatile tool for generating custom membranes for molecular simulations. *Journal of Chemical Theory and Computation* **11**, 2144-2155 (2015).

7. S. J. Marrink, H. J. Risselada, S. Yefimov, D. P. Tieleman, A. H. De Vries, The MARTINI force field: Coarse grained model for biomolecular simulations. *Journal of Physical Chemistry B* **111**, 7812-7824 (2007).

8. D. H. de Jong *et al.*, Improved Parameters for the Martini Coarse-Grained Protein Force Field. *Journal of Chemical Theory and Computation* **9**, 687-697 (2013).

9. M. J. Abraham *et al.*, GROMACS: High performance molecular simulations through multi-level parallelism from laptops to supercomputers. *SoftwareX* **1-2**, 19-25 (2015).

10. H. J. C. C. Berendsen, J. P. M. M. Postma, W. F. van Gunsteren, A. DiNola, J. R. Haak, Molecular dynamics with coupling to an external bath. *The Journal of Chemical Physics* **81**, 3684-3690 (1984).

11. M. Parrinello, A. Rahman, Polymorphic transitions in single crystals: A new molecular dynamics method. *Journal of Applied Physics* **52**, 7182-7190 (1981).

12. G. Bussi, D. Donadio, M. Parrinello, Canonical sampling through velocity rescaling. *Journal of Chemical Physics* **126**, 14101 (2007).

13. W. S. Horne *et al.*, Structural and biological mimicry of protein surface recognition by α/β-peptide foldamers. *Proceedings of the National Academy of Sciences of the United States of America* **106**, 14751-14756 (2009).

14. L. M. Pietrek, L. S. Stelzl, G. Hummer, Hierarchical Ensembles of Intrinsically Disordered Proteins at Atomic Resolution in Molecular Dynamics Simulations. *J Chem Theory Comput* **16**, 725-737 (2020).

15. R. B. Best, G. Hummer, Optimized molecular dynamics force fields applied to the helix-coil transition of polypeptides. *Journal of Physical Chemistry B* **113**, 9004-9015 (2009).

16. K. Lindorff-Larsen *et al.*, Improved side-chain torsion potentials for the Amber ff99SB protein force field. *Proteins: Structure, Function and Bioinformatics* **78**, 1950-1958 (2010).

17. R. B. Best, D. De Sancho, J. Mittal, Residue-specific α-helix propensities from molecular simulation. *Biophysical Journal* **102**, 1462-1467 (2012).
18. W. L. Jorgensen, J. Chandrasekhar, J. D. Madura, R. W. Impey, M. L. Klein, Comparison of simple potential functions for simulating liquid water. *The Journal of Chemical Physics* **79**, 926-935 (1983).
19. M. Källberg *et al.*, Template-based protein structure modeling using the RaptorX web server. *Nature Protocols* **7**, 1511-1522 (2012).
20. R. Guo, S. Zong, M. Wu, J. Gu, M. Yang, Architecture of Human Mitochondrial Respiratory Megacomplex I2III2IV2. *Cell* **170**, 1247-1257.e1212 (2017).
21. B. Aghazadeh *et al.*, Structure and mutagenesis of the Dbl homology domain. *Nature Structural Biology* **5**, 1098-1107 (1998).
22. Y. Watanabe *et al.*, Structure-based analyses reveal distinct binding sites for Atg2 and phosphoinositides in Atg18. *Journal of Biological Chemistry* **287**, 31681-31690 (2012).
23. S. Chowdhury *et al.*, Insights into autophagosome biogenesis from structural and biochemical analyses of the ATG2A-WIPI4 complex. *Proceedings of the National Academy of Sciences* **115**, E9792-E9801 (2018).
24. N. N. Noda, Y. Fujioka, T. Hanada, Y. Ohsumi, F. Inagaki, Structure of the Atg12–Atg5 conjugate reveals a platform for stimulating Atg8–PE conjugation. *EMBO reports* **14**, 206-211 (2013).
25. Y. Fujioka, N. N. Noda, H. Nakatogawa, Y. Ohsumi, F. Inagaki, Dimeric coiled-coil structure of Saccharomyces cerevisiae Atg16 and its functional significance in autophagy. *The Journal of biological chemistry* **285**, 1508-1515 (2010).
26. B. Webb, A. Sali, in *Current Protocols in Bioinformatics*. (John Wiley & Sons, Inc., Hoboken, NJ, USA, 2016), vol. 54, pp. 5.6.1-5.6.37.
27. Y. Yamada *et al.*, The crystal structure of Atg3, an autophagy-related ubiquitin carrier protein (E2) enzyme that mediates Atg8 lipidation. *The Journal of biological chemistry* **282**, 8036-8043 (2007).
28. H. Kumeta *et al.*, The NMR structure of the autophagy-related protein Atg8. *Journal of Biomolecular NMR* **47**, 237-241 (2010).
29. S. E. Kaiser *et al.*, Noncanonical E2 recruitment by the autophagy E1 revealed by Atg7–Atg3 and Atg7–Atg10 structures. *Nature Structural & Molecular Biology* **19**, 1242-1249 (2012).
30. K. Rostislavleva *et al.*, Structure and flexibility of the endosomal Vps34 complex reveals the basis of its function on membranes. *Science* **350**, aac7365 (2015).
31. A. Roy, A. Kucukural, Y. Zhang, I-TASSER: a unified platform for automated protein structure and function prediction. *Nature Protocols* **5**, 725-738 (2010).
32. J. Yang *et al.*, The I-TASSER Suite: protein structure and function prediction. *Nature Methods* **12**, 7-8 (2015).
33. R. M. Cleverley *et al.*, Structure and function of a spectrin-like regulator of bacterial cytokinesis. *Nature Communications* **5**, 5421 (2014).
34. Y. Fridmann-Sirkis, H. M. Kent, M. J. Lewis, P. R. Evans, H. R. B. Pelham, Structural analysis of the interaction between the SNARE Tlg1 and Vps51. *Traffic* **7**, 182-190 (2006).

35. J. Wang *et al.*, Epsin N-terminal homology domains bind on opposite sides of two SNAREs. *Proceedings of the National Academy of Sciences of the United States of America* **108**, 12277-12282 (2011).
36. F. M. Hughson, M. Munson, X. Chen, A. E. Cocina, S. M. Schultz, Interactions within the yeast t-SNARE Sso1p that control SNARE complex assembly. *Nature Structural Biology* **7**, 894-902 (2000).
37. P. Strop, S. E. Kaiser, M. Vrljic, A. T. Brunger, The structure of the yeast plasma membrane SNARE complex reveals destabilizing water-filled cavities. *The Journal of biological chemistry* **283**, 1113-1119 (2008).
38. B. Zens, J. Sawa-Makarska, S. Martens, In vitro systems for Atg8 lipidation. *Methods* **75**, 37-43 (2015).
39. J. Sanchez-Wandelmer *et al.*, Atg4 proteolytic activity can be inhibited by Atg1 phosphorylation. *Nat Commun* **8**, 295 (2017).
40. T. Pfaffenwimmer *et al.*, Hrr25 kinase promotes selective autophagy by phosphorylating the cargo receptor Atg19. *EMBO Rep* **15**, 862-870 (2014).
41. C. Kraft *et al.*, Binding of the Atg1/ULK1 kinase to the ubiquitin-like protein Atg8 regulates autophagy. *EMBO J* **31**, 3691-3703 (2012).

Mechanism of Atg9 recruitment by Atg11 in the cytoplasm-to-vacuole targeting pathway

During selective autophagy Atg9 vesicles are recruited to the cargo-receptor complex via the scaffold protein Atg11 (He et al., 2006; Matscheko et al., 2019; Sawa-Makarska et al., 2020). Previous studies have already described a direct interaction between Atg9 and Atg11 but the exact molecular details remained elusive. In the following study the aim was to map the interacting regions and to better understand the mechanisms that recruit Atg9 vesicles to Atg11 and the cargo-receptor complex.

By employing yeast two-hybrid analysis He et al. (2006) identified CC2 of Atg11 and a region in the Atg9 N-terminus as putative interaction sites. The soluble N-terminus of Atg9 is a disordered region facing the cytosol, making NMR (nuclear-magnetic-resonance) spectroscopy the method of choice to characterize its binding to Atg11 in closer detail (Figure 1). In line with previous studies, our NMR data revealed two PLF motifs being involved in the interaction (Figure 2). Mutation of either of these motifs (motif 1: $L_{164}A$, $F_{165}A$ and motif 2: $L_{188}A$, $F_{189}A$) leads to a significant reduction of Atg9-NTD recruitment to Atg11 (Figure 3). These *in vitro* assays were carried out by using EGFP-labelled Atg11 used as a bait coupled to GFP-trap agarose beads and mCherry-labelled Atg9-NTD as a prey. As expected, the mutation of both PLF motifs abolished the binding of Atg9-NTD to Atg11. Further ITC (isothermal titration calorimetry) analysis revealed a 1:1 stoichiometry between Atg11 and the Atg9-NTD with a K_D of about 1mM. Upon mutation of the PLF motifs affinities were too low to be reliably detected by ITC. To show whether these motifs also have a relevance for the Cvt-pathway *in vivo*, standard methods for following the efficiency of autophagy in cells were conducted namely prApe1-processing, Pho8delta60 assays and GFP-Atg8 cleavage assays (Figure 4). While individual mutation of PLF motif 1 and PLF motif 2 led to a decrease in autophagic activity under nutrient rich conditions down to 30% compared to cells expressing wild type Atg11, mutation of both motifs completely abolished it. However, bulk autophagy as measured by Pho8delta60 activity was only slightly affected by the mutations, strengthening the specific role of Atg11 during selective autophagy.

Another approach to test the importance of the Atg11-Atg9 interaction for selective autophagy *in vivo* is to assess Atg9 recruitment to the PAS, which is dependent on Atg11 (He et al., 2006; Matscheko et al., 2019; Sawa-Makarska et al., 2020). To this

end, I expressed Atg9-EGFP in *atg9*Δ cells and measured its colocalization with RFP-labelled Ape1 under the microscope (Figure 5). Consistent with the biochemical assays the live cell microscopy data displayed a severe decrease in Ape1/Atg9 colocalization when both PLF motifs were mutated.
With this study we were able to closely map the interaction sites between the Atg9-NTD and Atg11 needed for a successful recruitment of Atg9 at the PAS during the Cvt pathway. Based on these data, we propose that due to the relatively low affinity, indeed a clustering of Atg11 at the cargo, enabling a high avidity interaction, might be necessary to facilitate efficient Atg9 assembly. Further, we gained insights into the mechanism of the recruitment of Atg9 to cargo-receptor bound Atg11

I contributed to this work by designing and conducting experiments, as well as revising the article.
I performed the experiments/designed graphics shown in Figure 6A, B and Figure 7 as well as the statistical analyses for Figure 3B and 5A.

JBC RESEARCH ARTICLE

Mechanism of Atg9 recruitment by Atg11 in the cytoplasm-to-vacuole targeting pathway

Received for publication, December 22, 2021 Published, Papers in Press, January 8, 2022,
https://doi.org/10.1016/j.jbc.2022.101573

Nicolas Coudevylle[1,*], Bartłomiej Banaś[2], Verena Baumann[1,3], Martina Schuschnig[1], Anna Zawadzka-Kazimierczuk[2], Wiktor Koźmiński[2], and Sascha Martens[1,*]

From the [1]Max Perutz Laboratories, University of Vienna, Vienna, Austria; [2]Faculty of Chemistry, Biological and Chemical Research Centre, University of Warsaw, Warsaw, Poland; [3]Vienna BioCenter PhD Program, Doctoral School of the University of Vienna and Medical University of Vienna, Vienna, Austria

Edited by Wolfgang Peti

Autophagy is a lysosomal degradation pathway for the removal of damaged and superfluous cytoplasmic material. This is achieved by the sequestration of this cargo material within double-membrane vesicles termed autophagosomes. Autophagosome formation is mediated by the conserved autophagy machinery. In selective autophagy, this machinery including the transmembrane protein Atg9 is recruited to specific cargo material *via* cargo receptors and the Atg11/FIP200 scaffold protein. The molecular details of the interaction between Atg11 and Atg9 are unclear, and it is still unknown how the recruitment of Atg9 is regulated. Here we employ NMR spectroscopy of the N-terminal disordered domain of Atg9 (Atg9-NTD) to map its interaction with Atg11 revealing that it involves two short peptides both containing a PLF motif. We show that the Atg9-NTD binds to Atg11 with an affinity of about 1 μM and that both PLF motifs contribute to the interaction. Mutation of the PLF motifs abolishes the interaction of the Atg9-NTD with Atg11, reduces the recruitment of Atg9 to the precursor aminopeptidase 1 (prApe1) cargo, and blocks prApe1 transport into the vacuole by the selective autophagy-like cytoplasm-to-vacuole (Cvt) targeting pathway while not affecting bulk autophagy. Our results provide mechanistic insights into the interaction of the Atg11 scaffold with the Atg9 transmembrane protein in selective autophagy and suggest a model where only clustered Atg11 when bound to the prApe1 cargo is able to efficiently recruit Atg9 vesicles.

Autophagy is a conserved pathway for the delivery of cytoplasmic material into the lysosomal system for degradation. The material referred to as cargo is encapsulated within double-membrane vesicles, the autophagosomes. Upon induction of autophagy, either by the lack of nutrients or, in selective autophagy, by the presence of the cargo autophagosome biogenesis is initiated (1). Autophagosome formation progresses through the assembly of a small membrane structure termed phagophore (or isolation membrane), which gradually engulfs the cargo as it expands. Subsequently, a scission reaction mediates the closure of the phagophore resulting in the formation of an autophagosome. Finally, the outer membrane of the autophagosome fuses with the vacuole in yeast (or lysosome in mammals), wherein the inner membrane and the cargo are degraded.

Autophagosome biogenesis is mediated by a conserved set of functional modules forming the autophagy machinery. These modules are the Atg1 kinase complex, Atg9 vesicles, the class III phosphatidylinositol 3-phosphate kinase complex 1 (PI3KC3-C1), the Atg2-Atg18 lipid binding and transfer complex, Atg21 and the Atg8 lipidation machinery including the Atg12–Atg5-Atg16 complex (the nomenclature refers to the *Saccharomyces cerevisiae* proteins) (2–5). In selective autophagy, this machinery is recruited to the cargo material through cargo receptors, which first recruit the Atg11 scaffold protein to the cargo (6–9). The 135 kDa Atg11 forms homodimers that consist of four coiled-coil domains and a so-called "claw-domain" that specifically interacts with phosphorylated cargo receptors (7, 10–16). Atg11 in turn recruits the Atg1 kinase complex and Atg9 (6, 7, 11, 17–19).

Atg9 consists of a four-helices transmembrane core flanked by two large disordered and cytosolic termini (Fig. 1, *A* and *B*) (20–22). It forms trimers that localize to trans-Golgi-derived vesicles, a few of which are recruited to the site of autophagosome formation (23–25). Once recruited to the cargo, Atg9 vesicles function as seeds to initiate autophagosome formation (6, 23). Through its recently described scramblase activity, Atg9 allows phagophore elongation by distributing the ER-derived lipids transported by Atg2 between the two leaflets of the phagophore membrane (5, 6, 20, 21, 26–30). The recruitment of Atg9 to the site of autophagosome formation by Atg11 is therefore a crucial event in autophagosome biogenesis.

Some features of the interaction between Atg11 and Atg9 are already known. Atg11 was shown to bind to the intrinsically disordered N-terminal domain (NTD) of Atg9, and this interaction requires the coiled-coil domain 2 (CC2, residues 536–576) of Atg11 (6, 7, 19). However, the molecular details of this interaction as well as the spatiotemporal regulation of the recruitment of Atg9 vesicles to the cargo are still unclear. Here we show that the Atg9-NTD binds to Atg11 with an affinity of about 1 μM *via* two PLF motifs. Therefore, a productive high avidity interaction between Atg9 and Atg11 can only happen when Atg11 is clustered on the cargo, providing a mechanism for spatiotemporal regulation of the recruitment of Atg9 vesicles to the cargo site.

* For correspondence: Nicolas Coudevylle, nicolas.coudevylle@univie.ac.at; Sascha Martens, sascha.martens@univie.ac.at.

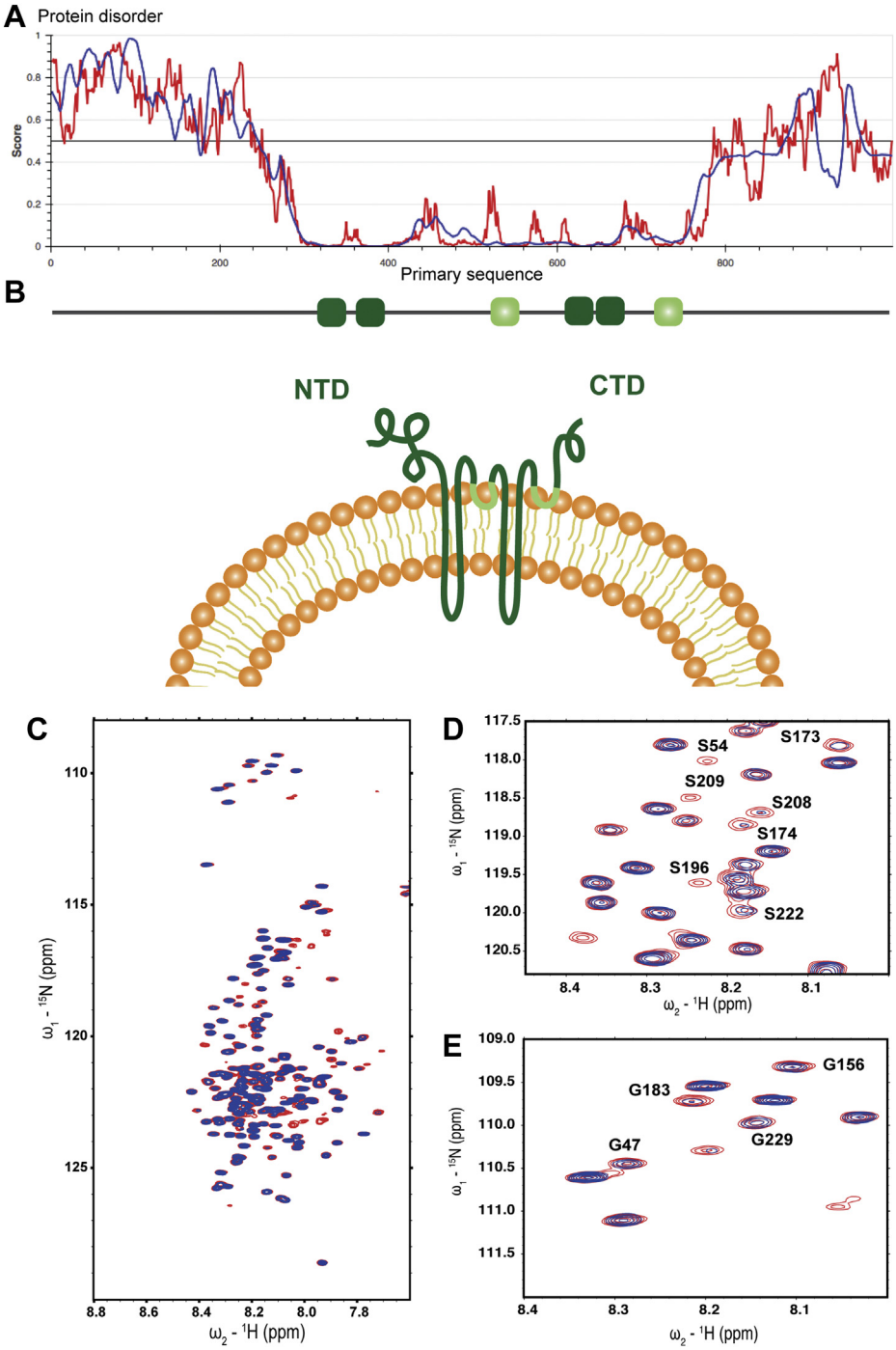

Figure 1. Atg9-NTD is disordered in solution and interacts with Atg11. *A*, predicted disorder score along the primary sequence of Atg9 according to the IUPred (*red trace*) and ANCHOR (*blue trace*) algorithms. *B*, schemes of Atg9. Transmembrane (TM) domains are represented as plain *dark green bars*, partially inserted helical segments as *light green bars*. *C*, overlay of the ^{1}H-^{15}N HSQC spectra of Atg9-NTD(1–285) in its free (*red resonances*) and of Atg11-bound (*blue resonances*) forms. The concentration of Atg9-NTD is 0.2 mM, the concentration of Atg11 in the bound sample is 0.04 mM. *D*, close-up on the Serine region of the HSQC spectra. *E*, close-up on the Glycine region of the HSQC spectra.

Results

Mapping of the Atg9-NTD–Atg11 interaction by NMR

In order to obtain mechanistic insights into the interaction of Atg9 with Atg11, we used nuclear magnetic resonance (NMR) spectroscopy, an ideal method to study intrinsically disordered proteins (IDPs). Using isotopically labeled samples and ^{1}H-^{15}N HSQC NMR, we concluded that, as predicted, the Atg9 NTD (residues 1–285) is largely disordered in solution (Fig. 1*C*). The spectrum of the protein exhibits sharp intense resonances together with the narrow chemical shift dispersion typical of IDPs. Upon addition of sub-stoichiometric amounts of Atg11, the intensities of individual

peaks decreased indicating that these residues are specifically involved in the interaction (Fig. 1, *C–E*). In order to identify the binding site in the Atg9-NTD for Atg11, we next performed a resonance assignment of the fragment 1 to 285. Since the resonance assignment of large IDPs (such as Atg9 NTD) is very challenging, we employed high-dimensionality techniques (5D) combined with fast pulsing techniques, nonlinear sampling, and automated assignment procedures. Following this strategy, we could assign the backbone as well as some side chain (up to Cβ and Hβ) for residues from Ser32 to Ser250 (BMRB accession number 51011). Secondary structure propensity calculation showed that this fragment (32–250) is completely devoid of secondary structures (Fig. S1). Fragments 1 to 31 and 251 to 285 are probably partially folded and/or undergoing intermediate conformational exchange. They do not seem to affect the structural dynamics of the 32 to 250 segment, as a shorter construct of Atg9-NTD (29–255) exhibits a nearly identical ^{1}H-^{15}N HSQC spectrum than the longer construct (Fig. S2). Based on this assignment and in order to optimize the spectral quality by limiting resonance overlap, we used this shorter fragment to perform a ^{1}H-^{15}N HSQC-based titration of Atg9-NTD (29–255) by Atg11 (Figs. 2*A* and S3). Due to the large size of the Atg11 dimer (270 kDa), addition of Atg11 to Atg9 NTD did not result in chemical shift changes but rather to an Atg11 concentration-dependent intensity decrease for a specific set of resonances. This titration in combination with the assignment allowed us to identify the putative binding site for Atg11 in the Atg9 NTD, which consists of two short stretches (Fig. 2*A*), both being centered on a PLF motif (Fig. 2*B*). A few unassigned resonances also seem to be affected upon Atg11 binding (Fig. S1), suggesting that part of the N- or C-terminus might also be involved in binding to Atg11.

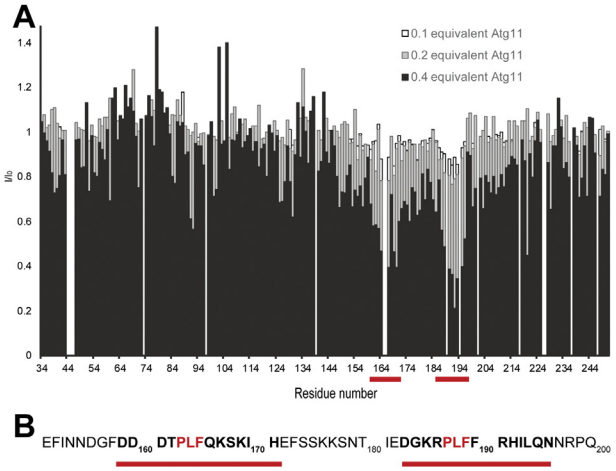

Figure 2. Atg9-NTD interacts with Atg11 through two short segments. *A*, intensity ratio of the ^{1}H-^{15}N HSQC resonances of Atg9-NTD(29–255) in the presence of increasing amount of unlabeled Atg11, the interacting regions in Atg9-NTD(29–255) are identified by *red bars*. The concentration of Atg9-NTD(29–255) was 0.2 mM, concentrations of Atg11 were 0.02, 0.04, and 0.08 mM (0.1, 0.2, and 0.4 equivalent, respectively). *B*, primary sequence of Atg9 (residues 151–200), the residues most affected by Atg11 binding are highlighted in *bold*, the two PLF motifs are colored in *red*.

Two PLF motifs in the Atg9-NTD are required for the interaction with Atg11

In order to test if these PLF motifs are required for the interaction of the Atg9-NTD with Atg11, we mutated the L and F of both motifs ($L_{164}F_{165}$ and $L_{188}F_{189}$) to A and tested the mutant proteins in a microscopy-based protein–protein interaction (MBPPI) assay (Fig. 3*A*). We immobilized the EGFP tagged Atg11 on GFP-Trap beads and added mCherry-tagged Atg9-NTD. As expected, we observed a robust recruitment of Atg9-NTD(1–255) to the beads coated with EGFP-Atg11 (Fig. 3, *A* and *B*). Mutation of the first PLF motif (M1) severely reduced the interaction, and mutation of the second PLF motif (M2) reduced the recruitment of the Atg9-NTD to the EGFP-Atg11-coated beads (Fig. 3, *A* and *B*) to a similar extent. Upon mutation of both motifs (M1+M2), the interaction between the Atg9-NTD and Atg11 became undetectable (Fig. 3, *A* and *B*).

Next, we characterized the interaction of the Atg9-NTD with Atg11 using ITC (Fig. 3*C*). Titration of the wild-type Atg9-NTD(1–255) into full-length Atg11 yielded a robust signal, fitting of which resulted in a K_D of around 1 μM and a stoichiometry of 1 (K_D = 1,086 ± 0,006 μM, n = 0,931 ± 0,004, Fig. S4). The affinity of the Atg9-NTD(1–255) M1 and M2 mutants for Atg11 was too low to be measured accurately by ITC.

The two PLF motifs in the Atg9-NTD are required for the Cvt pathway

Having established that the two PLF motifs are *bona fide* binding sites for Atg11, at least *in vitro*, we asked what the effect of their mutation on autophagic processes in cells might be. *A priori*, we expected the PLF motifs mediating the interaction of Atg9 with Atg11 to be particularly important for selective autophagy such as the Cvt pathway, which mediates the transport of prApe1 into the vacuole wherein its propeptide is cleaved off to produce active mApe1 (mature Ape1). We therefore expressed the mutant Atg9 proteins in *Atg9*Δ cells and assessed their effects on prApe1 processing under nutrient-rich conditions by the Cvt pathway and on rapamycin-induced bulk autophagy (Fig. 4*A*). The different mutations do not appear to affect expression levels of Atg9. However, individual mutation of motif 1 and 2 resulted in reduction of prApe1 transport into the vacuole of about 70% when compared with wild-type Atg9-TAP (Fig. 4*A*). Cells expressing Atg9 with mutations in motifs 1 and 2 showed no detectable prApe1 processing under nutrient-rich conditions. In contrast, upon induction of bulk autophagy by addition of rapamycin, single mutation of motif 1 and 2 resulted in a reduction of prApe1 processing of only about 30%. prApe1 processing was also readily detectable for the double mutant with disrupted motifs 1 and 2 (Fig. 4*A*). A similar picture emerged when we determined GFP-Atg8 processing under nutrient-rich conditions and upon rapamycin-induced bulk autophagy. This assay follows the transport of GFP-Atg8 into the vacuole, wherein the Atg8 moiety is rapidly degraded while the relatively more stable GFP accumulates. As expected,

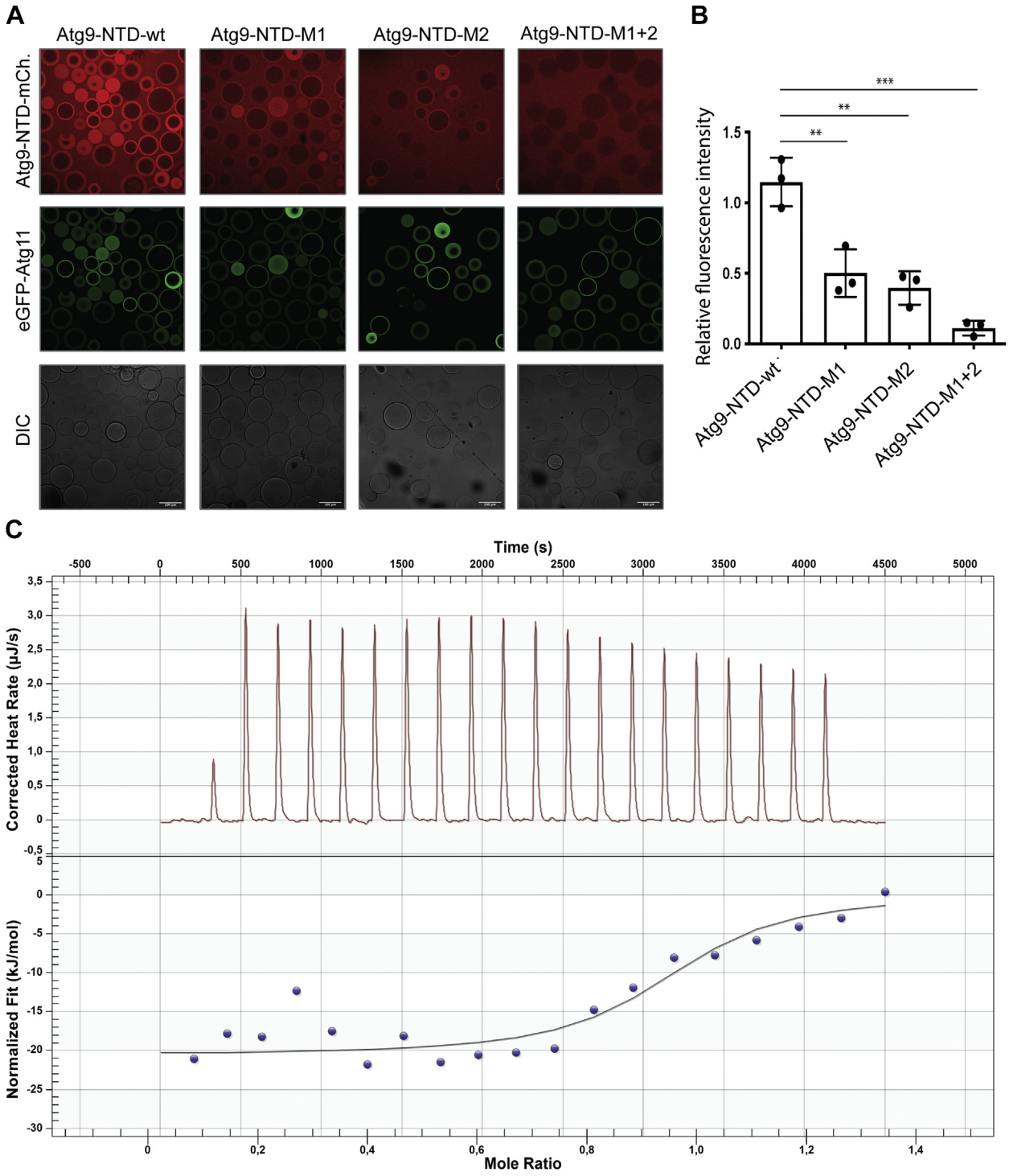

Figure 3. Atg9-NTD PLF motifs are essential for the interaction with Atg11. *A*, microscopy-based protein–protein interaction assays between GFP-Trap beads coated with EGFP-Atg11 and different forms of Atg9-NTD-(1–255)-mCherry, the scale bars represent 100 µm. *B*, quantification of the mCherry signal on the beads normalized to the EGFP signal, the error bars correspond to the standard deviation between three independent replicates. *C*, isothermal titration calorimetry traces of Atg9-NTD(1–255) binding to Atg11. For data fitting, the heat of dilution of Atg11 has been subtracted from the raw data (Fig. S4). Thermodynamic parameters of binding are: K_D = 1.089 µM, n = 0.94, ΔH = −24.55 ± 5.6 kJ mol^{-1}.

under nutrient-rich conditions, the levels of free GFP were low but detectable. Individual mutation of motifs 1 and 2 resulted in a reduction of the free GFP band, while the double mutation abolished GFP-Atg8 processing completely (Fig. 4*B*). In rapamycin-induced bulk autophagy, GFP-Atg8 processing was less severely reduced and detectable for all mutants. Thus, the Cvt pathway acting under nutrient-rich conditions appears to be particularly strongly affected by the mutation of the PLF motifs in Atg9. In order to evaluate the effect of these Atg9 mutations on bulk autophagy, we also performed a Pho8-Delta60 assay (31) (Fig. 4*C*). Only cells expressing Atg9 with mutations in motifs 1 and 2 exhibited a slight decrease in bulk

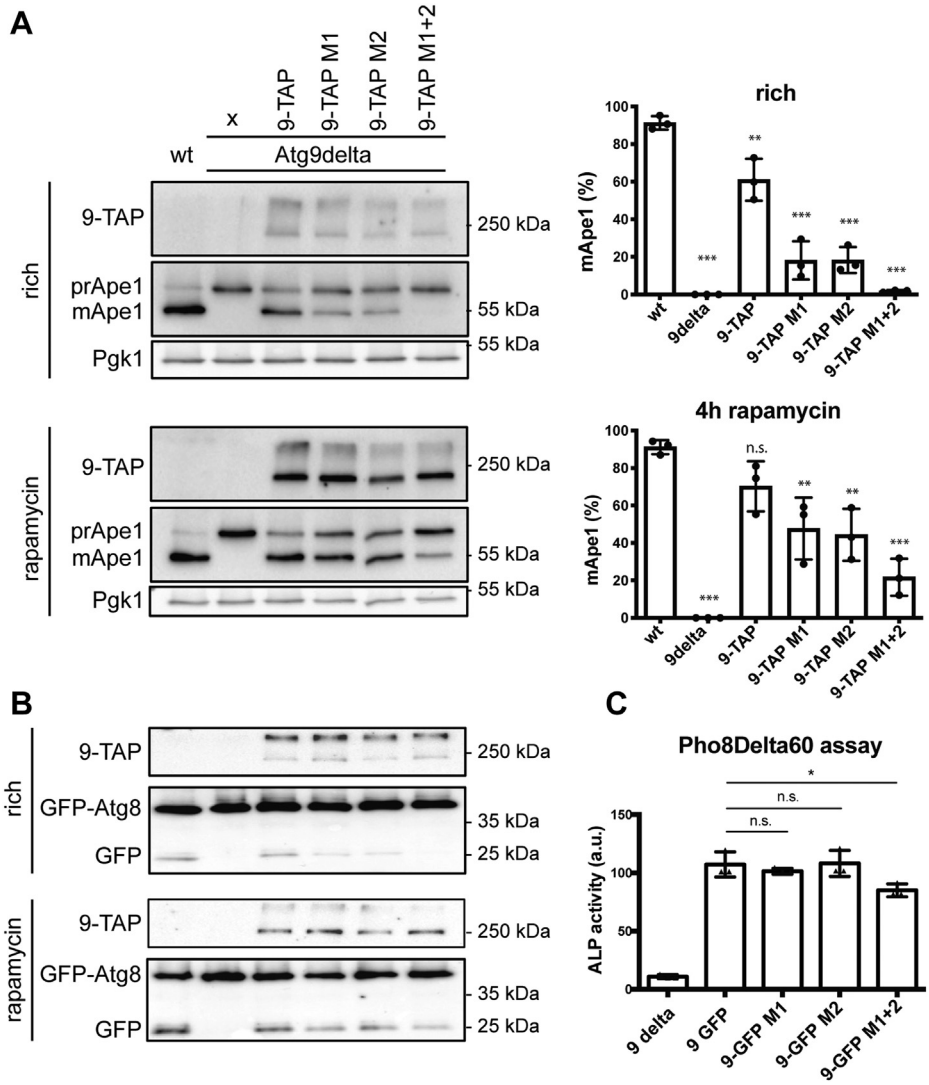

Figure 4. Atg9-NTD PLF motifs are essential for selective autophagy *in vivo*. *A*, Western blot analysis of Ape1 processing of different Atg9 constructs, in rich conditions and after 4 h of treatment with rapamycin, the quantification of the Ape1 bands are shown on the right. The percentage of mApe1 is calculated in reference to total Ape1 (mApe1 + prApe1). *B*, Western blot analysis of GFP-Atg8 processing of different Atg9 constructs in rich conditions and after 4 h of treatment with rapamycin. *C*, Pho8Delta60 assay, quantification of the alkaline phosphatase activity in strains carrying different version of Atg9. For all experiments, a total of three independent replicates were conducted. The graph shows the averages, and the error bars represent the standard deviations. *p* values were calculated using Student's *t* test. Significances are indicated with * when *p* value ≤ 0.05, ** when *p* value ≤ 0.01, and *** when *p* value ≤ 0.001.

autophagy, showing that, as expected, these mutations as well as the abolition of the Atg9/Atg11 interaction do not considerably affect bulk autophagy.

The PLF motifs in the Atg9-NTD contribute to the recruitment of Atg9 to the prApe1 cargo through its interaction with Atg11 in vivo

Finally, we asked what the basis for the block of the Cvt pathway as measured by prApe1 and GFP-Atg8 processing by mutations in the PLF motifs in the Atg9-NTD might be. Atg11 is recruited to the prApe1 cargo *via* the Atg19 cargo receptor and acts upstream of the autophagy machinery to initiate Cvt vesicle formation. We therefore expected that the loss of the Atg11–Atg9 interaction by the mutations in PLF motifs 1 and 2 results in reduced Atg9 recruitment to the prApe1 cargo. To test this hypothesis, we first checked the recruitment of Atg11 by Atg9 by coimmunoprecipitation (Fig. 5*A*). Quantification of the Atg11 Western blot signal reveals a strong binding of Atg11 to wild-type Atg9, whereas in the case of Atg9 mutated in motifs 1 and 2, the signal for Atg11 is reduced to background levels (Fig. 5*A*).

Next, we expressed wild-type and mutant Atg9-EGFP and prApe1-RFP in *Atg9*Δ cells and followed the recruitment of the two Atg9-EGFP proteins to the prApe1 cargo by fluorescence microscopy (Fig. 5*B*). Indeed, the PLF motifs 1 and 2 mutant showed a severely reduced recruitment to the prApe1 cargo suggesting that the interaction of Atg11 with the PLF motifs in the NTD of Atg9 contributes considerably to Atg9 recruitment (Fig. 5*C*).

Discussion

It has become clear that in selective autophagy, the recruitment of the autophagy machinery is induced by the cargo *via* its recognition by a cargo receptor that in turn

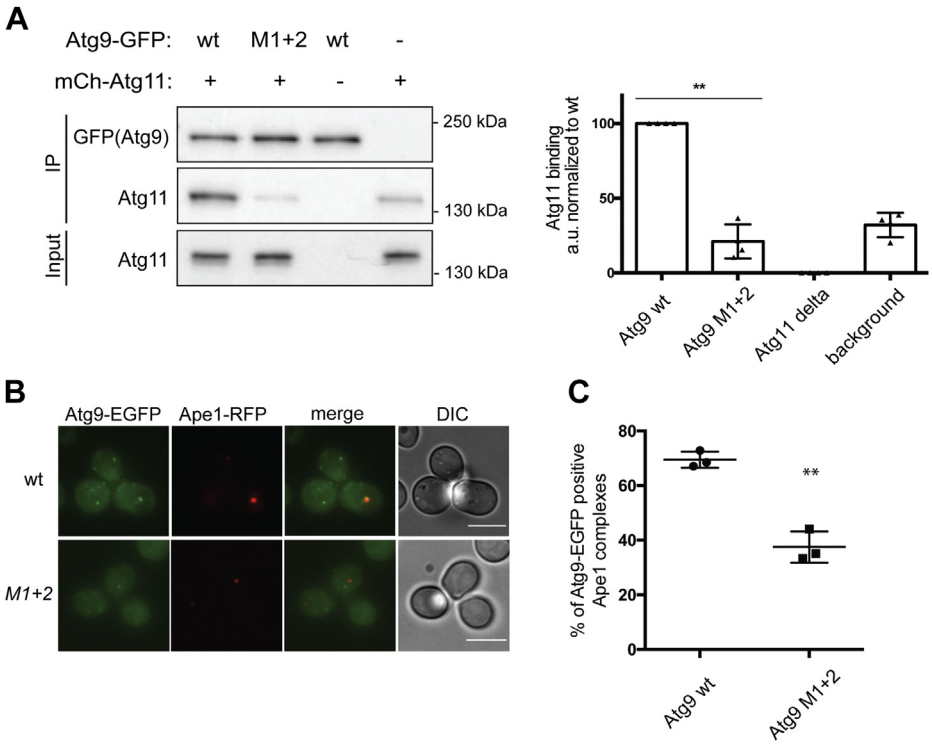

Figure 5. Atg9-NTD PLF motifs are essential for the recruitment of Atg9 to the PAS through its interaction with Atg11. *A*, Western blot analysis of Atg11 coimmunoprecipitation with different Atg9-EGFP constructs. *B*, recruitment of Atg9-EGFP and Atg9-EGFP L164A/F165A/L188A/F189A to the autophagosome formation site. Yeast cells of the indicated genotype expressing Ape1-RFP were imaged using a Deltavision ULTRA Epifluorescence microscope. *C*, percentage of Atg9-EGFP dots colocalizing with Ape1-RFP dots. In total, three independent experiments were conducted. The graph shows the averages, and the error bars represent the standard deviations. *p* values were calculated using Student's *t* test. Scale bars: 5 μm. Significances are indicated with * when *p* value ≤0.05, ** when *p* value ≤ 0.01, and *** when *p* value ≤ 0.001.

recruits the Atg11/FIP200 scaffold proteins (11). These scaffold proteins have a pivotal role by attracting the Atg1/ULK1 complex and Atg9 vesicles to initiate autophagosome formation *in situ*. However, the molecular details of these interactions are largely unknown as well as their mechanisms of regulation.

We recently gained insight into these processes by reconstituting *in vitro* the early steps of phagophore formation. We proposed a model in which Atg9 vesicles are recruited to the site of autophagosome biogenesis and serve as seeds for phagophore assembly by recruiting the rest of the autophagy machinery (6). Furthermore, the lipid scramblase activity of Atg9 in conjunction with Atg2 mediated transport of lipids into the phagophore and *de novo* lipid biosynthesis drive phagophore elongation (5, 6, 20, 21, 26–30, 32). However, in our reconstitutions (6), we used either endogenous Atg9 vesicles or reconstituted Atg9 proteoliposomes. In both cases, it is difficult to delineate the fine details of the molecular interactions and to differentiate the respective contributions of the protein and lipid parts of Atg9 vesicles.

Consequently, we focused on the soluble NTD of Atg9, which has been reported to interact with several autophagy factors, including Atg11 (19, 33, 34). Since the Atg9-NTD is predicted to be disordered, we used NMR spectroscopy to characterize the interaction between the Atg9-NTD and Atg11. Our NMR data confirm the disordered nature of the Atg9-NTD (at least for the residues 34–250). Our near-complete resonance assignment of the residues 34 to 250 of Atg9-NTD allowed us to map the binding site for Atg11. In particular, we identified two stretches of 13 and 14 residues respectively, both centered on a PLF motif. Mutation of the first or second motif to PAA resulted in a severely reduced affinity for Atg11, whereas mutation of both motifs to PAA completely abolished the interaction of the Atg9-NTD with Atg11. Our ITC measurement showed that the affinity of the Atg9-NTD for Atg11 is about 1 μM.

Such relatively low affinity is unlikely to result in a tight complex between Atg9 and an isolated Atg11 dimer. However, it may be sufficient to allow for an Atg9 vesicle to be robustly recruited to the cargo. Indeed, Atg11 clusters at the surface of the cargo (*via* its interaction with the cargo receptor) and will be able to form multiple interactions with several trimers of Atg9 at the surface of the vesicle, leading to a high avidity interaction between the cargo and the Atg9 vesicle (Fig. 6). In this model, the clustering of the scaffold protein to the cargo, which is regulated by the phosphorylation of the cargo receptor (35), is sufficient to lead to the recruitment of Atg9 vesicles.

Consistent with this model and the importance of the PLF motifs, we observed a reduced colocalization of prApe1 and Atg9 upon their mutation. Additionally, mutation of the PLF motifs reduced or even abolished the interaction with Atg11 *in vivo* and consequently prApe1 transport into the vacuole by the Cvt pathway. Upon induction of bulk autophagy by the

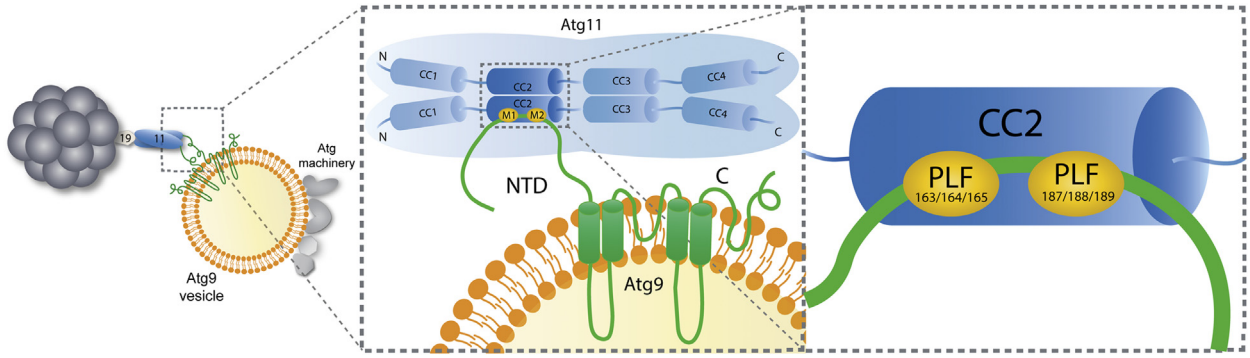

Figure 6. Model of the interaction between Atg11 and Atg9 vesicles. Atg9-NTD interacts with Atg11-CC2 through two PLF motifs. The clustering of Atg11 on prApe1 particles leads to a robust recruitment of Atg9 vesicles.

addition of the Tor inhibitor rapamycin, the block in prApe1 processing and GFP-Atg8 cleavage was partially overcome, presumably because Atg17, which also binds Atg9, can compensate for the loss of the ability of Atg11 to bind to Atg9 (34, 36). Additionally, our Pho8Delta60 assay shows that the interaction between Atg11 and Atg9 is not required for bulk autophagy and that mutations of the PLF motifs do not affect the other functions of Atg9.

Atg11 is not the only binding partner of Atg9-NTD, Atg17 and Atg13 also interact with this domain (19, 33, 34). The capacity of Atg9-NTD to engage in multiple interactions is in line with its disordered nature. Indeed, IDPs through the fast sampling of a large conformational space are able to form complexes with different ligands and to act as interacting hubs in highly regulated processes (37).

This work set the base for future characterization on the binding properties of Atg9-NTD in order to understand the interplay between the different binding partners of Atg9 during the formation of the phagophore and the assembly of the Atg1 complex in both selective and bulk autophagy.

Experimental procedures

Protein expression and purification

A list of constructs can be found in Table S1. Full-length yeast Atg11 was expressed and purified as described previously (6). For the NMR titration, Atg11 was dialyzed against 20 mM Bis-Tris pH 6, 300 mM NaCl. Atg9-NTD constructs were all expressed in *E. coli* Rosetta pLysS cells in minimal medium containing ^{15}N-labeled ammonium chloride and ^{13}C-glucose as sole nitrogen and carbon sources, respectively. Atg9-NTD expression was induced at an A_{600nm} of 0.6 by addition of 0.2 mM IPTG. The cells were collected after 16 h of expression at 18 °C by centrifugation at 6000 rpm for 10 min and resuspended in 30 ml per liter of bacterial culture of ice-cold lysis buffer containing 20 mM Tris pH 7.4, 300 mM NaCl 10 mM Imidazole, 2 mM $MgCl_2$, 2 mM β–mercaptoethanol, Roche complete protease inhibitors, and Benzonase (Sigma). Bacteria were lysed by passing through a French press, the cell lysate was then cleared by centrifugation at 20,000 rpm for 20 min. The supernatant containing the soluble protein fraction was loaded onto a HiTrap 5 ml affinity column (GE Healthcare) and eluted through an imidazole gradient. Protein-containing fractions were pooled, concentrated, applied onto a Superdex 200 column (16/600 prep grade, GE Healthcare), and eluted with a buffer containing 20 mM Bis-Tris pH 6, 300 mM NaCl for NMR experiments or 20 mM Tris pH 7.4, and 300 mM NaCl for interaction assays (MBPPI and ITC). For sample destined to resonance assignment, the EGFP tag was cleaved prior to the size-exclusion step through incubation overnight at 4 °C with 3C protease (1 mg of protease per 50 mg of protein).

NMR spectroscopy

For the resonance assignment, the sample consisted of 0.4 mM of uniformly ^{15}N, ^{13}C labeled Atg9-NTD (1–285). All spectra were acquired at 293 K on a Bruker AVANCE III HD 800 MHz spectrometer using the 5 mm TCI-HCN cryo-probe. Assignment of ^{1}H, ^{13}C, and ^{15}N backbone and (partial) side-chain resonances was achieved using three-dimensional (3D) HNCO experiment and a set of five-dimensional (5D) experiments: HN(CA)CONH (38), (HACA)CON(CA)CONH (39) and HabCabCONH (38). All experiments were performed using sparse nonuniform sampling of indirectly detected time domains in order to increase resolution. The 3D HNCO experiment was used as a base spectrum for SMFT (sparse multidimensional Fourier transform) processing of higher-dimensionality experiments (38). Sampling artifacts from all experiments were removed using SSA (signal separation algorithm (40)), implemented into "cleaner" program, available from http://nmr.cent3.uw.edu.pl/software. Detailed acquisition parameters are listed in Table S2.

The resonance assignment was performed using the TSAR program (41). The input data for TSAR were prepared using Sparky software. Chemical shifts were deposited in the BMRB (42) under the accession number 51011.

For ^{1}H-^{15}N HSQC-based titrations, the sample consisted of 0.2 mM of Atg9-NTD (29–255)-mCherry to which Atg11 was added stepwise from a 0.1 mM solution of EGFP-Atg11. All spectra were acquired at 298 K on a Bruker AVANCE spectrometers operating at 600 MHz. All spectra were processed using NMRPipe/NMRDraw (43) and analyzed with NMRFAM Sparky (44).

Microscopy-based protein–protein interaction assay

GFP trap beads were equilibrated with measurement buffer (20 mM Tris pH 7.4 and 300 mM NaCl) and incubated for 1 h with 10 μM of EGFP-Atg11. The beads were washed and incubated with 1 μM solution of Atg9-NTD in 20 mM pH 7.4 and 300 mM NaCl. The mixtures were incubated for at least 30 min at room temperature before imaging. Confocal images were acquired using a Zeiss LSM 700 with a Plan-Apochromat 20 × /0.8 objective. Quantification was done by drawing a line across each bead in Fiji. The intensity of the fluorescence along that line was integrated after background signal subtraction. The signal of the prey was normalized by the signal of the bait. Values were averaged for each condition within each replicate and then among replicates.

Isothermal titration calorimetry

Measurements were performed with a TA instrument Nano ITC microcalorimeter. Experiments were carried out at 25 °C in 20 mm Tris, pH 7.4, 300 mM NaCl. The reference cell contained Milli-Q water. The concentration of EGFP-Atg11 in the reaction cell was 50 to 100 μM. The concentration of Atg9-NTD in the syringe was 300 to 500 μM. The titration consisted of 19 successive injections of 4 μl, with a stirring speed of 350 rpm, separated by intervals of 300 s. The heat release induced by the injection of buffer in Atg11 was subtracted from the raw data before analysis (Fig. S4). Data analysis was done assuming a single binding site. Two replicates were used to calculate average values as well as standard deviations (Fig. S4).

Yeast strains and manipulation

Yeast strains are listed in Table S3. All experiments were performed with BY4741 yeast strains unless stated otherwise. Genetic modifications were done by PCR and/or homologous recombination using standard techniques. Multiple deletions were generated by mating and dissection. Plasmid DNA was transformed to yeast according to a LiOAc/ssDNA/PEG transformation protocol.

Ape1 processing assay

A yeast strain lacking Atg9 was transformed with plasmids expressing Atg9-TAP or mutations thereof, grown to mid-log phase in synthetic selection medium (SD: 0.17% yeast nitrogen base, 0.5% ammonium sulfate, 2% glucose, amino acids as required), and where indicated, treated with 220 nM rapamycin for 4 h at 30 °C. Cultures were precipitated with 7% trichloroacetic acid (TCA), pellets were washed with acetone, dried, and resuspended in urea loading buffer (120 mM Tris-HCl pH 6.8, 5% glycerol, 8 M urea, 143 mM beta-mercaptoethanol, 8% SDS). The samples were analyzed by immunoblotting using rabbit anti-CBP antibody kindly provided by C. Ungermann and rabbit anti-Ape1 antiserum kindly provided by C. Kraft. Results from three independent experiments were quantified using Image Lab (Bio-Rad).

GFP-Atg8 cleavage assay

A yeast strain lacking Atg9 was transformed with a GFP-Atg8 expressing plasmid and plasmids expressing Atg9-TAP or mutations thereof, grown to mid-log phase in synthetic selection medium (SD: 0.17% yeast nitrogen base, 0.5% ammonium sulfate, 2% glucose, amino acids as required), and where indicated, treated with 220 nM rapamycin for 4 h at 30 °C. Whole cell lysates were prepared by TCA extraction (described above) and analyzed by immunoblotting using rabbit anti-CBP antibody kindly provided by C. Ungermann and a mouse anti-GFP antibody (Max Perutz Labs, Monoclonal antibody facility).

Pho8Delta60 assay

Yeast cells were grown to mid-log phase in YPD (1% yeast extract, 2% peptone, 2% glucose) and starved for 4 h in nitrogen starvation medium (SD-N: 0.17% yeast nitrogen base without amino acids, 2% glucose).

In total, 50 OD600 units of yeast culture were harvested by centrifugation. The pellets were washed with dH2O and ice-cold 0.85% NaCl containing 1 mM PMSF and resuspended in 8 μl/OD600 unit lysis buffer [20 mM PIPES pH 6.8, 0.5% Triton X-100, 50 mM KCl, 100 mM potassium acetate, 10 mM MgSO4, 10 μM ZnSO4, 1 mM PMSF, cOmplete protease inhibitor cocktail (Roche)]. Cells were lysed by bead beating, and extracts were cleared by centrifugation. Protein concentration of the supernatant was adjusted to 50 μg in 100 μl lysis buffer. In total, 400 μl reaction buffer (0.4% Triton X-100, 10 mM MgSO4, 10 μM ZnSO4, and 250 mM Tris-HCl pH 8.5) containing 6.25 mM α-naphthylphosphate (Sigma-Aldrich) was added to enzymatic reactions, or only reaction buffer was added to control reactions. Reactions were incubated at 37 °C for 10 min and stopped by adding 500 μl stop buffer (1 M glycine pH 11). A 405 was measured using a plate reader. A standard curve was generated by using a dilution series of the product (1-naphtol, Sigma-Aldrich).

Three independent replicates were performed and activity was calculated the following: activity = [pNPP in nmol]/(t[min] *[protein in mg]).

Coimmunoprecipitation

S. cerevisiae Atg9-GFP Atg11Δ, Atg9-M1+2-GFP Atg11Δ, and Atg9Δ Atg11Δ cells were transformed with pRS316-mCh-Atg11 or empty pRS316 plasmid using the LiAc/SS carrier DNA/PEG method. Cells were grown to mid-log phase in YPD, harvested by centrifugation, and resuspended in IP buffer (25 mM Tris-HCl pH 7.4, 150 mM NaCl, 0.2% NP-40, 1 mM PMSF, Protease inhibitor cocktail [Roche], Protease inhibitor mix FY [Serva]). Droplets were frozen in liquid nitrogen and milled in a cryogenic grinder (SPEX Freezer mill). Yeast powder was resuspended in IP buffer and cleared by centrifugation at 5000*g* for 5 min at 4 °C. Lysates were incubated with GFP-trap magnetic agarose beads (Chromotek) o/n at 4 °C on a turning wheel. Beads were washed three times in IP buffer, resuspended in urea loading buffer (116 mM Tris-HCl pH 6.8, 4.9% glycerol, 8 M Urea, 8% SDS), and boiled for 10 min at 60 °C. Samples

were analyzed by Western blot using mouse anti-Atg11 and mouse anti-GFP antibodies (Max Perutz Labs antibody facility), and bands were quantified using the BioRad Image Lab program.

Quantitative live cell imaging

Plasmid DNA was transformed to yeast in stationary phase grown on YPD-agar according to a LiOAc/ssDNA/PEG transformation protocol. Transformed yeast strains were grown in synthetic defined minimal medium (SD; 1.7 g/l yeast nitrogen base without amino acids and ammonium sulfate (Formedium), 5 g/l ammonium sulfate, 2 g/l glucose) supplemented with the appropriate amino acid drop-out mix (CSM; Formedium) to log phase for imaging. Cells were immobilized with concavalinA (Sigma). Widefield images were obtained on a Deltavision ULTRA Epifluorescence Microscope using a UPlanSApo 100 × /1.4 Oil objective. Images were analyzed using the Fiji software. For the quantification, approximately 1000 cells were counted per construct (three experiments each). The plot was generated with GraphPad Prism.

Data availability

Chemical shifts were deposited in the BMRB under the accession number 51011.

Supporting information—This article contains supporting information (45).

Acknowledgments—We thank the Max Perutz Labs BioOptics Facility and NMR Facility for technical support. We thank Claudine Kraft for the generous gift of constructs (see Table S2) and the anti-Ape1 serum.

Author contributions—N. C., W. K., and S. M. conceptualization; N. C., B. B., V. B., M. S., A. Z.-K. investigation; S. M. supervision; N. C. and S. M. writing—original draft; A. Z.-K. and W. K. writing—review and editing.

Funding and additional information—This work has been funded by the ERC grant No.646653 and FWF grant (P32814-B) to S. M. and a grant from the Polish National Science Centre to W. K. (MAESTRO, 2015/18/A/ST4/00270).

Conflict of interest—Sascha Martens is member of the scientific advisory board of Casma Therapeutics.

Abbreviations—The abbreviations used are: Ape1, aminopeptidase 1; Cvt, cytoplasm-to-vacuole targeting; ER, endoplasmic reticulum; GFP, green fluorescent protein; HSQC, heteronuclear single-quantum coherence; IDP, intrinsically disordered protein; ITC, isothermal titration calorimetry; MBPPI, microscopy-based protein–protein interaction; NMR, nuclear magnetic resonance; NTD, N-terminal domain; SMFT, sparse multidimensional Fourier transform.

References

1. Zaffagnini, G., and Martens, S. (2016) Mechanisms of selective autophagy. *J. Mol. Biol.* **428**, 1714–1724
2. Mizushima, N., Yoshimori, T., and Ohsumi, Y. (2011) The role of Atg proteins in autophagosome formation. *Annu. Rev. Cell Dev. Biol.* **27**, 107–132
3. Melia, T. J., Lystad, A. H., and Simonsen, A. (2020) Autophagosome biogenesis: From membrane growth to closure. *J. Cell Biol.* **219**, e202002085
4. Lamb, C. A., Yoshimori, T., and Tooze, S. A. (2013) The autophagosome: Origins unknown, biogenesis complex. *Nat. Rev. Mol. Cell Biol.* **14**, 759–774
5. Chang, C., Jensen, L. E., and Hurley, J. H. (2021) Autophagosome biogenesis comes out of the black box. *Nat. Cell Biol.* **23**, 450–456
6. Sawa-Makarska, J., Baumann, V., Coudevylle, N., von Bülow, S., Nogellova, V., Abert, C., Schuschnig, M., Graef, M., Hummer, G., and Martens, S. (2020) Reconstitution of autophagosome nucleation defines Atg9 vesicles as seeds for membrane formation. *Science* **369**, eaaz7714
7. Yorimitsu, T., and Klionsky, D. J. (2005) Atg11 links cargo to the vesicle-forming machinery in the cytoplasm to vacuole targeting pathway. *Mol. Biol. Cell* **16**, 1593–1605
8. Shintani, T., Huang, W.-P., Stromhaug, P. E., and Klionsky, D. J. (2002) Mechanism of cargo selection in the cytoplasm to vacuole targeting pathway. *Dev. Cell* **3**, 825–837
9. Shintani, T., and Klionsky, D. J. (2004) Cargo proteins facilitate the formation of transport vesicles in the cytoplasm to vacuole targeting pathway. *J. Biol. Chem.* **279**, 29889–29894
10. Pfaffenwimmer, T., Reiter, W., Brach, T., Nogellova, V., Papinski, D., Schuschnig, M., Abert, C., Ammerer, G., Martens, S., and Kraft, C. (2014) Hrr25 kinase promotes selective autophagy by phosphorylating the cargo receptor Atg19. *EMBO Rep.* **15**, 862–870
11. Turco, E., Fracchiolla, D., and Martens, S. (2020) Recruitment and activation of the ULK1/atg1 kinase complex in selective autophagy. *J. Mol. Biol.* **432**, 123–134
12. Turco, E., Witt, M., Abert, C., Bock-Bierbaum, T., Su, M.-Y., Trapannone, R., Sztacho, M., Danieli, A., Shi, X., Zaffagnini, G., Gamper, A., Schuschnig, M., Fracchiolla, D., Bernklau, D., Romanov, J., *et al.* (2019) FIP200 claw domain binding to p62 promotes autophagosome formation at ubiquitin condensates. *Mol. Cell* **74**, 330–346.e11
13. Tanaka, C., Tan, L.-J., Mochida, K., Kirisako, H., Koizumi, M., Asai, E., Sakoh-Nakatogawa, M., Ohsumi, Y., and Nakatogawa, H. (2014) Hrr25 triggers selective autophagy–related pathways by phosphorylating receptor proteins. *J. Cell Biol.* **207**, 91–105
14. Mochida, K., Ohsumi, Y., and Nakatogawa, H. (2014) Hrr25 phosphorylates the autophagic receptor Atg34 to promote vacuolar transport of α-mannosidase under nitrogen starvation conditions. *FEBS Lett.* **588**, 3862–3869
15. Suzuki, H., and Noda, N. N. (2018) Biophysical characterization of Atg11, a scaffold protein essential for selective autophagy in yeast. *FEBS Open Bio* **8**, 110–116
16. Margolis, H. K., Katzenell, S., Leary, K. A., and Ragusa, M. J. (2020) The third coiled coil domain of Atg11 is required for shaping mitophagy initiation sites. *J. Mol. Biol.* **432**, 5752–5764
17. Kamber, R. A., Shoemaker, C. J., and Denic, V. (2015) Receptor-bound targets of selective autophagy use a scaffold protein to activate the Atg1 kinase. *Mol. Cell* **59**, 372–381
18. Torggler, R., Papinski, D., Brach, T., Bas, L., Schuschnig, M., Pfaffenwimmer, T., Rohringer, S., Matzhold, T., Schweida, D., Brezovich, A., and Kraft, C. (2016) Two independent pathways within selective autophagy converge to activate Atg1 kinase at the vacuole. *Mol. Cell* **64**, 221–235
19. He, C., Song, H., Yorimitsu, T., Monastyrska, I., Yen, W. L., Legakis, J. E., and Klionsky, D. J. (2006) Recruitment of Atg9 to the preautophagosomal structure by Atg11 is essential for selective autophagy in budding yeast. *J. Cell Biol.* **175**, 925–935
20. Matoba, K., Kotani, T., Tsutsumi, A., Tsuji, T., Mori, T., Noshiro, D., Sugita, Y., Nomura, N., Iwata, S., Ohsumi, Y., Fujimoto, T., Nakatogawa, H., Kikkawa, M., and Noda, N. N. (2020) Atg9 is a lipid scramblase that mediates autophagosomal membrane expansion. *Nat. Struct. Mol. Biol.* **27**, 1185–1193
21. Maeda, S., Yamamoto, H., Kinch, L. N., Garza, C. M., Takahashi, S., Otomo, C., Grishin, N. V., Forli, S., Mizushima, N., and Otomo, T. (2020)

Structure, lipid scrambling activity and role in autophagosome formation of Atg9A. *Nat. Struct. Mol. Biol.* **27**, 1194–1201
22. Guardia, C. M., Tan, X. F., Lian, T., Rana, M. S., Zhou, W., Christenson, E. T., Lowry, A. J., Faraldo-Gomez, J. D., Bonifacino, J. S., Jiang, J., and Banerjee, A. (2020) Structure of human Atg9A, the only transmembrane protein of the core autophagy machinery. *Cell Rep.* **31**, 107837
23. Yamamoto, H., Kakuta, S., Watanabe, T. M., Kitamura, A., Sekito, T., Kondo-Kakuta, C., Ichikawa, R., Kinjo, M., and Ohsumi, Y. (2012) Atg9 vesicles are an important membrane source during early steps of autophagosome formation. *J. Cell Biol.* **198**, 219–233
24. Ohashi, Y., and Munro, S. (2010) Membrane delivery to the yeast autophagosome from the golgi–endosomal system. *Mol. Biol. Cell* **21**, 3998–4008
25. Mari, M., Griffith, J., Rieter, E., Krishnappa, L., Klionsky, D. J., and Reggiori, F. (2010) An Atg9-containing compartment that functions in the early steps of autophagosome biogenesis. *J. Cell Biol.* **190**, 1005–1022
26. Orii, M., Tsuji, T., Ogasawara, Y., and Fujimoto, T. (2021) Transmembrane phospholipid translocation mediated by Atg9 is involved in autophagosome formation. *J. Cell Biol.* **220**, e202009194
27. Gómez-Sánchez, R., Rose, J., Guimarães, R., Mari, M., Papinski, D., Rieter, E., Geerts, W. J., Hardenberg, R., Kraft, C., Ungermann, C., and Reggiori, F. (2018) Atg9 establishes Atg2-dependent contact sites between the endoplasmic reticulum and phagophores. *J. Cell Biol.* **217**, 2743–2763
28. Valverde, D. P., Yu, S., Boggavarapu, V., Kumar, N., Lees, J. A., Walz, T., Reinisch, K. M., and Melia, T. J. (2019) Atg2 transports lipids to promote autophagosome biogenesis. *J. Cell Biol.* **218**, 1787–1798
29. Osawa, T., Kotani, T., Kawaoka, T., Hirata, E., Suzuki, K., Nakatogawa, H., Ohsumi, Y., and Noda, N. N. (2019) Atg2 mediates direct lipid transfer between membranes for autophagosome formation. *Nat. Struct. Mol. Biol.* **26**, 281–288
30. Maeda, S., Otomo, C., and Otomo, T. (2019) The autophagic membrane tether ATG2A transfers lipids between membranes. *Elife* **8**, e45777
31. Noda, T., Matsuura, A., Wada, Y., and Ohsumi, Y. (1995) Novel system for monitoring autophagy in the yeast Saccharomyces cerevisiae. *Biochem. Biophys. Res. Commun.* **210**, 126–132
32. Schütter, M., Giavalisco, P., Brodesser, S., and Graef, M. (2020) Local fatty acid channeling into phospholipid synthesis drives phagophore expansion during autophagy. *Cell* **180**, 135–149.e14
33. Suzuki, S. W., Yamamoto, H., Oikawa, Y., Kondo-Kakuta, C., Kimura, Y., Hirano, H., and Ohsumi, Y. (2015) Atg13 HORMA domain recruits Atg9 vesicles during autophagosome formation. *Proc. Natl. Acad. Sci. U. S. A.* **112**, 3350–3355
34. Sekito, T., Kawamata, T., Ichikawa, R., Suzuki, K., and Ohsumi, Y. (2009) Atg17 recruits Atg9 to organize the pre-autophagosomal structure. *Genes Cells* **14**, 525–538
35. Licheva, M., Raman, B., Kraft, C., and Reggiori, F. (2021) Phosphoregulation of the autophagy machinery by kinases and phosphatases. *Autophagy* **10**, 1–20
36. Rao, Y., Perna, M. G., Hofmann, B., Beier, V., and Wollert, T. (2016) The Atg1–kinase complex tethers Atg9-vesicles to initiate autophagy. *Nat. Commun.* **7**, 10338
37. Uversky, V. N. (2020) Analyzing IDPs in interactomes. *Methods Mol. Biol.* **2141**, 895–945
38. Kazimierczuk, K., Stanek, J., Zawadzka-Kazimierczuk, A., and Kozminski, W. (2010) Random sampling in multidimensional NMR spectroscopy. *Prog. Nucl. Magn. Reson. Spectrosc.* **57**, 420–434
39. Zawadzka-Kazimierczuk, A., Kozminski, W., Sanderova, H., and Krasny, L. (2012) High dimensional and high resolution pulse sequences for backbone resonance assignment of intrinsically disordered proteins. *J. Biomol. NMR* **52**, 329–337
40. Stanek, J., and Kozminski, W. (2010) Iterative algorithm of discrete Fourier transform for processing randomly sampled NMR data sets. *J. Biomol. NMR* **47**, 65–77
41. Zawadzka-Kazimierczuk, A., Kozminski, W., and Billeter, M. (2012) TSAR: A program for automatic resonance assignment using 2D cross-sections of high dimensionality, high-resolution spectra. *J. Biomol. NMR* **54**, 81–95
42. Ulrich, E. L., Akutsu, H., Doreleijers, J. F., Harano, Y., Ioannidis, Y. E., Lin, J., Livny, M., Mading, S., Maziuk, D., Miller, Z., Nakatani, E., Schulte, C. F., Tolmie, D. E., Kent Wenger, R., Yao, H., *et al.* (2008) BioMagResBank. *Nucleic Acids Res.* **36**, D402–408
43. Delaglio, F., Grzesiek, S., Vuister, G. W., Zhu, G., Pfeifer, J., and Bax, A. (1995) NMRPipe: A multidimensional spectral processing system based on UNIX pipes. *J. Biomol. NMR* **6**, 277–293
44. Lee, W., Tonelli, M., and Markley, J. L. (2015) NMRFAM-SPARKY: Enhanced software for biomolecular NMR spectroscopy. *Bioinformatics* **31**, 1325–1327
45. Tamiola, K., Acar, B., and Mulder, F. A. (2010) Sequence-specific random coil chemical shifts of intrinsically disordered proteins. *J Am Chem Soc* **132**, 18000–18003

Supporting information for

Mechanism of Atg9 recruitment by Atg11 in the cytoplasm-to-vacuole targeting pathway

Nicolas Coudevylle[1,*], Bartłomiej Banaś[2], Verena Baumann[1], Martina Schuschnig[1], Anna Zawadzka-Kazimierczuk[2], Wiktor Koźmiński[2] and Sascha Martens[1,*].

[1]Max Perutz Laboratories, University of Vienna, Dr.-Bohrgasse 9, 1030 Vienna, Austria
[2]Biological and Chemical Research Centre, Faculty of Chemistry, University of Warsaw, Żwirki i Wigury 101, 02-089 Warsaw, Poland

Supplementary figure 1: Neighbour corrected structural propensity {Tamiola, 2010 #540} of Atg9-NTD based on 1H, 15N, and 13C experimental chemical shifts.

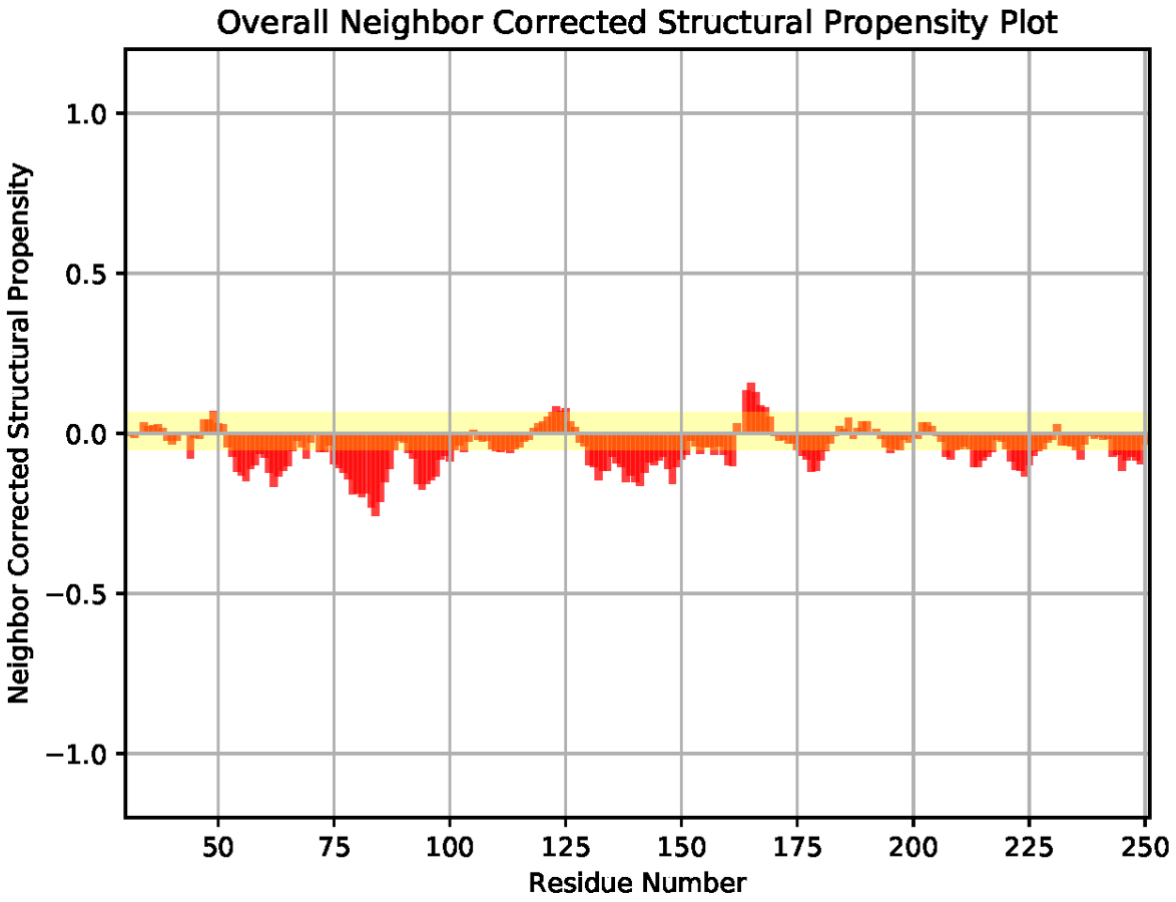

Supplementary figure 2: Overlay of the 1H-15N HSQC spectra of Atg9-NTD segment 1-285 (red resonances) and 29-255 (blue resonances).

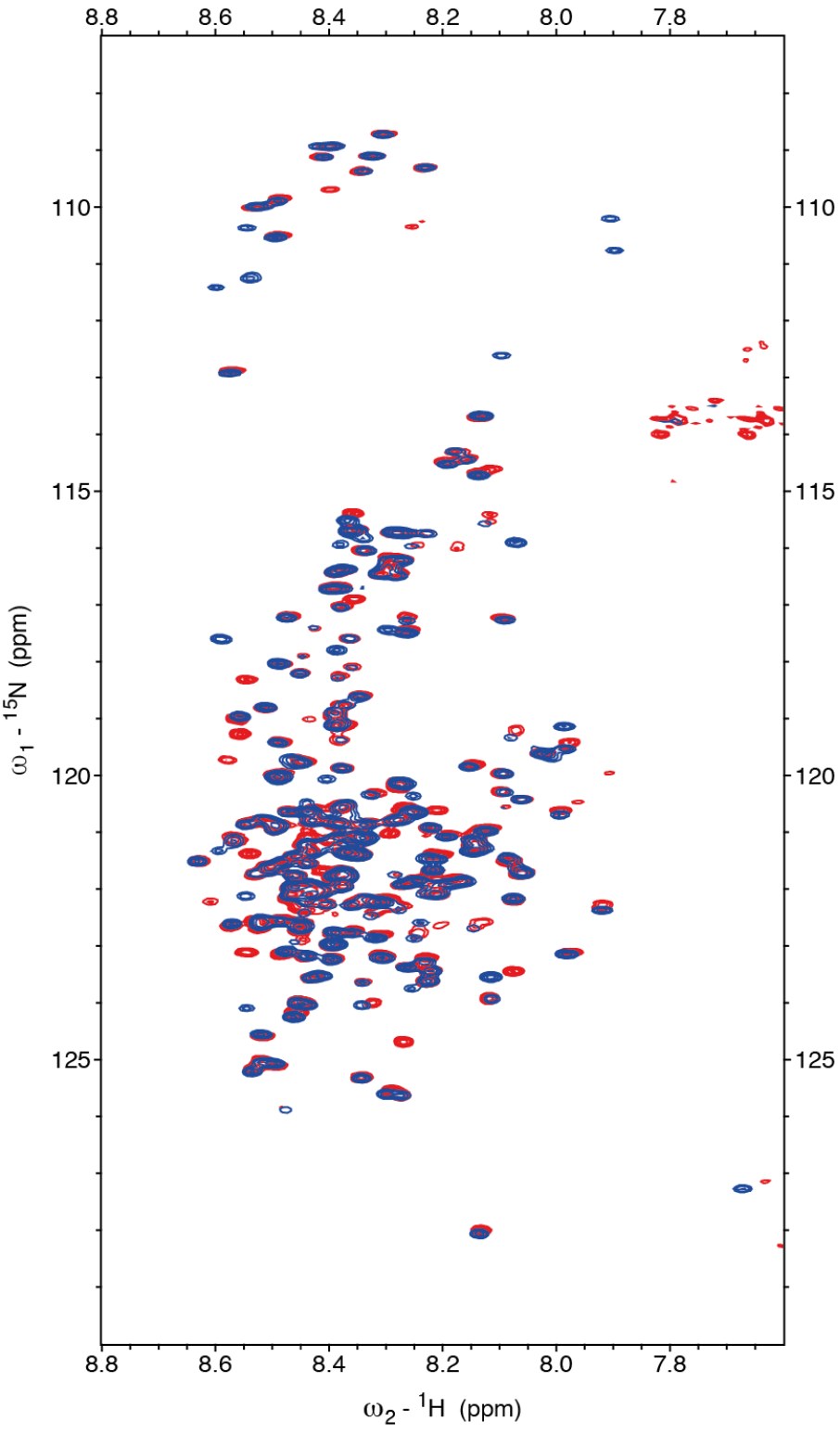

Table S1. Table of constructs

Identification Number	Vector	Expression system	Expressing	Published
SMC195	pRS316	yeast	-	
SMC327	pRS416	yeast	Atg9-TAP	Papinsky *et al.*, 2014
SMC1064	pFastBac HT	Sf9 cells	6xHis-TEV-mEGFP-Atg11	Sawa-Makarska *et al.*, 2020
SMC1340	pET-M11	*E. coli*	6xHis-TEV-Atg9(1-285)-3C-eGFP	This study
SMC1247	pET-Duet	*E. coli*	6xHis-Atg9(S19D)(1-255)-mCherry	This study
SMC1487	pET-Duet	*E. coli*	6xHis-Atg9(29-255)-mCherry	This study
SMC1510	pET-Duet	*E. coli*	6xHis-Atg9(S19D, L164A/F165A)(1-255)-mCherry	This study
SMC1511	pET-Duet	*E. coli*	6xHis-Atg9(S19D, L188A/F189A)(1-255)-mCherry	This study
SMC1512	pET-Duet	*E. coli*	6xHis-Atg9(S19D, L164A/F165A/L188A/F189A)(1-255)-mCherry	This study
SMC1574	pRS416	yeast	Atg9-TAP L164A/F165A	This study
SMC1575	pRS416	yeast	Atg9-TAP L188A/F189A	This study
SMC1576	pRS416	yeast	Atg9-TAP L164A/F165A/L188A/F189A	This study
SMC199	pRS315	yeast	GFP-Atg8	Kraft et al., 2012

Table S2. Parameters of the multidimensional NMR experiments used for the assignment of Atg9-NTD(1-285). (nucl: nucleus; indir dim: indirect dimension, sw: spectral width, t_{max}: maximum evolution time, ni: number of non-uniform sampling complex points).

Experiment	Experimental parameters													
	indir dim1			indir dim2			indir dim3			indir dim4			ni	exp time (h)
	nucl	sw (Hz)	t_{max} (ms)	nucl	sw (Hz)	t_{max} (ms)	nucl	sw (Hz)	t_{max} (ms)	nucl	sw (Hz)	t_{max} (ms)		
3D HNCO	C'	2500	50	N	2300	76	-	-	-	-	-	-	2500	16
5D HN(CA)CONH	H^N	2500	10	N	2300	27	C'	2500	27	N	2300	27	2800	72
5D (HACA)CON(CA)CONH	C'	2500	27	N	4000	54	C'	2500	27	N	2300	27	5850	155
5D HabCabCONH	Hab	5600	11	Cab	13000	7	C'	2500	27	N	2300	27	2000	43

Table S3. Table of yeast strains.

Name	Genotype	Background	Reference
BY4741	his3Δ1 leu2Δ0 met15Δ0 ura3Δ0 MATa	-	Euroscarf
SMY056	*atg9::kan* MATa	BY4741	Euroscarf

Discussion

Autophagy was first described in 1962 and about 30 years later most of the essential components required for the successful formation of an autophagosome had been identified. Since then, the field has constantly pushed towards a complete understanding of the molecular mechanisms that mediate the *de novo* formation of this double membrane bound structure. While for many aspects most of the crucial pieces of the puzzle seem to be identified and assembled correctly, some factors' functions and their roles within the autophagic orchestra are still enigmatic. One of these factors are the Atg9 vesicles. It has become clear early on that Atg9 is crucial for all types of autophagy and that recruitment of other Atg proteins like Atg14, Atg2, Atg18 and Atg8 to the PAS depends on them (Suzuki et al., 2007). Atg9 is the only transmembrane protein among the autophagic machinery and is embedded in small vesicles. Additionally, these Atg9 vesicles get incorporated into the membrane and Atg9 localizes to the rim of the isolation membrane together with Atg2-Atg18 (Suzuki et al., 2013; Yamamoto et al., 2012). All these observations lead to the hypothesis that Atg9 vesicles might actually provide the bulk of the autophagosomal membrane. It was further revealed that on average only three Atg9 vesicles are recruited to the PAS (Yamamoto et al., 2012). Considering an Atg9 vesicle diameter between 30 and 60 nm and an autophagosome diameter of 150 nm (Cvt vesicles) or even 300-900 nm (bulk autophagy) it became clear that these vesicles cannot be the major membrane source for autophagy (Baba et al., 1994, 1997; Scott et al., 1997). This left two open questions. First, what is the actual role of the Atg9 vesicles during autophagy? And second, where does the membrane for autophagosome formation come from?

Most autophagic research has been carried out by employing genetic and cell biological methods. These in vivo methods are extremely powerful and have gained us unique insights into a complex process involving many different factors. However, when it comes to studying the exact molecular mechanisms underlying a certain pathway, it is essential to have as much control over the experimental set up as possible. In vitro reconstitution approaches, utilizing purified proteins and artificial membranes, allow us to recapitulate a cellular process in the test tube while having full control over the experimental conditions. Through this, we are able to identify all the factors necessary and sufficient for a particular process to take place. Thus, in

vitro and in vivo approaches complement each other to provide a full picture of what is actually happening in a cell.

In vitro reconstitutions have already shed light into many different aspects from autophagy initiation down to fusion of the autophagosome with the vacuole. Therefore, we decided to introduce Atg9 vesicles into our reconstitution approach. We could show that artificial Atg9 proteoliposomes as well as endogenous Atg9 vesicles isolated from yeast cells act as an assembly platform for the complete autophagic machinery downstream of Atg9. They further serve as substrates for Atg8 conjugation, which in turn might enhance the ongoing recruitment of other autophagy factors, resulting in a positive feedback loop and promoting the efficient progress of autophagosome formation.
During selective autophagy, the Atg machinery has to be targeted to the cargo. We could show that interaction between Atg11 and Atg9 is sufficient to establish this connection by recruiting Atg9 vesicles and the assembled machinery to the cargo-receptor complex. The second study presented in this thesis focusses on this specific interaction. NMR spectroscopy revealed two stretches within the Atg9 N-terminus centering around two PLF motifs that are key for the interaction with the CC2 of Atg11 and subsequently the successful progression of selective autophagy. ITC analysis measured a relatively weak affinity between the scaffold and the Atg9 N-terminus and further identified a 1:1 stoichiometry. Both suggests that the interaction between clustered Atg11 at the cargo and Atg9 trimers on the vesicle is necessary to yield a high avidity. With this mechanism, a robust recruitment of the Atg9 vesicles and its harbored Atg-machinery to the cargo might be facilitated.

Among the factors being targeted to the Atg9 vesicles is the Atg2-Atg18 lipid binding/lipid transfer complex. Similar to Atg9, also the function of Atg2 during autophagosome formation was long unknown. Budding yeast with deleted Atg2 displays blocked bulk and selective autophagic activity and microscopy analysis revealed that isolation membrane elongation is compromised in *atg2*Δ strains (Obara et al., 2008; Suzuki et al., 2007). We observed that Atg2-Atg18 binds the Atg12 – Atg5-Atg16 complex in a way that is not mutually exclusive with Atg21 binding but rather suggests the formation of a holo-complex consisting of Atg21, Atg2-Atg18 and Atg12 – Atg5-Atg16. Moreover, the presence of both Atg21 and Atg2-Atg18 increased the

E3 recruitment to Atg9 PLs. In the cell, Atg21 and Atg2-Atg18 together enhance colocalization of Atg12 – Atg5-Atg16 with Ape1. A previous study has already identified Atg21 as a crucial factor for Atg12 – Atg5-Atg16 targeting to the PAS by binding Atg16 (Juris et al., 2015). Another group could pinpoint an interaction between the Atg1 complex component Atg17 and Atg12 as important for PAS-recruitment of the E3-like enzyme (Harada et al., 2019). Our data suggest that Atg2-Atg18 is an additional element for Atg12 – Atg5-Atg16 recruitment to the PAS. Atg8 lipidation to Atg9 PLs however was not compromised in our in vitro assay upon missing Atg2-Atg18. This is in line with the hierarchical in vivo studies of Suzuki et al., 2007 who did not observe a recruitment defect of Atg8 to the PAS in *atg2*Δ strains. Together with the observation that Atg2 deletion strains display a specific defect in autophagosome elongation this suggested that Atg2 takes over another major function.

Since autophagy targets many different cargoes, autophagosomes form at multiple sites within the cell. However, PAS assembly usually occurs in close proximity to the vacuole and special regions within the ER, so-called ER-exit sites (ERES) (Axe et al., 2008; Ylä-Anttila et al., 2009; Graef et al., 2013; Suzuki et al., 2013). More specifically, these ER-exit sites are linked to the rim of the growing autophagosomal membrane and their function is required for successful recruitment of the autophagic machinery downstream of the Atg1 kinase complex and isolation membrane nucleation (Graef et al., 2013b; Tan et al., 2013). ER-exit sites are also the origin of COPII-vesicles (coat protein complex II) which mediate transport from the ER to the Golgi (Jensen & Schekman, 2011). Mutants deficient for COPII-vesicle formation are incapable of generating autophagosomes and COPII-vesicles seem to be at least partially incorporated into the growing isolation membrane (Ishihara et al., 2001; Shima, Kirisako and Nakatogawa, 2019). Therefore, COPII vesicles are discussed as one possible membrane source for isolation membrane elongation. However, the fact that the autophagosomal membrane is almost devoid of transmembrane proteins, together with the observation that the early isolation membrane is a disc-shaped structure with little inner volume suggest another mechanism to be the main driving force for autophagosome elongation (Fengsrud et al., 2000).

Recent in vitro studies have identified Atg2 as a membrane tethering protein. Structural studies employing cryo-electron microscopy yielded a rod-shaped protein

conformation with two independent membrane binding domains, an N-terminal chorein domain and an amphipathic helix at the C-terminus. With the N-terminus associated with the ER and the C-terminus binding the isolation membrane Atg2 establishes an ER-isolation membrane contact site (Chowdhury et al., 2018; Gómez-Sánchez et al., 2018; Kotani et al., 2018). Additionally, Atg2 has been shown to transfer lipids between donor and acceptor membranes (Maeda et al., 2019; Osawa et al., 2019; Valverde et al., 2019). Coupled with our finding that Atg9 vesicles act as seeds for autophagosome formation an interesting hypothesis evolves. Atg2 would extract lipids from the ER membrane and shuttle them through a hydrophobic groove spanning the entire long axis of the protein into the outer membrane of the Atg9 vesicles. This non-vesicular transport model would account for the low inner volume of the growing isolation membrane as well as the low concentration of transmembrane proteins on the autophagosome membrane. In Sawa-Makarska et al. (2020) we show that indeed, Atg2 is able to transfer lipids between ER-like membranes and Atg9 PLs. Additionally, we could show that Atg2 mediated transfer of PE into Atg9 PLs lacking PE renders them a more efficient target for Atg8 lipidation. At the same time several questions arise. The first one is whether the lipid transfer rate of Atg2 is sufficient to form a complete autophagosome within several minutes. Analysis of the published lipid transfer experiments from Maeda et al. (2019), Osawa et al. (2019) and Valverde et al. (2019) by von Bülow and Hummer (2020) demonstrated that autophagosome generation would be kinetically feasible with transfer rates of about 750 lipids per minute per yeast Atg2 molecule. Even the slower transfer rates of mammalian ATG2A (about 115 lipids per second per molecule) would still provide a significant portion of the autophagosomal membrane.

Further it has to be considered that Atg2 transfers lipids only between the outer leaflets of donor and acceptor membranes. In order to facilitate proper membrane expansion around the cargo material it is therefore necessary that the lipids are distributed between the outer and the inner leaflet. This task could be taken over by Atg9, the only transmembrane protein and lipid scramblase of the autophagic machinery. Atg9 assembles into homo-trimers and thereby forms a central pore that spans the vesicle membrane from the luminal to the cytosolic side (Guardia et al., 2020; Lai et al., 2020). Atg2 directly interacts with Atg9 and has been shown to confine Atg9 to the edges of the isolation membrane, right where it is connected with the ER (Graef et al., 2013; Suzuki et al., 2013; Gómez-Sánchez et al., 2018). We therefore propose that Atg2

hands over the transferred lipids directly to Atg9, that subsequently re-establishes membrane balance by shuffling them to the inner leaflet of the vesicle (Figure 3). The exact molecular mechanism of this has to be elucidated in future experiments.

Both, Atg2 mediated lipid transfer and Atg9 scramblase activity are ATP-independent. Therefore, another upcoming question is, what mechanism establishes a directionality of the lipid transfer from the ER into the Atg9 vesicle. This issue is still highly debated in the field but one possible explanation might be found in de-novo phospholipid synthesis. In mammalian cells autophagosome formation initiates in close proximity to phosphatidylinositol synthase-enriched ER subdomains (Nishimura et al., 2017). Schütter et al. (2020) observed that the acyl-coenzyme A synthetase (ACS) Faa1 localizes to forming autophagosomes and that its activation of fatty acids at the nucleated isolation membrane is required for successful expansion of the isolation membrane. This is in line with our proteomics data of endogenous Atg9 vesicles. Faa1 is targeted to autophagosomes downstream of the core autophagic machinery. By locally activating fatty acids that are subsequently channeled into the lipid synthesis pathway at the ER, Faa1 might trigger the necessary lipid transfer directionality of the newly synthesized proteins from the ER via Atg2 into the isolation membrane. To make sure that the freshly imported phospholipids are not travelling back through Atg2, Atg8 lipidation, PI3P production or so far unknown mechanisms at the expanding isolation membrane might retain the lipids and thereby facilitate autophagosomal growth.

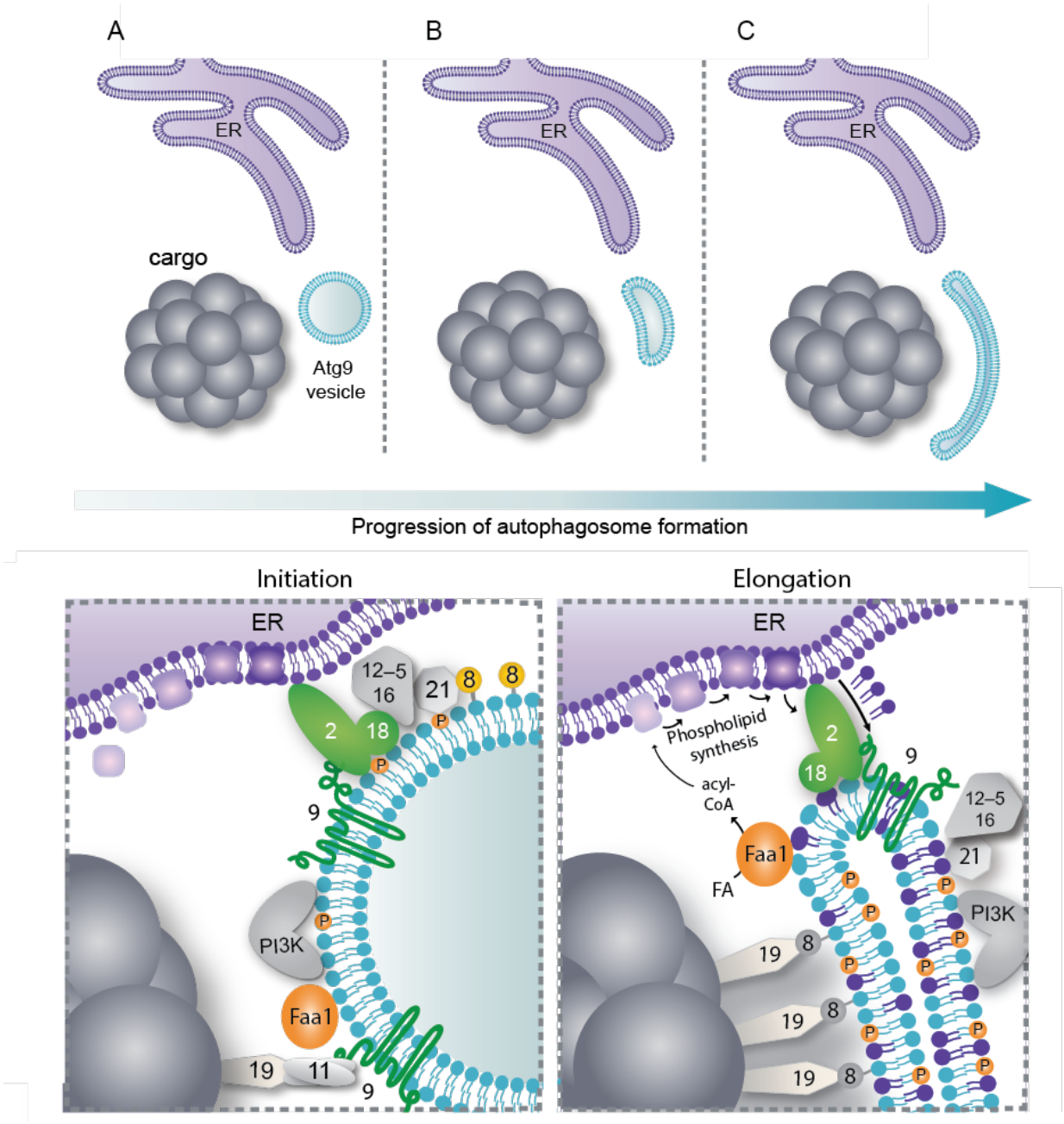

Figure *3*: Model for isolation membrane initiation and elongation.

Initiation: Atg9 vesicles are recruited to the cargo via the prApe1-Atg19-Atg11 axis. Upon generation of PI3P by the PI3KC3-C1 the further downstream factors Atg21 and Atg12–Atg5-Atg16 are assembled leading to Atg8–PE conjugation.

Elongation: Localization of Faa1 to the isolation membrane leads to fatty acid activation, which are then channeled into the local lipid synthesis on the ER side. Recruitment of Atg2-Atg18 catalyses lipid transfer from the ER and hands them over to the lipid scramblase Atg9, that re-establishes phospholipid balance between the outer and inner leaflet. Concomitant Atg8 conjugation and lipid transfer lead to the expansion of the vesicle surface, while the lumenal volume remains constant, resulting in vesicle flattening and expansion around the cargo.

References

Agarraberes, F. A., Terlecky, S. R., & Dice, J. F. (1997). An Intralysosomal hsp70 Is Required for a Selective Pathway of Lysosomal Protein Degradation. In *The Journal of Cell Biology* (Vol. 137, Issue 4). http://rupress.org/jcb/article-pdf/137/4/825/1269318/14318.pdf

Araki, Y., Ku, W. C., Akioka, M., May, A. I., Hayashi, Y., Arisaka, F., Ishihama, Y., & Ohsumi, Y. (2013). Atg38 is required for autophagy-specific phosphatidylinositol 3-kinase complex integrity. *Journal of Cell Biology*, *203*(2), 299–313. https://doi.org/10.1083/jcb.201304123

Ashford, T. P., & Porter, K. R. (1962). Cytoplasmic components in hepatic cell lysosomes. *The Journal of Cell Biology*. https://doi.org/10.1083/jcb.12.1.198

Axe, E. L., Walker, S. A., Manifava, M., Chandra, P., Roderick, H. L., Habermann, A., Griffiths, G., & Ktistakis, N. T. (2008). Autophagosome formation from membrane compartments enriched in phosphatidylinositol 3-phosphate and dynamically connected to the endoplasmic reticulum. *Journal of Cell Biology*. https://doi.org/10.1083/jcb.200803137

Baba, M., Osumi, M., Scott, S. v., Klionsky, D. J., & Ohsumi, Y. (1997). Two distinct pathways for targeting proteins from the cytoplasm to the vacuole/lysosome. *Journal of Cell Biology*, *139*(7), 1687–1695. https://doi.org/10.1083/jcb.139.7.1687

Baba, M., Takeshige, K., Baba, N., & Ohsumi, Y. (1994). Ultrastructural analysis of the autophagic process in yeast: Detection of autophagosomes and their characterization. *Journal of Cell Biology*. https://doi.org/10.1083/jcb.124.6.903

Backues, S. K., Orban, D. P., Bernard, A., Singh, K., Cao, Y., & Klionsky, D. J. (2015). Atg23 and Atg27 Act at the Early Stages of Atg9 Trafficking in S. cerevisiae. *Traffic*, *16*(2), 172–190. https://doi.org/10.1111/tra.12240

Bandyopadhyay, U., Kaushik, S., Varticovski, L., & Cuervo, A. M. (2008). The Chaperone-Mediated Autophagy Receptor Organizes in Dynamic Protein Complexes at the Lysosomal Membrane. *Molecular and Cellular Biology*, *28*(18), 5747–5763. https://doi.org/10.1128/mcb.02070-07

Barth, H., Meiling-Wesse, K., Epple, U. D., & Thumm, M. (2001). Autophagy and the cytoplasm to vacuole targeting pathway both require Aut10p. *FEBS Letters*, *508*(1), 23–28. https://doi.org/10.1016/S0014-5793(01)03016-2

Baskaran, S., Ragusa, M. J., Boura, E., & Hurley, J. H. (2012). Two-Site Recognition of Phosphatidylinositol 3-Phosphate by PROPPINs in Autophagy. *Molecular Cell*, *47*(3), 339–348. https://doi.org/10.1016/j.molcel.2012.05.027

Birgisdottir, Å. B., Lamark, T., & Johansen, T. (2013). The LIR motif - crucial for selective autophagy. In *Journal of Cell Science* (Vol. 126, Issue 15, pp. 3237–3247). https://doi.org/10.1242/jcs.126128

Busse, R. A., Scacioc, A., Krick, R., Pérez-Lara, Á., Thumm, M., & Kühnel, K. (2015). Characterization of PROPPIN-phosphoinositide binding and role of loop 6CD in PROPPIN-membrane binding. *Biophysical Journal*, *108*(9), 2223–2234. https://doi.org/10.1016/j.bpj.2015.03.045

Chavez-Dominguez, R., Perez-Medina, M., Lopez-Gonzalez, J. S., Galicia-Velasco, M., & Aguilar-Cazares, D. (2020). The Double-Edge Sword of Autophagy in Cancer: From Tumor Suppression to Pro-tumor Activity. *Frontiers in Oncology*, *10*(October), 1–19. https://doi.org/10.3389/fonc.2020.578418

Chew, L. H., Setiaputra, D., Klionsky, D. J., & Yip, C. K. (2013). Structural characterization of the Saccharomyces cerevisiae autophagy regulatory complex Atg17-Atg31-Atg29. *Autophagy*, *9*(10), 1467–1474. https://doi.org/10.4161/auto.25687

Chiang, H.-L., Terlecky, S. R., Plant, C. P., & Dice, J. F. (1989). A Role for a 70-Kilodalton Heat Shock Protein in Lysosomal Degradation of Intracellular Proteins. *Science*, *246*(4928), 382–385. https://doi.org/10.1126/science.2799391

Chowdhury, S., Otomo, C., Leitner, A., Ohashi, K., Aebersold, R., Lander, G. C., & Otomo, T. (2018). Insights into autophagosome biogenesis from structural and biochemical analyses of the ATG2A-WIPI4 complex. *Proceedings of the National Academy of Sciences of the United States of America*, *115*(42), E9792–E9801. https://doi.org/10.1073/pnas.1811874115

Crotzer, V. L., & Janice, S. (2010). *Autophagy and adaptive immunity*. 9–17. https://doi.org/10.1111/j.1365-2567.2010.03321.x

Cuervo, A. M., & Dice, J. F. (1996). A Receptor for the Selective Uptake and Degradation of Proteins by Lysosomes. *Science*, *273*(5274), 501–503. https://doi.org/10.1126/science.273.5274.501

Cuervo, A. M., & Wong, E. (2014). Chaperone-mediated autophagy: Roles in disease and aging. *Cell Research*, *24*(1), 92–104. https://doi.org/10.1038/cr.2013.153

Dooley, H. C., Razi, M., Polson, H. E. J., Girardin, S. E., Wilson, M. I., & Tooze, S. A. (2014). WIPI2 Links LC3 Conjugation with PI3P, Autophagosome Formation, and Pathogen Clearance by Recruiting Atg12–5-16L1. *Molecular Cell*, *55*(2), 238–252. https://doi.org/10.1016/j.molcel.2014.05.021

Dove, S. K., Piper, R. C., McEwen, R. K., Yu, J. W., King, N. C., Hughes, D. C., Thuring, J., Holmes, A. B., Cooke, F. T., Michell, R. H., Parker, P. J., & Lemmon, M. A. (2004). Svp1p defines a family of phosphatidylinositol 3,5-bisphosphate effectors. *EMBO Journal*, *23*(9), 1922–1933. https://doi.org/10.1038/sj.emboj.7600203

Efe, J. A., Botelho, R. J., & Emr, S. D. (2007). Atg18 Regulates Organelle Morphology and Fab1 Kinase Activity Independent of Its Membrane Recruitment by Phosphatidylinositol 3,5-Bisphosphate. *Molecular Biology of the Cell*, *18*(November), 4232–4244. https://doi.org/10.1091/mbc.E07

Feng, Y., He, D., Yao, Z., & Klionsky, D. J. (2014). The machinery of macroautophagy. *Cell Research*, *24*(1), 24–41. https://doi.org/10.1038/cr.2013.168

Fengsrud, M., Erichsen, E. S., Berg, T. O., Raiborg, C., & Seglen, O. (2000). Ultrastructural characterization of the delimiting membranes of isolated autophagosomes and amphisomes by freeze-fracture electron microscopy. In *European Journal of Cell Biology* (Vol. 79). http:/www.urbanfîscher.de/journals/ejcb

Fujioka, Y., Noda, N. N., Nakatogawa, H., Ohsumi, Y., & Inagaki, F. (2010). Dimeric coiled-coil structure of saccharomyces cerevisiae Atg16 and its functional significance in autophagy. *Journal of Biological Chemistry*, *285*(2), 1508–1515. https://doi.org/10.1074/jbc.M109.053520

Ganley, I. G., Lam, D. H., Wang, J., Ding, X., Chen, S., & Jiang, X. (2009). ULK1·ATG13·FIP200 complex mediates mTOR signaling and is essential for autophagy. *Journal of Biological Chemistry*, *284*(18), 12297–12305. https://doi.org/10.1074/jbc.M900573200

Gómez-Sánchez, R., Rose, J., Guimarães, R., Mari, M., Papinski, D., Rieter, E., Geerts, W. J., Hardenberg, R., Kraft, C., Ungermann, C., & Reggiori, F. (2018). Atg9 establishes Atg2-dependent contact sites between the endoplasmic reticulum and phagophores. *Journal of Cell Biology*, *217*(8), 2743–2763. https://doi.org/10.1083/jcb.201710116

Gopaldass, N., Fauvet, B., Lashuel, H., Roux, A., & Mayer, A. (2017). Membrane scission driven by the PROPPIN Atg18. *The EMBO Journal*. https://doi.org/10.15252/embj.201796859

Graef, M., Friedman, J. R., Graham, C., Babu, M., & Nunnari, J. (2013). ER exit sites are physical and functional core autophagosome biogenesis components. *Molecular Biology of the Cell*. https://doi.org/10.1091/mbc.E13-07-0381

Guan, J., Stromhaug, P. E., George, M. D., Habibzadegah-Tari, P., Bevan, A., Dunn, J., & Klionsky, D. J. (2001). Cvt18/Gsa12 is required for cytoplasm-to-vacuole transport, pexophagy, and autophagy in Saccharomyces cerevisiae and Pichia pastoris. *Molecular Biology of the Cell*, *12*(12), 3821–3838. https://doi.org/10.1091/mbc.12.12.3821

Guardia, C. M., Tan, X. F., Lian, T., Rana, M. S., Zhou, W., Christenson, E. T., Lowry, A. J., Faraldo-Gómez, J. D., Bonifacino, J. S., Jiang, J., & Banerjee, A. (2020). Structure of Human ATG9A, the Only Transmembrane Protein of the Core Autophagy Machinery. *Cell Reports*, *31*(13). https://doi.org/10.1016/j.celrep.2020.107837

Gubas, A., & Dikic, I. (2021). A Guide To… The regulation of selective autophagy receptors. *FEBS Journal*, *3*, 1–15. https://doi.org/10.1111/febs.15824

Hanada, T., Noda, N. N., Satomi, Y., Ichimura, Y., Fujioka, Y., Takao, T., Inagaki, F., & Ohsumi, Y. (2007). The Atg12-Atg5 conjugate has a novel E3-like activity for protein lipidation in autophagy. *Journal of Biological Chemistry*. https://doi.org/10.1074/jbc.C700195200

Hara, T., Takamura, A., Kishi, C., Iemura, S. I., Natsume, T., Guan, J. L., & Mizushima, N. (2008). FIP200, a ULK-interacting protein, is required for autophagosome formation in mammalian cells. *Journal of Cell Biology*, *181*(3), 497–510. https://doi.org/10.1083/jcb.200712064

Harada, K., Kotani, T., Kirisako, H., Sakoh-Nakatogawa, M., Oikawa, Y., Kimura, Y., Hirano, H., Yamamoto, H., Ohsumi, Y., & Nakatogawa, H. (2019). Two distinct mechanisms target the autophagy-related e3 complex to the pre-autophagosomal structure. *ELife*. https://doi.org/10.7554/eLife.43088

Harding, T. M., Morano, K. A., Scott, S. V, & Klionsky, D. J. (1995). Isolation and Characterization of Yeast Mutants in the Cytoplasm to Vacuole Protein Targeting Pathway. *The Journal of Cell Biology*, *131*(3), 591–602.

He, C., Song, H., Yorimitsu, T., Monastyrska, I., Yen, W. L., Legakis, J. E., & Klionsky, D. J. (2006). Recruitment of Atg9 to the preautophagosomal structure by Atg11 is essential for selective autophagy in budding yeast. *Journal of Cell Biology*, *175*(6), 925–935. https://doi.org/10.1083/jcb.200606084

Hosokawa, N., Hara, T., Kaizuka, T., Kishi, C., Takamura, A., Miura, Y., Iemura, S.-I., Natsume, T., Takehana, K., Yamada, N., Guan, J.-L., Oshiro, N., Mizushima, N., & Schmid, S. L. (1981). Nutrient-dependent mTORC1 Association with the ULK1-Atg13-FIP200 Complex Required for Autophagy. *Molecular Biology of the Cell*, *20*. https://doi.org/10.1091/mbc.E08

Hwa Jung, C., Bong Jun, C., Ro, S.-H., Kim, Y.-M., Michael Otto, N., Cao, J., Kundu, M., Kim, D.-H., & Schmid, S. L. (1992). ULK-Atg13-FIP200 Complexes Mediate

mTOR Signaling to the Autophagy Machinery. *Molecular Biology of the Cell*, *20*. https://doi.org/10.1091/mbc.E08

Ichimura, Y., Kirisako, T., Takao, T., Satomi, Y., Shimonishi, Y., Ishihara, N., Mizushima, N., Tanida, I., Kominami, E., Ohsumi, M., Noda, T., & Ohsumi, Y. (2000). A ubiquitin-like system mediates protein lipidation. *Nature*. https://doi.org/10.1038/35044114

Ishihara, N., Hamasaki, M., Yokota, S., Suzuki, K., Kamada, Y., Kihara, A., Yoshimori, T., Noda, T., & Ohsumi, Y. (2001). Autophagosome Requires Specific Early Sec Proteins for Its Formation and NSF/SNARE for Vacuolar Fusion. In *Molecular Biology of the Cell* (Vol. 12).

Jensen, D., & Schekman, R. (2011). COPII-mediated vesicle formation at a glance. In *Journal of Cell Science* (Vol. 124, Issue 1, pp. 1–4). https://doi.org/10.1242/jcs.069773

Jumper, J., Evans, R., Pritzel, A., Green, T., Figurnov, M., Ronneberger, O., Tunyasuvunakool, K., Bates, R., Žídek, A., Potapenko, A., Bridgland, A., Meyer, C., Kohl, S. A. A., Ballard, A. J., Cowie, A., Romera-Paredes, B., Nikolov, S., Jain, R., Adler, J., … Hassabis, D. (2021). Highly accurate protein structure prediction with AlphaFold. *Nature*, *596*(7873), 583–589. https://doi.org/10.1038/s41586-021-03819-2

Juris, L., Montino, M., Rube, P., Schlotterhose, P., Thumm, M., & Krick, R. (2015). PI 3P binding by Atg21 organises Atg8 lipidation. *The EMBO Journal*. https://doi.org/10.15252/embj.201488957

Kabeya, Y., Kamada, Y., Baba, M., Takikawa, H., Sasaki, M., & Ohsumi, Y. (2005). Atg17 functions in cooperation with Atg1 and Atg13 in yeast autophagy. *Molecular Biology of the Cell*, *16*(5), 2544–2553. https://doi.org/10.1091/mbc.e04-08-0669

Kabeya, Y., Noda, N. N., Fujioka, Y., Suzuki, K., Inagaki, F., & Ohsumi, Y. (2009). Characterization of the Atg17-Atg29-Atg31 complex specifically required for starvation-induced autophagy in Saccharomyces cerevisiae. *Biochemical and Biophysical Research Communications*, *389*(4), 612–615. https://doi.org/10.1016/j.bbrc.2009.09.034

Kabeya Y1, Mizushima N, Ueno T, Yamamoto A, Kirisako T, Noda T, Kominami E, Ohsumi Y, Y. T. (2000). LC3, a mammalian homologue of yeast Apg8p, is localized in autophagosome membranes after processing. *The EMBO Journal*, *19*(21), 5720–5728. https://doi.org/10.1093/emboj/19.21.5720

Kamada, Y., Funakoshi, T., Shintani, T., Nagano, K., Ohsumi, M., & Ohsumi, Y. (2000). Tor-mediated induction of autophagy via an Apg1 protein kinase complex. *Journal of Cell Biology*, *150*(6), 1507–1513. https://doi.org/10.1083/jcb.150.6.1507

Kamada, Y., Yoshino, K., Kondo, C., Kawamata, T., Oshiro, N., Yonezawa, K., & Ohsumi, Y. (2010). Tor Directly Controls the Atg1 Kinase Complex To Regulate Autophagy. *Molecular and Cellular Biology*, *30*(4), 1049–1058. https://doi.org/10.1128/mcb.01344-09

Kamber, R. A., Shoemaker, C. J., & Denic, V. (2015). Receptor-Bound Targets of Selective Autophagy Use a Scaffold Protein to Activate the Atg1 Kinase. *Molecular Cell*, *59*(3), 372–381. https://doi.org/10.1016/j.molcel.2015.06.009

Katheder, N. S., Khezri, R., O'Farrell, F., Schultz, S. W., Jain, A., Schink, M. K. O., Theodossiou, T. A., Johansen, T., Juhász, G., Bilder, D., Brech, A., Stenmark, H., & Rusten, T. E. (2017). Microenvironmental autophagy promotes tumour growth. *Nature*, *541*(7637), 417–420. https://doi.org/10.1038/nature20815

Kaushik, S., Bandyopadhyay, U., Sridhar, S., Kiffin, R., Martinez-Vicente, M., Kon, M., Orenstein, S. J., Wong, E., & Cuervo, A. M. (2011). Chaperone-mediated autophagy at a glance. *Journal of Cell Science*, *124*(4), 495–499. https://doi.org/10.1242/jcs.073874

Kawabata, T., & Yoshimori, T. (2020). Autophagosome biogenesis and human health. *Cell Discovery*, *6*(1). https://doi.org/10.1038/s41421-020-0166-y

Khandia, R., Dadar, M., Munjal, A., Dhama, K., Karthik, K., Tiwari, R., Yatoo, Mohd. I., Iqbal, H. M. N., Singh, K. P., Joshi, S. K., & Chaicumpa, W. (2019). A Comprehensive Review of Autophagy and Its Various Roles in Infectious, Non-Infectious, and Lifestyle Diseases: Current Knowledge and Prospects for Disease Prevention, Novel Drug Design, and Therapy. *Cells*. https://doi.org/10.3390/cells8070674

Khezri, R., Holland, P., Schoborg, T. A., Abramovich, I., Takáts, S., Dillard, C., Jain, A., O'Farrell, F., Schultz, S. W., Hagopian, W. M., Quintana, E. M., Ng, R., Katheder, N. S., Rahman, M. M., Teles Reis, J. G., Brech, A., Jasper, H., Rusan, N. M., Jahren, A. H., … Rusten, T. E. (2021). Host autophagy mediates organ wasting and nutrient mobilization for tumor growth. *The EMBO Journal*, *40*(18). https://doi.org/10.15252/embj.2020107336

Kihara, A., Noda, T., Ishihara, N., & Ohsumi, Y. (2001). Two distinct Vps34 phosphatidylinositol 3-kinase complexes function in autophagy and carboxypeptidase y sorting in Saccharomyces cerevisiae. *Journal of Cell Biology*. https://doi.org/10.1083/jcb.152.3.519

Kim, J., Dalton, V. M., Eggerton, K. P., Scott, S. V., & Klionsky, D. J. (1999). Apg7p/Cvt2p is required for the cytoplasm-to-vacuole targeting, macroautophagy, and peroxisome degradation pathways. *Molecular Biology of the Cell*, *10*(5), 1337–1351. https://doi.org/10.1091/mbc.10.5.1337

Kim, J., Kamada, Y., Strømhaug, P., Guan, J., Hefner-Gravink, A., Baba, M., Scott, S., Ohsumi, Y., Dunn, W., & Klionsky, D. (2001). Cvt9/Gsa9 Functions in Sequestering Selective Cytosolic Cargo Destined for the Vacuole. *The Journal of Cell Biology*, *153*, 381–396. https://doi.org/10.1083/jcb.153.2.381

Kim, J., Scott, S. V., Oda, M. N., & Klionsky, D. J. (1997). Transport of a large oligomeric protein by the cytoplasm to vacuole protein targeting pathway. *Journal of Cell Biology*, *137*(3), 609–618. https://doi.org/10.1083/jcb.137.3.609

Kirisako, T., Baba, M., Ishihara, N., Miyazawa, K., Ohsumi, M., Yoshimori, T., Noda, T., & Ohsumi, Y. (1999). Formation process of autophagosome is traced with Apg8/Aut7p in yeast. *Journal of Cell Biology*, *147*(2), 435–446. https://doi.org/10.1083/jcb.147.2.435

Kirisako, T., Ichimura, Y., Okada, H., Kabeya, Y., Mizushima, N., Yoshimori, T., Ohsumi, M., Takao, T., Noda, T., & Ohsumi, Y. (2000). The reversible modification regulates the membrane-binding state of Apg8/Aut7 essential for autophagy and the cytoplasm to vacuole targeting pathway. *Journal of Cell Biology*, *151*(2), 263–275. https://doi.org/10.1083/jcb.151.2.263

Kirkin, V., & Rogov, V. V. (2019). A Diversity of Selective Autophagy Receptors Determines the Specificity of the Autophagy Pathway. *Molecular Cell*, *76*(2), 268–285. https://doi.org/10.1016/j.molcel.2019.09.005

Klionsky, D. J., Cregg, J. M., Dunn, W. A., Emr, S. D., Sakai, Y., Sandoval, I. V., Sibirny, A., Subramani, S., Thumm, M., Veenhuis, M., & Ohsumi, Y. (2003). A unified nomenclature for yeast autophagy-related genes. *Developmental Cell*, *5*(4), 539–545. https://doi.org/10.1016/S1534-5807(03)00296-X

Kotani, T., Kirisako, H., Koizumi, M., Ohsumi, Y., & Nakatogawa, H. (2018). The Atg2-Atg18 complex tethers pre-autophagosomal membranes to the endoplasmic reticulum for autophagosome formation. *Proceedings of the National Academy of Sciences of the United States of America*. https://doi.org/10.1073/pnas.1806727115

Kraft, C., Kijanska, M., Kalie, E., Siergiejuk, E., Lee, S. S., Semplicio, G., Stoffel, I., Brezovich, A., Verma, M., Hansmann, I., Ammerer, G., Hofmann, K., Tooze, S., & Peter, M. (2012). Binding of the Atg1/ULK1 kinase to the ubiquitin-like protein Atg8 regulates autophagy. *EMBO Journal*, *31*(18), 3691–3703. https://doi.org/10.1038/emboj.2012.225

Krick, R., Busse, R. A., Scacioc, A., Stephan, M., Janshoff, A., Thumm, M., & Kühnel, K. (2012). Structural and functional characterization of the two phosphoinositide binding sites of PROPPINs, a β-propeller protein family. *Proceedings of the National Academy of Sciences of the United States of America*, *109*(30). https://doi.org/10.1073/pnas.1205128109

Krick, R., Muehe, Y., Prick, T., Bremer, S., Schlotterhose, P., Eskelinen, E.-L., Millen, J., Goldfarb, D. S., & Thumm, M. (2008). Piecemeal Microautophagy of the Nucleus Requires the Core Macroautophagy Genes. *Molecular Biology of the Cell*, *19*(10), 4492–4505. https://doi.org/10.1091/mbc.e08-04-0363

Krick, R., & Thumm, M. (2016). Atg8 lipidation is coordinated in a PtdIns3P-dependent manner by the PROPPIN Atg21. *Autophagy*, *12*(11), 2260–2261. https://doi.org/10.1080/15548627.2016.1221564

Krick, R., Tolstrup, J., Appelles, A., Henke, S., & Thumm, M. (2006). The relevance of the phosphatidylinositolphosphat-binding motif FRRGT of Atg18 and Atg21 for the Cvt pathway and autophagy. *FEBS Letters*, *580*(19), 4632–4638. https://doi.org/10.1016/j.febslet.2006.07.041

Kuma, A., Komatsu, M., & Mizushima, N. (2017). Autophagy-monitoring and autophagy-deficient mice. *Autophagy*, *13*(10), 1619–1628. https://doi.org/10.1080/15548627.2017.1343770

Kuma, A., Mizushima, N., Ishihara, N., & Ohsumi, Y. (2002). Formation of the ~350-kDa Apg12-Apg5·Apg16 multimeric complex, mediated by Apg16 oligomerization, is essential for autophagy in yeast. *Journal of Biological Chemistry*, *277*(21), 18619–18625. https://doi.org/10.1074/jbc.M111889200

Kumar, N., Leonzino, M., Hancock-Cerutti, W., Horenkamp, F. A., Li, P. Q., Lees, J. A., Wheeler, H., Reinisch, K. M., & De Camilli, P. (2018). VPS13A and VPS13C are lipid transport proteins differentially localized at ER contact sites. *The Journal of Cell Biology*. https://doi.org/10.1083/jcb.201807019

Kumeta, H., Watanabe, M., Nakatogawa, H., Yamaguchi, M., Ogura, K., Adachi, W., Fujioka, Y., Noda, N. N., Ohsumi, Y., & Inagaki, F. (2010). The NMR structure of the autophagy-related protein Atg8. *Journal of Biomolecular NMR*, *47*(3), 237–241. https://doi.org/10.1007/s10858-010-9420-1

Kundu, M., Lindsten, T., Yang, C. Y., Wu, J., Zhao, F., Zhang, J., Selak, M. A., Ney, P. A., & Thompson, C. B. (2008). Ulk1 plays a critical role in the autophagic clearance of mitochondria and ribosomes during reticulocyte maturation. *Blood*, *112*(4), 1493–1502. https://doi.org/10.1182/blood-2008-02-137398

Lai, L. T. F., Yu, C., Wong, J. S. K., Lo, H. S., Benlekbir, S., Jiang, L., & Lau, W. C. Y. (2020). Subnanometer resolution cryo-EM structure of Arabidopsis thaliana ATG9. *Autophagy*, *16*(3), 575–583. https://doi.org/10.1080/15548627.2019.1639300

Lang, T., Reiche, S., Straub, M., Bredschneider, M., & Thumm, M. (2000). Autophagy and the cvt pathway both depend on AUT9. *Journal of Bacteriology*, *182*(8), 2125–2133. https://doi.org/10.1128/JB.182.8.2125-2133.2000

Lang, T., Schaeffeler, E., Bernreuther, D., Bredschneider, M., Wolf, D. H., & Thumm, M. (1998). Aut2p and Aut7p, two novel microtubule-associated proteins are essential for delivery of autophagic vesicles to the vacuole. *EMBO Journal*, *17*(13), 3597–3607. https://doi.org/10.1093/emboj/17.13.3597

Legakis, J. E., Yen, W. L., & Klionsky, D. J. (2007). A cycling protein complex required for selective autophagy. *Autophagy*, *3*(5), 422–432. https://doi.org/10.4161/auto.4129

Levine, B., & Kroemer, G. (2008). Autophagy in the Pathogenesis of Disease. In *Cell*. https://doi.org/10.1016/j.cell.2007.12.018

Levine, B., & Kroemer, G. (2019). Biological Functions of Autophagy Genes: A Disease Perspective. In *Cell*. https://doi.org/10.1016/j.cell.2018.09.048

Li, P. Q., Lees, J. A., Lusk, C. P., & Reinisch, K. M. (2020). Cryo-EM reconstruction of a VPS13 fragment reveals a long groove to channel lipids between membranes. *The Journal of Cell Biology*. https://doi.org/10.1083/jcb.202001161

Li, W. W., Li, J., & Bao, J. K. (2012). Microautophagy: Lesser-known self-eating. *Cellular and Molecular Life Sciences*, *69*(7), 1125–1136. https://doi.org/10.1007/s00018-011-0865-5

Lynch-Day, M. A., & Klionsky, D. J. (2010). The Cvt pathway as a model for selective autophagy. *FEBS Letters*, *584*(7), 1359–1366. https://doi.org/10.1016/j.febslet.2010.02.013

Maeda, S., Otomo, C., & Otomo, T. (2019). The autophagic membrane tether ATG2A transfers lipids between membranes. *ELife*, *8*, 1–24. https://doi.org/10.7554/eLife.45777

Maeda, S., Yamamoto, H., Kinch, L. N., Garza, C. M., Takahashi, S., Otomo, C., Grishin, N. V., Forli, S., Mizushima, N., & Otomo, T. (2020). Structure, lipid scrambling activity and role in autophagosome formation of ATG9A. *Nature Structural and Molecular Biology*, *27*(12), 1194–1201. https://doi.org/10.1038/s41594-020-00520-2

Martens, S. (2016). No ATG8s, no problem? How LC3/GAB ARAP proteins contribute to autophagy. *Journal of Cell Biology*, *215*(6), 761–763. https://doi.org/10.1083/jcb.201611116

Martens, S., & Fracchiolla, D. (2020). Activation and targeting of ATG8 protein lipidation. In *Cell Discovery*. https://doi.org/10.1038/s41421-020-0155-1

Matoba, K., Kotani, T., Tsutsumi, A., Tsuji, T., Mori, T., Noshiro, D., Sugita, Y., Nomura, N., Iwata, S., Ohsumi, Y., Fujimoto, T., Nakatogawa, H., Kikkawa, M., & Noda, N. N. (2020). Atg9 is a lipid scramblase that mediates autophagosomal membrane expansion. *Nature Structural and Molecular Biology*. https://doi.org/10.1038/s41594-020-00518-w

Matscheko, N., Mayrhofer, P., Rao, Y., Beier, V., & Wollert, T. (2019). Atg11 tethers Atg9 vesicles to initiate selective autophagy. *PLoS Biology*. https://doi.org/10.1371/journal.pbio.3000377

Matsushita, M., Suzuki, N. N., Obara, K., Fujioka, Y., Ohsumi, Y., & Inagaki, F. (2007). Structure of Atg5·Atg16, a complex essential for autophagy. *Journal of Biological Chemistry*, *282*(9), 6763–6772. https://doi.org/10.1074/jbc.M609876200

Matsuura, A., Tsukada, M., Wada, Y., & Ohsumi, Y. (1997). Apg1p, a novel protein kinase required for the autophagic process in Saccharomyces cerevisiae. *Gene*, *192*(2), 245–250. https://doi.org/10.1016/S0378-1119(97)00084-X

Mizushima, N. (2010). The role of the Atg1/ULK1 complex in autophagy regulation. *Current Opinion in Cell Biology*, *22*(2), 132–139. https://doi.org/10.1016/j.ceb.2009.12.004

Mizushima, N., & Komatsu, M. (2011). Autophagy: Renovation of cells and tissues. In *Cell*. https://doi.org/10.1016/j.cell.2011.10.026

Mizushima, N., & Levine, B. (2010). Autophagy in mammalian development and differentiation. In *Nature Cell Biology*. https://doi.org/10.1038/ncb0910-823

Mizushima, N., Noda, T., & Ohsumi, Y. (1999). Apg16p is required for the function of the Apg12p-Apg5p conjugate in the yeast autophagy pathway. In *The EMBO Journal* (Vol. 18, Issue 14). http://www.isrec.isb-sib.ch/

Mizushima, N., Noda, T., Yoshimori, T., Tanaka, Y., Ishii, T., George, M. D., Klionsky, D. J., Ohsumi, M., & Ohsumi, Y. (1998). A protein conjugation system essential for autophagy. *Nature*, *395*(6700), 395–398. https://doi.org/10.1038/26506

Mochida, K., Oikawa, Y., Kimura, Y., Kirisako, H., Hirano, H., Ohsumi, Y., & Nakatogawa, H. (2015). Receptor-mediated selective autophagy degrades the endoplasmic reticulum and the nucleus. *Nature*, *522*(7556), 359–362. https://doi.org/10.1038/nature14506

Motley, A. M., Nuttall, J. M., & Hettema, E. H. (2012). Pex3-anchored Atg36 tags peroxisomes for degradation in Saccharomyces cerevisiae. *EMBO Journal*, *31*(13), 2852–2868. https://doi.org/10.1038/emboj.2012.151

Nair, U., Yen, W. L., Mari, M., Cao, Y., Xie, Z., Baba, M., Reggiori, F., & Klionsky, D. J. (2012). A role for Atg8-PE deconjugation in autophagosome biogenesis. *Autophagy*, *8*(5), 780–793. https://doi.org/10.4161/auto.19385

Nakatogawa, H., Ichimura, Y., & Ohsumi, Y. (2007). Atg8, a Ubiquitin-like Protein Required for Autophagosome Formation, Mediates Membrane Tethering and Hemifusion. *Cell*, *130*(1), 165–178. https://doi.org/10.1016/j.cell.2007.05.021

Nascimbeni, A. C., Codogno, P., & Morel, E. (2017). Phosphatidylinositol-3-phosphate in the regulation of autophagy membrane dynamics. *FEBS Journal*, *284*(9), 1267–1278. https://doi.org/10.1111/febs.13987

Nguyen, T. N., Padman, B. S., Usher, J., Oorschot, V., Ramm, G., & Lazarou, M. (2016). Atg8 family LC3/GAB ARAP proteins are crucial for autophagosome-lysosome fusion but not autophagosome formation during PINK1/Parkin mitophagy and starvation. *Journal of Cell Biology*, *215*(6), 857–874. https://doi.org/10.1083/jcb.201607039

Nishimura, T., Tamura, N., Kono, N., Shimanaka, Y., Arai, H., Yamamoto, H., & Mizushima, N. (2017). Autophagosome formation is initiated at phosphatidylinositol synthase-enriched ER subdomains . *The EMBO Journal*, *36*(12), 1719–1735. https://doi.org/10.15252/embj.201695189

Noda, N. N., Kobayashi, T., Adachi, W., Fujioka, Y., Ohsumi, Y., & Inagaki, F. (2012). Structure of the novel C-terminal domain of vacuolar protein sorting 30/autophagy-related protein 6 and its specific role in autophagy. *Journal of Biological Chemistry*, *287*(20), 16256–16266. https://doi.org/10.1074/jbc.M112.348250

Noda, N. N., Kumeta, H., Nakatogawa, H., Satoo, K., Adachi, W., Ishii, J., Fujioka, Y., Ohsumi, Y., & Inagaki, F. (2008). Structural basis of target recognition by

Atg8/LC3 during selective autophagy. *Genes to Cells*, *13*(12), 1211–1218. https://doi.org/10.1111/j.1365-2443.2008.01238.x
Noda, T., Kim, J., Huang, W. P., Baba, M., Tokunaga, C., Ohsumi, Y., & Klionsky, D. J. (2000). Apg9p/Cvt7p is an integral membrane protein required for transport vesicle formation in the Cvt and autophagy pathways. *Journal of Cell Biology*, *148*(3), 465–479. https://doi.org/10.1083/jcb.148.3.465
Obara, K., Sekito, T., Niimi, K., & Ohsumi, Y. (2008). The Atg18-Atg2 complex is recruited to autophagic membranes via phosphatidylinositol 3-phosphate and exerts an essential function. *Journal of Biological Chemistry*. https://doi.org/10.1074/jbc.M803180200
Obara, K., Sekito, T., & Ohsumi, Y. (2006). Assortment of Phosphatidylinositol 3-Kinase Complexes—Atg14p Directs Association of Complex I to the Pre-autophagosomal Structure in Saccharomyces cerevisiae. *Molecular Biology of the Cell*, *17*(4), 1527–1539. https://doi.org/10.1091/mbc.e05-09-0841
Ohashi, Y., & Munro, S. (2010). Membrane delivery to the yeast autophagosome from the golgi-endosomal system. *Molecular Biology of the Cell*. https://doi.org/10.1091/mbc.E10-05-0457
Ohashi, Y., Tremel, S., & Williams, R. L. (2019). VPS34 complexes from a structural perspective. In *Journal of Lipid Research* (Vol. 60, Issue 2, pp. 229–241). American Society for Biochemistry and Molecular Biology Inc. https://doi.org/10.1194/jlr.R089490
Ohsumi, Y. (2014). Historical landmarks of autophagy research. *Cell Research*, *24*(1), 9–23. https://doi.org/10.1038/cr.2013.169
Okamoto, K., Kondo-Okamoto, N., & Ohsumi, Y. (2009). Mitochondria-Anchored Receptor Atg32 Mediates Degradation of Mitochondria via Selective Autophagy. *Developmental Cell*, *17*(1), 87–97. https://doi.org/10.1016/j.devcel.2009.06.013
Olsvik, H. L., Svenning, S., Abudu, Y. P., Brech, A., Stenmark, H., Johansen, T., & Mejlvang, J. (2019). Endosomal microautophagy is an integrated part of the autophagic response to amino acid starvation. In *Autophagy* (Vol. 15, Issue 1, pp. 182–183). Taylor and Francis Inc. https://doi.org/10.1080/15548627.2018.1532265
Orii, M., Tsuji, T., Ogasawara, Y., & Fujimoto, T. (2020). Transmembrane phospholipid translocation mediated by Atg9 is involved in autophagosome formation. *Journal of Cell Biology*, *220*(3). https://doi.org/10.1083/JCB.202009194
Orsi, A., Razi, M., Dooley, H. C., Robinson, D., Weston, A. E., Collinson, L. M., & Tooze, S. A. (2012). Dynamic and transient interactions of Atg9 with autophagosomes, but not membrane integration, are required for autophagy. *Molecular Biology of the Cell*. https://doi.org/10.1091/mbc.E11-09-0746
Osawa, T., Ishii, Y., & Noda, N. N. (2020). Human ATG2B possesses a lipid transfer activity which is accelerated by negatively charged lipids and WIPI4. *Genes to Cells*. https://doi.org/10.1111/gtc.12733
Osawa, T., Kotani, T., Kawaoka, T., Hirata, E., Suzuki, K., Nakatogawa, H., Ohsumi, Y., & Noda, N. N. (2019). Atg2 mediates direct lipid transfer between membranes for autophagosome formation. *Nature Structural and Molecular Biology*, *26*(4), 281–288. https://doi.org/10.1038/s41594-019-0203-4
Papinski, D., Schuschnig, M., Reiter, W., Wilhelm, L., Barnes, C. A., Maiolica, A., Hansmann, I., Pfaffenwimmer, T., Kijanska, M., Stoffel, I., Lee, S. S., Brezovich, A., Lou, J. H., Turk, B. E., Aebersold, R., Ammerer, G., Peter, M., & Kraft, C. (2014). Early Steps in Autophagy Depend on Direct Phosphorylation of Atg9 by

the Atg1 Kinase. *Molecular Cell*, *53*(3), 471–483. https://doi.org/10.1016/j.molcel.2013.12.011
Paz, Y., Elazar, Z., & Fass, D. (2000). Structure of GATE-16, membrane transport modulator and mammalian ortholog of autophagocytosis factor Aut7p. *Journal of Biological Chemistry*, *275*(33), 25445–25450. https://doi.org/10.1074/jbc.C000307200
Pfaffenwimmer, T., Reiter, W., Brach, T., Nogellova, V., Papinski, D., Schuschnig, M., Abert, C., Ammerer, G., Martens, S., & Kraft, C. (2014). Hrr25 kinase promotes selective autophagy by phosphorylating the cargo receptor A tg19. *EMBO Reports*. https://doi.org/10.15252/embr.201438932
Pfisterer, S. G., Bakula, D., Frickey, T., Cezanne, A., Brigger, D., Tschan, M. P., Robenek, H., & Proikas-Cezanne, T. (2014). Lipid droplet and early autophagosomal membrane targeting of Atg2A and Atg14L in human tumor cells. *Journal of Lipid Research*, *55*(7), 1267–1278. https://doi.org/10.1194/jlr.M046359
Proikas-Cezanne, T., Takacs, Z., Dönnes, P., & Kohlbacher, O. (2015). WIPI proteins: essential PtdIns3 P effectors at the nascent autophagosome. *Journal of Cell Science*, *150*, 207–217. https://doi.org/10.1242/jcs.146258
Randow, F., MacMicking, J. D., & James, L. C. (2013). Cellular self-defense: How cell-autonomous immunity protects against pathogens. In *Science* (Vol. 340, Issue 6133, pp. 701–706). American Association for the Advancement of Science. https://doi.org/10.1126/science.1233028
Rieter, E., Vinke, F., Bakula, D., Cebollero, E., Ungermann, C., Proikas-Cezanne, T., & Reggiori, F. (2013). Atg18 function in autophagy is regulated by specific sites within its β-propeller. *Journal of Cell Science*, *126*(2), 593–604. https://doi.org/10.1242/jcs.115725
Rostislavleva, K., Soler, N., Ohashi, Y., Zhang, L., Pardon, E., Burke, J. E., Masson, G. R., Johnson, C., Steyaert, J., Ktistakis, N. T., & Williams, R. L. (2015a). Structure and flexibility of the endosomal Vps34 complex reveals the basis of its function on membranes. *Science*, *350*(6257). https://doi.org/10.1126/science.aac7365
Rozenknop, A., Rogov, V. v., Rogova, N. Y., Löhr, F., Güntert, P., Dikic, I., & Dötsch, V. (2011). Characterization of the interaction of GABARAPL-1 with the LIR motif of NBR1. *Journal of Molecular Biology*, *410*(3), 477–487. https://doi.org/10.1016/j.jmb.2011.05.003
Saha, S., Panigrahi, D. P., Patil, S., & Bhutia, S. K. (2018). Autophagy in health and disease: A comprehensive review. *Biomedicine and Pharmacotherapy*, *104*(April), 485–495. https://doi.org/10.1016/j.biopha.2018.05.007
Sakoh-Nakatogawa, M., Matoba, K., Asai, E., Kirisako, H., Ishii, J., Noda, N. N., Inagaki, F., Nakatogawa, H., & Ohsumi, Y. (2013). Atg12-Atg5 conjugate enhances E2 activity of Atg3 by rearranging its catalytic site. *Nature Structural and Molecular Biology*, *20*(4), 433–439. https://doi.org/10.1038/nsmb.2527
Salvador, N., Aguado, C., Horst, M., & Knecht, E. (2000). Import of a cytosolic protein into lysosomes by chaperone-mediated autophagy depends on its folding state. *Journal of Biological Chemistry*, *275*(35), 27447–27456. https://doi.org/10.1074/jbc.M001394200
Sawa-Makarska, J., Abert, C., Romanov, J., Zens, B., Ibiricu, I., & Martens, S. (2014). Cargo binding to Atg19 unmasks additional Atg8 binding sites to mediate membrane-cargo apposition during selective autophagy. *Nature Cell Biology*, *16*(5), 425–433. https://doi.org/10.1038/ncb2935

Sawa-Makarska, J., Baumann, V., Coudevylle, N., von Bülow, S., Nogellova, V., Abert, C., Schuschnig, M., Graef, M., Hummer, G., & Martens, S. (2020). Reconstitution of autophagosome nucleation defines Atg9 vesicles as seeds for membrane formation. *Science*, *369*(6508). https://doi.org/10.1126/SCIENCE.AAZ7714

Schreiber, A., Collins, B. C., Davis, C., Enchev, R. I., Sedra, A., D'Antuono, R., Aebersold, R., & Peter, M. (2021). Multilayered regulation of autophagy by the Atg1 kinase orchestrates spatial and temporal control of autophagosome formation. *Molecular Cell*. https://doi.org/10.1016/j.molcel.2021.10.024

Schu, P. V, Takegawa, K., Fry, M. J., Stack, J. H., Michael, D., Schu, P. V, Takegawa, K., Fry, M. J., Stack, J. H., Waterfield, M. D., & Emr, S. D. (1993). *Phosphatidylinositol 3-Kinase Encoded by Yeast VPS34 Gene Essential for Protein Sorting Waterfield and Scott D . Emr Published by: American Association for the Advancement of Science Stable URL : http://www.jstor.org/stable/2881128 JSTOR is a not-for-pro*. *260*(5104), 88–91.

Schuck, S. (2020). Microautophagy – distinct molecular mechanisms handle cargoes of many sizes. *Journal of Cell Science*, *133*(17). https://doi.org/10.1242/jcs.246322

Schütter, M., Giavalisco, P., Brodesser, S., & Graef, M. (2020). Local Fatty Acid Channeling into Phospholipid Synthesis Drives Phagophore Expansion during Autophagy. *Cell*, 1–15. https://doi.org/10.1016/j.cell.2019.12.005

Scott, S. v., Baba, M., Ohsumi, Y., & Klionsky, D. J. (1997). Aminopeptidase I is targeted to the vacuole by a nonclassical vesicular mechanism. *Journal of Cell Biology*, *138*(1), 37–44. https://doi.org/10.1083/jcb.138.1.37

Scott, S. V, Guan, J., Hutchins, M. U., Kim, J., & Klionsky, D. J. (2001). Cvt19 Is a Receptor for the Cytoplasm-to-Vacuole Targeting Pathway. *Molecular Cell*, *7*(6), 1131–1141. https://doi.org/10.1016/S1097-2765(01)00263-5

Scott, S. V., Hefner-Gravink, A., Morano, K. A., Noda, T., Ohsumi, Y., & Klionsky, D. J. (1996). Cytoplasm-to-vacuole targeting and autophagy employ the same machinery to deliver proteins to the yeast vacuole. *Proceedings of the National Academy of Sciences of the United States of America*, *93*(22), 12304–12308. https://doi.org/10.1073/pnas.93.22.12304

Sekito, T., Kawamata, T., Ichikawa, R., Suzuki, K., & Ohsumi, Y. (2009). Atg17 recruits Atg9 to organize the pre-autophagosomal structure. *Genes to Cells*, *14*(5), 525–538. https://doi.org/10.1111/j.1365-2443.2009.01299.x

Shima, T., Kirisako, H., & Nakatogawa, H. (2019). COPII vesicles contribute to autophagosomal membranes. *Journal of Cell Biology*, *218*(5), 1503–1510. https://doi.org/10.1083/jcb.201809032

Shintani, T., & Klionsky, D. J. (2004). Cargo proteins facilitate the formation of transport vesicles in the cytoplasm to vacuole targeting pathway. *Journal of Biological Chemistry*, *279*(29), 29889–29894. https://doi.org/10.1074/jbc.M404399200

Shintani, T., Mizushima, N., Ogawa, Y., Matsuura, A., Noda, T., & Ohsumi, Y. (1999). Apg10p, a novel protein-conjugating enzyme essential for autophagy in yeast. *EMBO Journal*, *18*(19), 5234–5241. https://doi.org/10.1093/emboj/18.19.5234

Sousa, C. M., Biancur, D. E., Wang, X., Halbrook, C. J., Sherman, M. H., Zhang, L., Kremer, D., Hwang, R. F., Witkiewicz, A. K., Ying, H., Asara, J. M., Evans, R. M., Cantley, L. C., Lyssiotis, C. A., & Kimmelman, A. C. (2016). Pancreatic

stellate cells support tumour metabolism through autophagic alanine secretion. *Nature*, *536*(7617), 479–483. https://doi.org/10.1038/nature19084
Stack, J. H., DeWald, D. B., Takegawa, K., & Emr, S. D. (1995). Vesicle-mediated protein transport: Regulatory interactions between the Vps15 protein kinase and the Vps34 PtdIns 3-kinase essential for protein sorting to the vacuole in yeast. *Journal of Cell Biology*, *129*(2), 321–334. https://doi.org/10.1083/jcb.129.2.321
Stack, J. H., & Emr, S. D. (1994). Vps34p required for yeast vacuolar protein sorting is a multiple specificity kinase that exhibits both protein kinase and phosphatidylinositol-specific PI 3-kinase activities. *Journal of Biological Chemistry*, *269*(50), 31552–31562. https://doi.org/10.1016/s0021-9258(18)31729-0
Strømhaug, P. E., Reggiori, F., Guan, J., Wang, C.-W., & Klionsky, D. J. (2004). Atg21 Is a Phosphoinositide Binding Protein Required for Efficient Lipidation and Localization of Atg8 during Uptake of Aminopeptidase I by Selective Autophagy. *Molecular Biology of the Cell*, *15*(8), 3553–3566. https://doi.org/10.1091/mbc.e04-02-0147
Strong, L. M., Chang, C., Riley, J. F., Boecker, C. A., Flower, T. G., Buffalo, C. Z., Ren, X., Stavoe, A. K., Holzbaur, E. L., & Hurley, J. H. (2021). Structural basis for membrane recruitment of ATG16L1 by WIPI2 in autophagy. *ELIFE*. https://doi.org/10.7554/eLife
Suzuki, H., & Noda, N. N. (2018). Biophysical characterization of Atg11, a scaffold protein essential for selective autophagy in yeast. *FEBS Open Bio*. https://doi.org/10.1002/2211-5463.12355
Suzuki, K., Akioka, M., Kondo-Kakuta, C., Yamamoto, H., & Ohsumi, Y. (2013). Fine mapping of autophagy-related proteins during autophagosome formation in Saccharomyces cerevisiae. *Journal of Cell Science*, *126*(11), 2534–2544. https://doi.org/10.1242/jcs.122960
Suzuki, K., Kondo, C., Morimoto, M., & Ohsumi, Y. (2010). Selective transport of α-mannosidase by autophagic pathways: Identification of a novel receptor, Atg34p. *Journal of Biological Chemistry*, *285*(39), 30019–30025. https://doi.org/10.1074/jbc.M110.143511
Suzuki, K., Kubota, Y., Sekito, T., & Ohsumi, Y. (2007). Hierarchy of Atg proteins in pre-autophagosomal structure organization. *Genes to Cells*, *12*(2), 209–218. https://doi.org/10.1111/j.1365-2443.2007.01050.x
Suzuki, S. W., Yamamoto, H., Oikawa, Y., Kondo-Kakuta, C., Kimurac, Y., Hirano, H., & Ohsumi, Y. (2015). Atg13 HORMA domain recruits Atg9 vesicles during autophagosome formation. *Proceedings of the National Academy of Sciences of the United States of America*. https://doi.org/10.1073/pnas.1421092112
Taherbhoy, A. M., Tait, S. W., Kaiser, S. E., Williams, A. H., Deng, A., Nourse, A., Hammel, M., Kurinov, I., Rock, C. O., Green, D. R., & Schulman, B. A. (2011). Atg8 transfer from Atg7 to Atg3: A distinctive E1-E2 architecture and mechanism in the autophagy pathway. *Molecular Cell*, *44*(3), 451–461. https://doi.org/10.1016/j.molcel.2011.08.034
Tan, D., Cai, Y., Wang, J., Zhang, J., Menon, S., Chou, H. T., Ferro-Novick, S., Reinisch, K. M., & Walz, T. (2013). The em structure of the TRAPPIII complex leads to the identification of a requirement for COPII vesicles on the macroautophagy pathway. *Proceedings of the National Academy of Sciences of the United States of America*, *110*(48), 19432–19437. https://doi.org/10.1073/pnas.1316356110

Tanaka, C., Tan, L. J., Mochida, K., Kirisako, H., Koizumi, M., Asai, E., Sakoh-Nakatogawa, M., Ohsumi, Y., & Nakatogawa, H. (2014). Hrr25 triggers selective autophagy-related pathways by phosphorylating receptor proteins. *Journal of Cell Biology*, *207*(1), 91–105. https://doi.org/10.1083/jcb.201402128

Tanida, I., Mizushima, N., Kiyooka, M., Ohsumi, M., Ueno, T., Ohsumi, Y., & Kominami, E. (1999). Apg7p/Cvt2p: A novel protein-activating enzyme essential for autophagy. *Molecular Biology of the Cell*, *10*(5), 1367–1379. https://doi.org/10.1091/mbc.10.5.1367

Thumm, M., Egner, R., Koch, B., Schlumpberger, M., Straub, M., Veenhuis, M., & Wolf, D. H. (1994). Isolation of autophagocytosis mutants of Saccharomyces cerevisiae. *FEBS Letters*. https://doi.org/10.1016/0014-5793(94)00672-5

Torggler, R., Papinski, D., Brach, T., Bas, L., Schuschnig, M., Pfaffenwimmer, T., Rohringer, S., Matzhold, T., Schweida, D., Brezovich, A., & Kraft, C. (2016). Two Independent Pathways within Selective Autophagy Converge to Activate Atg1 Kinase at the Vacuole. *Molecular Cell*, *64*(2), 221–235. https://doi.org/10.1016/j.molcel.2016.09.008

Tsuboyama, K., Koyama-Honda, I., Sakamaki, Y., Koike, M., Morishita, H., & Mizushima, N. (2016a). The ATG conjugation systems are important for degradation of the inner autophagosomal membrane. *Science*, *354*(6315), 1036–1041. https://doi.org/10.1126/science.aaf6136

Tsukada, M., & Ohsumi, Y. (1993). Isolation and characterization of autophagy-defective mutants of Saccharomyces cerevisiae. *FEBS Letters*. https://doi.org/10.1016/0014-5793(93)80398-E

Tucker, K. A., Reggiori, F., Dunn, W. A., & Klionsky, D. J. (2003). Atg23 Is Essential for the Cytoplasm to Vacuole Targeting Pathway and Efficient Autophagy but Not Pexophagy. *Journal of Biological Chemistry*, *278*(48), 48445–48452. https://doi.org/10.1074/jbc.M309238200

Turco, E., Witt, M., Abert, C., Bock-Bierbaum, T., Su, M. Y., Trapannone, R., Sztacho, M., Danieli, A., Shi, X., Zaffagnini, G., Gamper, A., Schuschnig, M., Fracchiolla, D., Bernklau, D., Romanov, J., Hartl, M., Hurley, J. H., Daumke, O., & Martens, S. (2019). FIP200 Claw Domain Binding to p62 Promotes Autophagosome Formation at Ubiquitin Condensates. *Molecular Cell*, *74*(2), 330-346.e11. https://doi.org/10.1016/j.molcel.2019.01.035

Valverde, D. P., Yu, S., Boggavarapu, V., Kumar, N., Lees, J. A., Walz, T., Reinisch, K. M., & Melia, T. J. (2019). ATG2 transports lipids to promote autophagosome biogenesis. *Journal of Cell Biology*, *218*(6), 1787–1798. https://doi.org/10.1083/JCB.201811139

Velikkakath, A. K. G., Nishimura, T., Oita, E., Ishihara, N., & Mizushima, N. (2012). Mammalian Atg2 proteins are essential for autophagosome formation and important for regulation of size and distribution of lipid droplets. *Molecular Biology of the Cell*, *23*(5), 896–909. https://doi.org/10.1091/mbc.E11-09-0785

von Bülow, S., & Hummer, G. (2020). Kinetics of Atg2-mediated lipid transfer from the ER can account for phagophore expansion. *BioRxiv*. https://doi.org/10.1101/2020.05.12.090977

Wen, X., & Klionsky, D. J. (2016). An overview of macroautophagy in yeast. *Journal of Molecular Biology*, *428*(9), 1681–1699. https://doi.org/10.1016/j.jmb.2016.02.021

Wing, S. S., Chiang, H. L., Goldberg, A. L., & Dice, J. F. (1991). Proteins containing peptide sequences related to Lys-Phe-Glu-Arg-Gln are selectively depleted in

liver and heart, but not skeletal muscle, of fasted rats. *Biochemical Journal*, *275*(1), 165–169. https://doi.org/10.1042/bj2750165
Wong, L. H., Čopič, A., & Levine, T. P. (2017). Advances on the Transfer of Lipids by Lipid Transfer Proteins. *Trends in Biochemical Sciences*, *42*(7), 516–530. https://doi.org/10.1016/j.tibs.2017.05.001
Xie, Z., Nair, U., & Klionsky, D. J. (2008). Atg8 Controls Phagophore Expansion during Autophagosome Formation. *Molecular Biology of the Cell*, *19*(8), 3290–3298. https://doi.org/10.1091/mbc.e07-12-1292
Yamada, T., Carson, A. R., Caniggia, I., Umebayashi, K., Yoshimori, T., Nakabayashi, K., & Scherer, S. W. (2005). Endothelial nitric-oxide synthase antisense (NOS3AS) gene encodes an autophagy-related protein (APG9-like2) highly expressed in trophoblast. *Journal of Biological Chemistry*, *280*(18), 18283–18290. https://doi.org/10.1074/jbc.M413957200
Yamamoto, H., Fujioka, Y., Suzuki, S. W., Noshiro, D., Suzuki, H., Kondo-Kakuta, C., Kimura, Y., Hirano, H., Ando, T., Noda, N. N., & Ohsumi, Y. (2016). The Intrinsically Disordered Protein Atg13 Mediates Supramolecular Assembly of Autophagy Initiation Complexes. *Developmental Cell*, *38*(1), 86–99. https://doi.org/10.1016/j.devcel.2016.06.015
Yamamoto, H., Kakuta, S., Watanabe, T. M., Kitamura, A., Sekito, T., Kondo-Kakuta, C., Ichikawa, R., Kinjo, M., & Ohsumi, Y. (2012a). Atg9 vesicles are an important membrane source during early steps of autophagosome formation. *Journal of Cell Biology*. https://doi.org/10.1083/jcb.201202061
Yamasaki, A., Alam, J. M., Noshiro, D., Hirata, E., Fujioka, Y., Suzuki, K., Ohsumi, Y., & Noda, N. N. (2020). Liquidity Is a Critical Determinant for Selective Autophagy of Protein Condensates. *Molecular Cell*, *77*(6), 1163-1175.e9. https://doi.org/10.1016/j.molcel.2019.12.026
Yamasaki, A., & Noda, N. N. (2017). Structural Biology of the Cvt Pathway. *Journal of Molecular Biology*, *429*(4), 531–542. https://doi.org/10.1016/j.jmb.2017.01.003
Yan, J., Kuroyanagi, H., Kuroiwa, A., Matsuda, Y. I., Tokumitsu, H., Tomoda, T., Shirasawa, T., & Muramatsu, M. A. (1998). Identification of mouse ULK1, a novel protein kinase structurally related to C. elegans UNC-51. *Biochemical and Biophysical Research Communications*, *246*(1), 222–227. https://doi.org/10.1006/bbrc.1998.8546
Yan, J., Kuroyanagi, H., Tomemori, T., Okazaki, N., Asato, K., Matsuda, Y. I., Suzuki, Y. I., Ohshima, Y., Mitani, S., Masuho, Y., Shirasawa, T., & Muramatsu, M. A. (1999). Mouse ULK2, a novel member of the UNC-51-like protein kinases: Unique features of functional domains. *Oncogene*, *18*(43), 5850–5859. https://doi.org/10.1038/sj.onc.1202988
Yang, A., Herter-Sprie, G., Zhang, H., Lin, E. Y., Biancur, D., Wang, X., Deng, J., Hai, J., Yang, S., Wong, K. K., & Kimmelman, A. C. (2018). Autophagy sustains pancreatic cancer growth through both cell-autonomous and nonautonomous mechanisms. *Cancer Discovery*, *8*(3), 276–287. https://doi.org/10.1158/2159-8290.CD-17-0952
Yeh, Y. Y., Shah, K. H., & Herman, P. K. (2011). An Atg13 protein-mediated self-association of the Atg1 protein kinase is important for the induction of autophagy. *Journal of Biological Chemistry*, *286*(33), 28931–28939. https://doi.org/10.1074/jbc.M111.250324
Yeh, Y. Y., Wrasman, K., & Herman, P. K. (2010). Autophosphorylation within the Atg1 activation loop is required for both kinase activity and the induction of

autophagy in Saccharomyces cerevisiae. *Genetics*, *185*(3), 871–882. https://doi.org/10.1534/genetics.110.116566

Ylä-Anttila, P., Vihinen, H., Jokitalo, E., & Eskelinen, E. L. (2009). 3D tomography reveals connections between the phagophore and endoplasmic reticulum. *Autophagy*. https://doi.org/10.4161/auto.5.8.10274

Yorimitsu, T., & Klionsky, D. J. (2005). Atg11 links cargo to the vesicle-forming machinery in the cytoplasm to vacuole targeting pathway. *Molecular Biology of the Cell*, *16*(4), 1593–1605. https://doi.org/10.1091/mbc.e04-11-1035

Young, A. R. J., Chan, E. Y. W., Hu, X. W., Köchl, R., Crawshaw, S. G., High, S., Halley, D. W., Lippincott-Schwartz, J., & Tooze, S. A. (2006). Starvation and ULK1-dependent cycling of mammalian Atg9 between the TGN and endosomes. *Journal of Cell Science*. https://doi.org/10.1242/jcs.03172

Yu, Z. Q., Ni, T., Hong, B., Wang, H. Y., Jiang, F. J., Zou, S., Chen, Y., Zheng, X. L., Klionsky, D. J., Liang, Y., & Xie, Z. (2012). Dual roles of Atg8 - PE deconjugation by Atg4 in autophagy. *Autophagy*, *8*(6), 883–892. https://doi.org/10.4161/auto.19652

Zaffagnini, G., & Martens, S. (2016). Mechanisms of Selective Autophagy. In *Journal of Molecular Biology*. https://doi.org/10.1016/j.jmb.2016.02.004

Zheng, J. X., Li, Y., Ding, Y. H., Liu, J. J., Zhang, M. J., Dong, M. Q., Wang, H. W., & Yu, L. (2017). Architecture of the ATG2B-WDR45 complex and an aromatic Y/HF motif crucial for complex formation. *Autophagy*, *13*(11), 1870–1883. https://doi.org/10.1080/15548627.2017.1359381

Zientara-Rytter, K., & Subramani, S. (2020). Mechanistic Insights into the Role of Atg11 in Selective Autophagy. *Journal of Molecular Biology*, *432*(1), 104–122. https://doi.org/10.1016/j.jmb.2019.06.017